Lipid-binding features and phosphoinositide-dependent function of the endocytic adaptor protein 2 (AP2)-complex from *Arabidopsis thaliana*

Dissertation

zur Erlangung des

Doktorgrades der Naturwissenschaften (Dr. rer. nat.)

Der Naturwissenschaftlichen Fakultät I

– Biowissenschaften –

der Martin-Luther-Universität

Halle-Wittenberg,

vorgelegt von

Frau Johanna Uhlenberg

Gutachter: Prof. Dr. Ingo Heilmann
Prof. Dr. Edgar Peiter
Prof. Dr. Erika Isono

Eingereicht am: 13.02.2025

Verteidigt am: 26.06.2025

Table of contents

Abbreviations

ΔCyt:PM	difference in Cyt:PM ratios over time
3-AT	3-amino-1,2,4-triazole
A	alanine
AP	alkaline phosphatase
A. tumefaciens	*Agrobacterium tumefaciens*
AAK1	adaptor-associated Kinase1
ANTH	AP180 N-terminal homology
AP180	assembly protein 180
AP2	adaptor protein complex 2
Arabidopsis	*Arabidopsis thaliana*
ARF-GEF	ADP-ribosylation factor -guanine nucleotide exchange factors
AtEH1/Pan1	*Arabidopsis thaliana* Eps15 Homology-domain-containing protein 1/2 homologous to Pan1p
ATM2	*Arabidopsis thaliana* Myosin 2
BFA	Brefeldin A
BCIP	5-bromo-4-chloro-3-indolyl phosphate disodium salt
BH	basic-hydrophobic
BiFC	bimolecular fluorescence complementation
BOR1	boron transporter 1
BRI1	Brassinosteroid Insensitive 1
C. elegans	*Caenorhabditis elegans*
CCP	clathrin coated pit
CCV	clathrin-coated vesicle
CD	circular dichroism
cDNA	complementary DNA
CDP-DAG	cytidine diphosphate diacylglycerol
CESA6	cellulose synthase A catalytic subunit 6
CHC	clathrin heavy chain
CHX	cycloheximide
CIE	clathrin independent endocytosis
CLC	clathrin light chain
CLSM	confocal laser-scanning microscopy
CME	clathrin mediated endocytosis
Col-0	Arabidopsis wild type Columbia 0

COPI/COPII	coat protein I/II
CSC	cellulose synthase complexes
CTAB	cetyltrimethylammonium bromide
Cyt	cytosol
D	aspartic acid
DAG	diacylglycerol
DMSO	dimethyl sulfoxide
DRP	dynamin-related protein
E. coli	*Escherichia coli*
EAP	endocytic accessory protein
ECA1	Epsin–like Clathrin Adaptor 1
EH	Eps15 Homology
ENTH	epsin N-Terminal homology
ER	endoplasmic reticulum
F	phenylalanine
Flot1	Flotillin1
FM4-64	N-(3-triethylammoniumpropyl)-4-(6-(4-(diethylamino) phenyl) hexatrienyl) pyridinium dibromide
FRET	Förster resonance energy transfer
GDI	guanidine nucleotide dissociation inhibitor
GIPC	glycosyl-inositol-phosphoryl-ceramide
GluCer	glucosyl-ceramide
GP	general polarization
GTPase	guanosine triphosphate hydrolase
His_6	hexa histidine
HRP	horse radish peroxidase
HSC70	heat shock cognate 70
I	isoleucine
IMAC	immobilized metal affinity chromatography
IPP	inositol polyphosphate
IPTG	isopropyl-β-thiogalactopyranoside
IR	infrared
K	lysine
K_D	dissociation constant
LCB	free long-chain base

Lin	linker
MBP	maltose-binding protein
mcs	multiple cloning site
MHD	μ-homology domain
MORN	membrane occupation and recognition nexus
MST	microscale thermophoresis
MVB/LE	multivesicular bodies/late endosomes
N	asparagine
NBT	p-nitrotetrazolium blue chloride
NECAP	adaptin ear-binding coat-associated protein
NT	N-terminus
Nub	N-terminal part of ubiquitin aa 1 – 38
NubG	N-terminal part of ubiquitin aa 1 – 38, I13 mutated to G
OD	optical density
OST4	oligosaccharyltransferase 4
P	proline
PCR	polymerase-chain-reaction
PEG	polyethylene glycol
PI	phosphoinositide
PI4K	phosphatidylinositol 4-kinase
PIN1/2	PIN-formed 1/2
PIP5K	phosphatidylinositol 4-phosphate 5-kinase
PIS	phosphatidylinositol synthase
PLC	phospholipase C
PLC-δ1PH	pleckstrin homology domain of phospholipase C-δ1
PM	plasma membrane
PtdCho	phosphatidylcholine
PtdEtn	phosphatidylethanolamine
PtdIns	phosphatidylinositol
PtdIns(3,4)P_2	phosphatidylinositol 3,4-bisphosphate
PtdIns(3,4,5)P_3	phosphatidylinositol 3,4,5-trisphosphate
PtdIns(3,5)P_2	phosphatidylinositol 3,5-bisphosphate
PtdIns(4,5)P_2	phosphatidylinositol 4,5-bisphosphate
PtdIns3P	phosphatidylinositol 3-phosphate
PtdIns4P	phosphatidylinositol 4-phosphate

PtdIns5P	phosphatidylinositol 5-phosphate
PtdOH	phosphatidic acid
PtdSer	phosphatidylserine
PTEN	phosphatase and tensin homolog deleted on chromosome 10
PTM	posttranslational modification
R	arginine
RAC	regulator of actin
RbohD	Respiratory Burst Oxidase Homolog D
ROP	Rho of Plant
ROS	reactive oxygen species
s	second
S. cerevisiae	*Saccharomyces cerevisiae*
SAC	suppressor of actin
SD	spinning disk microscopy
SDS-PAGE	sodium dodecyl sulfate polyacrylamide gel electrophoresis
sfGFP	superfolder green fluorescent protein
SH3	SRC homology 3
SLiM	short linear motif
SNARE	soluble *N*-ethylmaleimide-sensitive-factor attachment receptor
TASH3	TPLATE-associated SRC homology 3 domain-containing protein
T-DNA	transfer DNA of *A. tumefaciens*
TGN/EE	*trans*-Golgi network/early endosomes
TIRF	total internal reflection fluorescence
TML	TPLATE complex muniscin-like
tobacco	*Nicotiana tabacum*
TPC	TPLATE complex
TWD40-1/2	transducin/TPLATE WD40 repeat–containing protein 1/2
VirE2	virulence protein E2
VPS34	VACUOLAR PROTEIN SORTING 34
YTH	yeast two-hybrid

Summary

The ability to regulate the biochemical composition of the plasma membrane (PM) is crucial for cellular function. PM protein homeostasis depends on two complementary processes, exocytosis and endocytosis, with clathrin mediated endocytosis (CME) being the main pathway for internalizing cargo proteins from the PM in plants. Both exocytosis and endocytosis at the PM are dynamic and regulated in time and space. Anionic PM phospholipids, such as phosphoinositides (PIs), contribute to the regulation of CME, and protein recycling from the PM is impaired in plants with perturbed PI metabolism. The molecular mechanisms of CME regulation by PIs are currently not understood.

This thesis addresses the role of regulatory PM phospholipids in controlling CME in plants. Arabidopsis mutants with defects in PM lipid metabolism displayed altered patterns of membrane liquid-phase order when analyzed using the phase-sensitive fluorescent dye, Di-4-ANEPPDHQ, suggesting the pathways for the biosynthesis of different PM lipid classes might be mutually interconnected. Altered PM liquid phase order upon modulation of PI metabolism also resulted in reduced endocytosis of the fluorescent membrane tracer dye, FM4-64, as was previously reported for the Arabidopsis *pip5k1 pip5k2* mutant, which is defective in the formation of the PI, phosphatidylinositol 4,5-bisphosphate (PtdIns(4,5)P_2). The role of PIs in controlling endocytosis was investigated based on the hypothesis that the function of the adaptor protein complex 2 (AP2-complex), a key factor for initiating CME at the PM, is controlled by binding to PIs or to enzymes of PI biosynthesis. Subunits of the AP2-complex interacted with various lipid kinases important for PI biosynthesis, including PIP5K1, PIP5K2 and PIP5K6, which have been functionally implicated in CME. Moreover, the AP2-complex subunits, AP2-α1NT, AP2-σ and possibly AP2-μMHD, directly interacted with PIs, with a pronounced preference for binding PtdIns(4,5)P_2 over PtdIns-monophosphates. The binding of AP2-subunits to PIs is mediated by polybasic protein regions, and substitution variants of AP2-subunits in which key basic residues were altered to acidic residues (AP2-α1NT$_{DDDD}$, AP2-σ$_{DDD}$) showed significantly reduced lipid-binding capability *in vitro*. Compared to results upon overexpression of the respective wild type AP2-subunits, the overexpression of the substitution variants resulted in reduced uptake of FM4-64 in tobacco pollen tubes, or in reduced internalization of the CME cargo protein RbohD into BFA-bodies in Arabidopsis mesophyll protoplasts. While the overexpression of either, AP2-α1 or AP2-σ in tobacco pollen tubes caused abnormal cell morphologies, indicating a perturbed balance between endocytosis and exocytosis, the expression of AP2-subunits with defective PtdIns(4,5)P_2-binding capability had only less pronounced effects on cell morphology. The overall data indicate that the lipid-binding capability of AP2-subunits is important for CME *in vivo*. The data are consistent with the previously observed endocytosis defect of the Arabidopsis *pip5k1 pip5k2* mutant and suggest a possible molecular mechanism for how PtdIns(4,5)P_2 might contribute to controlling CME in plants.

Zusammenfassung

Die Fähigkeit, die biochemische Zusammensetzung der Plasmamembran (PM) zu regulieren, ist entscheidend für die zelluläre Funktion. Die Homöostase von PM-Proteinen hängt von zwei komplementären Prozessen ab, der Exozytose und der Endozytose, wobei die Clathrin-vermittelte Endozytose (CME) der Hauptweg für die Internalisierung von Frachtproteinen aus der PM in Pflanzen ist. Sowohl die Exozytose als auch die Endozytose an der PM sind dynamisch und sowohl zeitlich als auch räumlich reguliert. Anionische PM-Phospholipide, wie z. B. Phosphoinositide (PIs), tragen zur Regulation der CME bei und Recycling von Proteinen aus der PM ist in Pflanzen mit gestörtem PI-Stoffwechsel beeinträchtigt. Die molekularen Mechanismen der CME-Regulation durch PIs sind derzeit nicht verstanden.

Diese Arbeit beschäftigt sich mit der Rolle regulatorischer PM-Phospholipide bei der Kontrolle von CME in Pflanzen. Arabidopsis-Mutanten mit Defekten im PM-Lipidstoffwechsel zeigten bei der Analyse mit dem phasensensitiven Fluoreszenzfarbstoff Di-4-ANEPPDHQ eine veränderte Membranordnung der Plasmamembran, was darauf hindeutet, dass die Wege für die Biosynthese verschiedener PM-Lipidklassen miteinander verbunden sein könnten. Eine veränderte PM-Phasen-Ordnung durch einen veränderten PI-Metabolismus führte auch zu einer verminderten Endozytose des fluoreszierenden Membran-Farbstoffs FM4-64, wie zuvor für die Arabidopsis *pip5k1 pip5k2*-Mutante berichtet wurde, welche Defekte in der Bildung des PIs Phosphatidylinositol-4,5-bisphosphat (PtdIns(4,5)P_2) hat. Die Rolle von PIs bei der Kontrolle der Endozytose wurde auf der Grundlage der Hypothese untersucht, dass die Funktion des Adapterproteinkomplexes 2 (AP2-Komplex), ein Schlüsselfaktor für die Initiierung von CME an der PM, durch die Bindung an PIs oder an Enzyme der PI-Biosynthese gesteuert wird. Untereinheiten des AP2-Komplexes interagierten mit verschiedenen Lipidkinasen, die für die PI-Biosynthese wichtig sind. Darunter PIP5K1, PIP5K2 und PIP5K6, die funktionell an der CME beteiligt sind. Darüber hinaus interagierten die Untereinheiten des AP2-Komplexes, AP2-α1NT, AP2-σ und möglicherweise AP2-μMHD, direkt mit PIs, mit einer ausgeprägten Präferenz für die Bindung von PtdIns(4,5)P_2 gegenüber PtdIns-Monophosphaten. Die Bindung von AP2-Untereinheiten an PIs wird durch polybasische Proteinregionen vermittelt und Substitutionsvarianten von AP2-Untereinheiten, in denen wichtige basische Reste zu sauren Resten verändert wurden (AP2-α1NT_{DDDD}, AP2-σ_{DDD}), zeigten *in vitro* eine signifikant reduzierte Lipidbindungsfähigkeit. Im Vergleich zu den Ergebnissen bei Überexpression der jeweiligen Wildtyp-AP2-Untereinheiten führte die Überexpression der Substitutionsvarianten zu einer verminderten Aufnahme von FM4-64 in Tabakpollenschläuchen oder zu einer verminderten Internalisierung des CME-Frachtproteins RbohD in BFA-Körpern in Arabidopsis-Mesophyll-Protoplasten. Während die Überexpression von AP2-α1 oder AP2-σ in Tabakpollenschläuchen zu abnormalen Zellmorphologien führte, was auf ein gestörtes

Gleichgewicht zwischen Endozytose und Exozytose hindeutete, hatte die Expression von AP2-Untereinheiten mit defekter PtdIns(4,5)P_2-Bindungsfähigkeit nur schwächer ausgeprägte Auswirkungen auf die Zellmorphologie. Die Daten dieser Arbeit deuten darauf hin, dass die Lipidbindungsfähigkeit von AP2-Untereinheiten für CME *in vivo* wichtig ist. Die Daten stimmen mit dem zuvor beobachteten Endozytose-Defekt der Arabidopsis *pip5k1 pip5k2*-Mutante überein und deuten auf einen möglichen molekularen Mechanismus hin, wie PtdIns(4,5)P_2 zur Regulation von CME in Pflanzen beitragen könnte.

1. Introduction

1.1 The plant plasma membrane

In each cell, the plasma membrane (PM) serves as a hydrophobic barrier separating the cellular contents from its environment. However, the PM is far more than a simple boundary, and its functionality extends to the perception and transduction of environmental cues, the selective exchange of substances, intercellular communication, attachment of the cytoskeleton and the positioning of processes governing directed polarized cell growth. Fundamental for this variety of specialized functions are PM-associated proteins, which can be membrane-intrinsic proteins or proteins peripherally associated with the membrane. Important proteins in the PM of plant cells include proteins with functions in cell wall synthesis, signaling receptors or transporters for import and export of substances. While proteins for cell wall biosynthesis aid cell wall deposition and can serve as a morphogenic signal for cell growth, the cell wall separates each cell from its neighbors. Receptor proteins enable the perception of intercellular or exogenous cues like hormones, nutrients, or pathogen infection, and their transformation into intracellular signals, which in turn can trigger downstream signaling cascades into the cytoplasm. Transporter proteins are crucial for active and passive movements of ions, nutrients and other molecules across the membrane. This bidirectional transport plays a central role in cellular metabolism, osmotic regulation and the maintenance of chemical gradients. Together, the various membrane-associated proteins confer functionality to each PM area, building specialized hubs through a sub-compartmentalized nano-organization.

1.2 The PM is a complex multifunctional structure

The structural framework for membrane-associated proteins is provided by bilayer-forming amphiphilic lipids. The lipid composition of the PM is a complex mixture of structural lipids and regulatory lipids, comprised of the three main classes sphingolipids, sterols and glycerolipids, the latter mainly represented by phospholipids (Furt et al., 2011). Sphingolipids can be divided into four classes, free long-chain bases (LCBs), ceramides, glucosyl-ceramide (GluCer) and glycosyl-inositol-phosphoryl-ceramides (GIPCs, Mamode Cassim et al. (2020)). Sterols found in the PM are made up of a planar lipid backbone consisting of four condensed aliphatic rings. Molecular sterol species differ by a multitude of different phytosterol sidechains (Mamode Cassim et al., 2019). Glycerophospholipids are composed of a glycerol backbone with two esterified fatty acids and a phosphate group that links to a hydrophilic head group, which determines the phospholipid classes (Furt et al., 2011). Structural glycerophospholipids, like phosphatidylcholine (PtdCho), phosphatidylethanolamine (PtdEtn) or phosphatidylinositol (PtdIns), are the most abundant glycerophospholipids in plants. Some less abundant lipids include phosphatidic acid (PtdOH),

phosphatidylserine (PtdSer) or the phosphorylated derivates of PtdIns, the phosphoinositides (PIs), and all these minor lipids can exert regulatory roles (Colin & Jaillais, 2020; I. Heilmann, 2016). An overview of relevant lipid classes is given in Figure 1.

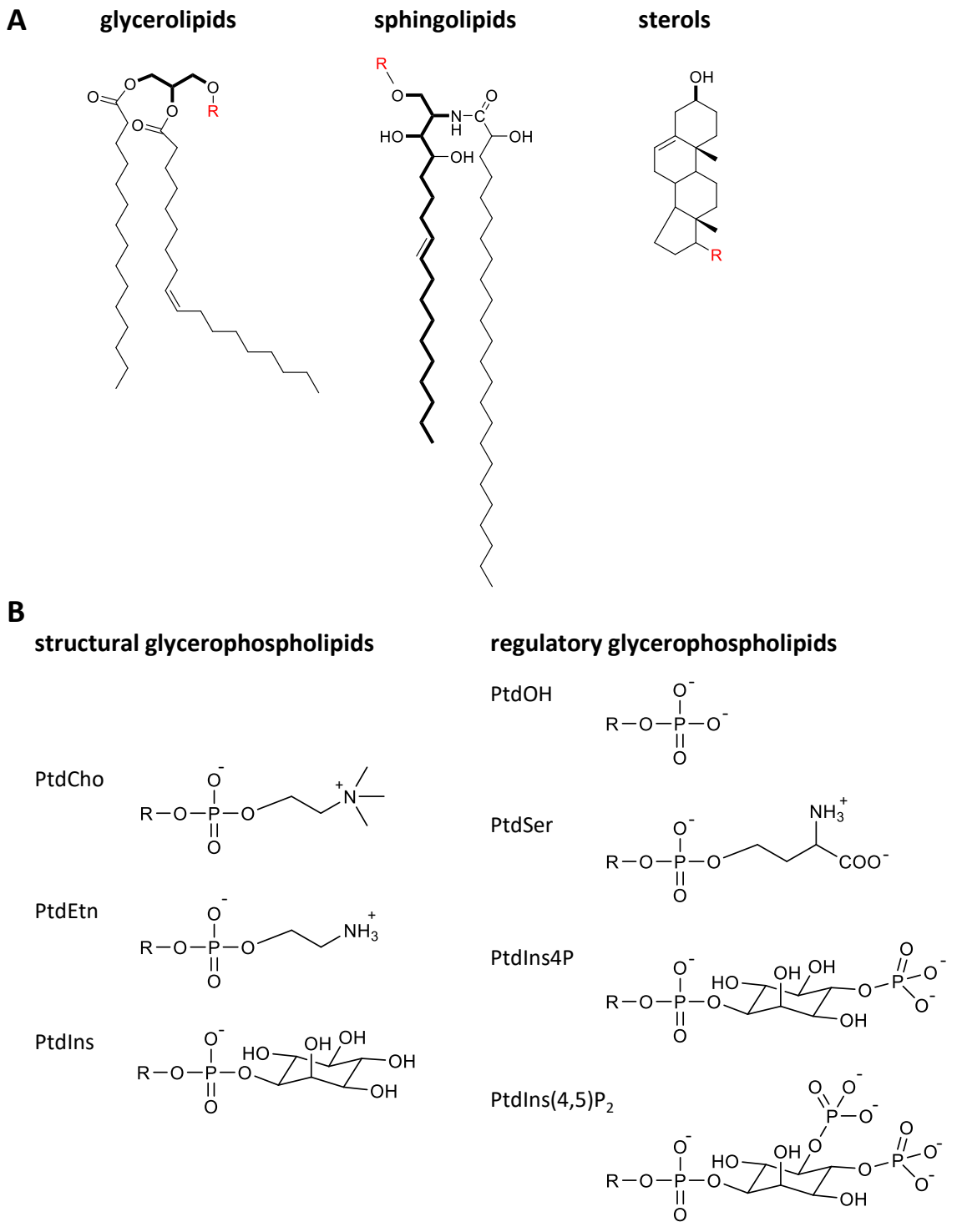

Figure 1. Chemical features of plant plasma membrane lipids. A The chemical structure of the three main classes glycerolipids, sphingolipids and sterols. Glycerolipids are made up of a glycerol backbone (bold lines) with two esterified fatty acyl chains and a hydrophilic head group (indicated by red R), which determines the different glycerolipid-classes. Sphingolipids are made up of a sphingoid backbone called the long-chain base (LCB, bold lines), a fatty acyl chain linked by an amide bond and a polar headgroup attached to the alcohol residue of the LCB (indicated by red R). Sterols are made up of a planar lipid backbone consisting of four condensed aliphatic rings. Molecular sterol species differ by a multitude of different phytosterol

sidechains, indicated by R in red **B** Chemical structure of the hydrophilic headgroups of glycerophospholipids. R indicates the glycerolipid structure as displayed in (A). Structural glycerophospholipids (PtdCho, phosphatidylcholine; PtdEtn, phosphatidyl-ethanolamine; PtdIns, phosphatidylinositol) are displayed left, regulatory glycerophospholipids (PtdOH, phosphatidic acid; PtdSer, phosphatidylserine; PtdIns4P, PtdIns 4-phosphate; PtdIns(4,5)P_2, PtdIns 4,5-bisphosphate) are displayed right.

The different PM lipid classes are not uniformly distributed throughout the bilayers, as initially proposed by the fluid mosaic model (Singer & Nicolson, 1972), but rather display a heterogenous distribution (Figure 2; Jaillais et al. (2024)). The asymmetry of the lipid bilayers between the inner and outer PM leaflets is not very well studied in plants, but sphingolipids together with phytosterols are proposed to mainly reside in the outer leaflet facing the apoplast, while most regulatory lipids are predominantly enriched in the inner leaflet, facing the cytosol (Mamode Cassim et al., 2019). Apart from the asymmetry in lipid composition between the inner and outer PM leaflets, the lateral distribution of lipids within each bilayer is also not homogenous, with local accumulations of certain lipid-classes forming membrane domains. According to a recent attempt to categorize elements of membrane structure, such membrane domains can be categorized as polar domains or as nanodomains (Jaillais et al., 2024). Polar domains are larger membrane regions considered at a cellular level, often linked to cell polarity and processes like cell division and directed growth. By contrast, nanodomains operate at a molecular level with diameters smaller than 1 µm and regulate local molecular interactions of a membrane. Together, the ensuing membrane domain structure impacts protein recruitment and protein distribution, or it may influence the biophysical properties of the membrane. Together, these effects enable the coordination of physiological processes in time and space. So far, the effects of membrane lipid composition on membrane nanostructure are not well understood in plants.

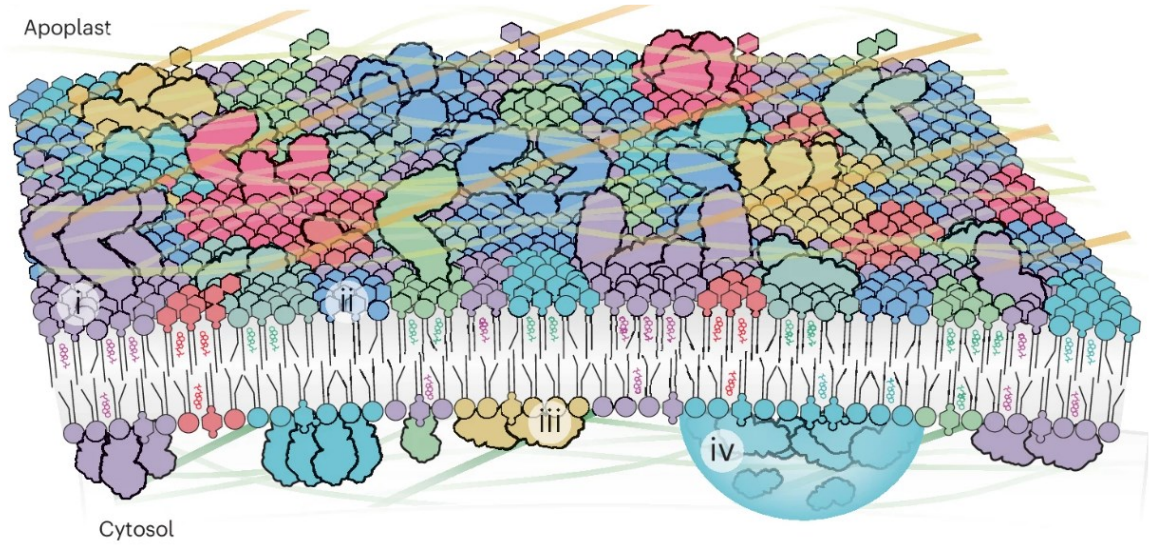

Figure 2. The plant plasma membrane (PM) is a complex multifunctional structure. PM lipids and proteins are arranged in numerous distinct nanodomains, indicated by different colors. Nanodomains can be defined by the assembly of molecules in both PM leaflets (i), in only the outer leaflet (ii) or only in the inner leaflet (iii). Molecular condensates that form associated to the PM can also define a nanodomain (iv). Figure modified from Jaillais et al. (2024).

1.3 Complementary trafficking pathways maintain the protein and lipid composition of the PM

The maintenance of the membrane protein and lipid compositions relies on the two complementary vesicle trafficking processes endocytosis and exocytosis. Newly synthesized or recycled membrane associated proteins and membrane material must be transported from their origin to the PM via exocytosis. The anterograde pathway is the trafficking starting from the endoplasmic reticulum (ER) to the Golgi. From there, material is moved via the *trans*-Golgi network/early endosomes (TGN/EE), which serves as a sorting station, either to the PM or the cell plate, or by passing through multivesicular bodies/late endosomes (MVB/LE) to the tonoplast (Arora & Van Damme, 2021). The vesicles destined for exocytosis are first tethered to the PM, supported by the octameric exocyst complex (Žárský et al., 2013). Through interaction with soluble *N*-ethylmaleimide-sensitive-factor attachment receptor (SNARE) proteins, the exocyst complex facilitates vesicle fusion with the membrane and the subsequent SNARE-mediated membrane fusion and integration of transported cargoes like membrane lipids or proteins into the PM (Mei & Guo, 2018). By contrast, the retrograde trafficking route, endocytosis, is the recycling of PM material or proteins via endocytic vesicles and their sorting via the TGN/EE into the endomembrane trafficking system. Both, the anterograde and retrograde endomembrane trafficking of vesicles requires coat proteins that stabilize and identify the respective types of vesicles. For instance, the coat protein I/II (COPI/COPII) associates with vesicles involved in ER-

Golgi transport, whereas the coat protein clathrin associates with clathrin-coated vesicles (CCVs) mostly involved in PM-TGN/EE transport, and possibly also with outbound vesicles trafficking from the TGN to the PM (Aniento et al., 2022). During trafficking to and from the PM, vesicles can move along cytoskeletal strands, which attach by an unknown mechanism to particular sites at the inner face of the PM (Aniento et al., 2022).

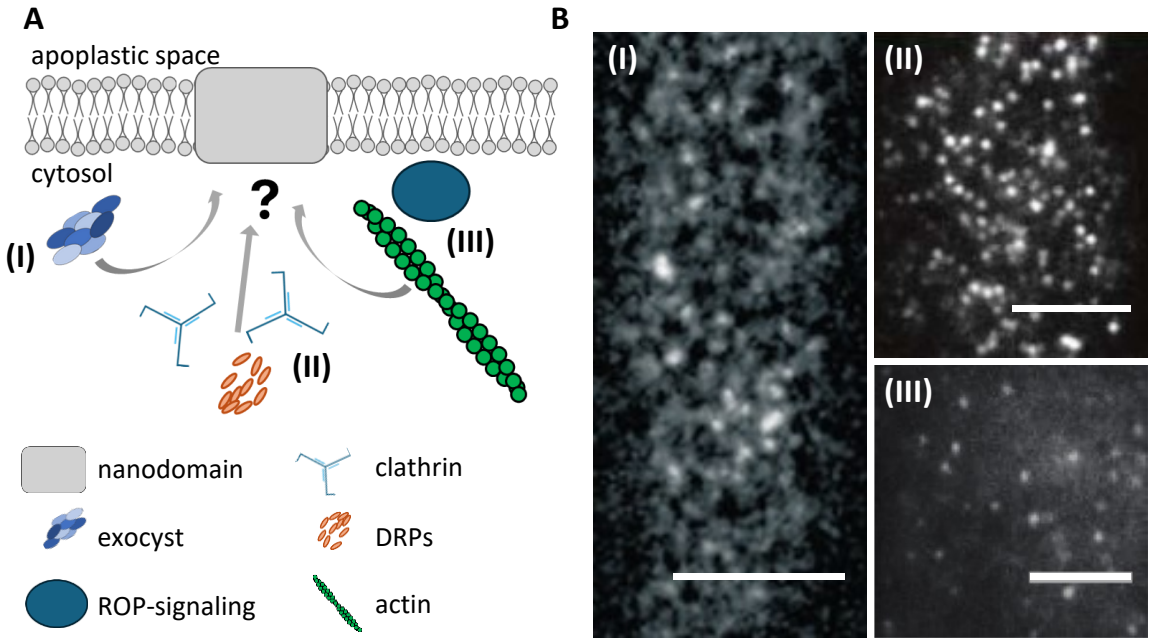

Figure 3. Exocytosis, endocytosis and cytoskeletal attachment occurs in membrane nanodomains. A Some markers for exocytosis (I)-represented by exocyst complex, endocytosis (II)- represented by Dynamin related proteins (DRPs) and clathrin and cytoskeletal attachment (III)- represented by actin and Rho of plants (ROP)-signaling occur in membrane nanodomains (depicted as grey box). The principles by which the membrane nanodomains are targeted are not understood. **B** Examples of markers of exocytosis (I), endocytosis (II) and cytoskeletal attachment (III) that show dynamic, punctate localization at the plasma membrane. (I) Arabidopsis exocyst subunit SEC3A-GFP in root epidermal cells. Scale bar=5 µm. Zhang et al. (2013). (II) Dynamin related protein DRP2A-GFP in root epidermal cells. Scale bar=5 µm. Gnyliukh et al. (2024). (III) Rho of plants isoform GFP-ROP6 after treatment with the synthetic auxin naphthalene-1-acetic acid (NAA) in root epidermal cells. Scale bar=5 µm. Platre et al. (2019).

The balance of insertion into and recycling from the PM defines the membrane-half-life of a protein and therefore controls the execution of certain processes. Hence the protein distribution by vesicular trafficking is tightly controlled and a multitude of different proteins are involved in the orchestration of vesicular trafficking in time and space. The sites of insertion and recycling are defined by a specific membrane composition, with regard to both proteins and lipids and can be visualized in living cells by expressing fluorescence-tagged variants of the relevant proteins and monitoring their subcellular distribution by confocal microscopy (Figure 3). The analysis of dynamic fluorescence markers at high resolution at the cell surface is achieved by total internal reflection fluorescence microscopy (TIRF) or spinning disk microscopy (SD, explained in more detail in section 5.26). Using TIRF or SD microscopy, markers for exocytosis, endocytosis or for cytoskeletal dynamics appear as punctate signals of <1 µm diameter at the cell surface, which

represent PM nanodomains (Figure 3B). Fluorescence-tagged proteins displaying such distribution patterns include SEC3A-GFP (Zhang et al., 2013), a subunit of the exocyst complex, dynamin-related proteins (DRPs) involved in endocytosis, such as DRP2A-GFP (Gnyliukh et al., 2024), or Rho of Plant (ROP) proteins (also called regulator of actin (Rac) proteins), which can mediate the assembly of PM-associated cytoskeletal structures, such as GFP-ROP6 (Figure 3B; Platre et al. (2019)). The molecular principles by which membrane areas are targeted for secretion, endocytosis or cytoskeletal attachment are currently not well known, but various studies indicate a role for regulatory membrane lipids and especially PIs in the control of these processes (Bloch et al., 2016; Ischebeck et al., 2013; Platre et al., 2019).

1.4 The plant PI system

PIs are the phosphorylated derivates of PtdIns and are formed by sequential phosphorylation at different position of the D-*myo*-inositol headgroup by specific lipid kinases (Figure 4). In plants there are five different PI species documented. These include the PtdIns-monophosphates, PtdIns 3-phosphate (PtdIns3P), PtdIns 4-phosphate (PtdIns4P) and PtdIns 5-phosphate (PtdIns5P) as well as the PtdIns-bisphosphates, PtdIns 3,5-bisphosphate (PtdIns(3,5)P_2) and PtdIns 4,5-bisphosphate (PtdIns(4,5)P_2). PtdIns 3,4-bisphosphate (PtdIns(3,4)P_2) and PtdIns 3,4,5-trisphosphate (PtdIns(3,4,5)P_3) known from other eukaryotic organisms have not been shown to be present in plants (M. Heilmann & Heilmann, 2015). In *Arabidopsis thaliana* (Arabidopsis), PtdIns is synthesized from D-*myo*-inositol and cytidine diphosphate diacylglycerol (CDP-DAG) by PtdIns synthase (PIS). Phosphorylation of PtdIns at the D3 or D4 position is mediated by PtdIns 3-kinase or PtdIns 4-kinase, respectively. The genome of Arabidopsis codes for one PtdIns 3-kinase, VACUOLAR PROTEIN SORTING 34 (VPS34), and for two subfamilies of PtdIns 4-kinases with two isoforms each (PI4Kα1/α2 and PI4Kβ1/β2; Mueller-Roeber & Pical (2002)). Further phosphorylation of PtdIns3P or PtdIns4P at the D5 position of the inositol rings is mediated by PtdIns3P 5-kinases and PtdIns4P 5-kinases (PI4P 5-kinases), resulting to the formation of PtdIns(3,5)P_2 and PtdIns(4,5)P_2, respectively. Four PtdIns3P 5-kinase isoforms (FAB1A-FAB1D), and eleven isoforms of PI4P 5-kinases (PIP5K1-PIP5K11) are encoded in the Arabidopsis genome (Mueller-Roeber & Pical, 2002). Despite the presence of PtdIns5P in plants, no enzyme has been identified that can form this lipid from PtdIns. Instead, it is assumed that PtdIns5P is formed by dephosphorylation of PtdIns(3,5)P_2 or PtdIns(4,5)P_2 by a lipid phosphatase (M. Heilmann & Heilmann, 2015; Meijer et al., 2001). Lipid phosphatases also counteract the biosynthesis of different PI species by lipid kinases by dephosphorylation, including phosphoinositide 5-phosphatases (5PTase), suppressor of actin (SAC) phosphatases or phosphatase and tensin homolog deleted on chromosome 10 (PTEN) phosphatases (Mueller-Roeber & Pical, 2002; Zhong

& Ye, 2003). PIs can also be degraded by hydrolytic removal of the lipid headgroup. The hydrolysis between glycerol and phosphate by phospholipase C (PLC) results in the formation of diacylglycerol (DAG) and the phosphorylated headgroups (inositol polyphosphates, IPPs), which can be further phosphorylated and exert functions as soluble messengers (M. Heilmann & Heilmann, 2024).

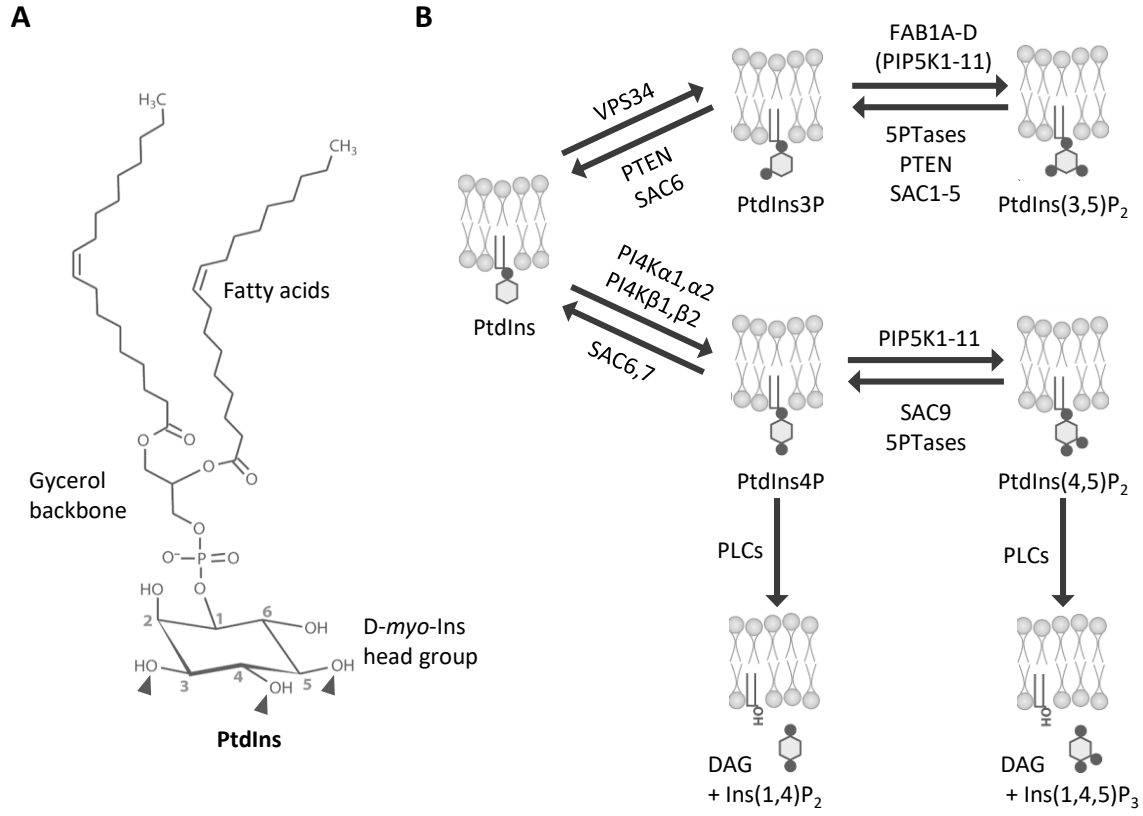

Figure 4. Phosphoinositide biosynthesis and degradation in plants. A Structure of phosphatidylinositol (PtdIns). PtdIns is composed of a glycerol backbone with two esterified fatty acids and an inositol headgroup. The positions of hydroxyl groups targeted by different PI kinases are marked by arrowheads (D3, D4 and D5). Positions D2 and D6 of the inositol ring are likely not available for phosphorylation due to sterical constraints at the membrane surface. **B** Schematic overview from the key reactions of the phosphoinositide (PI) biosynthesis and degradation, starting at PtdIns. The enzymes catalyzing the reactions are depicted together with arrows indicating each individual enzymatic step. Abbreviations: 5PTase, phosphoinositide 5-phosphatase; DAG, diacylglycerol; Ins(1,4)P_2, inositol 1,4-bisphosphate; Ins(1,4,5)P_3, inositol 1,4,5-trisphosphate; PI4K, phosphatidylinositol 4-kinase; PIP5K, phosphatidylinositol 4-phosphate 5-kinase; PLC, phospholipase C; PtdIns(3,5)P_2, PtdIns 3,5-bisphosphate; PtdIns(4,5)P_2, PtdIns 4,5-bisphosphate; PtdIns3P, PtdIns 3-phosphate; PtdIns4P, PtdIns 4-phosphate; PTEN, phosphatase and tensin homolog deleted on chromosome 10; SAC, suppressor of actin; VPS34, VACUOLAR PROTEIN SORTING 34. Figure modified from Gerth et al. (2017).

PtdIns(4,5)P_2 is among the best-studied PIs in plants, as numerous physiological processes at the PM can be attributed to a regulatory contribution of this lipid, including exocytosis, endocytosis or the attachment of cytoskeletal elements to the PM (M. Heilmann & Heilmann, 2024). As PtdIns(4,5)P_2 will also play an important role in this thesis, the enzymes involved in its biosynthesis shall be introduced with some additional detail. The eleven PI4P 5-kinase isoforms encoded in the Arabidopsis genome can be categorized into subfamily A (PIP5K10 and PIP5K11) and subfamily B

(PIP5K1-PIP5K9), according to their domain structure. Subfamily A has a domain structure highly similar to the PI4P 5-kinases from mammals, consisting largely of a dimerization domain and a catalytic domain (Mueller-Roeber & Pical, 2002). By contrast, PI4P 5-kinases of Arabidopsis subfamily B are characterized by plant specific additional N-terminal domains, the N-terminal domain (NT), the membrane occupation and recognition nexus (MORN) repeat domain and a variable linker region (Lin; M. Heilmann & Heilmann (2015)). The PI4P 5-kinases also differ in terms of their tissue-specific expression. While the promoters of the *PIP5K1, PIP5K2, PIP5K7, PIP5K8* and *PIP5K9* genes are ubiquitously active throughout Arabidopsis organs, the *PIP5K3* gene is expressed in a root-specific manner. *PIP5K6* is primarily expressed in pollen tubes, with only weak ubiquitous expression. The *PIP5K4, PIP5K5, PIP5K10* and *PIP5K11* genes are expressed in a pollen tube-specific manner (I. Heilmann, 2016).

While perturbance of PI-metabolism, especially the formation of PtdIns(4,5)P_2, has been shown to influence the secretory pathway, endocytosis and cytoskeletal attachment, the molecular targets for lipid-dependent regulation remain mostly unclear. This thesis addresses the role of PIs in the initiation of clathrin mediated endocytosis (CME).

1.5 Endocytosis in plant cells

Plant endocytosis can be divided into CME or clathrin independent endocytosis (CIE). While CME is the best studied and major mode of internalization in plants, much less is known about the mechanisms of CIE and most of the machinery involved is still not well understood (Paez Valencia et al., 2016; Reynolds et al., 2018). In mammalian cells, caveolins and flotillins are thought to participate in CIE. However, caveolins are not present in plants and only flotillins have been addressed in a number of previous studies (Borner et al., 2005; Frick et al., 2007). Flotillin1 (Flot1) from Arabidopsis forms membrane domains that differ in their localization as well as in their dynamic behavior from clathrin-decorated membrane domains (R. Li et al., 2012). It has been proposed that flotillin-associated endocytosis functions in seedling development, relies on sterols and is sensitive to environmental cues, including elicitor treatment (e.g., the flagellin-derived peptide elicitor flg-22) or salt stress (Baral et al., 2015; Cao et al., 2020; R. Li et al., 2012; Yu et al., 2017). For some protein cargoes, both CME and CIE are implicated as internalization mechanisms, however the regulation of the coordination between CME and CIE remains unclear (Kraus et al., 2024). Based on the abundance in cells and the mass of transported cargoes, the more prominent endocytic pathway in eukaryotic systems is CME.

1.5.1 Molecular components involved in CME

CME depends on various endocytic accessory proteins (EAPs) orchestrating the dynamic multistep process of membrane internalization. CME can be categorized into several steps (Figure 5), beginning with the initiation and cargo recognition, followed by the bending of the membrane and the subsequent assembly of the clathrin coat in clathrin coated pits (CCPs). A vesicle formed by these steps at the cytosolic membrane surface is then released from the membrane via scission and finally transported and uncoated. The whole process from initiation to the release of vesicle occurs in plant cells within a time frame of 20 to 70 s (Kraus et al., 2024).

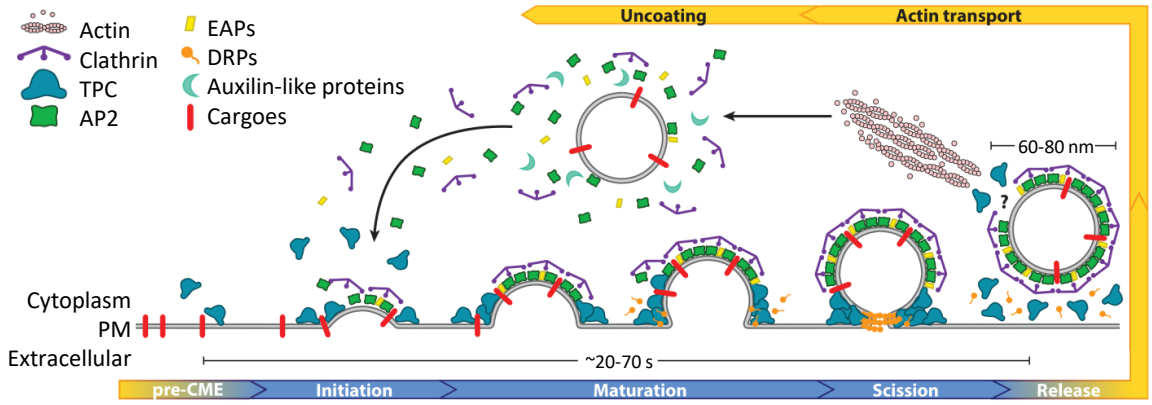

Figure 5. Schematic representation of clathrin mediated endocytosis in plant cells. CME occurs within a time interval of 20 s to 70 s, beginning with the initiation by cargo and lipid recognition, likely facilitated by the adaptor-protein complexes TPLATE complex (TPC) and the adaptor-protein complex 2 (AP2); followed by the recruitment of clathrin triskelia and other endocytic accessory proteins (EAPs); assembly of the clathrin coat and maturation of the clathrin coated vesicle with subsequent scission and release of the vesicle into the cytoplasm. Scission is aided by dynamin-related proteins (DRPs) and the released vesicle is transported along actin filaments to its destination, where it is uncoated with the help of auxilin-like proteins. Figure modified from Kraus et al. (2024).

The initiation and cargo recognition are mediated by different adaptor proteins, which can be monomeric like the assembly protein 180 (AP180), epsin or AP180 N-terminal homology (ANTH) and epsin N-Terminal homology (ENTH) proteins (Holstein & Oliviusson, 2005). Additionally, there are two multimeric adaptor protein complexes involved in CME in plants, the adaptor protein complex 2 (AP2) and the TPLATE complex (TPC), which both can mediate the important link between cargo recognition and clathrin recruitment (Reynolds et al., 2018). Cargo-proteins are recognized by their sorting motifs in the cytosolic facing domains of the protein. These motifs can either be short linear motifs (SLiMs) or posttranslational modifications (PTMs), such as phosphorylation or ubiquitination (Isono et al., 2024). The two most relevant SLiMs from mammalian systems, the tyrosin motif YXXΦ, with Φ being a bulky hydrophobic amino acid, and the acidic dileucine motif [DE]XXXL[LI] seem to be conserved in plants, but their relevance in internalizing plant cargoes from the PM remains unclear. Moreover, there may be also additional motifs like the “double NPF” (asparagine (N), proline (P), phenylalanine (F)) motif, recognized by a TPC subunit, or other yet uncharacterized SLiMs facilitating cargo recognition (De Meyer et al.,

2023). After cargoes are recognized by binding to an adaptor complex, the clathrin coat is assembled by the three-dimensional oligomerization of clathrin triskelia, which each consist of three clathrin heavy chains (CHCs) and three clathrin light chains (CLCs, Dahhan et al. (2022)). The Arabidopsis genome encodes two isoforms of CHCs and three isoforms of CLCs. Mature CCVs are released into the cytosol by scission, mediated by dynamins and DRPs. In plants, two out of the six DRP families (DRP1 and DRP2) function in context of CME (Bednarek & Backues, 2010). DRPs are large guanosine triphosphate hydrolases (GTPases), and are recruited early during CME to CCPs, forming oligomeric rings around the neck of maturing CCVs. Upon GTP hydrolysis and subsequent conformational change, DRPs promote the scission of the CCV from the membrane. The detachment of CCVs from a membrane enables directional trafficking of the vesicle along cytoskeletal strands, in plants supposably actin filaments (Narasimhan et al., 2020; P. Wang et al., 2019). Vesicles in transit are uncoated, but there is currently limited information about CCV uncoating in plants. In yeast and mammals, the uncoating of the CCV is mediated by auxilin and ATPase heat shock cognate 70 (HSC70; Ungewickell et al. (1995)). Although in plants two auxilin-like (AUXILIN-LIKE1/2) proteins have been identified, that can interact with clathrin and an ANTH domain protein, *auxilin-like1/2* loss-of-function lines did not display CME related phenotypic defects (Adamowski et al., 2018). Moreover, uncoating of CCVs in plant cells appears to be delayed compared to that in yeast or mammals, as the coat is not disassembled directly after scission but sequentially on the vesicle's way to the EE (Narasimhan et al., 2020). These findings suggest that the uncoating process in plants may function differently than in other eukaryotic systems. Another difference in CME between plants and yeast/mammals is the role of actin during CME. While actin is essential for the promotion of membrane bending and vesicle formation against turgor pressure in yeast and mammals (Kaksonen & Roux, 2018), in plants this process is possibly facilitated by the TPC and actin is only mandatory for the guidance of the CCVs to their destination (Johnson et al., 2021; Narasimhan et al., 2020). At the physiological level, plant endocytosis is regulated by multiple factors, including the phytohormones auxin, salicylic acid or strigolactone, by the presence of metal substrates, or by biotic interactions with pathogens or symbionts. Additionally, abiotic factors like light, temperature or gravity may also contribute to the regulation of endocytic cycling of protein cargoes (Paez Valencia et al., 2016). In sum, many aspects of CME in plants seem to be conserved in a similar manner as in other eukaryotic systems, yet there are several unique features in plants. One of the major differences in plants is the coexistence of two early adaptor protein complexes, the canonical AP2-complex and the plant specific TPLATE complex.

The structural elements of the AP2 or TPLATE complexes have been well studied. AP2 is a hetero-tetrameric complex formed by the subunits AP2-α, -β, -μ and -σ (Figure 6; Bashline et al., 2013; Di Rubbo et al., 2013; Fan et al., 2013; Kim et al., 2013; Yamaoka et al., 2013). The hetero-octameric

TPC consist of the subunits TPLATE, TPLATE-associated SRC homology 3 (SH3) domain-containing protein (TASH3), LOLITA, transducin/TPLATE WD40 repeat–containing protein 1/2 (TWD40-1, TWD40-2), TPLATE complex muniscin-like (TML), *A. thaliana* EH domain-containing protein 1/2 homologous to Pan1p (AtEH1/Pan1, AtEH2/Pan1; Figure 6; Gadeyne et al. (2014)).

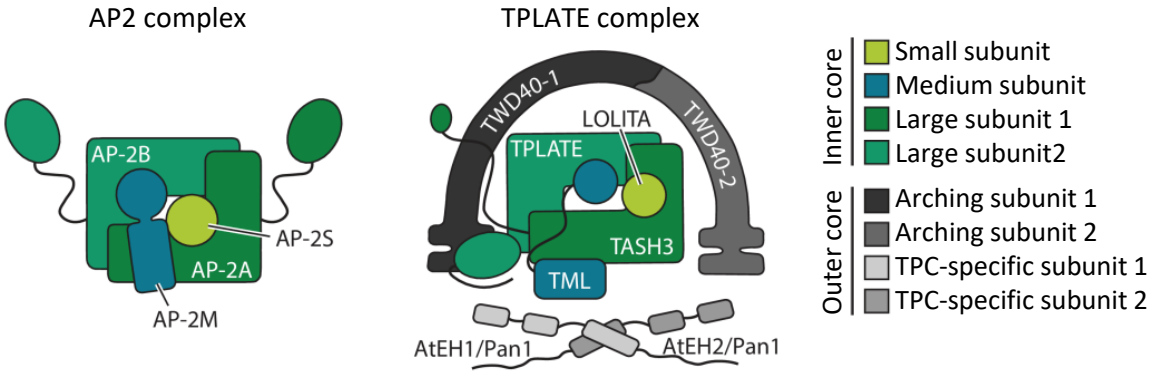

Figure 6. Schematic representation of the structure of the two adaptor protein complexes in plants. The tetrameric AP2-complex consists of the subunits AP2-α, AP2-β, AP2-μ and AP2-σ. TPLATE complex (TPC) is an octameric complex, consisting of the subunits TPLATE, TPLATE-associated SH3 domain-containing protein (TASH3), LOLITA, transducin/TPLATE WD40 repeat–containing protein 1/2 (TWD40-1, TWD40-2), TPLATE complex muniscin-like (TML) and *A. thaliana* EH domain-containing protein 1/2 homologous to Pan1p (AtEH1/Pan1, AtEH2/Pan1). The four inner core TPC-subunits are homologous to the AP2-subunits. Figure modified from Kraus et al. (2024).

While the TPC subunits AtEH1/Pan1 and AtEH2/Pan1 are most likely plant-specific with no homologs in other eukaryotes, homologs of the subunits TPLATE, TASH3, LOLITA, TML, TWD40-1 and TWD40-2 can also be found in the amoeba *Dictyostelium discoideum* as a hexamer complex called TSET (Hirst et al., 2014). The inner core subunits TPLATE, TASH3, LOLITA and TML are homologous to the AP2-subunits AP2-β, AP2-α, AP2-σ and AP2-μ, indicating that TPC and AP2 share their evolutional origin (Figure 6; Kraus et al. (2024)). TPC interacts with clathrin CHCs and CLCs, AP2, DRPs and proteins containing the ANTH domain (Gadeyne et al., 2014). Arabidopsis mutant lines lacking TPC subunits are pollen lethal, indicating a crucial role of the complex for certain endocytosis processes involved in apical tip growth (Reynolds et al., 2018). TPC is suggested to play a role in the early events of endocytosis as it is one of the first EAPs arriving at the PM, preceding dynamins and clathrin (Gadeyne et al., 2014; Narasimhan et al., 2020). Different previous studies describe the arrival of TPC and AP2 at the plasma membrane as concomitant for AP2-μ and TPLATE (Johnson et al., 2021), or as TPLATE and TML arriving slightly before AP2-α (Gadeyne et al., 2014). As TPC and clathrin only colocalize at the very beginning of CME and TPC is subsequently excluded from the clathrin assembly area and instead only localizes at the outer rim of the CCVs, it is proposed that TPC functions in membrane bending during CME (Johnson et al., 2021). TPLATE, TML and AtEH1/Pan1 can interact with anionic phospholipids and partly drive condensate formation through these interactions (Dragwidge et al., 2024; Kraus et al., 2024; P.

Wang et al., 2019; Yperman, Papageorgiou, et al., 2021). Both TPC and AP2 address some shared cargoes that are of great relevance for plant growth and development, including the auxin efflux carriers PIN-formed 1/2 (PIN1/2) or the receptor kinase Brassinosteroid Insensitive 1 (BRI1) (Fan et al., 2013; Gadeyne et al., 2014; Kim et al., 2013; D. Liu et al., 2020). Since the coordination between TPC, AP2 and other EAPs during cargo recognitions remains elusive, it is possible that the adaptor proteins get recruited together or that they recognize different motifs on the same cargo, leading to possibly different trafficking routes after CME (Zhang et al., 2015).

Many aspects suggest that TPC and AP2-complexes work in concert, while still maintaining distinct functions. So far, in plants TPC function is better studied than AP2 function. Therefore, this thesis focuses on the molecular function of the AP2-complex.

1.5.2 The adaptor protein complex 2 (AP2-complex)

The AP2-complex is one of the five adaptor complexes AP1 to AP5 in Arabidopsis. While AP1, AP3, AP4 and AP5 operate at endosomal membrane trafficking, the AP2-complex exclusively functions at the PM (Arora & Van Damme, 2021). As mentioned above, the hetero-tetrameric AP2-complex is composed of two large subunits AP2-α (~112 kDa) and AP2-β (~100 kDa), one medium-size subunit AP2-μ (~49 kDa) and a small subunit, AP2-σ (~17 kDa). The Arabidopsis genome encodes two isoforms for each of the large subunits AP2-α (AP2-α1 and AP2-α2) and AP2-β (AP2-β1 and AP2-β2). The β subunits are shared between the AP1 and AP2-complexes and can interact with subunits of either the AP1 or AP2-complexes, hence the β subunits are often referred to as AP1/2-β1 and AP1/2-β2 (C. Liu et al., 2022; Yamaoka et al., 2013). To avoid any confusion, in this thesis AP1/2-β1 and AP1/2-β2 are termed AP2-β1 and AP2-β2, respectively. Figure 7 shows a predicted structure of the assembled AP2-core-complex and the individual subunits from Arabidopsis, according to the Alphafold3 database (Abramson et al., 2024). The large AP2-subunits AP2-α and AP2-β are each composed of a trunk region with stacked α-helices forming a large solenoid domain, which connects through a disordered linker to an appendage domain, subdivided into a sandwich and a platform domain (Figure 7B and C, Kraus et al. (2024)). The medium subunit AP2-μ is structurally composed of an N-terminal globular Longin fold, an ancient feature of eukaryotic trafficking proteins (De Franceschi et al., 2014), that is connected by a small linker to a μ-homology (MHD) domain (Figure 7D). The Longin domain interacts with the α-solenoid domain of the AP2-β subunit (Figure 7A; Kraus et al. (2024)). The small subunit AP2-σ is structured as a globular Longin domain (Figure 7E), that interacts in mammals and most likely also in plants with the AP2-α α-solenoid domain (Figure 7A; Jackson et al. (2010)). Consistent with the role of the AP2-complex as an adaptor between cargo recognition and clathrin recruitment, AP2-α1 and AP2-σ from Arabidopsis physically interact and colocalize with clathrin (Di Rubbo et al., 2013; Fan et al., 2013;

Johnson & Vert, 2017). Mammalian AP2-β binds to clathrin trough a clathrin box motif in the linker region (Kovtun et al., 2020; D. J. Owen et al., 2004), however the molecular basis of the clathrin interaction in plants is not well characterized. Another aspect of AP2-function in plants that is not well understood and differs from other eukaryotic systems is the recognition of cargoes by specific motifs. While plant CME cargoes, such as PIN1, PIN2, BRI1, cellulose synthase A catalytic subunit 6 (CESA6), *Agrobacterium tumefaciens*–derived virulence protein E2 (VirE2) or boron transporter 1 (BOR1), have all been shown to be internalized in an AP2-mediated fashion (Bashline et al., 2013; Di Rubbo et al., 2013; Fan et al., 2013; Kim et al., 2013; X. Li & Pan, 2017; Yoshinari et al., 2019), a motif-specific binding mode of AP2 to cargo proteins has only been demonstrated for VirE2 and BRI1. Both cargo proteins interact via tyrosine motifs with AP2-μ, and mutation of these recognition motifs resulted in reduced endocytosis (X. Li & Pan, 2017; D. Liu et al., 2020). However, another study showed that the tyrosine motif in BOR1 is not recognized by AP2-μ, but instead AP2-μ interacts with the C-terminal tail of BOR1, a protein region devoid of canonical tyrosine motifs for recognition (Yoshinari et al., 2019). So far, no cargoes have been shown to be exclusively internalized via tyrosine or dileucine motif recognition by plant AP2, as has been shown in mammalian systems, indicating that cargo recognition by AP2 in plants is either facilitated by alternative, yet unidentified motifs, or requires other EAPs that mediate cargo recognition (Arora & Van Damme, 2021).

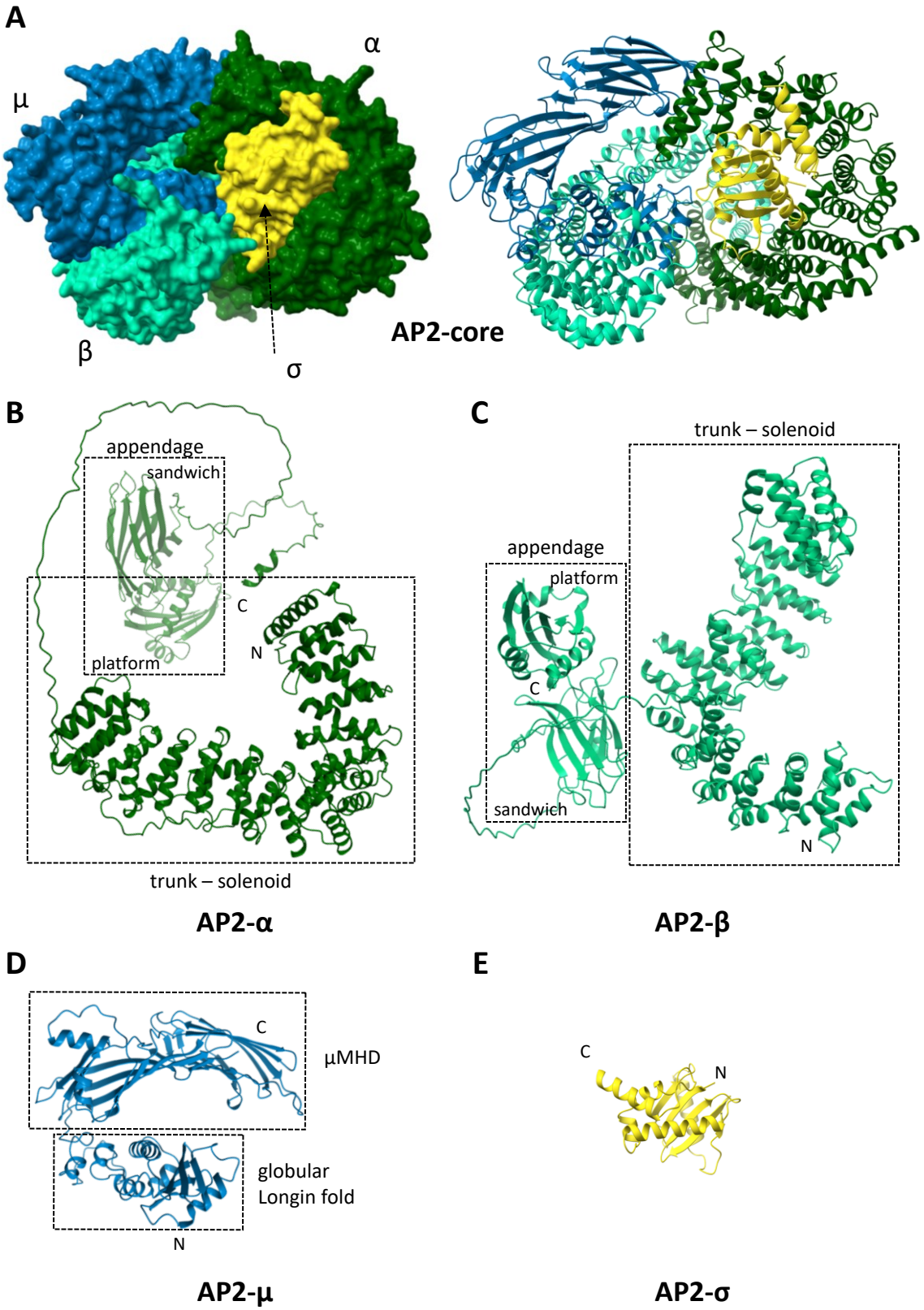

Figure 7. Structure prediction of the AP2-complex from *Arabidopsis thaliana*. A Structure prediction of the AP2-complex core composed of the trunk regions of the two large subunits AP2-α1 (green) and AP2-β2 (teal), the medium subunit AP2-μ (blue) and the small subunit AP2-σ (yellow). For clearer presentation of the structured domains, the disordered linker domain and the appendage domain of AP2-α1 and AP2-β2 are not depicted. Surface representation of AP2-complex core is shown left, ribbon representation in the same orientation is shown right. **B-E** Predicted structures of the individual AP2-subunits shown as ribbon representation colored by the same color key as in (A). Amino (N) terminus and carboxyl (C) terminus are indicated by letters. **B** AP2-α1 (representative for both AP2-α isoforms) is structurally composed of a trunk

region with stacked α-helices forming a large solenoid domain, connected through a disordered linker to an appendage domain, subdivided into sandwich and platform domain as indicated. **C** AP2-β2 (representative for both AP2-β isoforms) is structurally composed of a trunk region with stacked α-helices forming a large solenoid domain, connected through a disordered linker to an appendage domain, subdivided into sandwich and platform domain as indicated. **D** AP2-μ is structurally composed of an N-terminal globular Longin fold, connected by a small linker to a μ-homology (MHD) domain. **E** AP2-σ is structured as a globular Longin domain. Structure predictions of the complex assembly and the individual subunits were generated with the AlphaFold3 web-server application (Abramson et al., 2024); figures were generated with UCSF ChimeraX (Goddard et al., 2018).

Mammalian AP2-complexes can switch between two conformations, an open active form and a closed inactive form (Jackson et al., 2010). At the closed conformation, only one membrane-binding pocket in the α-subunit is exposed to the complex surface, whereas another membrane binding site in the μ-subunit as well as cargo recognition sites and most likely also the clathrin binding box on β are all occluded (Beacham et al., 2019). In this conformation, the AP2-complex will not be functional. The transition to the active conformation requires rearrangements that expose the binding sites for cargo proteins and clathrin and is thought to be stimulated by the interaction with membrane lipids, regulatory proteins, cargo protein-interaction or phosphorylation (Beacham et al., 2019; Partlow et al., 2022). Phosphorylation of Thr-156 in *Hs*AP2-μ by the Adaptor-associated Kinase1 (AAK1) has been suggested to either induce or stabilize the open active form of the mammalian AP2-complex, while some data also propose enhancing effects of the phosphorylation event on lipid and cargo binding (Beacham et al., 2019). Only recently phosphorylation of AP2-μ in plants by a protein kinase orthologous to mammalian AAK1 was discovered (Siao et al., 2023). Similar to the unclear physiological relevance of *Hs*AP2-μ phosphorylation, the effect of the phosphorylation of AP2-μ by AAK1 in Arabidopsis is not well understood, but it has been suggested to contribute to the fine-tuning of endocytosis in roots by regulating AP2 activity (Siao et al., 2023). In mammals, the transition of AP2-complexes from an active conformation back to an inactive conformation may be regulated by adaptin ear-binding coat-associated proteins (NECAPs; Beacham et al. (2018)). While NECAP proteins were also found in Arabidopsis, their function in CME has not been addressed to date (Kraus et al., 2024).

1.5.3 Physiological roles of the Arabidopsis AP2-complex

In contrast to mammals, where the genetic knockout of AP2-subunits is lethal, Arabidopsis AP2 single subunit mutants are viable (Paez Valencia et al., 2016). Mutants lacking AP2-μ were described to have smaller rosette leaves with shorter petioles, morphologically abnormal flowers, unfertilized pistils, shorter and thinner siliques and a significantly reduced seed yield. Additionally, the primary root length is longer in *ap2-μ* mutants than in wild type plants, with agravitropic, wavy and skewing growth (Bashline et al., 2013; Kim et al., 2013; Siao et al., 2023; Yamaoka et al., 2013). In Arabidopsis *ap2-μ* mutants, the endocytosis rate of the membrane-impermeable fluorescent

styryl dye, FM4-64, is reduced as well as that of fluorescently labeled PIN1 proteins (Bashline et al., 2013; Di Rubbo et al., 2013; Siao et al., 2023). Arabidopsis *ap2-σ* mutants exhibit defective organogenesis, a dwarf phenotype with smaller leaves, reduced inflorescence height, and shorter siliques, accompanied by reduced endocytic uptake of FM4-64 and PIN1-GFP compared to wild type plants (Fan et al., 2013). *AP2α-RNAi* lines of Arabidopsis, in which both AP2-α isoforms are targeted for RNAi-suppression, show similar phenotypes as *ap2-μ* mutants, with small siliques, fewer seeds and abnormal phyllotaxis as well as reduced FM4-64 internalization (Di Rubbo et al., 2013; Kim et al., 2013). Whereas Arabidopsis single mutants with defects in either *AP2*-β*1* or *AP2*-β*2* show no detectable phenotype, homozygous double mutants of both *AP2*-β genes are gametophytic lethal or embryo-lethal. Double mutants retaining one functional wild type allele of either *AP2*-β*1* or *AP2*-β*2* have abnormal pollen grains, smaller rosettes, shorter inflorescences and defects in endocytosis as well as in exocytosis (C. Liu et al., 2022).

Overall, the modest phenotypes of Arabidopsis single AP2-subunit knockouts compared to mammals may be explained by the existence of the plant specific alternative adaptor complex, TPC. While the functional relations between AP2 and TPC might, thus, be partially redundant, there might also be further interconnections. Based on work on *Caenorhabditis elegans* (*C. elegans*), AP2-complexes might also function as two independent hemicomplexes. In *C. elegans*, the analysis of single and double mutants with different combinations of defects in AP2-complex subunits suggests that AP2 can function as AP2-α/σ or AP2-β/μ subcomplexes, besides its function as a tetrameric AP2-complex (Gu et al., 2013). In Arabidopsis, some data also suggest a comparable situation, since AP2-μ and -σ still localize to the PM in the respective *ap2-σ* or *ap2-μ* mutant backgrounds (C. Wang et al., 2016). The stability of the tetrameric AP2-complex is controlled by the adaptin binding-like protein P34 (P. Wang et al., 2023). While P34 might also influence the stability of possible hemicomplexes, the existence of AP2 hemicomplexes and their possible regulation by P34 are currently still open questions (Kraus et al., 2024).

Before assembly into functional AP complexes, AP2-subunits are localized in a cytosolic pool and at the PM. The Arabidopsis subunits AP2-α1, AP2-μ and AP2-σ localize diffusely in the cytosol and associate in a transient manner with the PM in punctate structures that display minimal lateral movement (Bashline et al., 2013; Di Rubbo et al., 2013; Fan et al., 2013; Kim et al., 2013; Yamaoka et al., 2013). While PM recruitment of AP2-α1 seems to be concomitant with that of clathrin, AP2-μ and AP2-σ may arrive at the PM before clathrin upon initiation of an endocytic event (Fan et al., 2013; Johnson & Vert, 2017). For AP2-β subunits a dual localization between the PM and intracellular structures, likely the TGN, is reported, consistent with their shared association between AP2 and AP1 complexes in these subcellular locations (C. Liu et al., 2022; C. Wang et al., 2016). The discontinuous localization pattern of AP2-subunits is likely explained by the association

of CME with PM nanodomains. As mentioned above, these PM nanodomains are defined by certain membrane compositions, with regard to proteins and lipids (Jaillais et al., 2024). One of the membrane-lipids known to form dynamic nanodomains is the regulatory lipid PtdIns(4,5)P_2 (Fratini et al., 2021). While regulatory PIs, and especially PtdIns(4,5)P_2, play a role in the early stages of CME (Ischebeck et al., 2013; Y. Zhao et al., 2010), it remains unclear how PIs or PtdIns(4,5)P_2 contribute to AP2 recruitment and function at a molecular level.

1.6 The role of PIs in endocytosis: knowns and not-knowns

The regulation of CME by PIs is better studied and understood in other eukaryotic systems than in plants. In mammalian cells, the AP2-complex plays a fundamental role in regulating endocytosis by interacting with PtdIns(4,5)P_2 (Beacham et al., 2019). There are four putative PtdIns(4,5)P_2 binding sites in mammalian AP2, one within the N-terminus of AP2-α (Collins et al., 2002; Gaidarov & Keen, 1999), two in the subunit AP2-μ (Jackson et al., 2010; Rohde et al., 2002) and AP2-β is also proposed to have an N-terminal PtdIns(4,5)P_2 binding site (Jackson et al., 2010; Kadlecova et al., 2017). Binding to PtdIns(4,5)P_2 is not only described to target the AP2-complex to the PM, but also to activate the complex by mediating conformational rearrangements, enabling cargo binding and subsequent clathrin recruitment (Höning et al., 2005; Jackson et al., 2010; Zaccai et al., 2022). Additionally, human AP2-μ and -β interact with the human type I PI4P 5-kinase, PIPKIγ (Bairstow et al., 2006; Kahlfeldt et al., 2009).

Besides the information from mammalian systems, there are multiple observations from previous studies also in plant systems that implicate PIs in the regulation of CME. Cells displaying pronounced polar tip growth are a good model to study the coordination between secretion, endocytosis and cytoskeletal control, because the cell morphology will be altered upon perturbation of the balance between these processes. *Nicotiana tabacum* (tobacco) pollen tubes with altered PI4P 5-kinase expression show abnormal cell morphologies, likely caused by disruption of the balance between exocytosis and endocytosis. For instance, downregulation of *PIP5K6* expression results in inhibited clathrin assembly at the PM, whereas upregulation induced overactivation of early CME stages (Y. Zhao et al., 2010), similar to phenotypes observed upon *PIP5K4* and *PIP5K5* overexpression in tobacco pollen tubes (Ischebeck et al., 2008). Likewise, downregulation of *PIP5K4* expression inhibits membrane recycling, causing perturbed cell polarity and altered pollen tube growth (Sousa et al., 2008). Effects of PtdIns(4,5)P_2 on endocytosis are not limited to tip-growing cells, and the application of salt stress results in increased PtdIns(4,5)P_2 levels and colocalization of a fluorescence biosensor for PtdIns(4,5)P_2 with a fluorescence marker for CLC, accompanied by increased formation of CCVs (König et al., 2008). Altering PtdIns(4,5)P_2 patterning throughout plant cells by depletion of the PI phosphatase SAC9 results in partially

impaired endocytosis, which also indicates that the restriction of PtdIns(4,5)P_2 to the PM is essential for correct endocytic trafficking (Lebecq et al., 2022).

In addition to the described general effects of PtdIns(4,5)P_2 on the regulation of endocytosis, where the specific targeted steps remain somewhat unclear, there is also evidence suggesting a direct influence on the very early stages of CME, the initiation. The endocytic cycling of the integral membrane NADPH oxidase Respiratory Burst Oxidase Homolog D (RbohD), which generates reactive oxygen species (ROS) at the PM in response to pathogen infection, is reduced upon inactivation of PtdIns(4,5)P_2 production (Menzel et al., 2019). As the reduced PM recycling of RbohD is accompanied by increased ROS production, the defect in PtdIns(4,5)P_2 formation influences CME in such a manner that RbohD remains active at the PM (Menzel et al., 2019). This important observation supports the notion of PtdIns(4,5)P_2 influencing CME at the stage CCP initiation. Arabidopsis *pip5k1 pip5k2* double mutants lacking two ubiquitously expressed PtdIns(4,5)P_2 producing enzymes show severe phenotypic alterations compared to wild type plants, that have been linked to perturbed CME initiation. The *pip5k1 pip5k2* double mutant displays altered auxin distribution, due to defects in the polarization of PIN proteins, which usually requires rapid and efficient endocytic cycling of PIN cargoes (Ischebeck et al., 2013; Tejos et al., 2014). The *pip5k1 pip5k2* double mutant plants also accumulate more cellulose, and the abundance of membrane-associated CESA6 in pavement cells is higher, accompanied by an increased area density of PM localized DRP1C and clathrin foci (AG Heilmann, unpublished data). Together, the unpublished results suggest that cellulose synthase complexes (CSC) accumulate in the PM in an active state, similar to the situation with RbohD (Menzel et al., 2019), resulting in increased cellulose production. In sum, the published and unpublished data indicate that PtdIns(4,5)P_2 is required for the endocytosis of the proteins RbohD, PIN1/2 or CESA6, which are all known cargo proteins of the AP2-complex (Bashline et al., 2013; Fan et al., 2013; Kim et al., 2013). Therefore, experiments in this thesis were devised to address the potential molecular role of PtdIns(4,5)P_2 and other PIs in the function of the Arabidopsis AP2-complex.

2. Aims and objectives

Although it is known that anionic phospholipids, such as PIs, play a role in regulating clathrin mediated endocytosis, and that disruption of PI metabolism impairs endocytic cycling of various important cargo proteins in plants, the precise molecular mechanism by which membrane lipids regulate CME remain unclear. The aim of this thesis was to investigate whether the binding to PIs contributes to the function of the AP2-complex, a key factor for initiating CME at the PM, and the regulation of early endocytosis stages. Individual objectives were set as follows:

- To elucidate how changes in PM lipid composition affect the liquid ordered state of the PM and if the overall PM endocytosis is altered in membranes with a modified lipid composition.
- To elucidate biochemical connections between the AP2-complex and the PI system by testing AP2-subunits for possible protein-protein interaction with PI4P 5-kinases and for protein-lipid interactions with different PIs.
- To identify lipid-binding sites in the AP2-subunits and to generate substitution variants that show reduced or abolished lipid-binding capability.
- To determine whether altered lipid-binding capability of variant AP2-subunits results in impaired endocytosis, and whether it leads to morphological changes at the cellular level.

3. Results

This thesis addresses the influence of membrane lipids on the function of the endocytic adaptor complex AP2. While it is known that anionic phospholipids, such as PIs, contribute to the regulation of the early stages of clathrin mediated endocytosis (Ischebeck et al., 2013; Sousa et al., 2008; Y. Zhao et al., 2010), the precise molecular mechanisms by which membrane lipids influence CME remain unclear. It was the working hypothesis of this thesis that the AP2-complex represents a potential link between the PI system and the control of endocytosis in plants. In mammalian systems, it has been shown that subunits of the AP2-complex can interact with PIs and PI4P 5-kinases involved in PI-biogenesis (Bairstow et al., 2006; Kahlfeldt et al., 2009). Therefore, the objective of this thesis was to investigate possible interactions of Arabidopsis AP2-subunits and PI4P 5-kinases; to assess the lipid-binding capability of AP2-subunits; and to determine whether or not lipid-binding by AP2-complex subunits is important for the physiological functions of the AP2-complex during endocytosis.

3.1 Membrane composition is a complex interplay of different membrane lipids

To set the stage for the analysis of lipid-dependent effects on endocytosis and the AP2-complex, it was first analyzed how altered membrane lipid composition would influence liquid phase order of the PM of Arabidopsis root cells. The liquid phase order of membranes was of interest, because AP2-mediated endocytosis occurs in membrane nanodomains (Bashline et al., 2013; Fan et al., 2013; Yamaoka et al., 2013), likely representing specific liquid phase-ordered states based on a locally asymmetric membrane lipid composition. The liquid phase order of cellular membranes was analyzed by using the fluorescent probe Di-4-ANEPPDHQ, a phase-sensitive membrane dye (Roche et al., 2008). Di-4-ANEPPDHQ can be excited at 488 nm and displays a spectral shift of its emission spectrum depending on the liquid ordered state of the membrane environment into which it is inserted (Figure 8A). Emission spectra recorded at wavelengths between 500 to 580 nm for the liquid ordered state, and between 620 to 750 nm for the liquid disordered state, respectively, can be used to calculate general polarization (GP) values and ratiometric images in approximation of the ratio of liquid ordered vs. liquid disordered states in a membrane (D. M. Owen et al., 2012). The calculation of GP-values is explained in detail in the Material and Methods section 5.15. The degree of membrane liquid phase order was analyzed in roots of Arabidopsis wild type (Col-0), or in various mutants defective in the biosynthesis of relevant membrane lipids. The mutants analyzed included the Arabidopsis *loh1 loh3* double mutant lacking two out of three ceramide synthases (Luttgeharm et al., 2015; Markham et al., 2011; Ternes et al., 2011), the *smt1*^{ORC} mutant lacking a key sterol methyl transferase (Willemsen et al., 2003) or the *pip5k1 pip5k2* double mutant deficient in two key PI4P 5-kinases (Ischebeck et al., 2013; Tejos et

al., 2014). Figure 8B shows representative false colored images of wild type controls or the lipid biosynthesis-mutants *loh1 loh3, smt1*^{orc} or *pip5k1 pip5k2* stained side-by-side with Di-4-ANEPPDHQ. The mean GP-values in post-cytokinetic cell plates were increased in wild type controls compared to the mean PM-associated GP-values in the same cells, as shown in the representative Col-0 detail picture (Figure 8B). The increased GP-values of post-cytokinetic cell plates are consistent with previous findings (Frescatada-Rosa et al., 2014), indicating successful usage of the dye and correct data analysis. Both the *loh1 loh3* mutant as well as the *smt1*^{orc} mutant displayed significantly ($P < 0.001$) increased mean plasma membrane GP-values compared to the wild type controls, indicating a higher degree of membrane liquid phase order at the PM of these mutants. By contrast, the *pip5k1 pip5k2* mutant showed significantly lower GP-values at the PM, indicative of a lower degree of liquid phase order compared to the wild type controls (Figure 8C).

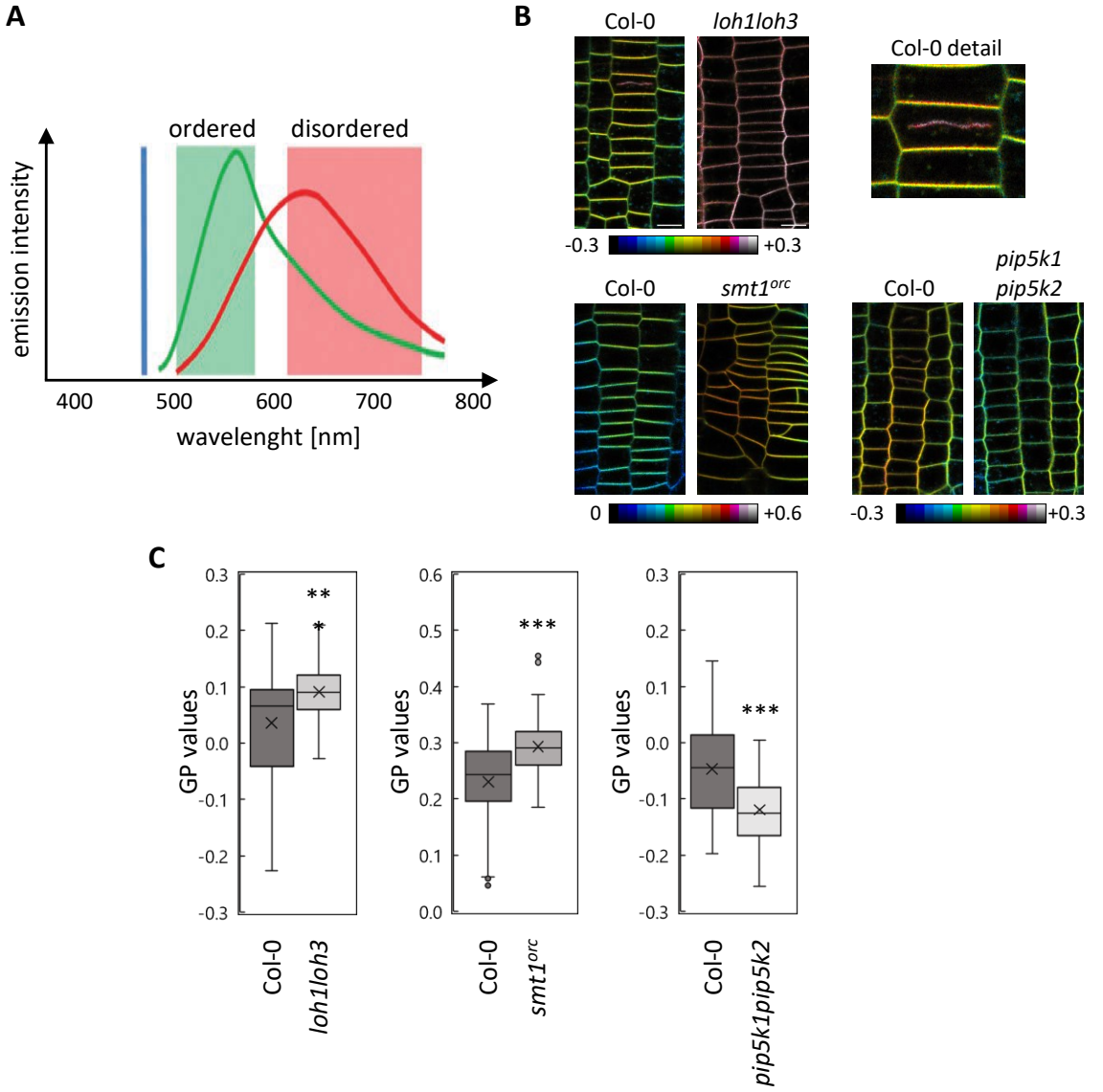

Figure 8. Altered membrane composition of sphingolipids, sterols or PIs influences membrane liquid phase order. The liquid phase order of the PM was analyzed in roots of five-day-old Arabidopsis seedlings using the phase-sensitive dye Di-4-ANEPPDHQ. Plant lines analyzed included Arabidopsis wild type (Col-0)

controls and mutant lines defective in sphingolipid-biosynthesis (*loh1 loh3*), sterol-biosynthesis (*smt1*^{orc}) or in PtdIns(4,5)P_2-biosynthesis (*pip5k1 pip5k2*). **A** Fluorescence properties of Di-4-ANEPPDHQ. The dye is excited at 488 nm (blue line) and displays different emission spectra dependent on insertion in a liquid ordered membrane environment (500 to 580 nm; green line) or in a liquid disordered membrane environment (620 to 750 nm; red line). Figure modified from D. M. Owen et al. (2012). **B** Representative ratiometric false-color images displaying the general polarization (GP) values calculated from the mutant lines and the respective Col-0 control. The Col-0 detail shows a dividing cell with higher GP-values at the cell plate. **C** Diagrams for GP-values recorded at the PM of root cells of various plant lines, as indicated. GP-values are shown as boxplots; x, mean; horizontal line, median; dots indicate outliers. Data represent 150 plasma membrane locations measured in ten seedlings per plant line in one experiment and are representative for three independent experiments with similar results. ***, Significant differences according to a Student's *t*-test ($P < 0.001$).

These analyses of roots in five-day-old seedlings indicate that altered membrane lipid composition, such as arises from defective biosynthesis of sphingolipids, sterols or PIs, is accompanied by altered degrees of overall membrane liquid phase order. While this notion has been reported before for sterols (Frescatada-Rosa et al., 2014; Men et al., 2008), it is worth noting that under the conditions used, the *pip5k1 pip5k2* double mutant with defective PtdIns(4,5)P_2 formation displayed a reduced degree of membrane order, suggesting that the highly charged lipid PtdIns(4,5)P_2 might be a relevant determinant of membrane liquid phase order. This appears especially relevant, because the *pip5k1 pip5k2* double mutant also displays severely reduced rates of CME from the PM (Ischebeck et al., 2013).

As this thesis addresses the influence of membrane lipids on the function of the endocytic adaptor complex AP2, it was next analyzed whether and how altered membrane lipid composition in the different mutants affected the overall rates of endocytosis. One tool to quantify endocytosis rates is the use of the fungal toxin Brefeldin A (BFA), which inhibits the trafficking of material from the trans-Golgi network/early endosome by disturbing the function of the catalytic sec7 domain of the ADP-ribosylation factor (ARF)-guanine nucleotide exchange factors (ARF-GEFs, Singh & Jürgens (2018)). Inhibition of the ARF-GEFs causes the accumulation of newly synthesized proteins as well as that of endocytosed protein cargoes in so called BFA-bodies. BFA-bodies derive from aggregating endosomal and trans-Golgi compartments (Reynolds et al., 2018) and can be visualized by using fluorescent dyes, such as FM4-64. BFA-bodies and endocytic rates can be visualized by monitoring the accumulation of fluorescence in BFA-bodies. The lipophilic dye FM4-64 is commonly used for analyzing the endocytosis of membranes, as it visualizes the endocytic pathway by first labelling the PM, followed by labelling the TGN/EE, multivesicular bodies/late endosome, and over time also the tonoplast (Dragwidge & Van Damme, 2020). For analyzing the rate of endocytosis in the lipid-biosynthesis mutant lines, five-day-old seedlings were stained with 2 µM FM4-64 and subsequently treated with 50 µM BFA. After 30 min of incubation the formation of BFA-bodies in root tip cells was monitored by confocal laser-scanning microscopy and the number of BFA-bodies per cell was quantified. All three mutant lines showed a significantly reduced ($P < 0.01$) number of BFA-bodies compared to wild type controls (Figure 9). There were

no significant differences between the different mutant lines analyzed. The data confirm that perturbed membrane lipid composition results in impaired endocytosis of the FM4-64 dye, as was also observed in previous reports (Ischebeck et al., 2013; Men et al., 2008; Wu et al., 2021).

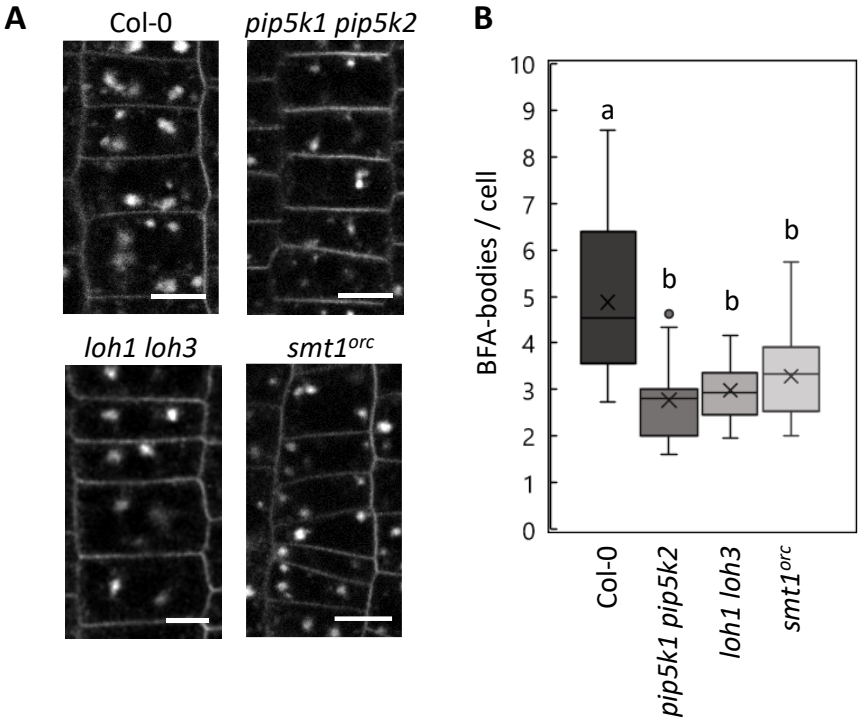

Figure 9. The endocytosis of the FM4-64 dye is reduced in the lipid-biosynthesis mutant lines *pip5k1 pip5k2, loh1 loh3* and *smt1^{orc}*. Five-day-old seedlings were stained with 2 µM FM4-64 and subsequently treated with 50 µM BFA. **A** Images were taken of the root tip as Z-stacks 30 min after BFA treatment. Images show representative Z-projections over few confocal planes. Scale bars = 10 µm. **B** Quantitative analysis of BFA-bodies per cell. Data are shown as boxplots; x, mean; horizontal line, median; dots indicate outliers. Data represents 165 to 250 cells in seven to eight seedlings per plant line from two independent experiments. Significant differences according to a Student's *t*-test ($P < 0.01$) with letters indicating significantly different categories.

The rates of endocytosis in the three mutant lines were all similarly reduced compared to the wild type control (Figure 9B), whereas varying degrees of membrane phase order were determined for the individual mutants and the wild type by the Di-4-ANEPPDHQ analysis (Figure 8C). These patterns suggest a differential contribution of individual lipid classes to functional membrane assemblies, possibly related to the asymmetric distribution of lipids in the PM: While sphingolipids and sterols are predominantly found in the outer leaflet facing the apoplastic space or are embedded into the bilayer, respectively, PIs and PtdIns(4,5)P_2 are thought to reside in the inner, cytosolic leaflet of the PM, making them ideal anchor-points for the recruitment of proteins or protein complexes (I. Heilmann, 2016; Jaillais & Ott, 2020; Mamode Cassim et al., 2019). Therefore, subsequent experiments addressing the contribution of lipids to the regulation of endocytosis focused on the role of membrane PIs, particularly on PtdIns(4,5)P_2. While

PtdIns(4,5)P_2 is associated with efficient endocytosis in plants (Ischebeck et al., 2013; König et al., 2008; Y. Zhao et al., 2010), the underlying molecular roles of PtdIns(4,5)P_2 are currently unclear.

3.2 Subunits of the AP2-complex interact with PI4P 5-kinases

Changes in membrane PI composition do not only influence the degree of overall membrane liquid phase order (Figure 8C), but also result in impaired endocytosis (Figure 9B). This effect has previously been described for Arabidopsis plants displaying depletion of PtdIns(4,5)P_2 upon altered expression of PI4P 5-kinases (Ischebeck et al., 2013; Y. Zhao et al., 2010), or upon posttranslational inhibition of PI4P 5-kinases by phosphorylation (Hempel et al., 2017; Menzel et al., 2019). Based on these findings and the known interaction between human PI4P 5-kinases and *Hs*AP2-μ and *Hs*AP2-β2 (Bairstow et al., 2006; Kahlfeldt et al., 2009; Nakano-Kobayashi et al., 2007), experiments were performed to test the AP2-subunits from Arabidopsis for interaction with different Arabidopsis PI4P 5-kinases (Figure 10).

Protein-protein interactions were first analyzed using the split-ubiquitin based yeast two-hybrid (YTH) system, testing the AP2-subunits against the PI4P 5-kinase isoforms PIP5K1, PIP5K2, PIP5K6 and PIP5K9 as candidate bait proteins (Figure 10A). PIP5K1, PIP5K2 and PIP5K6 all have demonstrated roles in regulating CME (Ischebeck et al., 2013; Menzel et al., 2019; Y. Zhao et al., 2010), whereas PIP5K9 was chosen as a ubiquitously expressed PI4P 5-kinase isoform, without reported relevance for trafficking processes (I. Heilmann, 2016). With AP2-μ or AP2-σ as prey proteins, positive yeast growth under selective conditions was observed for PIP5K1, PIP5K2 and PIP5K6, indicative of protein-protein interactions (Figure 10A). By contrast, no positive yeast growth was observed for AP2-μ or AP2-σ tested against PIP5K9 (Figure 10A). PIP5K1 and PIP5K6 showed additional interactions with AP2-β2 (Figure 10A). The AP2-subunits AP2-α1/2 and AP2-β1, showed no interaction with any of the tested PI4P 5-kinase isoforms in the yeast two-hybrid experiments (Figure 10A).

The candidate interactions from the yeast two-hybrid experiments were to be verified by immuno pull-down experiments. The AP2-subunits that were positive for interaction were immobilized as GST-fusion proteins on a glutathione agarose matrix and incubated with MBP-fused PIP5K1 or MBP-fused PIP5K6. Interacting proteins were then co-eluted with reduced glutathione and detected by using an αMBP antibody. The immuno-pull-down experiments verified interactions between AP2-β2 or AP2-σ with PIP5K1 as well as with PIP5K6 (Figure 10B). GST-μ was not visible in the input detection, indicating that the negative outcome of this interaction test might have been a technical issue with the abundance of one of the candidate proteins, and therefore no statement can be made about a possible interaction of GST-μ with MBP-PIP5K1 or with MBP-PIP5K6. Moreover, a weak signal for MBP-PIP5K1 and MBP-PIP5K6 was observed for the GST

control, indicating unspecific binding of these proteins to the glutathione matrix. The candidate interaction of AP2-subunits with PIP5K2 could not be tested successfully in an immuno pull-down assay, because the quality of the enriched recombinant MBP-PIP5K2 protein was not sufficient (data not shown).

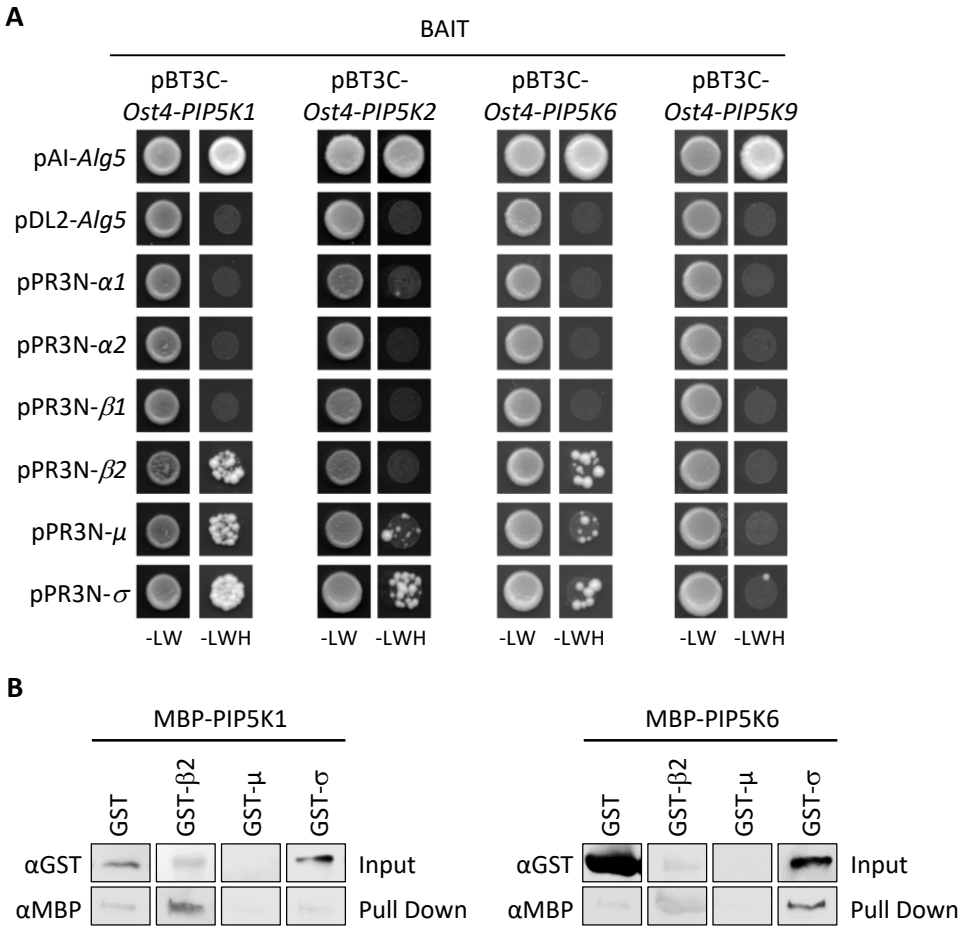

Figure 10. AP2-subunits interact with PIP5K1, PIP5K2 and PIP5K6. A Split-ubiquitin based yeast two-hybrid analysis. PIP5K1, PIP5K2, PIP5K6 and PIP5K9 were used as bait proteins fused to the C-terminal ubiquitin half, an Ost4 ER membrane-anchor and transcription factors. AP2-subunits were used as prey proteins fused to the N-terminal ubiquitin half, *pAI-Alg5* and *pDL2-Alg5* were used as positive and negative control, respectively. Transformed yeast was grown on selective media lacking leucine and tryptophan (-LW) as control for transformation with bait and prey vectors. Growth on media lacking additionally histidine (-LWH) indicated protein-protein interaction. Data is obtained from master thesis (Johanna Uhlenberg) and is representative for three independent experiments testing five colonies each per transformation. **B** *In vitro* immuno pull-down assays of recombinantly expressed MBP-PIP5K1 or MBP-PIP5K6 with recombinantly expressed GST-β2, GST-μ, GST-σ and GST as control. GST fusion proteins were immobilized on glutathione agarose and incubated with MBP fusion proteins. Protein input and co-eluted bound proteins were detected by immunodetection using αGST and αMBP antibody, respectively. Data is obtained from master thesis (Johanna Uhlenberg) and represents three (PIP5K1) or two (PIP5K6) independent experiments.

As there were technical difficulties verifying the interactions between AP2-subunits and PI4P 5-kinases in immuno pull-down assays, the relevant candidate interactions were analyzed by microscale thermophoresis (MST; Figure 11). MST detects changes in the diffusive movement of molecules within a microscopic temperature gradient applied by an infrared (IR)-laser. Upon interaction between molecules, molecular properties, such as charge, size or hydration shell,

change and alter their thermophoretic behavior (Figure 11A; Jerabek-Willemsen et al. (2011)). Such changes in the thermophoretic behavior can be detected and quantified for target molecules that are fluorescently labelled by titrating against candidate ligand molecules. From the MST traces F_{norm} values are calculated as the ratio of the fluorescence intensities recorded after an IR-laser impulse (F_1) and before the impulse (F_0, Figure 11A). The F_{norm} values calculated for ligand concentrations can then be used to calculate dissociation constants (K_D) of the interactions observed. The advantage of MST is the possibility of quantifying interactions between molecules in solution without the need of immobilizing one or both candidate interaction partners tested. To analyze possible interactions between AP2-subunits and PI4P 5-kinases by MST, enriched recombinant AP2-subunits fused to a superfolder green fluorescent protein-tag (sfGFP, appendix Figure 27-Figure 29) were used as targets and recombinant enriched MBP-tagged PI4P 5-kinases as ligands. The AP2-µ subunit was used as a truncated fusion protein consisting of the µ-homology-domain (MHD), because expression of the full-length protein did not yield sufficient amounts. As a negative control, the sfGFP-tag alone was tested for interaction with the PI4P 5-kinase ligands. All sfGFP-fusion proteins were used at a set concentration of approximately 40 nM and the recorded fluorescence intensities were normalized. MBP-tagged PI4P 5-kinases were serially diluted over sixteen concentrations, starting approximately at 0.355 mM for MBP-PIP5K1, 0.545 mM for MBP-PIP5K2 or 0.02 mM for MBP-PIP5K6-His_6. The concentrations of the target sfGFP-fusion proteins and of the MBP-tagged PI4P 5-kinase ligands were estimated by SDS-PAGE with subsequent Coomassie staining, or by immunodetection (Figure 11F; appendix Figure 30). In the MST analysis, the MBP-tagged PI4P 5-kinase ligands were tested in 16 different concentration ratios against a fixed concentration of sfGFP-fused target proteins. MST analyses were performed at an MST-on time of 2.5 s, and binding affinities were estimated as K_D-values according to automated data-curve fitting using the MO.Affinity Analysis software. Every tested PI4P 5-kinase showed interaction with sfGFP-β2-His_6, sfGFP-µMHD-His_6 and sfGFP-σ-His_6, whereas no interaction was detectable with the negative control sfGFP-His_6 (Figure 11B-D). Even though the automated data-curve fitting for the MST analysis between MBP-PIP5K1 and sfGFP-His_6-control resulted in a binding affinity curve, the proteins were considered as not interacting because the signal-to-noise ratio as well as the response amplitude were low, which represent two important quality-check values and are indicative of only minor differences between the MST signals of target and target-ligand complex (appendix Table 14). It is remarkable that the interactions of the sfGFP-tagged AP2-subunits were overall notably weaker for MBP-PIP5K2 compared to the interaction with both MBP-PIP5K1 or MBP-PIP5K6-His_6 (Figure 11E). This difference was most pronounced for sfGFP-σ-His_6, which displayed a ~10^4-fold stronger interaction with MBP-PIP5K6-His_6 compared to the interaction with MBP-PIP5K2. In fact, even with the highest concentration

ratios of MBP-PIP5K2 against the sfGFP-tagged AP2-subunits saturation of the MST affinity curve was not reached, indicative of only weak binding that was nonetheless stronger than that of the negative control, sfGFP-His_6 (Figure 11C). While MBP-PIP5K1 and MBP-PIP5K6-His_6 both displayed stronger interactions with sfGFP-tagged AP2-β2, AP2-μMHD or AP2-σ than MBP-PIP5K2, interactions were overall stronger for MBP-PIP5K6-His_6 than for MBP-PIP5K1 (Figure 11E). As MBP-PIP5K6-His_6 was the only ligand protein tested with an additional C-terminal His_6-tag, the possibility is given that the His_6-tag influences the higher affinities of the target proteins to MBP-PIP5K6-His_6 than to MBP-PIP5K1 or MBP-PIP5K2. sfGFP-μMHD-His_6 displayed the lowest affinity to the three MBP-tagged PI4P 5-kinases tested, with K_D-values that were between 1.5-fold (MBP-PIP5K2) to 57.9-fold (MBP-PIP5K1) lower than those determined for sfGFP-σ-His_6 and sfGFP-β2-His_6, respectively. The lower binding affinity of sfGFP-μMHD-His_6 might be due to the properties of the enriched sfGFP-μMHD-His_6 protein, as fusion proteins of the AP2-μ subunit were showing "sticky" behavior in various experiments, for instance in the immuno pull-down assays, or during lipid-binding studies by liposome sedimentation assays. The tendency to "stick" caused adsorption of the sfGFP-μMHD-His_6 protein to the MST-capillaries, possibly impacting its thermophoretic behavior and subsequently the data on the recorded binding affinities (appendix Figure 31).

Overall, the results of the *in vitro* protein interaction analyses (Figure 10 and Figure 11) indicate specific binding of the AP2-subunits β2, μMHD and σ to the PI4P 5-kinases PIP5K1, PIP5K2 and PIP5K6. The interactions of PIP5K1, PIP5K2 and PIP5K6 with the AP2-complex appear relevant, as all three PI4P 5-kinases have been shown to be involved in the control of plant CME.

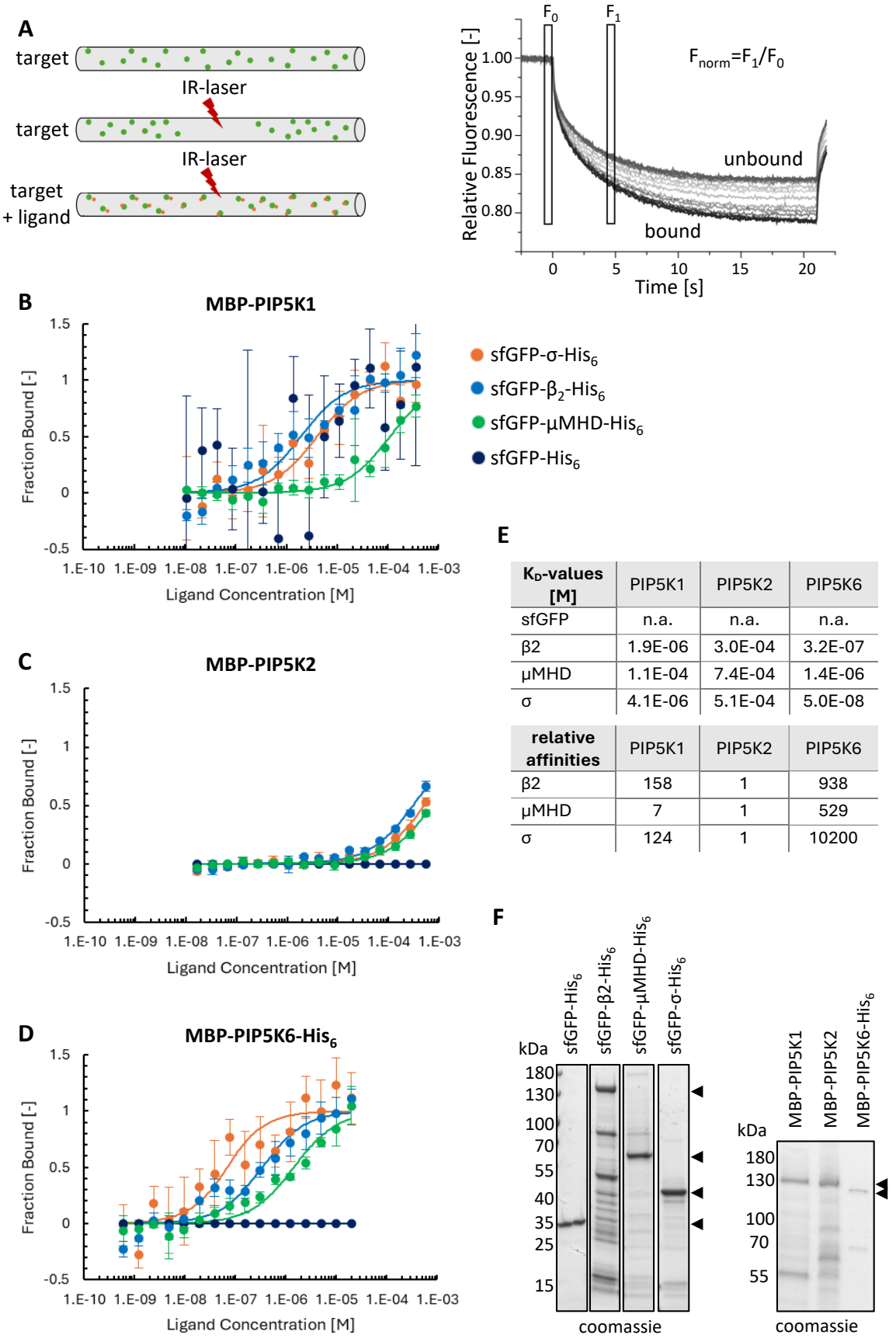

K_D-values [M]	PIP5K1	PIP5K2	PIP5K6
sfGFP	n.a.	n.a.	n.a.
β2	1.9E-06	3.0E-04	3.2E-07
μMHD	1.1E-04	7.4E-04	1.4E-06
σ	4.1E-06	5.1E-04	5.0E-08

relative affinities	PIP5K1	PIP5K2	PIP5K6
β2	158	1	938
μMHD	7	1	529
σ	124	1	10200

Figure 11. Thermophoretic analyses of the interaction from AP2-β2, -μMHD, or -σ with PIP5K1, PIP5K2 or PIP5K6. A A schematic illustration of an MST-event is shown left. Without heating, the target molecules in solution are homogenously distributed throughout the capillary. After the capillary is heated by an infrared (IR)-laser, target molecules diffuse out of the heated area, leading to a drop in detected fluorescence within

the sampling volume. Upon addition of a possible ligand, the diffusion of the target + ligand complex (bound state) within the temperature gradient may change, causing differences in the detected fluorescence compared to target only or unbound state. Illustration adapted from van den Bogaart et al. (2012). On the right, typical MST traces for a detected binding event. F_{norm} is calculated as the ratio of the fluorescence after the IR-laser impulse (F_1) and before the impulse (F_0). Figure from NanoTemper Technologies GmbH (Munich, Germany) **B, C**, **D** Binding affinity curves shown as fraction bound dependent on ligand concentration. sfGFP-β2-His_6 (light blue), sfGFP-μMHD-His_6 (green), sfGFP-σ-His_6 (orange) were used as target proteins and sfGFP-His_6 (dark blue) as negative control with a fixed concentration of approximately 40 nM. MBP-PIP5K1 (**B**), MBP-PIP5K2 (**C**) and MBP-PIP5K6-His_6 (**D**) were used as ligand protein with sequential dilutions over sixteen concentrations starting approximately at 0.355 mM (MBP-PIP5K1), 0.545 mM (MBP-PIP5K2) or 0.02 mM (MBP-PIP5K6-His_6) respectively. An MST-on time of 2.5 s was used for analysis and data was fitted using K_D-fit model. Each data point represents four independent MST-measurements, error bars represent standard deviation. **E** K_D-values derived from (B)-(D) (top table) and relative affinities of the interactions compared to the MBP-PIP5K2 interaction (bottom table) **F** Coomassie stained SDS-PAGE from the target proteins (left panel) and ligand proteins (right panel) with concentration ratios used in MST measurements. Black arrowheads mark the expected molecular size of the fusion proteins: sfGFP-β2-His_6, 127.5 kDa; sfGFP-μMHD-His_6, 58.26 kDa; sfGFP-σ-His_6, 45.5 kDa; sfGFP-His_6, 28.5 kDa; MBP-PIP5K1/2, 128 kDa; MBP-PIP5K6-His_6, 123 kDa. MBP-PIP5K1/2 was enriched by Dr. Lennart Schwalgun (Dept. of Plant Biochemistry) and MBP-PIP5K6-His_6 by Dr. Alexandra Schutkowski (Dept. of Plant Biochemistry).

3.3 Lipid-binding characteristics of AP2-subunits

PIs, especially PtdIns4P and PtdIns(4,5)P_2 play a role in the regulation of endocytosis (Ischebeck et al., 2013; Lin et al., 2019; Sousa et al., 2008; Y. Zhao et al., 2010) and together with the observed interaction of several AP2-subunits with different PI4P 5-kinases, the AP2-complex is a possible target for PI-mediated regulation of CME in plants. The interaction of the PI4P 5-kinases, PIP5K1, PIP5K2 and PIP5K6, with subunits of the AP2-complex (Figure 10 and Figure 11) raised the question whether PIs might also be ligands for the AP2-complex. For mammals including humans, it has previously been shown, that *Hs*AP2-α, *Hs*AP2-μ and possibly *Hs*AP2-β bind to PtdIns(3,4,5)P_3 and to PtdIns(4,5)P_2, and it has been suggested that this protein-lipid interaction is important for endocytic function (Gaidarov & Keen, 1999; Kadlecova et al., 2017; Rohde et al., 2002). To address whether AP2-subunits from Arabidopsis display binding capabilities for PIs, enriched recombinant MBP fusion proteins of AP2-α1, AP2-β2, AP2-μ and AP2-σ were first tested for lipid-binding by lipid overlay assays using PIP strips (Figure 12). AP2-α1 was used for subsequent experiments representative for both AP2-α isoforms, as the isoforms AP2-α1 and AP2-α2 share a high sequence identity of 98.5 %. Moreover, as the enrichment of full length MBP-AP2-α1 was unfeasible, a truncated variant consisting of the first 200 N-terminal amino acids (MBP-α1NT) was tested for lipid interaction, with the identified PtdIns(4,5)P_2 binding sites of *Hs*AP2-α laying within this N-terminal region. Enriched MBP and a GST-tagged pleckstrin homology domain of phospholipase C-δ1 (PLC-δ1PH) served as negative and positive controls, respectively (Figure 12). MBP-α1NT, MBP-μ and MBP-σ displayed binding to PtdIns-monophosphates, with binding to PtdIns3P being the most pronounced, whereas MBP-β2 showed no binding to any of the lipids tested. In the lipid overlay assays, lipids are immobilized individually on a membrane, and this mode of lipid

presentation does not reflect a physiological membrane environment for lipid-binding. As moreover even slight variations in pH or ionic strength might influence protein-lipid interactions *in vitro* (I. Heilmann, 2016; M. Heilmann & Heilmann, 2024), the observed interaction of MBP-α1NT, MBP-μ and MBP-σ with PtdIns-monophosphates might best be interpreted as a general ability of the proteins to bind anionic phospholipids, and no binding preference for any specific lipid can be deduced.

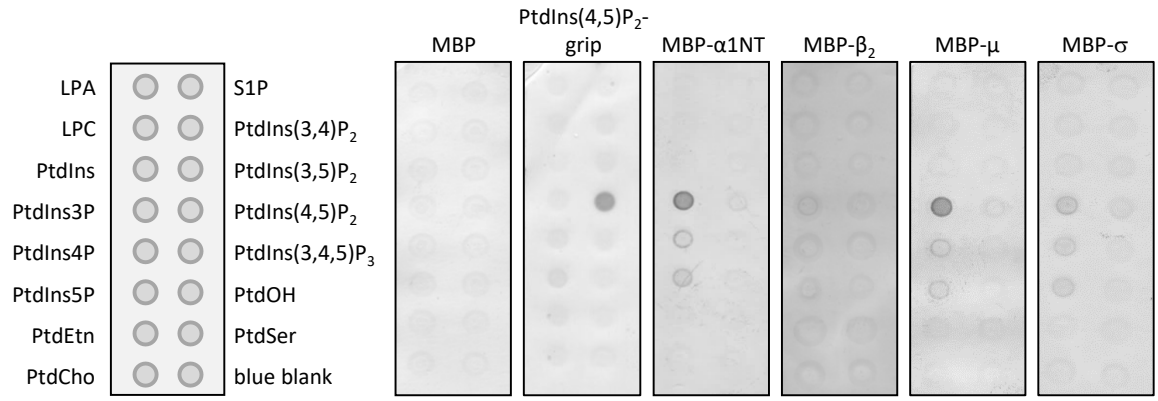

Figure 12. AP2-subunits interact with anionic phospholipids. Lipid interaction studies were performed by lipid-overlay assay using commercial PIP strips. A schematic representation of the PIP strip layout is shown left. MBP was used as negative control and recombinant GST-tagged pleckstrin homology domain of phospholipase C-δ1 (PLC-δ1PH, PtdIns(4,5)P_2-grip) as positive control (N=1). α1NT are the first 200 amino acids of the AP2-α1 subunit. Lipid-overlay assay with MBP-tagged AP2-subunits was performed once with commercial PIP strips (Johanna Uhlenberg master thesis) and three to four times with self-prepared membranes showing similar results. Membranes were incubated with enriched proteins with a concentration of 0.5 mg/ml. Bound proteins were detected by using primary αMBP or αGST antibody followed by secondary antibody conjugated to alkaline phosphatase.

To identify and ultimately modify candidate regions in the AP2-subunits that may confer the observed lipid-binding capability, computer-based sequence analysis was used to suggest regions enriched in basic and hydrophobic amino acids (BH-search, Brzeska et al. (2010)). In this analysis, each amino acid residue is assigned a specific BH-score, and values over 0.6 indicate binding sites for anionic lipids (Figure 13). For AP2-α1, two sequence sections in the N-terminal part of the protein displayed BH-scores over 0.6 (Figure 13A). The first one included a cluster of four lysine (K_{48-51}), corresponding to the lysine triad (K_{55-57}) in human AP2-α that is responsible for PtdIns(4,5)P_2 binding (appendix Figure 24; Gaidarov & Keen (1999)). The analysis of AP2-μ identified one potential binding region with a BH-score above 0.6 for the residues I_{353}, D_{354} and C_{355} (Figure 13B). Further arginine and lysin residues in the vicinity of the BH-peak in AP2-μ correspond to previously identified lipid-binding sites in human AP2-μ (appendix Figure 24, Höning et al. (2005), Rohde et al. (2002)).

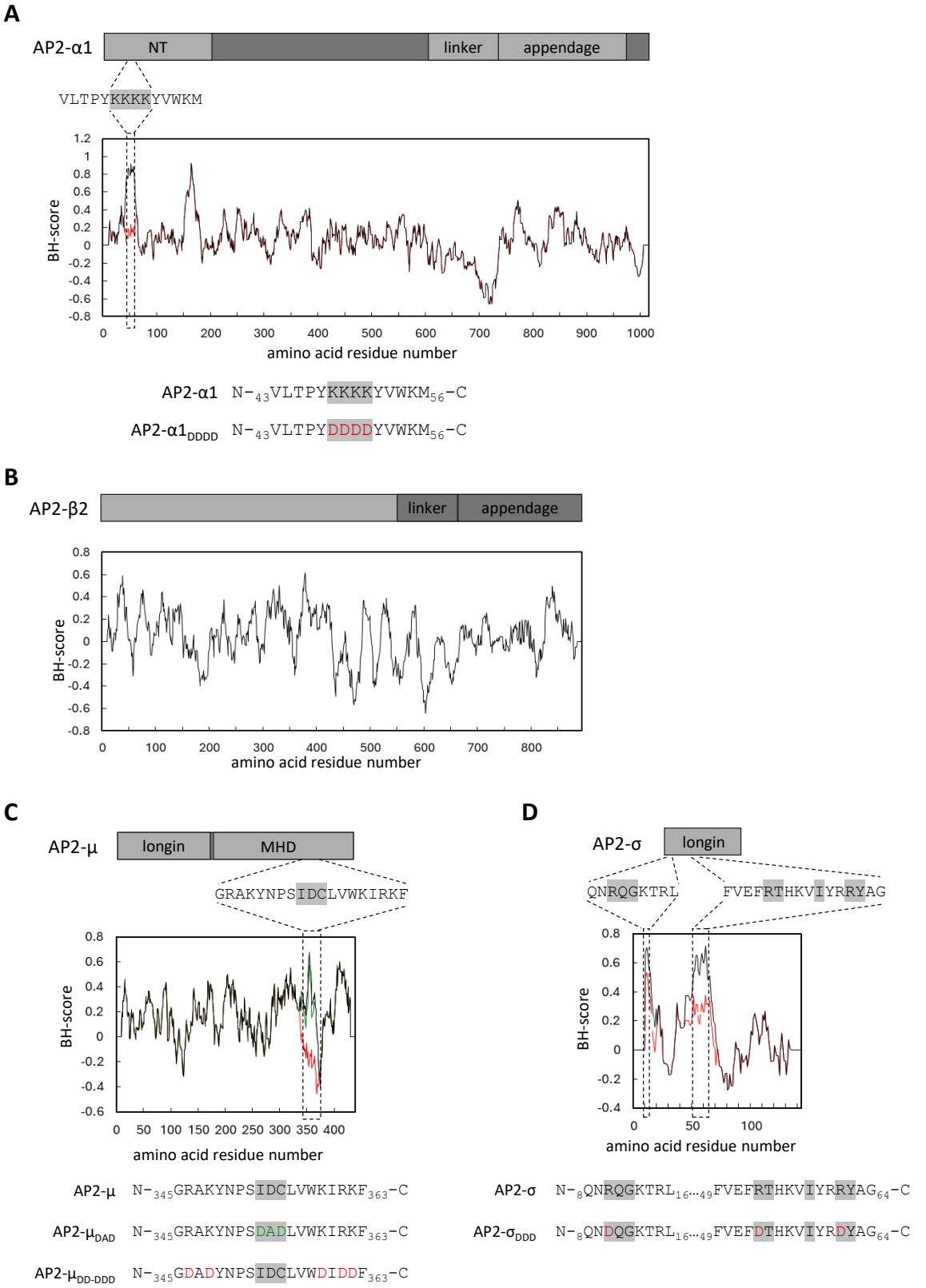

Figure 13. Identification and substitution of candidate lipid-binding sites in AP2-subunits. The amino acid sequences of **A** AP2-α1, **B** AP2-β2 **C** AP2-μ and **D** AP2-σ were analyzed for possible lipid-binding regions via a computer-aided sequence analysis based on basic-hydrophobicity (BH)-scores (Brzeska et al., 2010). BH-scores of wild type AP2-subunits are displayed as black lines, substitution variants as red or green lines. Amino acid sequences are displayed schematically above BH-plots. Residues with BH-scores over 0.6, which indicates a possible binding region for anionic lipids, are highlighted in grey. Amino acids that are substituted for the creation of substituted AP2-α1, -μ and -σ variants are marked red or green. NT: N-terminal part of AP2-α1 from aa 1-200; MHD: μ-homology domain.

The BH-search for AP2-σ suggested two basic-hydrophobic regions within the protein, that could be responsible for the lipid-binding capability (Figure 13D). No lipid-binding sites have been reported for mammalian AP2-σ, and the BH-search analysis for Arabidopsis AP2-σ suggested three arginine residues (R_{10}, R_{53} and R_{61}) in a sequence region with BH-scores over 0.6. The AP2-β2 subunit was also analyzed for basic-hydrophobic regions by BH-search, but no region in the protein was indicated with BH-scores above 0.6 (Figure 13B). The absence of predicted lipid-binding regions is consistent with no detectable lipid-binding capability of AP2-β2 in the *in vitro* lipid overlay assays (Figure 12).

To examine whether the amino acids identified by the BH-search analysis are responsible for the lipid-binding capability of the respective proteins, first sequence variants were devised where the predicted residues were substituted *in silico* with the acidic amino acid aspartic acid (D) or the nonpolar amino acid alanine (A). An AP2-$\alpha1_{DDDD}$ variant was created, where the four lysins $K_{48\text{-}51}$ were all substituted for Ds (Figure 13A, as indicated). For the AP2-μ_{DAD} variant, the residues I_{353}, D_{354} and C_{355} were substituted for D or A, respectively. An additional AP2-$\mu_{DD\text{-}DDD}$ variant was created, in which further arginine and lysin residues (R_{346}, K_{348}, K_{359}, R_{361}, K_{362}) in the immediate vicinity of the BH-peak were also substituted by Ds (Figure 13C, as indicated). For AP2-σ_{DDD}, three arginines (R_{10}, R_{53}, R_{61}) were substituted with Ds (Figure 13D, as indicated).

As a first test of the influence of the substituted amino acid positions on the lipid-binding capability, lipid-overlay assays were performed side-by-side with the respective wild type proteins. For this purpose, AP2-α1NT, AP2-μ and AP2-σ as well as the substitution variants were recombinantly expressed and enriched as MBP-fusion proteins (for SDS-PAGE and protein quality, see appendix Figure 26). In the lipid-overlay assays using self-spotted lipid-membranes, the lipid-binding of MBP-$\alpha1NT_{DDDD}$ and MBP-σ_{DDD} seemed to be notably reduced compared to MBP-α1NT and MBP-σ. By contrast, MBP-μ_{DAD} and MBP-$\mu_{DD\text{-}DDD}$ did not show a pronounced reduction in lipid-binding compared to MBP-μ, and signals for PtdSer- and PtdIns5P-binding were still detected (Figure 14). The negative control MBP did not show any lipid-binding. It is noteworthy that these experiments using self-spotted lipid-membranes showed differing results for the wild type subunits than the commercially available PIP strips (Figure 12), supporting the conclusion that lipid-overlay assays only indicate the capability of AP2-subunits to interact with anionic phospholipids, but do not reliably indicate any lipid-binding preference.

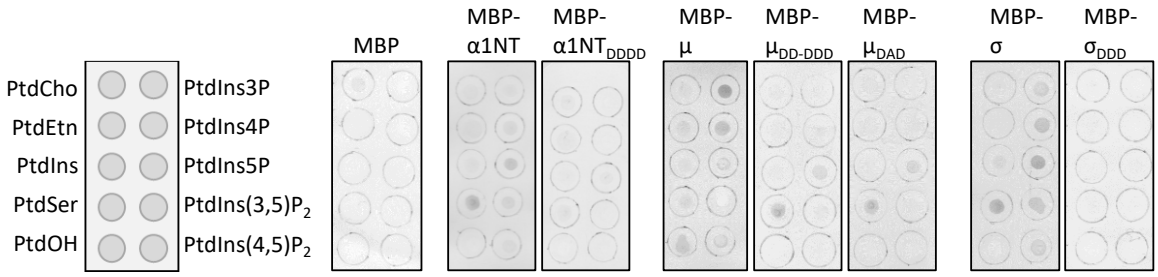

Figure 14. Lipid-overlay assays show a possible reduction of lipid-binding capability of substituted AP2-subunits. Lipid interaction studies were performed by lipid-overlay assay using self-prepared membranes. A schematic representation of the membrane layout is shown left. MBP was used as negative control. α1NT are the first 200 amino acids of the AP2-α1 subunit. Membranes were incubated with enriched proteins with a concentration of 0.5 mg/ml. Bound proteins were detected by using primary αMBP or αGST antibody followed by secondary antibody conjugated to alkaline phosphatase. Lipid-overlay assays were performed three to four times showing similar results.

As an experimental approach that resembles the physiological membrane environment more closely than lipid-overlay assays, liposome binding experiments were performed. In these experiments, lipid ligands are presented in liposomes, which are bilayer membranes composed of structural lipids, such as PtdCho or PtdEtn, and a fraction of the possible ligand lipid. Liposome binding assays were performed both as liposome-sedimentation assays, where bound proteins co-sediment with dense raffinose filled liposomes (Julkowska et al., 2013), or as liposome-flotation assays, in which the interacting proteins float with the liposomes on top of a denser aqueous sucrose gradient (Posor et al., 2013). In either case, the bound or unbound proteins can be visualized by immunodetection. Binding tests without liposomes or with liposomes not containing any indicated ligand lipids served as negative controls. These negative controls were important in the analysis of AP2-complex subunits, as the tested proteins MBP-α1NT and MBP-μ were detected in the respective negative controls, both in liposome-sedimentation tests and in liposome-flotation tests (appendix Figure 25). This behavior indicates a technical issue with binding of the recombinant proteins to either the surfaces of the tubes or to structural lipids *in vitro*. Even with different experimental conditions tested, including varying the protein concentrations or several liposome compositions normally inclined to resolve false positive lipid-binding results, this issue could not be resolved for the AP2-complex subunits tested here. To overcome these experimental limitations, an alternative experimental approach was used, and the lipid-binding capability of AP2-α1, AP2-μ and AP2-σ in comparison to their substitution variants was analyzed using MST. MST has the advantage of being a quantitative method, and moreover only small sample volumes and therefore small amounts of protein and liposomes are needed for the quantitative analysis of protein-lipid-binding.

AP2-subunits and their respective substitution variants were recombinantly expressed and enriched as sfGFP-His_6 fusion proteins. The N-terminal sfGFP-tag promoted solubility and served as the fluorescent label for detection, while the C-terminal His_6-tag was used for the enrichment

of the full-length proteins by immobilized metal affinity chromatography (IMAC, appendix Figure 27-Figure 29). The sfGFP-fusions of the AP2-complex subunits were used at an approximate concentration of 40 nM, which was normalized to the total fluorescence count signal and additionally verified by SDS-PAGE (Figure 15C). The sfGFP-His_6-fusion tag alone was used as negative control for protein-lipid-binding. Ligand molecules were presented as liposomes prepared in the same manner as for the liposome-sedimentation assays (Julkowska et al., 2013), and the proportion of the tested PIs in the liposomes comprised 10 mol % in a liposome structure consisting of 90 mol % of PtdCho. Liposomes were used in the MST titration so that different concentrations of lipids were presented, with 45.78 nM of total liposomal lipids as the lowest and 1.5 mM as the highest lipid concentration. Ligand lipids tested included PtdIns(4,5)P_2, which has a proven role in CME regulation, as well as PtdIns4P or PtdOH. PtdIns4P was chosen because the lipid overlay assays showed PtdIns-monophosphate binding and PtdIns4P, like PtdIns(4,5)P_2, is proposed to associate with the PM, where endocytosis takes place (Gerth et al., 2017). As one of the TPLATE subunits, AtEH1/Pan1, and other plant proteins involved in CME like AP180 and Epsin–like Clathrin Adaptor 1 (ECA1) were described to interact with PtdOH (Kaneda et al., 2019; Putta et al., 2020; Yperman, Papageorgiou, et al., 2021), the AP2-subunits were also tested for interaction with PtdOH.

In the MST measurements (Figure 15), sfGFP-α1NT-His_6 had the highest affinity to liposomes containing PtdIns(4,5)P_2, with K_D-values being almost 200-fold or 2,500-fold lower than those obtained for liposomes containing PtdIns4P or PtdOH, respectively (Figure 15A and B). The substitution variant sfGFP-α1NT_{DDDD}-His_6 showed a substantially (60-fold) reduced affinity to PtdIns(4,5)P_2 compared to the wild type variant, indicating effective interference with lipid-binding in the sfGFP-α1NT_{DDDD}-His_6 variant. The affinity of the sfGFP-α1NT_{DDDD}-His_6 variant for PtdIns4P was also reduced compared to that of the wild type protein, but only by approximately 4-fold. The already low affinity to liposomes containing PtdOH seemed to be unaffected by the sfGFP-α1NT_{DDDD}-His_6 substitution. sfGFP-σ-His_6 showed the highest affinity to liposomes containing PtdIns(4,5)P_2 and liposomes containing PtdIns4P or PtdOH were bound with substantially lower affinity. In the MST measurements, even the highest PtdOH concentrations used did not result in a saturating titration curve for any of the AP2-subunits tested. In comparison to sfGFP-α1NT-His_6, the binding of sfGFP-σ-His_6 to PtdIns(4,5)P_2-containing liposomes was approximately 12-fold weaker (Figure 15A and B). Upon substituting the possible lipid-binding region of sfGFP-σ-His_6, lower affinities of sfGFP-$σ_{DDD}$-His_6 were observed towards any of the liposomes tested, indicating reduced lipid-binding capability of the modified protein as was observed for the sfGFP-α1NT_{DDDD}-His_6 substitution variant. The sfGFP-His_6 negative control displayed no or negligible binding to any of the tested liposomes (Figure 15A, B).

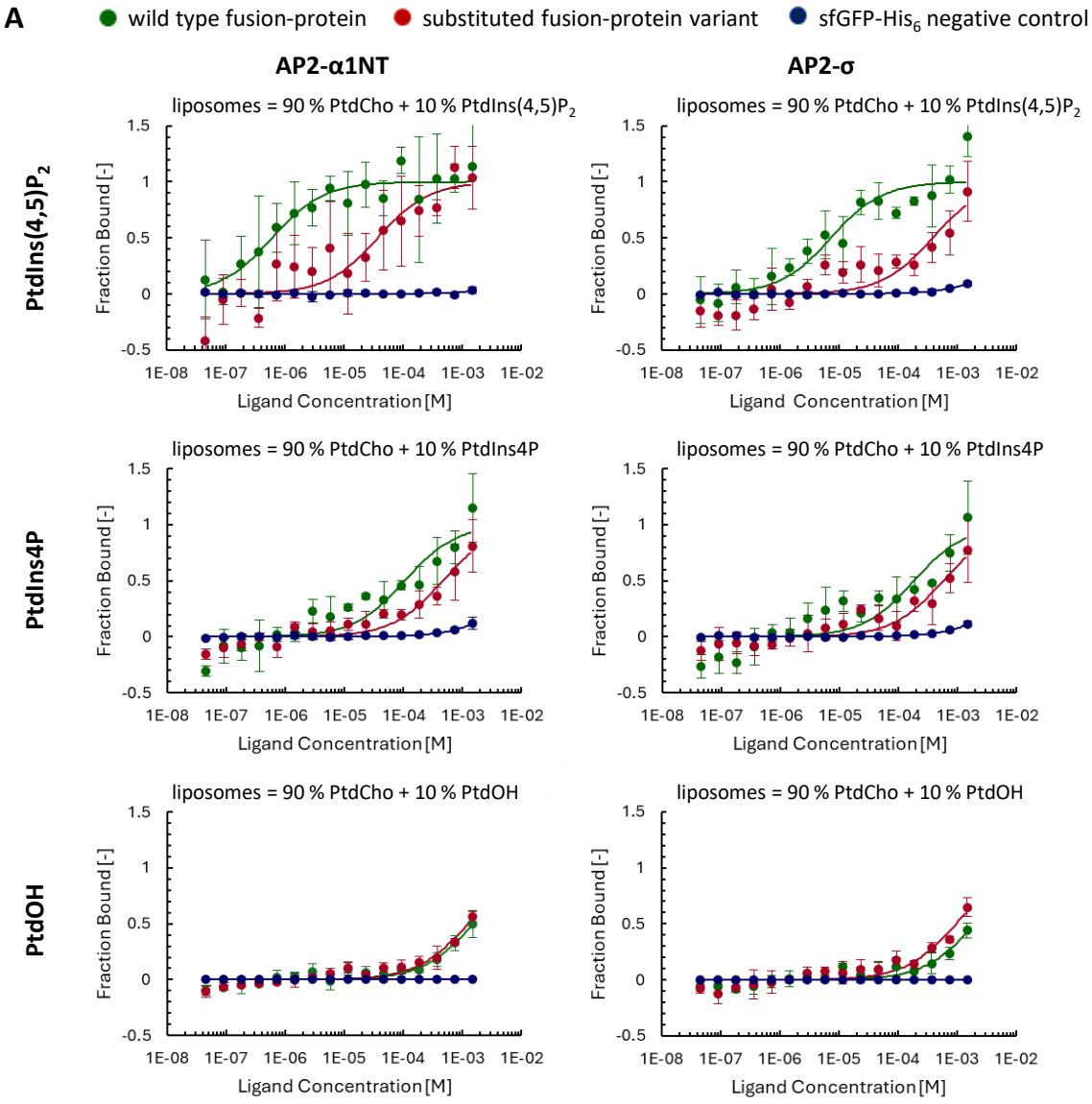

B

K_D-values [M]	PtdIns(4,5)P_2	PtdIns4P	PtdOH
α1NT	6.0E-07	1.1E-04	1.5E-03
α1NT$_{DDDD}$	3.7E-05	4.7E-04	1.3E-03
sfGFP	n.a.	1.1E-02	n.a.

K_D-values [M]	PtdIns(4,5)P_2	PtdIns4P	PtdOH
σ	7.3E-06	1.8E-04	2.0E-03
σ$_{DDD}$	3.8E-04	5.7E-04	6.0E-04
sfGFP	1.5E-02	1.2E-02	n.a.

C

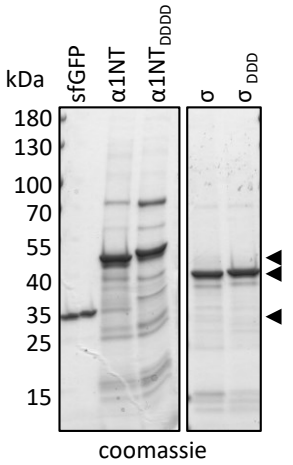

Figure 15. Thermophoretic analyses of phospholipid-binding of wild type AP2-α1NT, AP2-σ or their substitution variants, AP2-α1NT$_{DDDD}$ or AP2-σ$_{DDD}$. MST measurements were performed using enriched fusion proteins of AP2-α1NT/α1NT$_{DDDD}$ and AP2-σ/σ$_{DDD}$ containing an N-terminal sfGFP-tag and a C-terminal His$_6$-tag. Enriched sfGFP-His$_6$ fusion protein was used as a negative control. Proteins were used at a concentration of approximately 40 nM. Liposomes composed of 90 mol % PtdCho and 10 mol % of either PtdIns(4,5)P_2, PtdIns4P or PtdOH were used as ligands with total lipid concentrations between 45.78 nM to 3 mM over 16 serial dilutions. **A** Binding affinity curves shown as fraction bound dependent on the ligand

concentration. Binding curves for wild type AP2-α1NT and AP2-σ fusion proteins are displayed in green, for substituted AP2-α1NT$_{DDDD}$ and AP2-σ$_{DDD}$ fusion proteins in red and for the sfGFP-His$_6$ control in blue. An MST-on time of 2.5 s was used for analysis and data was fitted using K_D-fit model. Each data point represents four independent MST-measurements, error bars represent standard deviation. **B** K_D-values derived from (A). **C** Coomassie stained SDS-PAGE of the target proteins with relative concentrations as used in MST measurements. Black arrowheads mark the expected molecular size of the fusion proteins: sfGFP-α1NT/α1NT$_{DDDD}$-His$_6$, 50.9 kDa; sfGFP-σ/σ$_{DDD}$-His$_6$, 45.5 kDa; sfGFP-His$_6$, 28.5 kDa.

In contrast to the results for the AP2-subunits shown above, MST analyses of lipid-binding features of the AP2-μMHD wild type or substitution variant did not yield interpretable results. At first approximation, sfGFP-μMHD-His$_6$ displayed binding to liposomes containing PtdOH, slightly less to liposomes containing PtdIns4P and even less to liposomes containing PtdIns(4,5)P_2 (Figure 16A and B). The resulting K_D-values for the affinity to the different lipids differed only within a range of 1.1-fold to 1.6-fold from one another. Moreover, there were no major differences in the lipid-binding affinities between wild type sfGFP-μMHD-His$_6$ and its substitution variant, sfGFP-μMHD$_{DAD}$-His$_6$, and the affinities of sfGFP-μMHD$_{DD\text{-}DDD}$-His$_6$ to PtdIns(4,5)P_2 or PtdOH were reduced by only 2.6-fold and 3.9-fold, respectively compared to that of the wild type protein. All these results must be reviewed with caution, as the enriched sfGFP-μMHD-His$_6$ or sfGFP-μMHD$_{DAD}$-His$_6$ fusion proteins displayed non-optimal behavior. Both recombinant fusion proteins showed frequent unspecific adsorption to the walls of the MST capillaries, which was documented based on a fluorescence profile recorded along the diameter of the capillary (Figure 16D). While the sfGFP-μMHD$_{DD\text{-}DDD}$-His$_6$ variant did not show this adsorption behavior, it displayed a bigger molecular size than expected in an SDS-PAGE (Figure 16C). As this can be an indication that the protein is not correctly folded, circular dichroism (CD) spectra were recorded for all fusion proteins used, and spectra for the respective wild type and substitution variants were compared (appendix Figure 32). Clear CD spectra were obtained for sfGFP-α1NT-His$_6$, sfGFP-α1NT$_{DDDD}$-His$_6$, sfGFP-σ-His$_6$ and sfGFP-σ$_{DDD}$-His$_6$. The CD spectra recorded for sfGFP-His$_6$ and the AP2-subunit fusion proteins differed markedly, whereas the spectra of sfGFP-α1NT-His$_6$ vs. sfGFP-α1NT$_{DDDD}$-His$_6$ or the spectra of sfGFP-σ-His$_6$ vs. sfGFP-σ$_{DDD}$-His$_6$ were almost indistinguishable (appendix Figure 32A). The CD spectra indicate that the wild type and substituted AP2-α1NT or AP2-σ fusion proteins did not display significantly different secondary or tertiary structures. This was also supported by the capillary scans during MST measurements, where the wild type and substituted AP2-α1NT and AP2-σ fusion proteins showed similar behaviors (appendix Figure 31). By contrast, CD spectra of sfGFP-μMHD-His$_6$, sfGFP-μMHD$_{DAD}$-His$_6$ or sfGFP-μMHD$_{DD\text{-}DDD}$-His$_6$ showed a low signal to noise ratio and could not easily be compared (appendix Figure 32B). The low data quality might be attributed to the described “sticky“ behavior of the proteins. Moreover, the enrichment of the measured proteins for sfGFP-μMHD$_{DAD}$-His$_6$ and especially sfGFP-μMHD$_{DD\text{-}DDD}$-His$_6$ was not as high (Figure 16C), which could lead to other proteins masking the signal of the targeted full length fusion protein. Thus, the CD spectra of the AP2-μMHD wild type protein and its substitution

variants are not conclusive and no statements on the effect of the introduced substitutions on the secondary structure of the proteins can be made.

Taken together, the results of the *in vitro* lipid-binding studies indicate that the AP2-subunits α1, μ and σ can bind to anionic phospholipids and display the highest affinity binding to PtdIns(4,5)P_2. Polybasic protein regions mediating the interaction of AP2-α1 and AP2-σ with PIs were identified, and substitution variants AP2-α1$_{DDDD}$ and AP2-σ$_{DDD}$ were created, which display reduced lipid-binding capability with no detectable misfolding of the enriched proteins *in vitro*. Based on these results, the lipid-binding deficient proteins were used to next test whether lipid-binding was required for the physiological function of the proteins in mediating endocytosis *in vivo*.

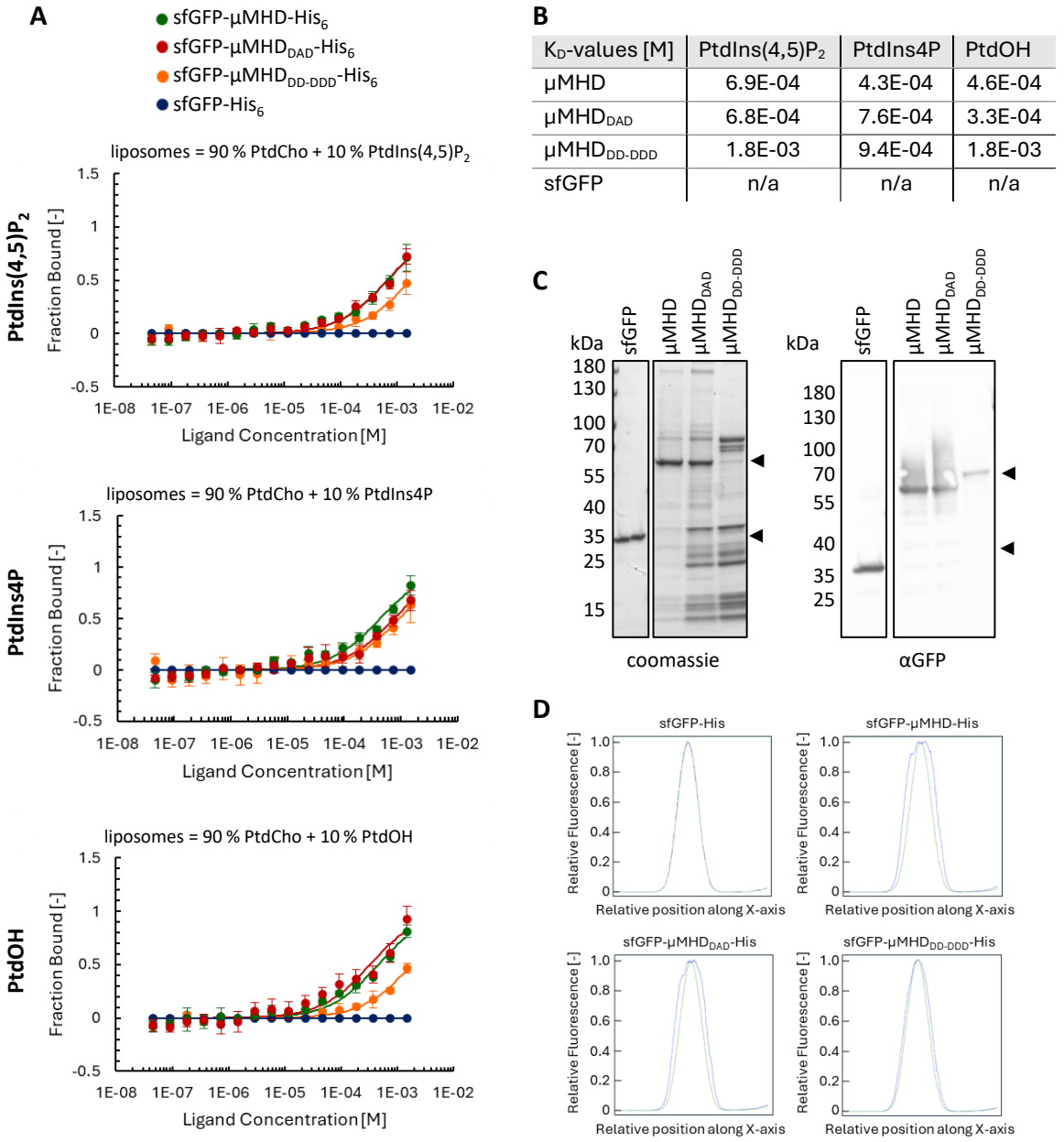

K_D-values [M]	PtdIns(4,5)P_2	PtdIns4P	PtdOH
µMHD	6.9E-04	4.3E-04	4.6E-04
$µMHD_{DAD}$	6.8E-04	7.6E-04	3.3E-04
$µMHD_{DD-DDD}$	1.8E-03	9.4E-04	1.8E-03
sfGFP	n/a	n/a	n/a

Figure 16. Thermophoretic analyses of phospholipid-binding of wild type AP2-µMHD and its substitution variants, AP2-$µMHD_{DAD}$ or AP2-$µMHD_{DD-DDD}$. MST measurements were performed using enriched fusion proteins of AP2-µMHD, AP2-$µMHD_{DAD}$ or AP2-$µMHD_{DD-DDD}$ containing an N-terminal sfGFP-tag and a C-terminal His_6-tag. Enriched sfGFP-His_6 fusion protein served as a negative control. Proteins were used at a concentration of approximately 40 nM. Liposomes composed of 90 mol % PtdCho and 10 mol % of either PtdIns(4,5)P_2, PtdIns4P or PtdOH were used as ligands with total lipid concentrations between 45.78 nM to 3 mM over 16 serial dilutions. **A** Binding affinity curves shown as fraction bound dependent on the ligand concentration. Binding curves for wild type sfGFP-µMHD-His_6 shown in green, for sfGFP-$µMHD_{DAD}$-His_6 in red, for sfGFP-$µMHD_{DD-DDD}$-His_6 in orange and for the sfGFP-His_6 control in blue. An MST-on time of 2.5 s was used for analysis and data was fitted using K_D-fit model. Each data point represents four independent MST-measurements, error bars represent standard deviation. **B** K_D-values derived from (A). **C** Coomassie stained SDS-PAGE (left panel) and αGFP immunodetection (right panel) of the target proteins with relative concentrations as used in MST measurements. Black arrowheads mark the expected molecular size of the fusion proteins: sfGFP-µMHD/$µMHD_{DAD}$/$µMHD_{DD-DDD}$-His_6, 58.26 kDa; sfGFP-His_6, 28.5 kDa. **D** Capillary scans reflecting the fluorescence profile recorded along the diameter of the capillary measured before the IR-laser impulse (green curve) and after the IR-laser impulse (blue curve). Representative capillary scans are shown for sfGFP-His_6 and sfGFP-µMHD/$µMHD_{DAD}$/$µMHD_{DD-DDD}$-His_6 from one capillary each.

3.4 Influence of lipid-binding properties of AP2-subunits on endocytosis

3.4.1 Analysis of AP2-function mediating FM4-64 dye-uptake into tobacco pollen tubes

The analyses so far indicated that AP2-α1 or AP2-σ bind to anionic phospholipids (Figure 13-Figure 15) with a pronounced preference for binding to PtdIns(4,5)P_2 (Figure 15). To determine whether or not lipid-binding by AP2-α1 or AP2-σ is important for the physiological function of the proteins in mediating endocytosis, it was next tested whether the predicted lipid-binding sites (Figure 13) were required for mediating endocytosis *in vivo*. For this purpose, wild type AP2-α1 or AP2-σ or their respective lipid-binding-defective variants AP2-α1$_{DDDD}$ or AP2-σ$_{DDD}$ were transiently expressed in tobacco pollen tubes as fusions to N-terminal EYFP-tags, and endocytic uptake of the membrane dye FM4-64 into the transgenic cells was recorded over time by confocal laser-scanning microscopy (Figure 17). Endocytic dye-uptake was then assessed by quantitative image analysis. The transformed pollen tubes were stained with 2.5 µM FM4-64 and confocal single plane images were acquired at the median optical sections of the pollen between 0-15 min and again between 60-85 min after staining. The endocytic rates were then evaluated by quantification of the plasma membrane (PM) and cytosolic (Cyt) FM4-64-fluorescence intensities and calculating the difference in Cyt:PM ratios (ΔCyt:PM h^{-1}) observed over the time of observation. The fluorescence intensities were measured at the lateral subapical region of the pollen tube, starting 6-10 µm distal from the tip, as this is the region where endocytosis of clathrin coated vesicles takes place (Zonia & Munnik, 2008). In control pollen tubes expressing EYFP alone, FM4-64 was endocytosed normally, resulting in the uptake of the initially PM-localized FM4-64 signal into the cytosol after 60-85 min (Figure 17A). When the Cyt:PM ratio of FM4-64 fluorescence observed after 60-85 min was compared between cells expressing EYFP controls, wild type EYFP-α1 or EYFP-α1$_{DDDD}$, dye-uptake was substantially reduced upon expression of either EYFP-α1 variant (Figure 17B and C). This observation was unexpected and might be due to the N-terminal EYFP-tag, which might impair the *in vivo*-functionality of the expressed fusion proteins. When dye-uptake was compared between cells overexpressing EYFP-α1 or its substitution variant EYFP-α1$_{DDDD}$, the lipid-binding-deficient EYFP-α1$_{DDDD}$-variant displayed a significantly reduced degree of dye uptake (Figure 17B and C), indicating both, functionality of the EYFP-α1 fusion and a contribution of the lipid-binding region to its effect on endocytosis. Cyt:PM ratios determined for cells overexpressing EYFP-α1$_{DDDD}$ were approximately two-fold lower than those observed upon overexpression of wild type EYFP-α1 ($P < 0.005$; Figure 17B). By contrast, when the corresponding analysis was performed for overexpression of EYFP-σ or its lipid-binding-deficient variant, EYFP-σ$_{DDD}$, neither the overexpression of EYFP-σ nor that of EYFP-σ$_{DDD}$ had a significant effect on the Cyt:PM ratio of FM4-64 fluorescence after 60-85 min compared to the EYFP-control.

It is worth noting that the viability of pollen tubes transformed with EYFP-σ or EYFP-σ_{DDD} was apparently reduced after staining with FM4-64, as it was difficult to find pollen tubes on the microscopy slides, that were not bursting during imaging compared to the ones transformed with EYFP control or EYFP-α1/$\alpha1_{DDDD}$. The expression of EYFP-α1, EYFP-σ or their respective lipid-binding-deficient variants in tobacco pollen tubes indicates that lipid-binding is required for the function of the proteins *in vivo*.

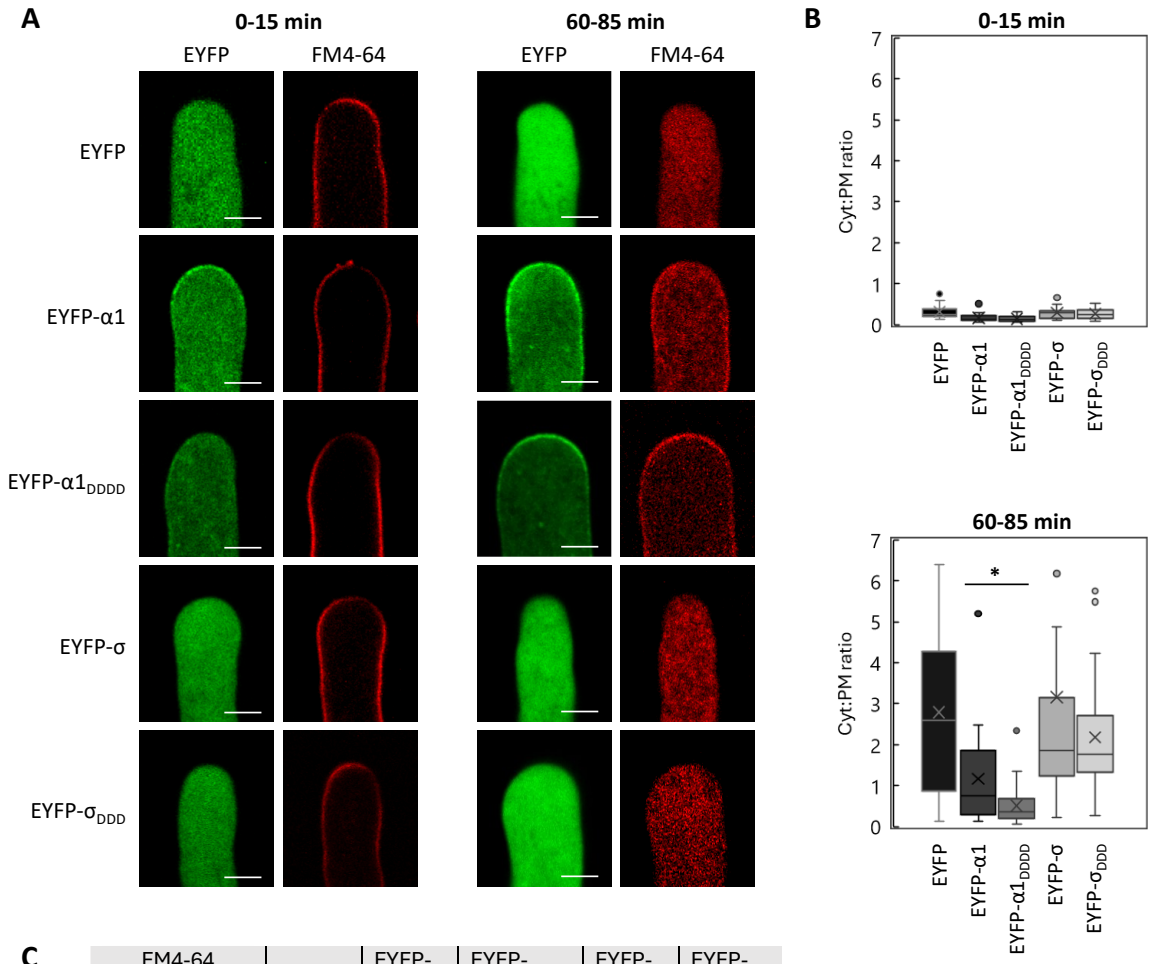

C

FM4-64 internalization	EYFP	EYFP-AP2α1	EYFP-AP2α1$_{DDDD}$	EYFP-AP2σ	EYFP-AP2σ$_{DDD}$
ΔCyt/PM h^{-1}	2.80	0.71	0.25	2.02	1.35

Figure 17. Endocytosis of FM4-64 in pollen tubes expressing fluorescent fusion proteins of AP2-α1, AP2-σ or their respective lipid-binding deficient variants. Tobacco pollen tubes were transiently transformed by particle bombardment with *EYFP*, *EYFP-α1*, *EYFP-α1$_{DDDD}$*, *EYFP-σ* or *EYFP-σ$_{DDD}$* in *pEntryA* vector under the control of the pollen-specific promoter *pLAT52.* Pollen tubes were stained with 2.5 µM FM4-64. **A** Representative single focal plane images of transformed pollen tubes between 0-15 min (left) and between 60-85 min (right) after application of FM4-64. EYFP fluorescence is displayed in green, FM4-64 fluorescence in red. Scale bar = 5 µm. **B** Quantification of the cytosol to plasma membrane ratio of the FM4-64 signal shown as boxplots; x, mean; horizontal line, median; dots indicate outliers. Top panel shows the ratios up to 15 min after dye application, bottom panel shows ratios between 60–85 min after dye application. Numbers represent data from 24-38 pollen tubes per construct, obtained in three independent experiments. Significant differences according to a Student's *t*-test ($P < 0.05$) with letters indicating significantly different categories. **C** Endocytosis rates calculated as the difference in Cyt:PM ratios from (B) (ΔCyt:PM h^{-1}) observed over the time of observation.

3.4.2 Analysis of AP2-function mediating endocytosis of a fluorescence-tagged RbohD protein cargo in Arabidopsis mesophyll protoplasts

As the dye-uptake experiments so far were performed in the heterologous tobacco pollen tube-system, next the internalization of a fluorescently labelled CME cargo protein in transiently transformed Arabidopsis protoplasts was analyzed. To analyze endocytic rates in Arabidopsis protoplasts, the CME cargo protein RbohD was used. RbohD undergoes constitutive endocytic turnover via CME, accumulates in endosomal BFA-bodies and is thus suitable to indicate perturbations of endocytosis, as in previous studies (Hao et al., 2014; Menzel et al., 2019). Arabidopsis Col-0 protoplasts were co-transformed with EYFP-RbohD and α1/$\alpha1_{DDDD}$-mCherry, σ/σ_{DDD}-mCherry or mCherry alone as negative control. The expression of the fusion proteins was driven by the *pCaMV35S* promoter. Transformed protoplasts were pretreated for 30 min with 10 µM cycloheximide (CHX) to inhibit *de novo* protein biosynthesis, followed by treatment with 50 µM BFA. Images were acquired 30-60 min after BFA treatment by recording single focal plane images of chlorophyll A, mCherry and EYFP fluorescence channels, verifying the expression of the respective fusion proteins. Z-stack projections of the EYFP-RbohD fluorescence were used for the quantification of the number of BFA-bodies per cell, as the 3D-projection covers the volume of the cells. Figure 18A shows representative images for each co-transformation. As described before, the EYFP-labelled RbohD showed PM localization as well as accumulation in BFA-bodies upon BFA treatment in control cells co-expressing mCherry (Hao et al., 2014). The AP2-subunit fusions, α1/$\alpha1_{DDDD}$-mCherry and σ/σ_{DDD}-mCherry, all localized to the plasma membrane and in the cytosol, with no obvious difference between the localization patterns of the wild type subunits or the respective lipid-binding deficient substitution variants. Overexpression of either wild type subunit, α1-mCherry or σ-mCherry, resulted in a significantly increased number of BFA-bodies compared to the mCherry control (Figure 18B), indicating an increased rate of EYFP-RbohD endocytosis. This effect was significantly reduced, when the substitution variants $\alpha1_{DDDD}$-mCherry and σ_{DDD}-mCherry were co-expressed with the EYFP-RbohD cargo (Figure 18B). While overexpression of $\alpha1_{DDDD}$-mCherry resulted in a number of BFA-bodies at the level of the mCherry control, the number of BFA-bodies formed in protoplasts expressing σ_{DDD}-mCherry was significantly lower than with the overexpression of σ-mCherry, but still higher than with the mCherry control (Figure 18B, as indicated). It should be noted that the transformed Arabidopsis protoplasts as well as the tobacco pollen tubes are still expressing intrinsic AP2-subunits at an endogenous level, which has to be considered for interpreting the results of the endocytosis assays.

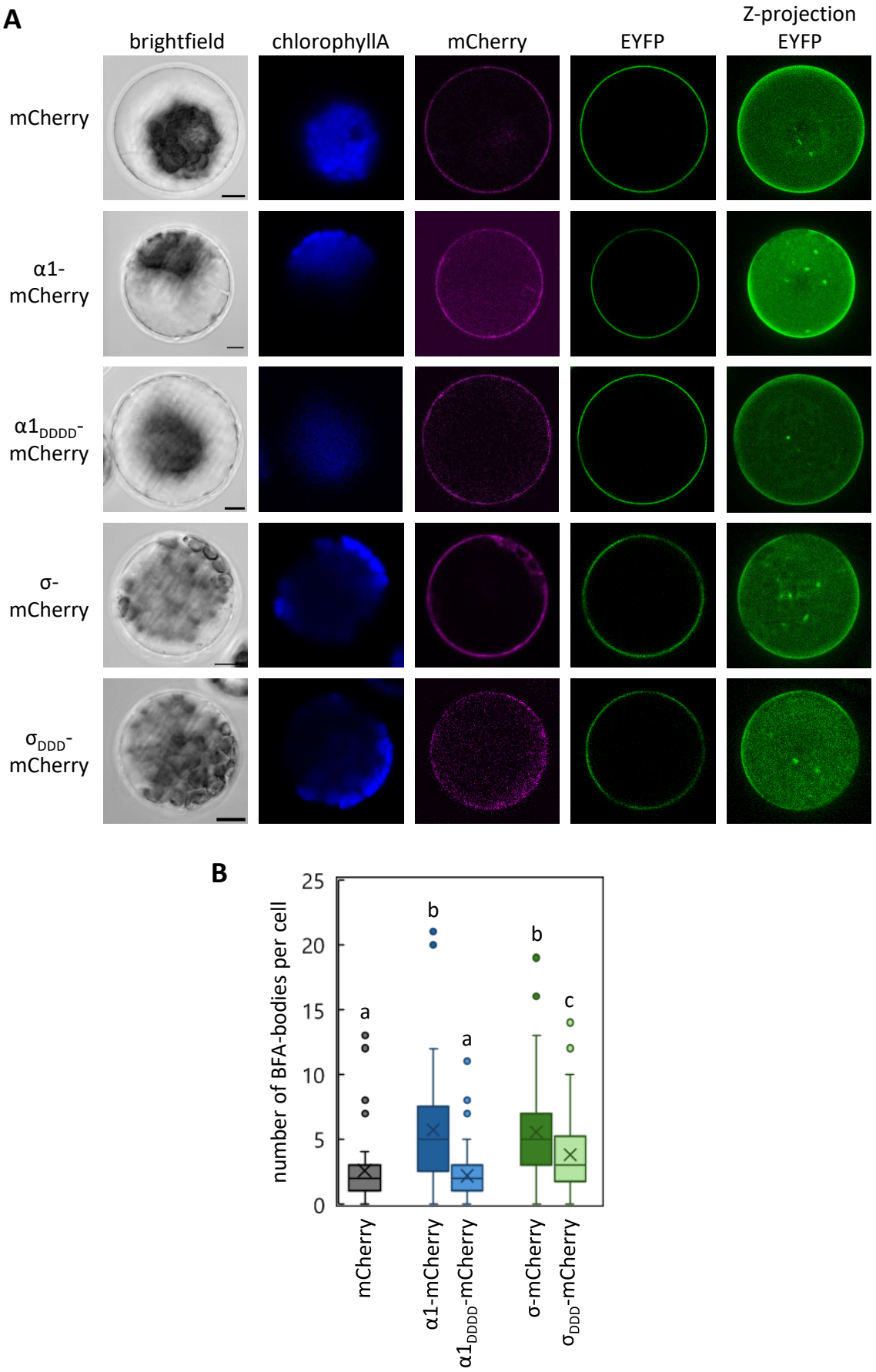

Figure 18. The endocytosis of EYFP-RbohD is reduced in protoplasts expressing fluorescent fusion proteins of lipid-binding deficient AP2-α1 and AP2-σ. Arabidopsis wild type protoplasts were co-transformed with *pEntryA-pCaMV35S::EYFP-RbohD* and *α1-mCherry*, *α1$_{DDDD}$-mCherry*, *σ-mCherry*, *σ$_{DDD}$-mCherry* or *mCherry* as

control in *pEntryD* vector under the control of *pCaMV35S* promoter. Transformed protoplasts were pretreated with 10 µM cycloheximide for 30 min before treatment with 50 µM Brefeldin A (BFA). Cells were imaged 30-60 min after BFA treatment using a confocal laser-scanning microscope. **A** Representative images showing chlorophyll A (blue), mCherry (magenta), and EYFP (green) fluorescence in single focal plane and additional Z-projection of EYFP fluorescence. Scale bar = 10 µm. **B** Quantification of the number of formed EYFP-RbohD decorated BFA-bodies per cell. Quantification was done by analyzing the EYFP-channel Z-projections using ImageJ/Fiji 3D Objects Counter (Schindelin et al., 2012). Data is shown as boxplots; x, mean; horizontal line, median; dots indicate outliers. Data represent 43 to 59 recorded protoplasts per construct from three to four independent experiments. Significant differences according to a Student's *t*-test ($P < 0.05$) with letters indicating significantly different categories.

Together, the protein cargo-internalization experiments in Arabidopsis mesophyll protoplasts show that the lipid-binding deficiency of AP2-α1$_{DDDD}$ and AP2-σ$_{DDD}$ leads to impaired endocytosis *in vivo*, indicating that the lipid-binding capability is important for the physiological function of both, AP2-α1 and AP2-σ.

3.5 Tobacco pollen tubes show altered cell morphologies upon overexpression of AP2-subunits

The data so far demonstrated that the interaction of AP2-subunits and membrane PIs is important for the physiological function of the AP2-complex, and that a reduced lipid-binding capability of the AP2-subunits EYFP-α or EYFP-σ resulted in a reduced rate of endocytosis *in vivo.* To assess whether these findings have relevance at a larger scale, it was next investigated, whether and how the presence of lipid-binding deficient AP2 variants affect cell shape. The focus of these analyses was on EYFP-α and EYFP-σ, as previous data for EYFP-µ were inconclusive. The impact of overexpressing EYFP-µ and the respective substitution variants was thus not assessed, because the proteins were challenging to analyze and showed difficult behavior in the *in vitro* experiments. Pollen tube growth is essential for fertilization in higher plants. The extreme polar tip growth of pollen tube cells depends on the directional secretion of material for apical expansion of PM and cell wall. In this process, the amount of inserted secretory vesicles is much higher than the amount of membrane material needed for the PM expansion, and excess incorporated membrane material is recycled by endocytosis (Grebnev et al., 2017). Therefore, the balance between exocytosis and endocytosis is crucial for pollen tube growth, and any perturbance might result in abnormal pollen tube morphologies.

N. tabacum pollen tubes were transiently transformed by particle bombardment. Protein expression was driven by the pollen specific *pLAT52* promoter to achieve overexpression and the distribution of fluorescent markers was analyzed by spinning disk microscopy four to six hours after transformation. When the fluorescence distribution of the EYFP control was analyzed, it displayed diffuse cytosolic fluorescence, as in previous studies (Figure 19A) (Ischebeck et al., 2008, 2010, 2011). By contrast, EYFP-α1 formed cytosolic puncta and showed additional PM localized fluorescence. The PM-associated fluorescence signal of EYFP-α1 was not evenly distributed and

formed punctate signals at or in close proximity to the membrane (Figure 19A). A large proportion of the pollen tubes overexpressing EYFP-α1 showed PM deformations, where the apical PM was invaginated in an irregular pattern, accompanied by thickened cell walls visible in the bright field images, possibly representing enhanced pectin deposition (Figure 19B; Ischebeck et al. (2008)). The PM deformations occurred at different degrees, where few pollen tubes had an almost normal PM (19.3 %), most had moderate deformations (53.8 %) and some showed severe PM invagination (26.9 %; Figure 19A). The apical PM invaginations resemble patterns observed upon overexpression of the PI4P 5-kinases, PIP5K4 or PIP5K5 in tobacco pollen tubes (Ischebeck et al., 2008). No PM deformations were observed when the EYFP control was expressed under identical conditions (Figure 19A, as indicated). Upon co-expression of the PtdIns(4,5)P_2 biosensor RedStar$_{PLC-PH}$, EYFP-α1 and RedStar$_{PLC-PH}$ seemed to largely colocalize in all observed pollen tubes (Figure 19C, D). Correlation analysis of the fluorescence pattern at the cell surface focal plane by calculating the Pearson coefficient *R*, which ranges from 0 for no correlation to 1 for perfect correlation, indicated a close correlation with a mean *R*-value of 0.86 (17 cells), suggesting that AP2-α1 might localize to PtdIns(4,5)P_2 decorated nanodomains at the PM.

The subcellular localization of the lipid-binding deficient variant EYFP-α1$_{DDDD}$ did not seem to differ from the wild type EYFP-α1, and it also formed cytosolic and PM localized puncta (Figure 19E). Nonetheless, the percentage of the degrees of PM deformation was changed, with only 11.1 % of transformed pollen tubes showing severe PM invagination, 27.8 % showing a moderately altered cell morphology and the majority, 61.1 %, showing a normal PM appearance. While overall EYFP-α1$_{DDDD}$ still largely colocalized with the RedStar$_{PLC-PH}$ marker for PtdIns(4,5)P_2, a substantial proportion of the pollen tubes co-expressing EYFP-α1$_{DDDD}$ and RedStar$_{PLC-PH}$ showed the EYFP-α1$_{DDDD}$ marker further inward from the PM into the cell periphery, in a pattern distinct from that of RedStar$_{PLC-PH}$ (44 % of observed pollen tubes; Figure 19G, H). However, correlation analysis of EYFP-α1$_{DDDD}$ and RedStar$_{PLC-PH}$ signals at the cell surface focal plane resulted in a mean *R*-value of 0.85 (18 cells), indicating an overall close correlation of the markers.

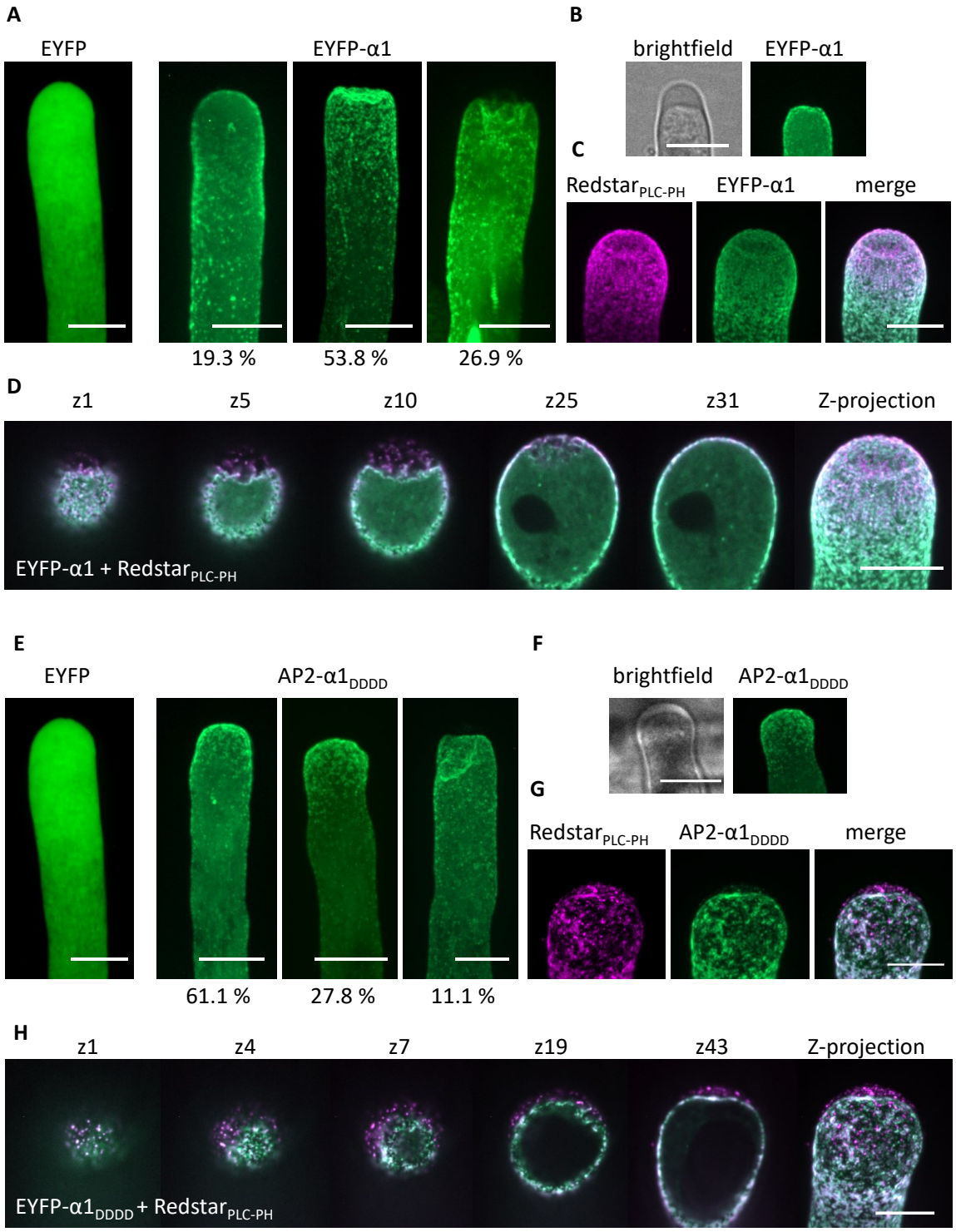

Figure 19. Subcellular localization of EYFP-α1 and EYFP-α1$_{DDDD}$ in tobacco pollen tubes and the influence on pollen tube cell morphology. Tobacco pollen tubes were transiently transformed by particle bombardment and expression was driven by the pollen specific promoter *pLAT52.* Pollen tubes were analyzed 4-6 h after transformation by spinning disk microscopy. EYFP fluorescence is displayed in green, Redstar fluorescence in magenta. **A** Cell morphologies and respective percent proportions of cells observed upon overexpression of EYFP-α1 in comparison to EYFP-control (left). Left to right, normal cell morphology; moderate PM deformation; severe PM invagination. **B** Representative brightfield and EYFP fluorescence images for a pollen tube expressing EYFP-α1 with PM deformation. **C** Fluorescence distribution of EYFP-α1 upon co-expression with the PtdIns(4,5)P_2-marker RedStar$_{PLC-PH}$. **D** Sequential representation of confocal sections of 0.3 µm thickness covering the cell shown in (C) from the periphery towards the median confocal section. Right panel, 3D-projection of the confocal image stack. **E** Cell morphologies and respective percent proportions of cells observed upon overexpression of EYFP-α1$_{DDDD}$ in comparison to EYFP-control (left). Left

to right, normal cell morphology; moderate PM deformation; severe PM invagination. **F** Representative brightfield and EYFP fluorescence images for a pollen tube expressing EYFP-$\alpha1_{DDDD}$ with PM deformation. **G** Fluorescence distribution of EYFP-$\alpha1_{DDDD}$ upon co-expression with the PtdIns(4,5)P_2-marker $RedStar_{PLC\text{-}PH}$. **H** Sequential representation of confocal sections of 0.3 µm thickness covering the cell shown in (G) from the periphery towards the median confocal section. Right panel, 3D-projection of the confocal image stack. **A-C** and **E-G** are Z-projections of confocal image stacks (0.3 µm slices). Percentage values indicate the proportion of observed phenotypes. Scale bars = 10 µm. **A-D** Images are representative for 26 (EYFP-α1) and 17 (EYFP-α1 + $Redstar_{PLC\text{-}PH}$) transformed pollen tubes. **E-H** Images are representative for 18 (EYFP-$\alpha1_{DDDD}$) and 18 (EYFP-$\alpha1_{DDDD}$ + $Redstar_{PLC\text{-}PH}$) transformed pollen tubes.

Upon overexpression of EYFP-σ, the fluorescence of the marker was mainly diffuse in the cytosol and only very few cytosolic puncta were detected (Figure 20A). Most of the transformed pollen tubes displayed unaltered cell morphology when compared to that of the EYFP control (51.9 %). Additionally, pollen tubes with deformed cell shapes were also observed, and 22.2 % showed a narrowing tip, 18.5 % had an indented PM region between 10-20 µm distal from the tip, and 7.4 % showed a moderate PM invagination similar to that described above for EYFP-α1/$\alpha1_{DDDD}$ overexpression. Interestingly, the subcellular localization of the EYFP-σ marker changed upon co-expression of the PtdIns(4,5)P_2-marker $RedStar_{PLC\text{-}PH}$, resulting in the common association of EYFP-σ with $RedStar_{PLC\text{-}PH}$ in punctate signals that were observed both at the PM and in the cytosol (77.3 % of pollen tubes; Figure 20B, C). Correlation analysis of the two markers at the cell surface focal plane for pollen tubes showing punctate signals suggested a close correlation of EYFP-σ and $RedStar_{PLC\text{-}PH}$ with a mean *R*-value of 0.88 (16 cells).

While the lipid-binding deficient variant EYFP-σ_{DDD} also showed diffuse cytosolic fluorescence as the wild type EYFP-σ variant and the observed pollen tube shapes were also very similar (Figure 20D), only very few (3.7 %) of the transformed pollen tubes displayed the indented PM region distal from the tip. In consequence, the proportion of pollen tubes with unaltered cell morphology (66.7 %) was substantially higher than what was observed for pollen tubes expressing EYFP-σ. Pollen tubes with a narrowing tip or moderate PM invagination were observed upon overexpression of EYFP-σ_{DDD} at similar percentages as for the wild type variant EYFP-σ (18.5 % and 11.1 %). In contrast to the observation with wild type EYFP-σ, the co-expression of $RedStar_{PLC\text{-}PH}$ with EYFP-σ_{DDD} did not result in colocalization of the two markers in punctate signals, and even in the presence of $RedStar_{PLC\text{-}PH}$ the fluorescence of EYFP-σ_{DDD} remained diffuse in the cytosol and uniformly distributed at the PM (73.7 % of pollen tubes, Figure 20E, F). The observed differences in the colocalization pattern of EYFP-σ or EYFP-σ_{DDD} with the PtdIns(4,5)P_2 biosensor could not be evaluated in a quantitative manner using the Pearson's correlation coefficient, because it is not suitable for comparing the correlation between diffuse signals and punctate signals. Other usual published algorithms like comparing the standard deviations of pixel intensity values (Fratini et al., 2021) were also tested for analysing the difference in the colocalization of EYFP-σ or EYFP-σ_{DDD} with $RedStar_{PLC\text{-}PH}$ in a quantitative manner, but none of the tested methods were eligible.

However, the observed pattern indicates that the lipid-binding features of EYFP-σ were required for the colocalization of the protein with the RedStar$_{PLC-PH}$-marker for PtdIns(4,5)P_2 in punctate signals (see Figure 20B), and that the formation of puncta was not a consequence of aggregating fluorophores.

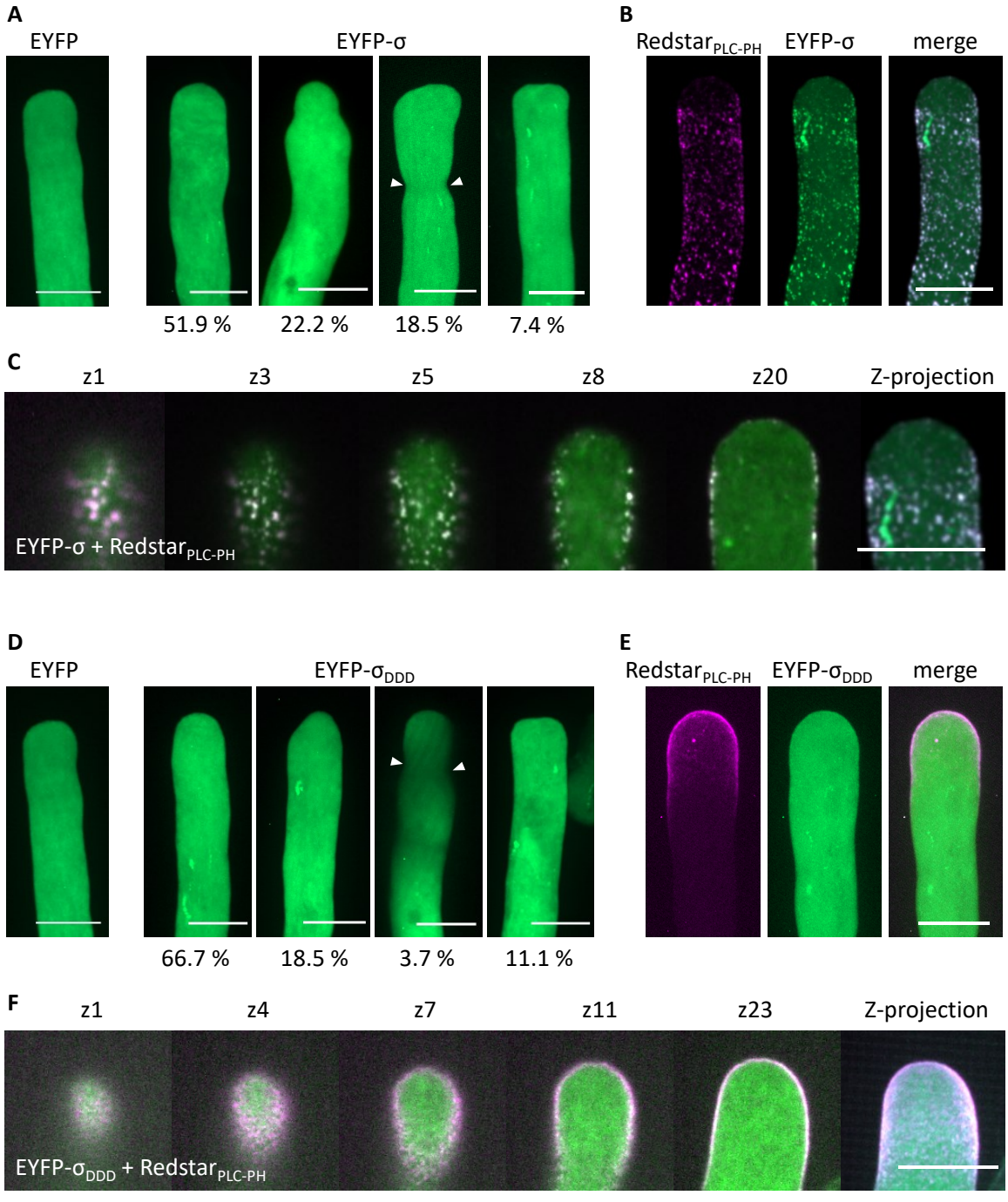

Figure 20. Subcellular localization of EYFP-σ and EYFP-σ$_{DDD}$ in tobacco pollen tubes and the influence on pollen tube cell morphology. Tobacco pollen tubes were transiently transformed by particle bombardment and expression was driven by the pollen specific promoter *pLAT52.* Pollen tubes were analyzed 4-6 h after transformation by spinning disk microscopy. EYFP fluorescence is displayed in green, Redstar fluorescence in magenta. **A** Cell morphologies and respective percent proportions of cells observed upon overexpression of EYFP-σ in comparison to EYFP-control. Left to right, normal cell morphology; apical narrowing; subapical PM indentation (marked by white arrowheads); flattened cell apex. **B** Fluorescence distribution of EYFP-σ upon co-expression with the PtdIns(4,5)P_2-marker RedStar$_{PLC-PH}$. **C** Sequential representation of confocal sections of 0.3 µm thickness covering the cell shown in (B) from the periphery towards the median confocal

section. Right panel, 3D-projection of the confocal image stack. **D** Cell morphologies and respective percent proportions of cells observed upon overexpression of EYFP-σ_{DDD} in comparison to EYFP-control. Left to right, normal cell morphology; apical narrowing; subapical PM indentation (marked by white arrowheads); flattened cell apex. **E** Fluorescence distribution of EYFP-σ_{DDD} upon co-expression with the PtdIns(4,5)P_2-marker, RedStar$_{PLC\text{-}PH}$. **F** Sequential representation of confocal sections of 0.3 µm thickness covering the cell shown in (E) from the periphery towards the median confocal section. Right panel, 3D-projection of the confocal image stack. **A-B** and **D-E** are Z-projections of confocal image stacks (0.3 µm slices). Percentage values indicate the proportion of observed phenotypes. Scale bars = 10 µm. **A-C** Images are representative for 27 (EYFP-σ) and 21 (EYFP-σ + RedStar$_{PLC\text{-}PH}$) transformed pollen tubes **D-F** Images are representative for 27 (EYFP-σ_{DDD}) and 19 (EYFP-σ_{DDD} + RedStar$_{PLC\text{-}PH}$) transformed pollen tubes.

Overall, the analysis of tobacco pollen tubes expressing wild type EYFP-α1 or EYFP-σ or their respective lipid-binding deficient variants, EYFP-α1$_{DDDD}$ and EYFP-σ_{DDD}, showed fluorescent fusions of AP2-complex subunits in a narrow area of the subapical PM. The overexpression of fluorescent fusions of AP2-complex subunits had an impact on cell morphology, and a substantial proportion of cells displayed apical PM invaginations or aberrant cell shapes. As the pollen tube shapes were altered by overexpression of wild type EYFP-α1 and EYFP-σ, it is likely that the important balance between endo- and exocytosis in the pollen tube tip was perturbed. The proportion of "normal" growing pollen tubes was substantially higher in cells expressing wild type EYFP-σ (51.9 %) compared to cells expressing wild type EYFP-α1 (19.3 %), indicating that overexpression of EYFP-α1 had a stronger functional effect *in vivo* than that of EYFP-σ. The overexpression of lipid-binding deficient EYFP-α1$_{DDDD}$ resulted in a substantially lower effect on cell morphologies, with now 61.1 % of the cells displaying normal cell shapes, compared to only 19.3 % when expressing wild type EYFP-α1. Together with the different colocalization pattern of EYFP-α1 or EYFP-α1$_{DDDD}$ with the RedStar$_{PLC\text{-}PH}$-marker for PtdIns(4,5)P_2, this observation indicates a contribution of lipid-binding to the localization and function of AP2-α1. Effects were not as clear for EYFP-σ variants, as overexpression of either wild type EYFP-σ or of EYFP-σ_{DDD} resulted in mostly normal-growing tubes (51.9 % and 66.7 %, respectively). An effect of lipid-binding features was nonetheless also observed for EYFP-σ variants, as only the wild type EYFP-σ displayed an interaction with the RedStar$_{PLC\text{-}PH}$-marker, an effect not observed for the lipid-binding-deficient EYFP-σ_{DDD} variant.

4. Discussion

4.1 Lipid composition modulates membrane liquid phase order and influences the rate of endocytosis

The various lipid classes constituting the PM are not uniformly distributed throughout the membrane. Instead, lipids can occupy laterally segregated regions, with specific enrichment of certain lipid classes. The asymmetric distribution of lipids in the plane of the membrane can encompass larger regions of many µm in diameter, termed membrane polar domains, or it can occur at a much smaller scale below µm diameters, then termed membrane nanodomains (Jaillais et al., 2024). Membrane nanodomains have been already postulated for a long time, formerly also referred to as lipid-rafts or microdomains (Simons & Ikonen, 1997). The lipid-raft hypothesis suggests, that certain membrane nanodomains display a higher degree of liquid-phase order due to the interaction of sterols and sphingolipids enriched in such domains, and experimental data was primary dependent on biochemical methods like the isolation of detergent-resistant or detergent-insoluble membranes (DRMs/DIMs, Bhat & Panstruga (2005). In contrast to the initial assumption that membrane domains with high liquid-phase order are principally composed of sterols, that serve as space fillers between associated sphingolipids, a few years later PIs have also been shown to be enriched in membrane patches derived from plant PM (Furt et al., 2010). While previous definitions of membrane nanodomains resorted to an association with certain lipid classes, such as sterols or sphingolipids, a more recent definition views membrane nanodomains as mere specialized hubs that can serve as platforms for membrane bound processes, including membrane trafficking processes, such as exocytosis or endocytosis (Jaillais et al., 2024).

In this thesis, the PM liquid-phase order of Arabidopsis lines with defects in different aspects of lipid-biosynthesis was analyzed using the fluorescent phase-sensitive dye Di-4-ANEPPDHQ. The liquid ordered state of cytokinetic cell plates compared to the PM was used as a validation of correct dye-use and data evaluation, because such cell plates display a higher liquid-ordered phase state than the PM (Frescatada-Rosa et al., 2014). Intriguingly, mutants with defects in the biosynthesis of sphingolipids or sterols, such as the *loh1 loh3* double mutant and *smt1*^{orc} mutant, showed an effect on the degree of membrane phase-order that was opposite to what was expected based on the literature. In both mutant lines, the PM showed a higher degrees of PM liquid-phase order than the wild type control, whereas the *pip5k1 pip5k2* mutant displayed a reduced degree of PM liquid phase-order (Figure 8B and C). For cell plates in seedlings with altered sterol composition upon treatment with the sterol biosynthesis inhibitors fenpropimorph or lovastatin, or caused by the mutation of sterol biosynthesis gene *Cyclopropylsterol Isomerase1* (*CPI1*), a reduced degree of membrane liquid-phase order was reported (Frescatada-Rosa et al., 2014). However, this reduced degree was only reported for cell plates and not for the PM. Other

data suggesting that highly ordered liquid-phases depend on sterols or sphingolipids are either from different plant species, such as a decrease in membrane liquid-phase order upon decreasing the level of sphingolipids containing 2-hydroxy fatty acids in rice (Nagano et al., 2016), or from different experimental setups, for instance analyzing isolated DRMs or artificial model membranes (Mamode Cassim et al., 2019). Moreover, different zones in Arabidopsis roots may have different GP-values, possibly associated with different functions of the PM in different cells and tissues (X. Zhao et al., 2015). To accommodate such uncertainties and obtain comparable readings, here the data analysis and the determination of GP-values was performed always using epidermal cells at the root apex transition zone. However, the shapes of root cells were not consistently the same in all mutants analyzed, and for instance the *smt1*^{orc} mutant showed severely influenced cell shape and sizes, making it difficult to compare data between all mutant lines tested. Therefore, the differentiation between the functional root zones was not as easy and might have influenced the GP-values obtained. Another important note is, that Di-4-ANEPPDHQ is an intercalating membrane dye and may by itself impact membrane properties (Jaillais & Ott, 2020). Despite these caveats, the data in this thesis indicate that PM liquid-phase order as indicated by Di-4-ANEPPDHQ is influenced by membrane lipid composition, and that PtdIns(4,5)P_2 may has a reinforcing effect on the liquid ordered state of the PM. Importantly, the observed membrane liquid-phase order with altered lipid composition did not only impact on the membrane ordered state, but also influenced endocytosis. The lipid-biosynthesis mutants tested, *loh1 loh3*, *smt1*^{orc} and *pip5k1 pip5k2*, all displayed reduced endocytosis of FM4-64 compared to wild type controls (Figure 9), consistent with previous studies using *pip5k1 pip5k2* or *cpi1-1*, another mutant in sterol biosynthesis. In both mutant lines the endocytosis of FM4-64 as well as that of PIN-protein cargoes was defective (Ischebeck et al., 2013; Men et al., 2008). To interpret the effects of altered lipid biosynthesis on membrane liquid-phase order, it should be taken into account that there is limited information on how the abundance of different lipid classes exerts an influence on the formation of the respective other lipids (Mamode Cassim et al., 2019). Clearly, the regulatory interrelations of lipid biosynthesis pathways are complex, and modulating the abundance of one lipid by applying pharmacological inhibitors or in lipid biosynthesis mutants might influence any other lipid, regardless of how “specific” the intended modulation approach was designed to be.

4.2 The AP2-complex is a possible link between the phosphoinositide network and the early stages of endocytosis

The experiments initiating this study showed that PM lipid composition influences the degree of membrane liquid-phase order and that endocytosis is a process depending on PM lipid composition. While the molecular function of membrane lipids during endocytosis are not well

understood, this thesis followed the working hypothesis that lipid-dependent regulation of endocytosis is based on the recruitment of peripheral membrane proteins to the inner, cytosolic surface of the PM. As sphingolipids or sterols do not likely present recruitment beacons at the cytosolic face of the PM, whereas PIs contain large, charged head groups that protrude from the PM into the cytosol, the analyses in this thesis addressed whether and how PIs might interact with key protein elements of the plant endocytic machinery.

4.2.1 AP2-subunits interact with PI4P 5-kinases controlling endocytosis

As a first step to test whether the AP2-complex represents a mechanistic link between the PI system and the regulation of the early stages of endocytosis, the interaction of AP2-subunits with different PI4P 5-kinases that are known to contribute to endocytic function in plants (Hempel et al., 2017; Ischebeck et al., 2013; Menzel et al., 2019; Y. Zhao et al., 2010) was tested. The positive interactions of the AP2-subunits AP2-β2, AP2-μ and AP2-σ with PIP5K1, PIP5K2 and PIP5K6, but not with PIP5K9 (Figure 10) support the proposed role of AP2 linking CME to the PI system, as the three kinases positive for interaction have reported roles in the regulation of endocytosis, whereas PIP5K9 has not been linked to any endocytic processes (I. Heilmann, 2016). With regard to the specificity of the binding assays, it must be noted that only positive interactions from the yeast two-hybrid analyses were verified using alternative experimental approaches (Figure 10), and some interactions might have been missed by the experimental design. For instance, as no immuno detection for the verification of protein expression was performed for the yeast two-hybrid experiments, it is possible that AP2-α1/2 and AP2-β1 were not expressed in yeast or that the proteins were not functional for interaction. Therefore, other *in vitro* or *in vivo* approaches might be used in the future to also verify negative AP2-subunit interactions with PI4P 5-kinases. During this thesis there were also approaches in testing the AP2-subunits via bimolecular fluorescence complementation (BiFC) for interaction with PI4P 5-kinases, and different combinations of fluorophore orientations or protein fusions were tested in different plant tissues. However, no reconstitution of fluorescence was observed. Even though AP2-subunits have been tested positive in BiFC assays for interaction with various proteins including other AP2-subunits, TPC-subunits or cargo proteins (Di Rubbo et al., 2013; D. Liu et al., 2020; P. Wang et al., 2023), it is possible that the tagged YFP-halves may mask protein interface areas responsible for a possible interaction with PI4P 5-kinases. Furthermore, it is possible that an assembly of the AP2-subunits into the functional complex is necessary to provide a possible site for the interaction with the PI4P 5-kinases, which might be difficult to obtain if the ratio of the available subunits is shifted upon overexpression of only one subunit. In the future, more combinations of tags should be tested to further employ BiFC, or other *in planta* methods like the imaging based Förster

resonance energy transfer (FRET) might be worthwhile to test. Additionally, to assess the relevance of the observed interactions, different functional analyses could be tested. For instance, human PIPK type I isoform γ interacts with the human AP2-complex via the *Hs*AP2-μ subunit, and *Hs*AP2-μ bound to tyrosine-based endocytic sorting signals stimulates *Hs*PIPK Iγ-mediated PtdIns(4,5)P_2 synthesis (Krauss et al., 2006). A similar positive feedback loop providing a PtdIns(4,5)P_2 pool dedicated to AP2 mediated endocytosis is also conceivable for plants. Preliminary experiments testing the catalytic activity of purified recombinant PIP5K2 and PIP5K6 proteins upon addition of purified recombinant AP2-subunits showed no clear effect (Dr. Alexandra Schutkowski, data not shown). In the future, this experiment might be repeated, also including combinations of AP2-subunits with cargo proteins. Moreover, the physiological role of interactions between AP2-complex subunits and PIP5Ks might be revealed by analysis on a time resolved basis. The order of recruitment of AP2-subunits and possibly PIP5Ks to sites of CME events in relation to other EAPs like clathrin or dynamins might give information about the functional interconnections between these proteins and the function of CME.

Besides the interaction of AP2-subunits with PI4P 5-kinases, AP2-subunits can also bind the PI 3-kinase VPS34, according to yeast two-hybrid assays (appendix Figure 33). VPS34 is an endosomal protein (Gerth et al., 2017), and the interaction suggests that the AP1 complex, which is mainly responsible for transport during vacuolar sorting and secretion from the TGN to the PM, to sites of cell division or to the apoplast, is interconnected with the AP2-complex (Arora & Van Damme, 2021; C. Liu et al., 2022). The interconnection might not be limited to the shared AP1/2-β1/2 subunits and similar structural folds of the subunits but might also involve the stability regulating protein P34 (P. Wang et al., 2023). The coordination of both post-Golgi trafficking and CME in plants has been proposed to involve clathrin and adaptor protein recruitment (Yan et al., 2021). Since the VPS34 is mainly localized to late endosomes, the TGN/EE and tonoplast (Gerth et al., 2017), which also represent the sites of AP1 complex operation, the possible connection between the adaptor complexes might explain why subunits of the AP2-complex also interact with VPS34 *in vitro.* Whether this interaction also happens *in vivo* remains currently unresolved, and the physiological relevance of this possible interaction remains elusive.

4.2.2 AP2-subunits bind PIs, with a high affinity for PtdIns(4,5)P_2

Mammalian AP2-subunits as well as subunits of the other multimeric adaptor protein complex in plants, TPC, have previously been shown to bind PIs. To date, no information about the lipid-binding capability of the plant AP2-complex is available. Data in this thesis demonstrate that the AP2-α1NT, AP2-μ, and AP2-σ subunits can bind to anionic phospholipids, with a notable

preference for PtdIns(4,5)P_2, based on the highest binding affinity for PtdIns(4,5)P_2 in the MST experiments (Figure 12, Figure 15 and Figure 16). The AP2-α1NT and AP2-σ proteins contain sequence regions to which the lipid-binding capability can be attributed, as substitutions of amino acids proposed by basic hydrophobicity analysis showed significantly reduced lipid-binding affinities, again with the most pronounced effect on the binding of PtdIns(4,5)P_2 (Figure 15). As lipid-binding of the respective substitution variants was substantially reduced but not completely abolished, it can be concluded that the substituted proteins were not grossly misfolded. This conclusion is supported by CD spectroscopy, where spectra of AP2-α1NT_{DDDD} or AP2-$σ_{DDD}$ did not detectably differ from those of the respective wild type proteins (Figure 32). Alternatively, residual lipid-binding capability of the substitution variants might result from other, additional lipid-binding regions within the proteins. In fact, for AP2-α1 another possible lipid-binding region was identified by the computer-aided sequence analysis, and no substitutions in this region were tested in this thesis (Figure 13). Therefore, in the future further substitution variants with either additional substituted regions or targeting different individual residues for substitution might be tested to further refine residues responsible for PI interaction. The *in vitro* lipid-binding studies were performed using a truncated variant of AP2-α1, and it is possible that the full-length protein may behave differently from the truncation. While the affinity of AP2-α1NT or AP2-σ to PtdIns(4,5)P_2 was the highest among all lipids tested, weaker binding was observed also to PtdIns4P, and low-affinity binding to PtdOH. Since PtdIns4P and PtdOH have been proposed to primary recruit TPC to the PM, these differences in binding preferences of AP2-subunits support the notion that the two adaptor complexes TPC and AP2 might be differentially regulated (Dragwidge et al., 2024; Yperman, Papageorgiou, et al., 2021; Yperman, Wang, et al., 2021). A regulation based on lipid-binding might be mediated by different molecular mechanisms, as AP2-subunits bind with lower affinities to PtdIns4P or other anionic phospholipids than to PtdIns(4,5)P_2. From mammalian systems it is known that the AP2-complex occurs in at least two conformations, and that conformational rearrangements of the AP2-complex might to be mediated by phosphorylation, cargo-binding or by lipid-binding (Beacham et al., 2019; Wrobel et al., 2019). While it was also shown that the AP2-complex from Arabidopsis can be phosphorylated at AP2-μ by a specific protein kinase, there is currently no information about conformational rearrangements of the AP2-complex or their triggers (Kraus et al., 2024; Siao et al., 2023). The interaction of AP2-subunits with PtdIns(4,5)P_2 might promote an active conformation of the AP2-complex, possibly when bound to a budding CCV, or enabling the interaction with other EAPs or with cargo proteins. It appears possible that conversion of PtdIns(4,5)P_2 to PtdIns4P might promote an inactive form of lipid-bound AP2, possibly followed by its release from the CCV. This hypothesis needs investigation in future experiments, where for instance the interplay of AP2-

subunits with PtdIns(4,5)P_2-degrading enzymes could be tested, such as the PtdIns(4,5)P_2-specific lipid phosphatases SAC9 or PI 5-phosphatases. Additionally, more information about the structural conformation of AP2 in its PtdIns4P-bound or PtdIns(4,5)P_2-bound forms might reveal the role of protein-lipid-interactions during AP2-complex assembly.

In contrast to the analysis of recombinant AP2-α1 or AP2-σ proteins, the analyses of the AP2-µ subunit, proved technically difficult. While recombinant AP2-µ protein displayed rather unspecific binding PIs in lipid-overlay assays *in vitro* (Figure 12), these experiments did not indicate preferential binding to one specific PI nor were they suitable to identify specific residues responsible for lipid-binding. Aggregation of AP2-µ/µMHD fusion proteins and their adherence to labware precluded meaningful use of liposome-sedimentation assays, MST assays or CD spectroscopy (Figure 14, Figure 16 and Figure 32). While thus no immediate conclusions can be drawn about potential lipid-binding features of AP2-µ/µMHD, interestingly, the AP2-µMHD_{DAD} and AP2-µ$MHD_{DD\text{-}DDD}$ substitution variants generated based on predicted lipid-binding motifs to interfere with protein-lipid-binding did not show this adhesive behavior to the same extend. However, the AP2-µ$MHD_{DD\text{-}DDD}$ variant still displayed a deviating molecular size when analyzed by SDS-PAGE, suggesting unexpected (mis-)folding or differences in secondary structure. While misfolding could not be verified by CD spectroscopy, it was nonetheless assumed that protein quality was not optimal for further analysis. Overall, the AP2-µ/µMHD wild type protein and its substituted variants posed a challenge for the *in vitro* experiments, and no reliable characterization of the lipid-binding capability was possible. Further *in vivo* approaches might help in solving this issue as they might bypass the difficulties with *in vitro* protein analysis. Even in the absence of interpretable *in vitro* data, AP2-µ likely plays a role mediating binding of the AP2-complex to PtdIns(4,5)P_2, because artificial PtdIns(4,5)P_2 depletion from the PM leads to reduced PM recruitment of AP2-µ in Arabidopsis (Doumane et al., 2021). The *in vitro* analyses on recombinant proteins provide evidence for protein-lipid interaction for several subunits of the Arabidopsis AP2-complex. The *in vitro* characterization of individual AP2-subunits that are each naturally part of a larger protein complex may lead to incomplete conclusions, as mutual effects the subunits might exert on each other may not manifest. For instance, it is possible that binding pockets or interaction interfaces only constitute or are only accessible upon previous interaction between AP2-subunits and certain conformational arrangements. Moreover, as the AP2-subunits have no measurable biochemical activity that can be determined *in vitro*, there was no experiment available to test the recombinant AP2-subunits for functionality. The lipid-binding data for recombinant AP2-subunits are, thus, true *in vitro* results, and may reflect only part of the intrinsic lipid-binding capabilities of the fully assembled AP2-complex. Nonetheless, the specific and highly affine binding of several AP2-subunits to PtdIns(4,5)P_2 represents a feature of the respective

proteins that was positively determined and that may be involved in the functionality of these proteins *in vivo*, even as parts of the larger AP2-complex.

Together, the data from the protein-protein and protein-lipid interaction studies support the hypothesis that CME is driven by accumulation of PtdIns(4,5)P_2 at the PM and that AP2-complexes may associate with PM nanodomains containing PtdIns(4,5)P_2 and the respective PI4P 5-kinases. The physiological relevance of the observed protein-lipid-interactions was analyzed using tobacco pollen tubes and Arabidopsis protoplasts as model systems.

4.3 Lipid-binding regions of AP2-subunits are important for the physiological function *in vivo*

The impact of substitutions in lipid-binding regions of AP2-subunits on CME was first analyzed by monitoring the uptake of the lipophilic dye FM4-64 into tobacco pollen tubes expressing either AP2-subunits or their respective lipid-binding-defective substitution variants. Pollen tubes expressing the lipid-binding deficient AP2-α1 variant, EYFP-α1$_{DDDD}$, showed significantly lower endocytic uptake of FM4-64 than control tubes expressing wild type EYFP-α1 (Figure 17). This observation is consistent with the notion that lipid-binding of AP2-α1 is important for the function of AP2-complexes, as complexes incorporating the expressed AP2-α1$_{DDDD}$ substitution variant were not as efficient in mediating the endocytic uptake of the tracer dye. Alternatively, it is possible that the AP2-α1$_{DDDD}$ substitution variant was not properly folded, even considering that no differences between wild type AP2-α1 and AP2-α1$_{DDDD}$ were observed by CD spectroscopy (appendix Figure 32). The expression of EYFP-σ or EYFP-σ$_{DDD}$ did not result in differences in the endocytosis of the tracer dye. It is possible that the lipid-binding capability of AP2-σ is not important for the internalization of FM4-64. However, these results should be interpreted with caution, since it was also observed that the viability of pollen tubes expressing EYFP-σ or EYFP-σ$_{DDD}$ upon dye application was reduced. The application of FM4-64 can change the localization of integral membrane proteins, as has previously been shown for PIN1, and it is also debated whether dye incorporation into the membrane could lead to temporary changes in membrane fluidity, or lipid phase segregation (Jelínková et al., 2010), possibly with functional consequences for the cell. Reduced viability of cells expressing EYFP-σ or EYFP-σ$_{DDD}$ might indicate that the overexpression of these proteins in pollen tubes alters membrane stability, possibly by mediating defective membrane trafficking. It should be noted that overexpression of EYFP-tagged wild type AP2-α1 or AP2-σ subunits by itself resulted in decreased endocytosis compared to that observed in the EYFP-controls (Figure 17). One feasible explanation would be that the fluorescence tag of the proteins interferes with the physiological function of the proteins. Alternatively, it is possible that overexpression of any one AP2-subunit alone influences the stoichiometry of AP2-complex

assembly, possibly resulting in the formation of partial sub-complexes that then preclude intrinsic subunits from forming functional full-size complexes. While such possibilities cannot be excluded in the experimental setup used, such considerations would apply equally for the wild type AP2-subunits used and for their respective lipid-binding deficient substitution variants. Moreover, the reduced endocytosis observed indicates that the expressed fluorescent fusion proteins have in fact been incorporated into the complex, that they influenced endocytosis, and that thus a meaningful *in vivo* reconstitution of AP2-complexes with the expressed proteins has taken place. As the comparison between EYFP-α1 and EYFP-α1$_{DDDD}$ indicated a significant difference in endocytosis (Figure 17), it appears as if, the pollen tube system gives a hint about the functional importance of the lipid-binding capability of AP2-α1. In previous studies, defects in endocytosis have been found to be more pronounced when monitoring the endocytosis of specific cargo proteins, rather than monitoring membrane tracer dyes (Ischebeck et al., 2013). To assess the effects of defective lipid-binding of AP2-subunits by following a fluorescence-tagged cargo protein, Arabidopsis mesophyll protoplasts transiently expressing the known CME cargo protein, RbohD, were used for further studies. The identical experimental setup was used before to evaluate effects on RbohD endocytosis (Menzel et al., 2019), and the use of Arabidopsis protoplasts has the added advantage of representing a homologous expression system for the Arabidopsis AP2-complex subunits analyzed. Interestingly, when the endocytosis of a fluorescence-tagged EYFP-RbohD fusion was analyzed in protoplasts overexpressing wild type α1-mCherry or σ-mCherry, the endocytic uptake of EYFP-RbohD cargo was enhanced compared to that in the mCherry-expressing control cells (Figure 18). This observation is consistent with an increased abundance of functionally reconstituted AP2-complexes. The different effect on endocytosis of overexpressing AP2-subunits in pollen tubes or protoplasts may be explained by a molecular crowding effect. Pollen tubes display pronounced polar tip growth with strictly regulated zones of endocytosis, whereas mesophyll protoplasts have no polarity and do not display cell expansion based on membrane trafficking. Thus, it is possible that the CME machinery in pollen tubes is already running at maximum capacity and that overexpressing AP2-subunits disturbs the process. In protoplasts on the other hand, there may be more free capacities to accommodate additional overexpressed AP2-complexes at the PM, resulting in an enhanced rate of endocytosis. Alternatively, the differences in the rates of endocytosis observed in pollen tubes or in mesophyll protoplasts might be a consequence of using N-terminally-tagged AP2-subunits in pollen tubes vs. C-terminally-tagged AP2-subunits in protoplasts. Future experiments will address whether the N-terminal or C-terminal positioning of the fluorescence-tags might have different effects on the functionality of the respective fusion proteins.

Any effect of enhanced EYFP-RbohD-internalization in protoplasts upon overexpressing α1-mCherrry or σ-mCherry was abrogated when the lipid-binding deficient substitution variants $\alpha1_{DDDD}$-mCherry or σ_{DDD}-mCherry were expressed. Pronounced differences in endocytosis were observed upon expressing wild type α1-mCherry vs. the $\alpha1_{DDDD}$-mCherry variant (Figure 18) and also upon expressing σ-mCherry vs. σ_{DDD}-mCherry (Figure 18), indicating that the lipid-binding-deficient substitution variants displayed reduced physiological functionality *in vivo*. While the differences between wild type proteins and the respective substitution variants were both significant, the effect of the substituted $\alpha1_{DDDD}$-mCherry vs. its parental protein was more pronounced than for the analysis of σ-mCherry vs. σ_{DDD}-mCherry. This observation implies that the lipid-binding-capability of AP2-α1 and AP2-σ might have differing functions in the spatial-temporal control of CME. Another explanation could be that correct complex assembly is more important for a functional AP2-σ lipid-binding than for AP2-α1. Considering a contribution of AP2-complex assembly, it is also not surprising that the endocytosis of EYFP-RbohD in the Arabidopsis protoplasts was not completely abolished upon overexpression of the lipid-binding deficient variants, as there are still intrinsic wild type AP2-complexes present in the cells. Moreover, a dominant negative effect of the overexpressed variant might outweigh the function of the intrinsic wild type subunits, an effect that might be less pronounced when functional intrinsic hemicomplexes can be formed (C. Wang et al., 2016). It is also possible that the intrinsic TPC contributes to RbohD internalization. Regardless of these considerations, and while no reliable conclusions about the molecular mechanism are possible, the results indicate that the lipid-binding capability of AP2-α1 and AP2-σ is required for the internalization of the CME cargo protein RbohD. Importantly, the findings are in line with previous studies showing reduced rates of endocytosis upon diminished PtdIns(4,5)P_2 abundance (Doumane et al., 2021; Ischebeck et al., 2013; Menzel et al., 2019; Y. Zhao et al., 2010).

To better understand which step of CME is affected by a reduced lipid-binding capability of the AP2-complex, time-resolved imaging of the cooperative recruitment of the individual AP2-subunits, or of different EAPs like monomeric adaptor proteins, clathrin, DRPs or AUXL1/2 in dependency of the wild type vs. lipid-binding deficient AP2-variants could be helpful. Furthermore, future research using stable transformed lines and/or different cargo proteins would be worth trying.

The comparison of endocytosis patterns observed in the pollen tube model or in the protoplast system raises additional questions that may help to understand how AP2-complex assembly is achieved *in vivo*. By overexpressing any one subunit in *in vivo* experiments, the stoichiometry between the heterologous-expressed AP2-subunit and the other, intrinsic AP2-subunits will be altered, and could therefore impact AP2-complex assembly. For instance, subunits might become

sequestered in incomplete complexes and thus may no longer be available for the assembly of full-size AP2-complexes, resulting in a reduced rate of endocytosis despite of overexpression, as observed in pollen tubes (Figure 17). By contrast, in protoplast cells the overexpression of individual AP2-α1 or AP2-σ subunits resulted in an increased rate of endocytosis in both cases. As neither the AP2-α1 nor the AP2-σ subunit can mediate endocytosis by itself, it must be assumed that functional AP2-complexes were assembled at an increased abundance upon overexpression of the AP2-α1 or AP2-σ subunits. Such assembly would require an abundant pool of intrinsic AP2-subunits to complete the respective full-size AP2-complexes that must be postulated to account for the increased rates of endocytosis observed (Figure 18). As already mentioned, it is possible that pollen tubes and protoplasts differ in the abundance of "free" AP2-subunits that are available for forming additional AP2-complexes. Pollen tubes must expand at the maximum-possible speed to fulfil their role in sexual reproduction, where they must "race" other pollen tube cells to deliver the sperm cells to the female ovules for fertilization. It appears obvious that the membrane trafficking machinery mediating apical tip expansion of pollen tubes would, therefore, accommodate the maximum possible number of protein complexes for exocytosis and also for endocytosis. The ensuing crowding of AP2-complexes in the subapical endocytic PM zone of pollen tube cells might preclude the insertion of more AP2-complexes upon overexpression of an AP2-subunit. By contrast, mesophyll protoplasts do not display detectable cell expansion, and there is no reason to assume that these cells display crowding of endocytic complexes. In consequence, additional AP2-complexes might be more easily accommodated at the PM to mediate enhanced rates of endocytosis, as observed in Figure 18. However, in the absence of experimental data, such explanations remain highly speculative.

Issues arising from unbalanced stoichiometries might be bypassed by using complemented knockout lines, that express AP2-complex subunits in a stable fashion under their native promoters. cDNA constructs for the stable expression of AP2-subunits or their substitution variants in the respective Arabidopsis mutant backgrounds were generated in this thesis. However, no fluorescence was detected in any of the transgenic lines even though the correct genotypes were obtained according to PCR analysis. While it would have been informative to have data from stable Arabidopsis transformants to complement the data from the transient expression in tobacco pollen tubes or in Arabidopsis mesophyll protoplasts, it was not possible to troubleshoot and complete the stable Arabidopsis expression experiments within the scope of this project. Future experiments will pursue this approach with more time, and it will be interesting to see whether or not the stable Arabidopsis transformants will confirm the results so far, or whether they might even yield additional information.

4.4 AP2-subunits are positioned at the PM by PtdIns(4,5)P_2 and influence polar tip growth of pollen tubes

Based on numerous lines of evidence, the AP2-complex subunits AP2-α1 and AP2-σ bind to anionic phospholipids and PtdIns(4,5)P_2, and this binding is required for their function in mediating endocytosis. When fluorescence-tagged EYFP-α1 or EYFP-σ proteins or their respective substitution variants were expressed in tobacco pollen tubes, the fluorescent fusion proteins localized in a punctate pattern at the cell periphery of the subapical PM region, consistent with a role in mediating endocytosis related to polar tip growth (Figure 19 and Figure 20). Both EYFP-α1 and EYFP-σ showed colocalization with a fluorescent biosensor for PtdIns(4,5)P_2, consistent with their binding capability for that lipid (Figure 19C and Figure 20B).

The distribution of the lipid-binding deficient variant EYFP-α1$_{DDDD}$ was similar to that of EYFP-α1, but displayed a different pattern of colocalization with the PtdIns(4,5)P_2 biosensor (Figure 19G). While most of the punctate membrane signals of either marker proteins resided in an overall similar pattern, for some pollen tubes it was observed that EYFP-α1$_{DDDD}$ occupied a peripheral region slightly more inward from the PM than the PtdIns(4,5)P_2 biosensor, a pattern that has previously been reported also for the distribution of PIP5K2-EYFP in tobacco pollen tubes (Fratini et al., 2021). In comparison to the pattern displayed by EYFP-σ (Figure 20B), EYFP-σ$_{DDDD}$ coincided even less with the PtdIns(4,5)P_2 biosensor and was almost exclusively cytosolic or uniformly distributed at the PM (Figure 20E). It is interesting to note that neither fluorescent AP2-σ variant (EYFP-σ or EYFP-σ$_{DDD}$) displayed a localization in punctate structures in the absence of a co-expressed RedStar$_{PLC\text{-}PH}$ biosensor (Figure 20A and D), suggesting an artificial contribution of the co-expression to the fluorescence patterns observed. While this impairs interpretation of the data, nonetheless the lipid-binding-deficient variants of both AP2-complex subunits also showed an altered colocalization pattern with the PtdIns(4,5)P_2 biosensor (Figure 19G, H; Figure 20E, F). It will remain to be elucidated whether PM association of AP2-subunits might be tested by other, more quantitative means, such as fluorescence recovery after photobleaching (FRAP)-analysis to monitor membrane-association dynamics of the fluorescent markers.

Overall, despite some differences, the PM recruitment of EYFP-α1 or EYFP-σ was not abolished when the lipid-binding deficient fusion proteins EYFP-α1$_{DDDD}$ or EYFP-σ$_{DDD}$ were analysed side-by-side with their respective parental proteins. It appears possible that the PM-association even of the lipid-binding deficient substitution variants was facilitated by heteromerization with intrinsic, functional AP2-subunits. Also, further lipid-binding regions that were not modified in the EYFP-α1$_{DDDD}$ or EYFP-σ$_{DDD}$ substitution variants might have contributed to PM-association of these proteins, possibly by binding to PtdOH or PtdSer in addition to binding PIs. Previous studies have

reported a role of PtdOH and PtdIns4P in recruiting TPC to the PM, with TPC proposedly arriving prior to AP2 at the PM (Dragwidge et al., 2024; Gadeyne et al., 2014; Johnson et al., 2021).

Besides a potential role of other, unknown factors, such as other EAPs, it must be also considered that this study mainly focused on AP2-α1 and AP2-σ, whereas AP2-μ was not examined to the same extent. However, loss of AP2-μ impairs the recruitment of other AP2-subunits to the PM more substantially than the loss of AP2-σ (C. Wang et al., 2016). AP2-μ has also been proposed to arrive prior to CLC or AP2-α1 and concomitant with TPC-subunits at the PM sites of future endocytic events, in contrast to other AP2-subunits, which are recruited only after TPC-subunits (Bashline et al., 2015; Johnson & Vert, 2017). This implies that AP2-μ could have a similar role in the positioning of the CME machinery as TPC, which is thought to initiate CME through the binding to PtdIns4P or PtdOH (Dragwidge et al., 2024; Yperman, Papageorgiou, et al., 2021). Even if the observations from the subcellular localization analysis regarding AP2-α1 and AP2-σ do not conclusively support a role of PtdIns(4,5)P_2-binding in the initiation or positioning of CME, by comparing AP2-α1 and AP2-σ it was obvious that the subunits may exert differential functions in CME regulation, leaving the possibility that the observed but not well investigated PtdIns(4,5)P_2 interaction of AP2-μ is responsible during the positioning and initiation of CME events.

Effects of lipid-binding by AP2-subunits at a larger scale included altered cell morphology of tobacco pollen tubes, which are especially suitable for this analysis, because their extreme, polarized cell shape requires the perfect coordination of cytoskeletal control, exocytosis and endocytosis (Grebnev et al., 2017). In consequence, altered cell morphologies can indicate perturbations in the coordination of the cellular machinery for polar tip growth. Most (53.8 %) of the pollen tubes overexpressing EYFP-α1 showed moderate to severe membrane invagination at the pollen tube tip, in addition to smaller proportions of normal growing cells (19.3 %) or extreme invaginations (26.9 %; Figure 19). The apical PM invagination is similar to that previously observed upon overexpression of the PI4P 5-kinases PIP5K4, PIP5K5 (Ischebeck et al., 2008) and PIP5K6 (Y. Zhao et al., 2010), suggesting a link to regulatory effects of PtdIns(4,5)P_2. The apical PM invagination has been attributed to enhanced cell wall deposition limiting apical cell expansion and subsequent „protoplast trapping“, resulting in excess membrane material folding inwards (Ischebeck et al., 2008; Y. Zhao et al., 2010). While pollen tube PM invagination morphology was formerly attributed to an overstimulated secretion/exocytosis of pectin, the coordinated secretion requires balanced rates of exocytosis and endocytosis. In line with this notion, PM invagination morphology can also be a consequence of over-initiated but abortive endocytosis, as has previously been reported (Y. Zhao et al., 2010). With regard to the PM invagination cell morphology observed upon overexpression of EYFP-α1 (Figure 19), the intrinsic elements of the machinery finalizing CME might be less abundant than the overexpressed AP2-subunits and

therefore initiation of CME might be promoted but not result in completion of CME. This interpretation is also in line with the reduced rates of endocytosis of the tracer dye, FM4-64, shown in Figure 17. The reduction of the lipid-binding capability of EYFP-α1$_{DDDD}$ shifted the proportion of observed morphological pollen tube categories towards control-like cell shapes, with clearly less severe effects on cell morphology (Figure 19E). This observation indicates that lipid-binding of the AP2-α1 might be required for the effect observed upon overexpressing EYFP-α1 (Figure 19A). As the overexpression of wild type EYFP-α1 resulted in similar cell morphologies as the overexpression of PIP5Ks, and this effect was less pronounced upon overexpression of the lipid-binding defective variant, the observations presented in Figure 17 and Figure 19 would support the hypothesis that AP2-α1 regulates endocytic events in a PtdIns(4,5)P_2-dependent manner.

By comparison, the majority of pollen tubes expressing EYFP-σ looked similar to EYFP controls (Figure 20A), with only 48.1 % pollen tubes showing any detectable morphological alterations. The morphological alterations observed upon expression of EYFP-σ (Figure 20A) were overall much milder than those seen upon expressing EYFP-α1 (see Figure 19A) and included a narrow cell tip (22.1 %), mild PM invagination (7.4 %), or lateral subapical indentations 10-20 µm distal from the tip (18.5 %). As with EYFP-α1 vs. EYFP-α1$_{DDDD}$, the expression of EYFP-σ$_{DDD}$ (Figure 20D) resulted in a reduction of morphological alterations compared to those observed upon expression of EYFP-σ, even though the morphological effects in that case had already been rather mild (see Figure 20A). This observation is in principle also consistent with a role of lipid-binding also in the function of EYFP-σ.

The evaluation of pollen tube cell morphologies showed that the overexpression of either, AP2-α1 or AP2-σ, caused abnormal cell morphologies, such as have previously been proposed to arise from a perturbed balance between endocytosis and exocytosis. Importantly, effects on cell morphologies were less pronounced when AP2-subunits with defective PtdIns(4,5)P_2 binding capability were expressed, supporting the hypothesis that PIs, especially PtdIns(4,5)P_2, contribute to the function of the AP2-complex and the regulation of CME. Since the overexpression of AP2-α1 or AP2-σ had different effects, it appears plausible that the subunits may have separate functions within the AP2-complex during the course of CME. It is difficult to interpret the precise effects of EYFP-α1 and EYFP-σ on cell morphologies or on their individual functionality, as both proteins are part of a multimeric protein complex, and the stoichiometry of complex assembly might be altered by overexpressing any one subunit. Moreover, the contribution of the intrinsic AP2-subunits present in the tobacco pollen tubes on the recruitment and positioning of the overexpressed AP2-α1 and AP2-σ from Arabidopsis remains unclear.

With regard to the effects of lipid-binding, both the experiments testing endocytosis (Figure 17 and Figure 18) and the analysis of cell morphologies (Figure 19 and Figure 20) indicate that a reduced lipid-binding capability of AP2-α1 has a bigger influence on the functionality of the AP2-complex than that of AP2-σ.

4.5 Conclusions and future perspectives

The results of this thesis show that subunits of the AP2-complex from Arabidopsis are capable of interacting with PIs, with a high affinity towards binding PtdIns(4,5)P_2. Together with the observed interaction of AP2-complex subunits with PI4P 5-kinases, that have reported roles in the regulation of endocytosis in plants, the data demonstrates that the AP2-complex is part of the molecular mechanism by which the PI system regulates CME in plants. The precise molecular role of the interaction of AP2-subunits with PtdIns(4,5)P_2 is not yet clarified, but it might be related to the coordination between membrane trafficking by exocytosis/endocytosis and cytoskeletal dynamics, a coordination thought to be substantially influenced by PtdIns(4,5)P_2. Besides a PtdIns(4,5)P_2-dependent regulatory role of AP2 in CME, preliminary experiments revealed an additional and novel link of the AP2-complex to cytoskeletal regulation: AP2-β2, AP2-μ and AP2-σ all displayed potential interactions with the ROP2 and ROP8; with the guanidine nucleotide dissociation inhibitors (GDIs) GDI1, GDI2 and GDI3, which control ROP function; as well as with a C-terminal fragment of the class VIII-myosin $ATM2_{972\text{-}1220}$, which has been shown to stabilize actin (Vera Wagner, Dept. of Plant Biochemistry, unpublished results) (Figure 21). Such interactions might be highly relevant, as, e.g., ROP proteins mediate the assembly of cytoskeletal structures at the PM. It has been shown that membrane PIs can exert regulatory effects on ROP signaling and that interfering with ROP signaling leads to stabilized actin dynamics and membrane trafficking defects (Chen et al., 2012; Fratini et al., 2021; Ischebeck et al., 2011; Kost, 2008; Yalovsky et al., 2008). At this stage there are many open questions on how AP2 could be implemented at the interface between membrane trafficking and ROP signaling, but a possible hypothesis is that AP2 mediates the guidance of budding or newly released CCVs towards actin to enable the directed movement along the filaments. It has been proposed that actin filaments are involved in the detachment of CCVs directly from the site of CME and that actin may mediate the organization of early post-endocytic CCV trafficking (Kraus et al., 2024; Narasimhan et al., 2020), but the molecular details of this proposed process remain unclear. PtdIns(4,5)P_2, PIP5K2 (Fratini et al., 2021) and ATM2 (Vera Wagner, Dept. of Plant Biochemistry, unpublished results) reside in PM nanodomains that facilitate the stabilization of membrane-proximal actin filaments (Fratini et al., 2021; Kastner et al., 2022). As AP2 interacts with all three listed components, PtdIns(4,5)P_2, PIP5K2 and ATM2, *in vitro*, it is conceivable that AP2 plays a so far unknown role in the coordination of trafficking and

actin dynamics, and possibly even in the PM nano-organization and the formation of PtdIns(4,5)P_2-nanodomains. In the future, it will be very interesting to test if AP2 can also directly interact with actin. It is noteworthy, that in the yeast two-hybrid tests, no growth was visible for AP2-α1 with the positive control (Figure 21). The failure to grow for the positive control suggests that AP2-α1 might not have been expressed in the yeast system, raising the question, whether negative results from previous YTH interaction studies between AP2-α1 and the PI4P 5-kinases (Figure 10A) will have to be re-visited.

The novel interaction between the AP2-complex and components of ROP signaling, and the actin-stabilizing machinery needs further investigation and provides an exciting clue that the AP2-complex may play a role in connecting ROP signaling and actin dynamics with endocytosis.

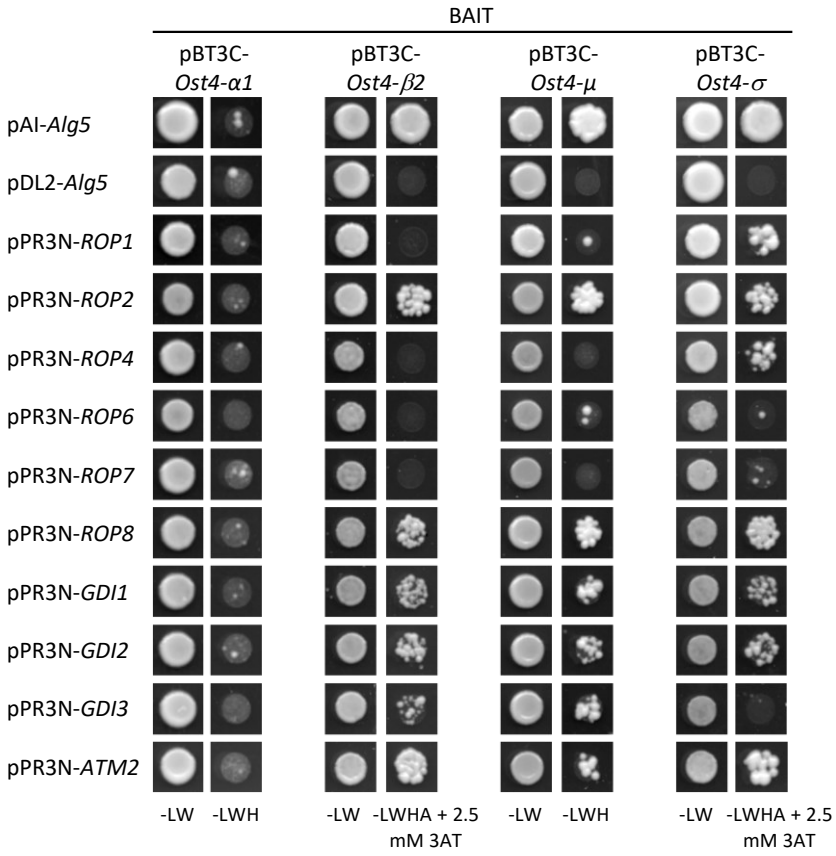

Figure 21. AP2-subunits interact with ROPs, GDIs and ATM2 in yeast two-hybrid analysis. Split-ubiquitin based YTH with AP2-α1/β2/μ/σ fused to the C-terminal ubiquitin half, an Ost4 ER membrane-anchor and transcription factors as bait proteins. Rho of plant (ROP1/2/4/6), guanidine nucleotide dissociation inhibitors (GDI1/2/3) and a C-terminal fragment of the class VIII-myosin ($ATM2_{972-1220}$) were used as prey proteins fused to the N-terminal ubiquitin half, *pAI-Alg5* and *pDL2-Alg5* were used as positive and negative control. Transformed yeast was grown on selective media lacking leucine and tryptophan (-LW) as control for transformation with bait and prey vectors. Growth on media lacking additionally histidine (-LWH) or histidine and adenine (-LWHA) indicated protein-protein interaction. 3-amino-1,2,4-triazole (3-AT) was added for a more stringent selection. Data is representative for two independent experiments testing five colonies each per transformation.

Drawing on all the available information, several models are conceivable to integrate the observed AP2-PtdIns(4,5)P_2 interaction with fine tuning CME (Figure 22). These models are not mutually exclusive, and combinations of the proposed effects as well as additional further effects are possible.

I) One possible role for the interaction of AP2-complex subunits with PtdIns(4,5)P_2 is a PI-dependent role of AP2 in CME initiation and positioning of the CME machinery. This hypothesis was proposed based on endocytic defects observed in the Arabidopsis *pip5k1 pip5k2* double mutant (Ischebeck et al., 2013). The observation of extended PM half-life of active endocytosis cargoes upon depletion of PtdIns(4,5)P_2 (Menzel et al., 2019; Rausche et al., 2021) further suggested that PtdIns(4,5)P_2 is required for the very early stages of CME, since cargo proteins remain active in the membrane. The data presented in this thesis are consistent with this first hypothesis, as the observed high affinity binding of AP2-α1 and AP2-σ to PtdIns(4,5)P_2 provides a possible molecular basis for the effects observed. However, not all data obtained in this thesis fully support this model. For instance, the localization of lipid-binding-deficient AP2-subunits was not drastically changed in tobacco pollen tubes; or the internalization of the endocytic tracer dye or a cargo protein was reduced but not fully abrogated. Taken into account the unknown interdependence of TPC and AP2 and the proposed role of TPC as one of the first arriving adaptors, it is possible that AP2 and TPC fulfill similar regulatory roles. The physiological importance of the two adaptor complexes might change depending on environmental cues or depending on cargo-selection. For the pollen tube data, this means that binding of AP2-complex subunits to PtdIns(4,5)P_2 will be one but not the only one factor determining PM association and PM positioning of the AP2-complex. Moreover, results from this thesis indicate different roles of the individual AP2-subunits AP2-α1 and AP2-σ during CME initiation, and it is possible that the observed PtdIns(4,5)P_2-binding capability also of AP2-μ is important during the early stages of CM. While localization or function of AP2-μ was not further analyzed due to technical limitations, AP2-μ is still proposed to be one of the earliest AP2-subunits recruited to the PM during the initiation of CME (Bashline et al., 2015; Johnson & Vert, 2017). Future experiments will address the relations between the formation of PtdIns(4,5)P_2 and a possibly AP2-μ-dependent recruitment of other AP2-subunits to the PM.

II) In an alternative model, the PtdIns(4,5)P_2 interaction of AP2-α1 and AP2-σ is important not at the initiation and correct PM positioning of CME events, but at other stages of CME. This idea is supported by the observation that AP2, other than TPC, is still enriched in mature CCVs, and departures later from the CCVs than TPC (Johnson et al., 2021). In this context it is relevant to

note that also PI4P 5-kinase activity (Ischebeck et al., 2013) and PtdIns(4,5)P_2 (König et al., 2008) have independently been detected by direct biochemical analysis in isolated mature CCVs formed upon salt treatment of Arabidopsis plants. The observed interaction between AP2-subunits and PtdIns(4,5)P_2 as well as with corresponding PI4P 5-kinases might be part of a self-reinforcing mechanism to promote PtdIns(4,5)P_2 production, building a specific localized PtdIns(4,)P_2 pool that serves as an interaction hub for CME components leading to the recruitment of other EAPs. In this context, AP2 might serve as a checkpoint at later stages to inhibit the progressing of CME if certain conditions are not met. The ratio between PtdIns4P and PtdIns(4,5)P_2 seems to be involved in the regulation of CME, as it was observed that co-expression of PI4Kβ1, which increases the pool of PtdIns4P, the precursor to PtdIns(4,5)P_2, partially rescues altered cell morphologies observed upon PIP5K6 overexpression in tobacco pollen tubes (Y. Zhao et al., 2010). AP2 could serve as a checkpoint by either influencing the ratio between PtdIns4P and PtdIns(4,5)P_2 or by itself being influenced by the ratio between the PIs.

One possible target for such secondary PtdIns(4,5)P_2-dependent protein recruitment through AP2 are DRPs, as the density of DRP1C was reduced upon lower PtdIns(4,5)P_2 levels (unpublished data AG Heilmann). This could also be an indirect effect, as it is proposed that TPC could play a role in recruiting DRPs (Dragwidge et al., 2024; Gadeyne et al., 2014). As plant DRP2s implicated in CME possess a PtdIns(4,5)P_2-binding pleckstrin homology (PH) domain (Kraus et al., 2024), it is possible that AP2-dependent upregulation of PI4P 5-kinase-mediated PtdIns(4,5)P_2 production is necessary for the finalization of CME progress. This would be in line with the findings that clathrin appears in fewer but larger PM foci in the *pip5k1 pip5k2* double mutant, hinting towards an aborted CME and not an inhibition of the early stages (Ischebeck et al., 2013).

III) A third model how lipid-binding of AP2-complexes might influence CME is related to the preliminary results showing a possible interaction between AP2 and the actin stabilizing machinery involving the ROP-signaling pathway. In this context, AP2 might mediate the guidance of nascent or mature CCVs towards the actin filaments. At which timepoint of the CME progression AP2 mediated guidance through interaction with ATM2 or with components of the ROP signaling pathway might take place remains elusive.

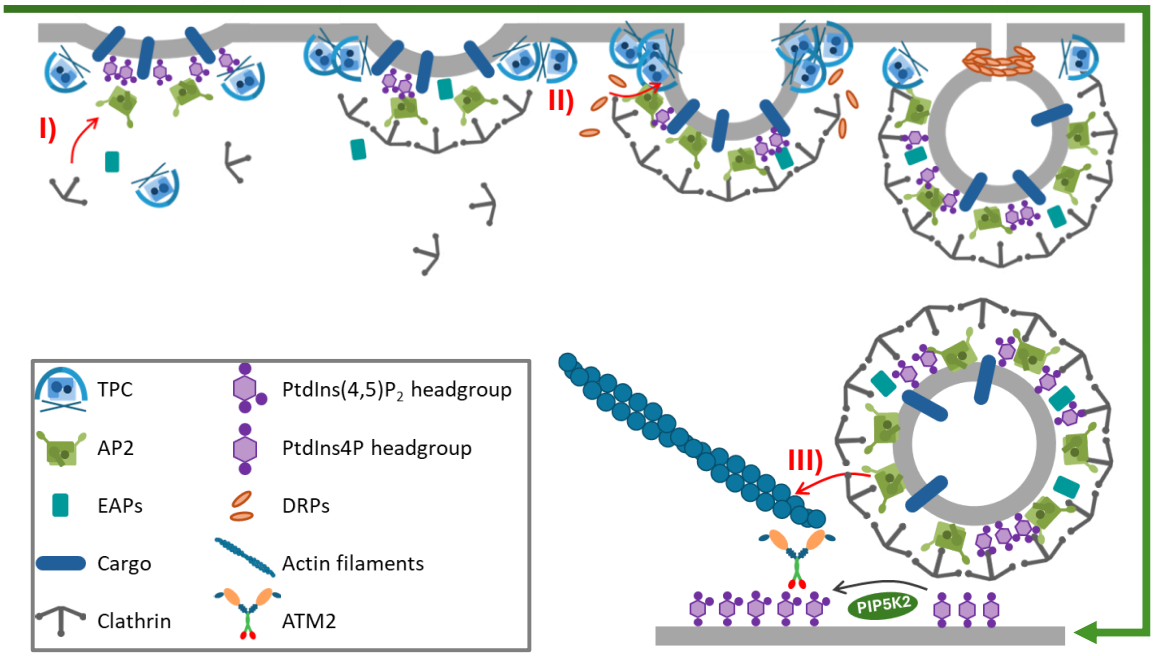

Figure 22. Schematic overview of CME and the possible roles for AP2-PI interaction. The scheme is representatively displaying the progress of CME in plants with red arrows and numbers indicating possible stages in CME where the lipid-binding capability of AP2 could play a role. All processes, structures, sizes and arrangements are only representative. TPC, TPLATE complex; AP2, adaptor-protein complex 2; EAPs, endocytic accessory proteins; DRPs, dynamin-related proteins; ATM2, *Arabidopsis thaliana* Myosin 2.

Overall, the contemplated different possible roles for a PtdIns(4,5)P_2 dependent regulation of AP2 in plant CME are not exclusive and may involve differential functions of the individual subunits at different steps of CME. Many additional factors might also contribute, such as the interdependence with the TPLATE-complex, with other EAPs, and prerequisites like environmental stress, cargo specificity or developmental processes that influence the CME mechanisms have not been considered in the model shown in Figure 22. Nonetheless, based on the data in this thesis new hypotheses can be formulated about how the AP2-complex is linked to the PI-system to better understand the molecular details of how membrane lipids contribute to the regulation of CME regulation in plants.

5. Material and methods

5.1 Devices and Equipment

The devices and equipment used in this thesis are listed in the respective method sections.

5.2 Chemicals

All chemicals that are not specifically mentioned were obtained from Carl Roth GmbH (Karlsruhe, Germany), AppliChem (Darmstadt, Germany), Merck (Darmstadt, Germany) or VWR International GmbH (Darmstadt, Germany).

5.3 Kits, consumables and enzymes

All restriction enzymes were purchased from New England Biolabs Inc. (Frankfurt am Main, Germany). Other enzymes, kits and consumables used in this thesis are listed in the respective method sections.

5.4 Plant lines

A. thaliana	wild type, ecotype *Columbia-0* (Col-0):	originally obtained from Lehle seeds (http://www.arabidopsis.com)
	pip5k1 pip5k2 in Col-0 background:	crossing of *pip5k1* (SALK_146728) and *pip5k2* (SALK_012487), heterozygous for *PIP5K1* (Ischebeck et al., 2013).
	loh1 loh3 in Col-0 background:	crossing of *loh1* (SALK_080371) and *loh3* (SALK_150849), heterozygous for *LOH3* (Markham et al., 2011).
	smt1^{orc} in Utr background:	ethyl methanesulfonate mutagenesis line, mutation in *SMT1* gene (Willemsen et al., 2003).
N. tabacum	wild type, ecotype *Samsun N*	
N. benthamiana	wild type	

5.5 Microorganisms

for molecular cloning:

Escherichia coli (*E. coli*) NEB5α (New England Biolabs Inc., Frankfurt am Main, Germany)

Genotype: *fhuA2 Δ(argF-lacZ)U169 phoA glnV44 Φ80 Δ(lacZ)M15 gyrA96 recA1 relA1 endA1 thi-1 hsdR17*

for recombinant protein expression:

Escherichia coli (*E. coli*) Rosetta2(DE3) (Merck (Novagen), Darmstadt, Germany)

Genotype: *F- ompT hsdS$_B$ (r$_B$- m$_B$-) gal dcm (DE3) pRARE2 (CamR)*

Escherichia coli (*E. coli*) BL21 (DE3) (Thermo Fisher Scientific, Schwerte, Germany)
Genotype: *F– ompT hsdS$_B$ (r_B–, m_B–) gal dcm (DE3)*

for plant transformation:
Agrobacterium tumefaciens (*Agrobacterium/A. tumefaciens*) AGL-0 (Lazo et al., 1991)
Genotype: *C58 pTiBo542; recA::bla Tregion deletiert Mop(+) Cb(R)*

for yeast two-hybrid analysis:
Saccharomyces cerevisiae (*S. cerevisiae*) NMY51 (Dualsystems Biotech AG, Zurich, Switzerland)
Genotype: *MATa, his3Δ200, trp1-901, leu2-3,112, ade2, LYS2::(lexAop)4-HIS3, ura3::(lexAop)8-lacZ (lexAop)8-ADE2 GAL4)*

5.6 Vectors

pBT3-C-OST4	*Kan^R*, bait vector for yeast two-hybrid analyses based on *pBT3-C*, *LEU2* auxotrophic marker for selection in yeast. Contains a multiple cloning site (mcs) for C-terminal fusions to C-terminal ubiquitin half (*Cub*, aa 34-76) and transcription factor LexA-VP16. cDNA for the oligosaccharyltransferase 4 (OST4) was inserted via an XbaI restriction sites. Gene expression is controlled by *CYC1* promoter and terminator. (Dualsystems Biotech AG, Zurich, Switzerland; modified by Dr. Mareike Heilmann, MLU Halle-Wittenberg)
pPR3-N	*Amp^R,* prey vector for yeast two-hybrid analyses, *TRP1* auxotrophic marker for selection in yeast. Contains a mcs for N-terminal fusions to N-terminal mutated ubiquitin half (*NubG*, aa 1-38, I13 mutated to G) and HA-tag. Gene expression is controlled by *CYC1* promoter and terminator. (Dualsystems Biotech AG, Zurich, Switzerland)
pAI-Alg5	*Amp^R,* prey vector as positive control for yeast two-hybrid analyses, *TRP1* auxotrophic marker for selection in yeast. Contains wild type *Nub* fused to the cDNA of *dolichyl-phosphate beta-glucosyl-transferase* (*Alg5*). (Dualsystems Biotech AG, Zurich, Switzerland)
pDL2-Alg5	*Amp^R,* prey vector as negative control for yeast two-hybrid analyses, *TRP1* auxotrophic marker for selection in yeast. Contains *NubG* fused to *Alg5*. (Dualsystems Biotech AG, Zurich, Switzerland)

pGEX-6P-1	*Amp*^{R}, vector for protein expression, containing mcs for N-terminal fusions to Glutathion-S-Transferase (GST) under control of *tac* promoter. (GE Healthcare GmbH, Solingen, Germany)
pMAL-c5G	*Amp*^{R}, vector for protein expression, containing mcs for N-terminal fusions to maltose-binding-protein (MBP) under control of *tac* promoter. Contains cleavage site for specific protease Genenase™ I. (New England Biolabs Inc., Frankfurt am Main, Germany)
pET-28b(+)	*Kan*^{R}, vector for protein expression, containing mcs for N-terminal hexa histidine (His_6)-tag, followed by thrombin cleavage site, T7-tag and C-terminal His_6-tag. Gene expression under control of *T7* promoter and terminator. (Merck (Novagen), Darmstadt, Germany)
pEntryA	*Amp*^{R}, based on *pUC18*, contains sfiIA/B restriction sites for promoter insertion and mcs followed by *polyA* terminator of *octopin-synthase (OCS)* from *A. tumefaciens.* Promoter, mcs and terminator are flanked by *att*-sites (5' *att*L1 and 3' *att*L4) for recombination with the dual Gateway™ system. (Dr. Mareike Heilmann, MLU Halle Wittenberg)
pEntryD	*Amp*^{R}, based on *pUC18*, contains sfiIA/B restriction sites for promoter insertion and mcs followed by *polyA* terminator of *OCS* from *A. tumefaciens.* Promoter, mcs and terminator are flanked by *att*-sites (5' *att*L4 and 3' *att*L2) for recombination with the dual Gateway™ system. (Dr. Mareike Heilmann, MLU Halle Wittenberg)
pCAMBIA3300.0GC	*Kan*^{R} in bacteria, Phosphinothricin resistance in plants. Contains a *ccdB* gene flanked by *att*R1 and *att*R2 sites for recombination with the Clonase™-mediated dual Gateway™ system. Contains the left border sequence and right border sequence for Agrobacterium mediated stable transformation in plants. (Dr. Ellen Hornung, Göttingen)
pDONR™221-P1P4	*Kan*^{R}, donor vector for Clonase™-mediated dual Gateway™ system. Contains a *ccdB* gene and *Cm*^{R} gene flanked by the recombination sites *att*P1 and *att*P4. For replication in *E. coli*, the vector contains a *pUC ori.* (Thermo Fisher Scientific, Schwerte, Germany)

pDONR^{TM}221-P3P2	*Kan^{R},* donor vector for Clonase^{TM}-mediated dual Gateway^{TM} system. Contains a *ccdB* gene and *Cm^{R}* gene flanked by the recombination sites *att*P3 and *att*P2. For replication in *E. coli*, the vector contains a *pUC ori.* (Thermo Fisher Scientific, Schwerte, Germany)
pBiFCt-2in1	*Spec^{R},* target vector Clonase^{TM}-mediated dual Gateway^{TM} system. Contains the *lacZ* gene flanked by the recombination sites *att*R3 and *att*R2. *Cm^{R}* gene and *ccdB* gene are flanked by *att*R1 and *att*R4. The N-terminal half of YFP (nYFP) is either located N-terminal or C-terminal to *att*R2 and the C-terminal half of YFP (cYFP) is either located N-terminal or C-terminal to *att*R4. The Gene for *mRFP1* is located between the two expression cassettes. All expression cassettes are under the control of the *pCaMV35S* promoter and terminator. The vector can be used for the transformation of *A. tumefaciens* as it contains left border sequence and right border sequence. (Grefen & Blatt, 2012)

5.7 Media and growth conditions

All media was autoclaved for 15 min at 121 °C before use. Stock solutions for supplemented antibiotics, glucose and amino acids were sterilized by filtration. Supplemented antibiotics and the used concentrations are listed in Table 1.

Table 1. Antibiotics used for selection of bacteria.

Antibiotic	Concentration stock solution	Final concentration
Carbenicillin	100 mg/ml	100 µg/ml
Kanamycin	50 mg/ml	50 µg/ml
Rifampicin	50 mg/ml	50 µg/ml
Spectinomycin	50 mg/ml	50 µg/ml

5.7.1 Growth conditions for *E. coli*

E. coli cells were grown at 37 °C in LB media (0.5 % (w/v) yeast extract, 1 % (w/v) tryptone, 0.5 % (w/v) NaCl) with antibiotics added for selection (see Table 1). Liquid cultures were incubated shaking at 180 rpm. For solid media 1.5 % (w/v) micro-agar (Duchefa, Haarlem, Netherlands) was added to the media.

5.7.2 Growth conditions for *S. cerevisiae*

S. cerevisiae was cultivated at 30 °C. Liquid cultures were incubated shaking at 180 rpm. For the maintenance of the yeast strain NMY51, colonies were plated out every two weeks on solid YPAD media (1 % (w/v) yeast extract, 2 % peptone, 0.004 % (w/v) adenine hemi sulfate, 2 % (w/v) glucose, 1.5 % (w/v) micro-agar for solid media), incubated for two days at 30 °C and then stored at 4 °C. For selection of transformed yeast, amino acid stock solutions were added to solid SD media (0.17 % (w/v) yeast nitrogen base without amino acids and ammonium sulfate, 0.5 % (w/v) $(NH_4)_2SO_4$, 1.5 % (w/v) micro-agar for solid media, 2 % (w/v) glucose added after autoclaving).

Amino acid stock solutions (10x):

-LW: 200 mg/l L-adenine hemi sulfate, 200 mg/l L-arginine HCl, 200 mg/l L-histidine HCl monohydrate, 300 mg/l L-isoleucine, 300 mg/l L-lysine HCl, 200 mg/l L-methionine, 500 mg/l L-phenylalanine, 2000 mg/l L-threonine, 300 mg/l L-tyrosine, 200 mg/l L-uracil, 1500 mg/l L-valine und 200 mg/l L-serine.

-LWH: same as -LW, without L-histidine HCl monohydrate

-LWHA: same as -LW, without L-histidine HCl monohydrate and L-adenine hemi sulfate

5.7.3 Growth conditions for *A. tumefaciens*

A. tumefaciens cells were grown at 28 °C in YEB media (0.5 % (w/v) beef extract, 0.1 % (w/v) yeast extract, 0.1 % (w/v) tryptone, 0.5 % (w/v) saccharose, 0.123 % (w/v) $MgSO_4 \bullet 7\ H_2O$) with antibiotics added for selection (see Table 1). For solid media 1.5 % (w/v) micro-agar was added to the media. Liquid cultures were shaken at 180 rpm.

5.7.4 Growth conditions for *A. thaliana*

A. thaliana grown on soil were cultivated in plant chambers (AES System GmbH, Treuen, Germany) under short-day conditions (8 h light at 21 °C, 16 h darkness at 18 °C) for 6-8 weeks. For seed propagation and stable transformation, the plants were transferred to long day-conditions (16 h light at 21 °C, 8 h darkness at 18 °C) after 4-6 weeks. The soil mixture consisted of nine parts substrate 1 (Klasmann-Deilmann GmbH, Geeste, Germany) mixed with one part vermiculite and was steamed at 80 °C for 12 h before use.

For the growth of *A. thaliana* seedlings on ½ MS media (0.22 % (w/v) Murashige & Skoog medium incl. modified vitamins (Duchefa, Haarlem, Netherlands), 1 % (w/v) sucrose, 0.8 % (w/v) micro-agar, pH 5.6 with 1 M KOH), the seeds were sterilized for 10 min with 6 % (w/v) sodium-hypochlorite solution and 0.1 % (v/v) Triton X-100. The seeds were then washed four times with sterile water and resuspended in 0.1 % (w/v) sterile agarose. The plated seeds were stratified for two days at 4 °C in the dark and afterwards cultivated under long-day conditions.

5.7.5 Growth conditions for *N. tabacum*

N. tabacum plants for pollen tube experiments were grown in a greenhouse on soil at 21-26 °C with a minimum of 16 h light per day. Pollen were collected from eight to nine-week-old plants.

5.8 Molecular biology methods

5.8.1 Isolation of RNA

For RNA isolation from leaves or seedlings the plant material was harvested and ground to a fine powder in liquid nitrogen using mortar and pestle. The powder was resuspended in 1 ml Trizol solution (38 % (v/v) Phenol (saturated with 0.1 M citrate buffer, pH 4.3 (#P4682, Sigma-Aldrich, Munich, Germany), 0.8 M guanidinium thiocyanate, 0.4 M ammonium thiocyanate, 0.1 M sodium acetate pH 5.0, 5 % (v/v) glycerol) and centrifuged at 20,000 x *g* at 4 °C for 10 min. The supernatant was transferred to a new tube, mixed with 200 µl chloroform and after incubating for 3 min centrifuged for 10 min as described above. The upper phase was mixed with 0.5 volumes isopropanol and 0.5 volumes high salt precipitation buffer (0.8 M sodium citrate, 1.2 M NaCl). After incubating for 10 min at room temperature (RT), the samples were centrifuged at 20,000 x *g* at 4 °C for 20 min. The precipitate was washed two times with 900 µl 75 % (v/v) ethanol and centrifuged again at 20,000 x *g* at 4 °C for 5 min. After drying the precipitate for 10 min at RT, the RNA was resuspended in 20 µl ddH_2O. RNA concentration was measured using the NanoDrop 2000 spectrophotometer (Thermo Fisher Scientific, Schwerte, Germany) and the quality was determined by agarose gel electrophoresis (see section 5.8.5).

5.8.2 cDNA-Synthesis

Complementary DNA (cDNA) was synthesized from 5 µg total RNA using the RevertAid H Minus first-strand cDNA synthesis kit (#K1632; Thermo Fisher Scientific, Schwerte, Germany) according to the manufacturer's instructions.

5.8.3 Isolation of genomic DNA

Genomic DNA as a template for cloning PCRs was isolated from leaves using the GeneJET™ Plant Genomic DNA Purification Kit (Thermo Fisher Scientific, Schwerte, Germany) according to manufacturer's instructions. For genotyping, the genomic DNA was isolated following the cetyltrimethylammonium bromide (CTAB) method (Murray & Thompson, 1980). Pulverized plant material was suspended in 250 µl CTAB extraction solution (2 % (w/v) CTAB, 100 mM Tris/HCl pH 8.0, 20 mM EDTA pH 8.0, 1.4 M NaCl, 2 % (v/v) 2-mercaptoethanol) and incubated for 30 min at 65 °C. After mixing with equal volume of chloroform:isoamyl alcohol (24:1 (v/v)) the samples were centrifuged at 7,500 x *g* at RT for 3 min. 200 µl of the upper phase were transferred into a new tube and mixed with 20 µl of CTAB/NaCl solution (10 % (w/v) CTAB, 0.7 % (w/v) NaCl, preheated to 65°C). After incubating for 2 min at RT, equal volume of 2-propanol was added, samples were mixed by inverting several times and incubated again for 2 min at RT. The DNA was

precipitated by centrifuging at 20,000 x *g* and 4 °C for 10 min and washed with 100 µl 75 % (v/v) ethanol. After another centrifugation step at 20,000 x *g* and 4 °C for 5 min the ethanol was removed, the DNA was dried for 10 min and dissolved in 30 µl ddH_2O.

5.8.4 Amplification of DNA fragments using polymerase-chain-reaction (PCR)

To amplify DNA fragments for inserting into vector backbones, the Phusion® High Fidelity DNA-Polymerase (New England Biolabs Inc., Frankfurt am Main, Germany) with proofreading activity was used according to manufacturer's instructions. Template DNA was either plasmid DNA including the gene of interest, prepared cDNA (see section 5.8.2) or isolated genomic DNA (see section 5.8.3) for the amplification of promoter fragments. The primers used are listed in appendix Table 18. The annealing temperature was adjusted to the primers used in the reaction. The amplified DNA fragments were separated via gel electrophoresis and purified as described in section 5.8.5.

For genotyping Arabidopsis plants, TAQ-DNA-Polymerase (VWR International GmbH, Darmstadt, Germany or New England Biolabs Inc., Frankfurt am Main, Germany) was used according to the manufacturer's instructions. The PCRs were performed in a total reaction volume of 25 µl with 2 µl isolated DNA (see section 5.8.3). For the identification of T-DNA insertions, the respective left border primer of the T-DNA insertion (appendix Table 17; Salk_LB3.1 or Sail_LB1) in combination with the respective genomic right border primer (appendix Table 17, labelled RP) were used. Wild type alleles were identified by using the primer combination of respective genomic left border primer (appendix Table 17, labelled LP) and respective genomic right border primer. The presence of transgenic expression cassettes was detected by using a forward primer specific for the gene of interest (appendix Table 20) and a reverse primer specific for *EYFP* (VYFP-rev, appendix Table 20). The amplified DNA fragments were separated and analyzed via gel electrophoresis as described in section 5.8.5.

5.8.5 Electrophoretic separation of DNA fragments

To separate DNA fragments according to their size agarose gel electrophoresis was used. DNA samples were mixed with 5x sample buffer (60 % (v/v) glycerol, 0.4 % (w/v) Orange G, 0.03 % (w/v) bromophenol blue, 0.03 % (w/v) xylene cyanol PP) and loaded onto 1 % agarose gels (1 % agarose (w/v), 0.004 % (v/v) MIDORI green advance (Nippon genetics EUROPE GmbH, Düren Germany) in TAE buffer). TAE buffer (40 mM Tris, 20 mM glacial acetic acid, 1 mM EDTA) was used as running buffer. For molecular size markers GeneRuler™ 1 kb DNA Ladder or GeneRuler™ 100 bp DNA Ladder (both Thermo Fisher Scientific, Schwerte, Germany) were used. After separation by applying a voltage of 140 V, the gels were analyzed under UV-light with the help of Gel iX Imager (INTAS, Göttingen Germany). In the case of a preparative agarose gel, the desired DNA fragments were cut out and the DNA was extracted using the GeneJET™ gel extraction kit (Thermo Fisher

Scientific, Schwerte, Germany) according to the manufacturer's instructions. The isolated DNA was eluted with 20 to 50 µl elution buffer.

5.8.6 Restriction of DNA

Prior to ligation, DNA fragments and vector backbones were digested using specific restriction enzymes (New England Biolabs Inc., Frankfurt am Main, Germany). Plasmid DNA was digested to control the insertion of genes of interest. The reactions were incubated at least 1 h or overnight at the optimum temperature for the respective enzyme according to the manufacturer's instructions and analyzed by gel electrophoresis as described in section 5.8.5.

5.8.7 DNA Ligation

For the insertion of DNA fragments into vector backbones the T4-DNA-Ligase (New England Biolabs Inc., Frankfurt am Main, Germany) was used according to manufacturer's instructions. The reaction was incubated for 1 h or overnight at RT and then transformed in *E. coli* NEB5α (see section 5.9.1).

5.8.8 Gateway® Clonase™ reaction

Gateway® cloning technology was used to create plasmids for bimolecular fluorescence complementation (BiFC) and the *pCambia3300.0* plasmids for stably transformed plant lines. Both Gateway™ LR Clonase™ II Enzym-Mix and Gateway™ BP Clonase™ II Enzym-Mix (Thermo Fisher Scientific, Schwerte, Germany) were used according to the manufacturer's instructions.

5.9 Amplification of plasmid DNA in *E. coli*

5.9.1 Preparation and transformation of chemo-competent *E. coli*

Chemically competent *E. coli* cells were prepared and transformed according to the protocol of Inoue and colleagues (Inoue et al., 1990). 500 ml LB-media was inoculated with an overnight preculture to an optical density of 0.05 at 600 nm (OD_{600}). The cells were grown at 30 °C and 180 rpm to an OD_{600} of 0.6 and then harvested in 50 ml aliquots by centrifugation at 3,220 x *g* and 4 °C for 10 min. After the supernatant was thoroughly removed, the cells were resuspended in 10 ml each of TFB buffer (10 mM HEPES pH 6.7, 15 mM $CaCl_2$ x 2 H_2O, 250 mM KCl, 55 mM $MnCl_2$) and incubated for 10 min on ice. Subsequently, centrifugation was repeated as described, the supernatant was removed and the sedimented cells were resuspended in 4 ml TFB buffer each. Dimethyl sulfoxide (DMSO) was added to the cell suspension at a final concentration of 7.5 % (v/v). After incubation on ice for 10 min, the cells were aliquoted, frozen in liquid nitrogen and stored at -80 °C.

For transforming chemo competent *E. coli*, 30-100 µl of competent cells were mixed with 1 µl of plasmid DNA or the entire ligation mixture (see section 5.8.7) and incubated on ice for 30 min. After a one-minute heat shock at 42 °C, the cells were cooled on ice for 2 min, mixed with 900 ml LB media and incubated at 37 °C for one hour. Finally, 50 µl of cell suspension for retransformed

plasmid DNA or the entire transformation batch for transformed ligation mixture was plated on LB solid medium with the appropriate antibiotic for selection.

5.9.2 Isolation of plasmid DNA from *E. coli*

To isolate plasmid DNA from *E. coli* liquid cultures, the GeneJET™ Plasmid-Miniprep-Kit (Thermo Fisher Scientific, Schwerte, Germany) or the HiYield® Plasmid Mini Kit (Süd-Laborbedarf GmbH, Gauting, Germany) were used for cultures with a volume of 2.5 ml and the CompactPrep Plasmid Midi Kit (Qiagen, Hilden, Germany) was used for cultures with a volume of 50 ml. All Kits were used according to the manufacturer's instructions. DNA concentrations were measured at 260 nm using the NanoDrop 2000 spectrophotometer (Thermo Fisher Scientific, Schwerte, Germany).

5.10 Sequencing

Plasmid DNA was checked for the correct sequence of the gene of interest by Sanger sequencing. The sequencing was performed by Eurofins Genomics Germany GmbH (Ebersberg, Germany) and Genewiz Germany GmbH (Leipzig, Germany). The plasmid DNA was mixed with gene- or vector-specific oligonucleotides listed in appendix Table 20. The obtained data was analyzed using Chromas (version 2.6.6, Technelysium Pty Ltd, South Brisbane, Australia) and the webtool Multalin (Corpet, 1988).

5.11 Cloning strategies

For all constructs generated during this thesis, the respective cDNAs encoding the proteins of interest were amplified by PCR (see section 5.8.4) using the oligonucleotides listed in appendix Table 18 or Table 19 and the cDNAs were introduced in the respective vectors as described in section 5.8.6 and 5.8.7.

5.11.1 Generation of AP2-subunit substitution variants

Plasmids encoding substitution variants of AP2-subunits were generated by amplifying the respective cDNA in two fragments using mutagenesis primers (appendix Table 19), followed by fusion-PCR. The respective mutagenesis primers carried the sequence for the substitution flanked by at least nine bases of the wild type sequence at both the 3’ and 5’ ends. Forward and reverse primers were then used in individual PCR reactions with the corresponding wild type reverse or forward primers to generate the modified cDNA fragments. The resulting fragments had an overlapping sequence with the length of the mutagenesis primers. The fragments were combined in a fusion-PCR using forward and reverse primers coding for the full-length gene. The cDNA for the substituted variants was first cloned into the *pMAL-c5G* vector and the constructs were then used as template DNA for generating other plasmids. The introduced amino acid substitutions are described in Table 2.

Table 2. Amino acid substitutions of AP2-subunit variants generated in this thesis.

Variant	Substitution
AP2-α1$_{DDDD}$	K48D, K49D, K50D, K51D
AP2-μ$_{DAD}$	I353D, D354A, C355D
AP2-μ$_{DD-DDD}$	R346D, K348D, K359D, R361D, K362D
AP2-σ$_{DDD}$	R10D, R53D, R61D

5.11.2 Recombinant plasmids for heterologous protein expression in *E. coli*

AP2-subunits from Arabidopsis were recombinantly expressed in *E. coli* as GST-, MBP-, and sfGFP-His$_6$-tagged fusion proteins. For GST fusion proteins *pGEX-6P-1* was used, for MBP fusion proteins *pMAL-c5G*. For sfGFP-His$_6$ fusion proteins with N-terminal sfGFP-tag and C-terminal His$_6$-tag, *pET-28b(+)* was used. PI4P 5-kinases from Arabidopsis were recombinantly expressed in *E. coli* as MBP-, and MBP-His$_6$-tagged fusion proteins using *pMAL-c5G*. The constructs used and the respective restriction sites for the insertion of the cDNA fragments into the vector backbones are listed in Table 3.

Table 3. Construct for recombinant protein expression in *E. coli.* MH: Dr. Mareike Heilmann; JU: Johanna Uhlenberg, created in this study; JU(MA): Johanna Uhlenberg, created previously in master thesis. JN: Johanna Nordmeier.

Construct	Restriction sites GOIs	Source
pGEX-6P-1-AP2-β2	SalI-NotI	MH
pGEX-6P-1-AP2-μ	EcoRI-NotI	MH
pGEX-6P-1-AP2-σ	EcoRI-NotI	JU(MA)
pMAL-c5G-AP2-α1	SalI-EcoRI	JU(MA)
pMAL-c5G-AP2-α1NT/α1NT$_{DDDD}$	NotI-BamHI	JU(MA)/JU
pMAL-c5G-AP2-α2NT	NotI-BamHI	JU(MA)
pMAL-c5G-AP2-β2	NotI-SalI	JU(MA)
pMAL-c5G-AP2-μ/μ$_{DAD}$/μ$_{DD-DDD}$	NotI-SalI	JU(MA)/JU/JU
pMAL-c5G-AP2-μMHD	NotI-SalI	JU
pMAL-c5G-AP2-σ/σ$_{DDD}$	NdeI-EcoRI	JU(MA)/JU
pMAL-c5G-PIP5K1		MH
pMAL-c5G-PIP5K2	NotI-EcoRI	MH
pMAL-c5G-PIP5K6		MH
pMAL-c5G-PIP5K6-His$_6$		JN
pET-28b-sfGFP-His$_6$	NcoI-SalI	JU
pET-28b-sfGFP-AP2-α1NT/α1NT$_{DDDD}$-His$_6$	NcoI-SalI-NotI	JU

pET-28b-fGFP-AP2-β2-His$_6$	NcoI-SalI-NotI	JU
pET-28b-sfGFP-μMHD/μMHD$_{DAD}$/ μMHD$_{DD-DDD}$-His$_6$	NcoI-SalI-NotI	JU
pET-28b-sfGFP-σ/σ$_{DDD}$-His$_6$	NcoI-SalI-NotI	JU

5.11.3 Recombinant plasmids for yeast two-hybrid analysis

For yeast two-hybrid analysis AP2-subunits and PI4P 5-kinases were used as bait in the vector *pBT3-C-OST4.* As prey AP2-subunits as well as ROP proteins, GDIs and ATM2 were used in the vector *pPR3-N.* For all constructs the gene of interest was inserted in the corresponding vector through SfiIA and SfiIB restriction sites. The constructs used are described in Table 4.

Table 4. Constructs used for YTH analyses. MH: Dr. Mareike Heilmann; JU: Johanna Uhlenberg, created in this study; JU(MA): Johanna Uhlenberg, created previously in master thesis; VW: Vera Wagner.

Construct	Source
pBT3-C-OST4-PIP5K1/2/6/9	MH
pBT3-C-OST4-AP2-α1/2	JU
pBT3-C-OST4-AP2-β1/2	JU
pBT3-C-OST4-AP2-μ	JU
pBT3-C-OST4-AP2-σ	JU
pPR3-N-AP2-α1/2	JU(MA)
pPR3-N-AP2-β2	JU(MA)
pPR3-N-AP2-μ	JU(MA)
pPR3-N-AP2-σ	JU(MA)
pPR3-N-ROP1/2/4/6/8	MH
pPR3-N-GDI1/2/3	MH
pPR3-N-ATM2$_{CT}$	VW

5.11.4 Recombinant plasmids for bimolecular fluorescence complementation (BiFC)

For protein-protein interaction analyses by BiFC asssays, the 2in1 cloning system described by Grefen and Blatt was used, allowing the introduction of multiple expression cassettes within a single vector backbone (Grefen & Blatt, 2012). Genes of interest were amplified by PCR (section 5.8.4) using the primers listed in appendix Table 18, introducing *att*-recombination sites. After the cDNA fragments were introduced in the respective donor vectors pDONR^{TM}221-P1P4 or pDONR^{TM}221-P3P2, the resulting vectors were combined into the destination *pBiFCt-2in1* vector. By choosing different *pBiFCt-2in1* destination vectors, the N-terminal half of YFP (nYFP) is either located N-terminal or C-terminal to *att*R2 and the C-terminal half of YFP (cYFP) is either located N-

terminal or C-terminal to *att*R4. Donor and destination vectors were generated by Clonase™-mediated Gateway™ recombination described in section 5.8.8. The constructs used are listed in Table 5.

Table 5. Constructs used for BiFCs assays. JU: Johanna Uhlenberg, created in this study; JU(MA): Johanna Uhlenberg, created previously in master thesis

Destination vector	pDONR™221-P3P2	pDONR™221-P1P4	Source
pBiCt-2in1-CC	*PIP5K1-nEYFP*	*AP2α1-cEYFP*	JU (MA)
	PIP5K1-nEYFP	*AP2β2-cEYFP*	JU (MA)
	PIP5K1-nEYFP	*AP2μ-cEYFP*	JU (MA)
	PIP5K1-nEYFP	*AP2σ-cEYFP*	JU (MA)
	AP2μ-nEYFP	*AP2α1-cEYFP*	JU (MA)
pBiCt-2in1-NN	*nEYFP-AP2μ*	*cEYFP-PIP5K1*	JU
	nEYFP-AP2σ	*cEYFP-PIP5K1*	JU
pBiCt-2in1-CN	*AP2μ-nEYFP*	*cEYFP-PIP5K1*	JU
	AP2σ-nEYFP	*cEYFP-PIP5K1*	JU

5.11.5 Recombinant plasmids for transient heterologous protein expression in plant cells and stable transformation of Arabidopsis

For the transient expression of EYFP or mCherry fusion proteins in Arabidopsis protoplasts the cDNA for the genes of interest were introduced in the plant expression vectors *pEntryA* or *pEntryD* under the control of the *pCaMV35S* promoter, which was inserted via SfiIA and SfiIB restriction sites. For the transient transformation of *N. tabacum* pollen tubes, the vector *pEntryA* with the pollen specific *pLAT52* promoter was used. The promoter was inserted over SfiIA and SfiIB restriction sites. The constructs used and the respective restriction sites for the insertion of the cDNA fragments into the vector backbone are listed in Table 6.

Table 6. Constructs used for heterologous protein expression in plant cells. Promoters are inserted via SfiIA and SfiIB restriction sites. MH: Dr. Mareike Heilmann; JU: Johanna Uhlenberg, created in this study; JU(MA): Johanna Uhlenberg, created in master thesis

Construct	Restriction sites GOIs	Source
pEntryD-pCaMV35S::mCherry	NheI-NotI	MH
pEntryD-pCaMV35S::AP2-α1/α1$_{DDDD}$-mCherry	AscI-NheI-NotI	JU(MA)/JU
pEntryD-pCaMV35S::AP2-σ/σ$_{DDD}$-mCherry	AscI-NheI-NotI	JU(MA)/JU
pEntryA-pCaMV35S::EYFP-RbohD	SalI-AscI-BamHI	JU
pEntryA-pLAT52::EYFP	SalI-AscI	MH
pEntryA-pLAT52::EYFP-AP2-α1/α1$_{DDDD}$	SalI-AscI-NotI	JU

pEntryA-pLAT52::EYFP-AP2-μ/μ_{DAD}/μ_{DD-DDD}	SalI-AscI-NotI	JU
pEntryA-pLAT52::EYFP-AP2-σ/σ_{DDD}	SalI-AscI-NotI	JU
pEntryA-Redstar-PLC-PH		AG Heilmann

For stable transformation of Arabidopsis, the cDNA for AP2-subunits or their substitution variants with a C-terminal EYFP-fusion was introduced in the *pEntryA* vector under the control of the respective endogenous promoter, which was inserted via SfiIA and SfiIB. For the promoter of AP2-α1 (*pAP2-α1*), 1616 bp upstream of the start codon were amplified. For the promoter of AP2-μ (*pAP2-μ*), 1451 bp upstream of the start codon were amplified as previously described (Bashline et al., 2013). For the promoter of AP2-σ (*pAP2-σ*) 1459 bp upstream of the start codon were amplified. The PCR was performed as described in section 5.8.4 and the oligonucleotides used are listed in appendix Table 18. The *pEntryA* donor vectors were introduced into the destination vector *pCAMBIA3300.0GC* by Clonase™-mediated Gateway™ recombination as described in section 5.8.8. The constructs generated and the respective restriction sites for the insertion of the cDNA fragments into the donor *pEntryA* vectors are listed in Table 7.

Table 7. Constructs used for stable transformation of Arabidopsis. Promoters are inserted via SfiIA and SfiIB restriction sites. JU: Johanna Uhlenberg, created in this study

Construct	Restriction sites GOIs	Source
pCambia3300.0GC-pAP2α1::AP2α1-EYFP	AscI-NheI-BamHI	JU
pCambia3300.0GC-pAP2α1::AP2α1$_{DDDD}$-EYFP	AscI-NheI-BamHI	JU
pCambia3300.0GC-pAP2μ::AP2μ-EYFP	AscI-NheI-BamHI	JU
pCambia3300.0GC-pAP2μ::AP2μ_{DAD}-EYFP	AscI-NheI-BamHI	JU
pCambia3300.0GC-pAP2μ::AP2μ_{DD-DDD}-EYFP	AscI-NheI-BamHI	JU
pCambia3300.0GC-pAP2σ::AP2σ-EYFP	AscI-NheI-BamHI	JU
pCambia3300.0GC-pAP2σ::AP2σ_{DDD}-EYFP	AscI-NheI-BamHI	JU

5.12 Preparation and transformation of chemo competent *A. tumefaciens*

The preparation of chemo competent *A. tumefaciens* was performed according to the protocol of An (An, 1987). Using an overnight culture, 200 ml of YEB media containing rifampicin were inoculated to an OD_{600} of 0.15 and incubated at 30 °C and shaking at 180 rpm until an OD_{600} of 0.5 was reached. The cells were then sedimented at 3,220 x *g* and 4 °C for 10 min, resuspended in 40 ml 150 mM NaCl solution and sedimented again as described. The cells were then resuspended in 4 ml 75 mM $CaCl_2$ (4 °C) solution and aliquoted. After freezing in liquid nitrogen, the cell suspension was stored at -80 °C.

For transformation of chemo competent *A. tumefaciens*, the protocol from Lazo and colleagues (Lazo et al., 1991) was used. 200 µl of cell suspension were mixed with 3 µg plasmid DNA and incubated on ice for 30 min, followed by a cold shock by freezing the cells in liquid nitrogen. After thawing at 37 °C for 10 min, 800 µl YEB media were added, and the mixture was incubated at 30 °C for two hours. The complete transformation mixture was plated on solid YEB medium containing rifampicin and appropriate antibiotics. The plates were incubated at 30 °C for two days.

5.13 Transient transformation of *N. benthamiana* and Arabidopsis with *A. tumefaciens*

A. tumefaciens was used to transiently transform *N. benthamiana* by infiltrating the leaves of four- to six-week-old plants. In addition to the constructs to be examined (Table 5), agrobacteria transformed with the RNA silencing suppressor p19 were also grown. For transiently transforming *N. benthamiana*, an overnight culture was inoculated with the transformed agrobacteria and incubated at 30 °C and 10 rpm. Using the overnight culture, 50 ml YEB media were inoculated to an OD_{600} of 0.2 and allowed to grow at 28 °C and 180 rpm until an OD_{600} of 1.0 was reached. Cells were then sedimented at 3220 x *g* for 15 min and resuspended in infiltration buffer (10 mM $MgCl_2$, 5 mM MES/KOH pH 5.6, 200 µM acetosyringone) to an OD_{600} of 1.0. After a three-hour incubation at RT in the dark, the cell suspensions were diluted 1:1 (v/v) with infiltration buffer and the suspension with the p19 transformed cells was then added to the other cell suspensions in a ratio of 2:1 (v/v). Infiltration of the leave undersides with the bacterial suspensions was carried out using a 1 ml syringe without a needle. The transient transformation of Arabidopsis plants was performed as described for *N. benthamiana*, with a different infiltration buffer (1/4 MS media pH 6.0 (section 5.7.4), 1 % (w/v) sucrose, 100 µM acetosyringone, 0.005 % (v/v) Silwet® L-77) according to Zhang and colleagues (Zhang et al., 2020). The infiltrated leaves were analyzed 24-72 h after infiltration as described in section 5.26.

5.14 Generation of stably transformed Arabidopsis lines

For generating stably transformed *A. thaliana* lines, the floral dipping protocol of Clough and Bent was followed (Clough & Bent, 1998). Plants were grown as described in section 5.7.4 until flowering. An overnight culture of 30 ml YEB media containing appropriate antibiotics was inoculated with transformed *A. tumefaciens* colony containing the desired plasmid (Table 7). Using the overnight culture, a fresh 400 ml culture was adjusted to an OD_{600} of 0.15 and grown at 28 °C and 180 rpm until an OD_{600} of 0.8 was reached. Cells were harvested at 3,200 x *g* and 4 °C for 30 min, washed with 200 ml 5 % (w/v) saccharose and sedimented again. After resuspending in 200 ml 5 % (w/v) saccharose with 0.2 mM acetosyringone, the cells were incubated on ice for 30 min. Prior to dipping the flowers for 5 s in the suspension, 0.05 % (v/v) Silwet® L-77 (Lehle seeds; www.arabidopsis.org) was added. Dipped plants were kept under low light and with high humidity overnight before returning to growth chambers.

Harvested seeds (T1) were grown for seven days on solid ½ MS medium (see section 5.7.4) containing 10 µg/ml DL-Phosphinotricin (Duchefa, Haarlem, Netherlands) for selection of transgenic plants, before transferring to soil. Plants were genotyped as described in section 5.8.4.

5.15 Determination of membrane liquid phase order in Arabidopsis seedlings

Five-day-old Arabidopsis seedlings were incubated for 5 min in liquid ½ MS medium containing 5 µM of the phase sensitive dye Di-4-ANEPPDHQ (#D36802, Invitrogen, Thermo Fisher Scientific, Schwerte, Germany). Afterwards the seedlings were washed twice in fresh liquid ½ MS medium for 5 min each. The root tips were mounted on microscope slides with a drop of liquid ½ MS medium and examined with a LSM880 (Carl Zeiss, Jena, Germany) equipped with a 40x water immersion objective. During imaging, Di-4-ANEPPDHQ was excited at 488 nm and the emitted fluorescence was detected in two separate channels: 499 to 580 nm (ordered phase) and 619 to 750 nm (disordered phase). Images were captured within the root elongation zone. All images were processed with ImageJ/fiji software (Schindelin et al., 2012) using the macro provided by Owen and colleagues (D. M. Owen et al., 2012) to generate false color images and to calculate generalized polarization (GP) values. For each imaged root, the GP-values from 15 individual plasma membranes were measured.

5.16 Recombinant expression and enrichment of fusion proteins in *E. coli*

For expression of recombinant proteins *E. coli* Rosetta2 or BL21 DE3 cells were used. The cells were transformed with the corresponding plasmid (Table 3) as described in section 5.9.1. First, a preculture was incubated overnight at 30 °C and 180 rpm. The main expression culture was inoculated with the preculture, resulting in an OD_{600} of 0.05. The culture was then incubated at 37 °C and 180 rpm until an OD_{600} of 0.6-0.8 was reached. After cell growth was stopped for 30 min on ice, protein expression was induced with isopropyl-β-thiogalactopyranoside (IPTG). Expression and induction were performed as shown in Table 8. The cells were harvested at 3,220 x *g* and 4 °C for 30 min, frozen in liquid nitrogen and stored at -20 °C.

Table 8. Conditions for expression of recombinant proteins. All expressions were performed in LB media supplemented with appropriate antibiotics. MBP-fusion proteins were expressed in 300 ml cultures, sfGFP-His_6-fusion proteins were expressed in 600-900 ml cultures.

Protein	Cells	Induction	Expression conditions
MBP-α1NT/α2NT	BL21 DE3	1 mM IPTG	4 h 37 °C
MBP-µ/μ_{DAD}/$\mu_{DD\text{-}DDD}$	BL21 DE3	1 mM IPTG	18 h 18 °C
MBP-σ/σ_{DDD}	BL21 DE3	0.1 mM IPTG	18 h 18 °C
sfGFP-His_6	Rosetta2	1 mM IPTG	3 h 37 °C, 95 rpm
sfGFP-α1NT/α1NT_{DDDD}-His_6	Rosetta2	0.1 mM IPTG	18 h 18 °C, 95 rpm
sfGFP-β2-His_6	Rosetta2	0.5 mM IPTG	18 h 18 °C, 95 rpm

sfGFP-µMHD/µMHD$_{DAD}$/µMHD$_{DD-DDD}$-His$_6$	Rosetta2	0.5 mM IPTG	18 h 18 °C, 95 rpm
sfGFP-σ/σ$_{DDD}$-His$_6$	Rosetta2	0.1 mM IPTG	18 h 18 °C, 95 rpm

5.16.1 Cell disruption and lysis

Harvested cells were resuspended in lysis buffer as listed in Table 9. After incubating the lysates on ice for 30 min, for MBP-tagged proteins, cells were sonicated using the Vibra-Cell™ 72442 (Bioblock Scientific, Sonics und Materials Inc., Newton CT, USA) with 2,000 J total energy in 2 s pulses with an amplitude of 60 % alternating with 2 s pauses. For sfGFP-His$_6$-tagged proteins the Branson 250 Digital Sonifier (Branson, Emerson Electric Co., Dietzenbach, Germany) was used with a total sonication time of 1 min in 10 s pulses with an amplitude of 50 % alternating with 40 s pauses.

Cell debris was sedimented at 20,000 x *g* and 4 °C for 30 min (MBP-tagged proteins) or at 20,000 x *g* and 6 °C for 35 min (sfGFP-His$_6$-tagged proteins) using an Optima L-90K Ultracentrifuge with a 70 Ti rotor (Beckman Coulter, Krefeld, Germany). Afterwards the supernatant was harvested and used for enrichment of fusion proteins by affinity chromatography (see section 5.16.2).

Table 9. Buffers used for cell lysis. cOmplete™ EDTA-free protease inhibitor-cocktail was obtained from Merck (#11873580001, Darmstadt, Germany).

Protein tag	Buffer
MBP	20 mM Tris/HCl, pH 7.5 200 mM NaCl 1 mM EDTA pH 8.0 0.1 mM DTT 10 % (v/v) glycerol 0.5 % (v/v) triton X-100 1 mg/ml lysozyme 1 x protease inhibitor
sfGFP-His$_6$	25 mM Tris/HCl, pH 7.5 300 mM NaCl 5 % (v/v) glycerol 0.1 % (v/v) triton X-100 2 mg/ml lysozyme 1 x protease inhibitor

5.16.2 Enrichment of recombinant fusion proteins

MBP-tagged fusion proteins were enriched using amylose resin (New England Biolabs Inc., Frankfurt, Germany) and Pierce™ centrifuge columns (Thermo Fisher Scientific, Schwerte, Germany). 500 µl resin was washed three times with 3 ml equilibration buffer (25 mM Tris/HCl pH 7.5, 75 mM NaCl), before incubating the soluble fraction of the cell lysates for one hour at RT. Flow trough was discarded and the columns were washed three times with equilibration buffer. Elution was performed four times with 300 µl elution buffer each (20 mM Tris/HCl pH 7.5, 200 mM NaCl, 1 mM EDTA pH 8.0, 10 mM maltose) by incubating the puffer 10 min before eluting. Elution fractions were analyzed by SDS-PAGE (see section 5.17) and protein concentrations were determined as described in section 5.18.

Enrichments of recombinant sfGFP-His_6 fusion proteins was performed using the chromatography system ÄKTA pure™ (Cytiva Europe GmbH, Freiburg, Germany). For His_6-tagged fusion proteins, a 1 ml HisTrap™ HP column (Cytiva Europe GmbH, Freiburg, Germany) was used according to manufactures instructions. The column was equilibrated with 10 column volumes (CV) of washing buffer (500 mM NaCl, 50 mM Tris/HCl pH 7.5, 40 mM imidazole) before applying the sample using Superloop™ (Cytiva Europe GmbH, Freiburg, Germany) at a flow rate of 1 ml/min. After washing the column with 15 CV washing buffer, bound fusion proteins were eluted with elution buffer (500 mM NaCl, 50 mM Tris/HCl pH 7.5, 500 mM imidazole) at a flow rate of 0.8 ml/min applying a linear gradient over 2 CV, followed by a step elution over 10 CV. The eluted proteins were collected in 0.5 ml fractions and analyzed by SDS-PAGE (see section 5.17).

Afterwards, the buffer was exchanged to remove low molecular weight contaminants and residual imidazole using a 5 ml HiTrap™ Desalting Column (Cytiva Europe GmbH, Freiburg, Germany). The column was equilibrated with 5 CV desalting buffer (200 mM NaCl, 50 mM Tris/HCl pH 7.5) before loading four combined elution fractions using a 2 ml capillary loop (Cytiva Europe GmbH, Freiburg, Germany). The proteins were eluted at a flow rate of 0.8 ml/min over 2 CV and collected in 0.5 ml fractions, which were then analyzed by SDS-PAGE (see section 5.17). Protein concentrations were determined as described in section 5.18. All buffers used at the ÄKTA pure™ were filtrated and degassed with a vacuum filter (0.2 µm polyethersulfone membrane, #10040-460 VWR International GmbH, Darmstadt, Germany) before use.

5.17 Sodium dodecyl sulfate polyacrylamide gel electrophoresis (SDS-PAGE)

Proteins were separated according to their molecular size using sodium dodecyl sulfate polyacrylamide gel electrophoresis (SDS-PAGE) as described by Laemmli (Laemmli, 1970). The samples were mixed with 4x sample buffer (0.25 M Tris/HCl pH 6.8, 8 % (w/v) SDS, 0.04 % (w/v) bromophenol blue, 40 % (v/v) glycerol, 0.4 M dithiothreitol (DTT)), heated for 5 min at 95 °C and loaded onto SERVAGel™ Neutral HSE gels (SERVA Electrophoresis GmbH, Heidelberg, Germany)

or self-casted polyacrylamide gels. Self-casted gels were prepared with a 5 % stacking gel and 10 % separation gel (Table 10). As size standards, either the PageRuler™ Unstained Protein Ladder or the PageRuler™ Prestained Protein Ladder (both Thermo Fisher Scientific, Schwerte, Germany) was applied. Proteins were separated for 30 to 45 min at 300 V and a current of 35 mA in SDS running buffer (0.3 % (w/v) Tris, 1.44 % (w/v) glycine, 0.1 % (w/v) SDS) in a SE250 Electrophorese Chamber (Hoefer Inc., SERVA Electrophoresis GmbH, Heidelberg, Germany). Afterwards the gels were either stained with Quick Coomassie® Stain (SERVA Electrophoresis GmbH, Heidelberg, Germany) or used for immunodetection as described in 5.19.

Table 10. Composition of self-casted SDS-PAGE gels.

Component	Separation gel (10 %)	Stacking gel (5 %)
Rotiphorese® Gel 30 (37,5:1) (Carl Roth, Karlsruhe, Germany)	10 % (w/v)	5 % (w/v)
Tris/HCl, pH 8.8	370 mM	-
Tris/HCl, pH 6.8	-	120 mM
ddH_2O	45 % (v/v)	62 % (v/v)
SDS	0.1 % (w/v)	0.1 % (w/v)
ammonium persulfate (APS)	0.06 % (w/v)	0.09 % (w/v)
N,N,N´,N´-tetramethyl-ethylenediamine (TEMED)	0.01 % (v/v)	0.01 % (v/v)

5.18 Determination of protein concentrations

Total protein concentrations were determined by Bradford Assay (Bradford, 1976). 10 µl of protein sample were combined with 990 µl 1x Bradford reagent (SERVA Electrophoresis GmbH, Heidelberg, Germany) and incubated for 5 min at RT. Absorption was measured at 595 nm and protein concentrations were calculated using a bovine serum albumin (BSA) standard curve.

5.19 Immunodetection of fusion proteins

For the detection of epitope tagged fusion proteins after SDS-PAGE, proteins were first transferred from polyacrylamide gels to a nitrocellulose membrane (Amersham Protran 0,45 NC, Cytiva Europe GmbH, Freiburg, Germany) according to Towbin et al. (1979). The transfer was performed in a Mini-PROTEAN® Tetra System Blotting Chamber (BioRad Laboratories GmbH, Munich, Germany) at 60 V and 400 mA over a period of 60 min using blotting buffer (0.582 % (w/v) Tris, 0.293 % (w/v) glycine, 0.375 % (w/v) SDS, 20 % (v/v) methanol). The membrane was blocked for 30 min with 3 % BSA or milk powder (SERVA Electrophoresis GmbH, Heidelberg, Germany) in TBS buffer (50 mM Tris/HCl pH 7.5, 150 mM NaCl), before incubating the primary antibody (Table 11) for 1 h at RT or overnight at 4 °C. Afterwards, the membrane was washed three times 5 min each with TBS buffer before applying the secondary antibody for 60 min at RT (Table 11), followed by three additional washing steps. If the secondary antibody was horse radish peroxidase (HRP)-

conjugated, chemiluminescent detection was performed using SuperSignal™ West Femto Maximum Sensitivity Substrate (#34095; Thermo Fisher Scientific, Schwerte, Germany) and Fusion Solo S (Vilber Lourmat Deutschland GmbH, Eberhardzell, Germany) with the software FusionCapt Advance Solo 7 (version 17.01). When alkaline phosphatase (AP)-conjugated secondary antibodies were used, one additional washing step with AP buffer (100 mM Tris/HCl pH 9.5, 100 mM NaCl, 5 mM $MgCl_2$) was performed prior to detection. For AP detection, the membrane was incubated with AP buffer mixed with 5-bromo-4-chloro-3-indolyl phosphate disodium salt (BCIP, 0.175 mg/ml) and p-nitrotetrazolium blue chloride (NBT, 0.338 mg/ml) in AP buffer.

Table 11. Primary and secondary antibodies. NEB: New England Biolabs Inc., Frankfurt, Germany; TF: Thermo Fisher Scientific, Schwerte, Deutschland; ME: Merck, Darmstadt, Germany.

Epitope	Host	Conjugate	Dilution	Product no.; supplier
anti-MBP	mouse	-	1:10,000	#E8032S; NEB
anti-GFP	rabbit	-	1:2,000	#A-11122; TF
anti-GST	goat	-	1:2,000	#27-4577-01; ME
anti-mouse	goat	AP	1:30,000	#A3562; ME
anti-mouse	goat	HRP	1:7,500	#AP130P; ME
anti-rabbit	goat	HRP	1:7,000	#A6154; ME
anti-goat	rabbit	HRP	1:7,500	#A5420; ME

5.20 Circular dichroism spectroscopy

Protein secondary structure was analyzed by circular dichroism (CD) spectroscopy using a J-710 spectropolarimeter (JASCO Deutschland GmbH, Pfungstadt, Germany) with a NESLAB RTE-111 peltier element (Thermo Fisher Scientific, Schwerte, Deutschland). Proteins were centrifuged at 20,000 x *g* at 4 °C for 30 min before spectroscopy. Measurements were performed in a 1 mm precision cell (Starna GmbH, Pfungstadt, Germany) at 20 °C, with 50 nm min^{-1} scan speed, 1 nm pitch, 1 nm slit widths and 1 s response time and 16 accumulations. CD-spectra were corrected by the buffer-signal and converted to the mean residue ellipticity (Kelly et al., 2005) by using the equation:

$$[\Theta]_{\mathrm{MRW}} = \frac{\Theta * \mathrm{M}}{10 * \mathrm{d} * \mathrm{c} * \mathrm{N}} \text{ in } [\mathrm{deg} * \mathrm{cm}^2 * \mathrm{dmol}^{-1}]$$

Θ: ellipticity [mdeg]

M: molecular weight [g mol^{-1}]

d: light path length [cm]

c: protein concentration [mg/ml]

N: number of amino acids

5.21 Analysis of protein-protein interactions

The analysis of protein-protein interactions was performed by alternative genetic or biochemical methods.

5.21.1 Split-ubiquitin yeast two-hybrid analysis

The split-ubiquitin based yeast two-hybrid (YTH) test is based on the system developed by Johnsson and Varshavsky for the *in vivo* analysis of protein-protein interactions in yeast cells (Johnsson & Varshavsky, 1994). The split-ubiquitin based YTH analysis is based on the proteolytic cleavage of ubiquitinated proteins in eukaryotic cells. Bait and prey proteins are each fused to one half of the ubiquitin with the bait protein additionally being fused to the transcription factor LexA-VP16. Upon interaction of the bait and prey fusion proteins, the ubiquitin halves reconstitute, and the transcription factor is cleaved by a ubiquitin-specific protease. The transcription factor activates the reporter genes *HIS3*, *ADE2* and *LacZ*, which enables the yeast cells to grow on selective media. Additionally, the bait protein is bound to the ER membrane via fusion to the yeast protein oligosaccharyltransferase 4 (Ost4), to create a cytosol-localized YTH test (Möckli et al., 2007). To prevent independent reconstitution of the ubiquitin halves, isoleucine 13 was mutated to glycine in the N-terminal half of the ubiquitin (Nub). As a negative control Alg5 fused to the mutated Nub (*pDL2-Alg5*) was used. The vector *pAI-Alg5*, in which the unmodified wild-type Nub guarantees assembly of the ubiquitin halves, serves as a positive control. The vectors are described in section 5.6 and the constructs used are described in section 5.11.3.

5.21.2 Preparation and transformation of chemo-competent *S. cerevisiae* cells

The preparation and transformation of chemo-competent *S. cerevisiae* cells was carried out according to the protocol of Ito et al. (1983). 30 ml of YPAD media (section 5.7.2) was inoculated with NMY51 yeast cells and grown overnight at 30 °C and shaking at 170 rpm. For the main culture, 50 ml of YPAD media was inoculated with the preculture to an OD_{600} of 0.15 and incubated at 30 °C and shaking at 170 rpm until an OD_{600} of 0.6 was reached. The cells were sedimented at 2500 x *g* for 5 min and washed with 20 ml TE buffer (10 mM Tris, 1 mM EDTA, pH 7.5). After repeated sedimentation as above, the cells were resuspended in 1 ml lithium acetate/TE buffer (110 mM lithium acetate, 11 mM Tris/HCl pH 7.5, 1.1 mM EDTA pH 8.0) and repeatedly sedimented at 2500 x *g* for 3 min. After resuspending in 0.7 ml lithium acetate/TE buffer, the yeast cells were transformation competent.

For transformation, approximately 1 µg each of bait and prey plasmid DNA were mixed with 100 µl of competent cells and 0.7 ml PEG/lithium acetate mix (40 % (w/v) polyethylene glycol (PEG), 100 mM lithium acetate, 10 mM Tris/HCl pH 7.5, 1 mM EDTA pH 8.0). After incubating for 30 min at 30 °C and shaking at 180 rpm, 80 µl DMSO was added, and the reaction was incubated again for 15 min at 42 °C and 180 rpm. Subsequently the cells were sedimented at 750 x *g* for 5 min, washed

with 300 µl of 0.9 % (w/v) NaCl and sedimented again at 750 x *g* for 30 s. The transformed cells were then resuspended in 100 µl of 0.9 % (w/v) NaCl and plated on selective media (section 5.7.2). After incubating for three to four days at 30 °C, positive transformed colonies were resuspended in TE buffer to an OD_{600} of 0.5. For selection of interaction, 3 µl each of the cell suspension was spotted onto SD-LW, SD-LWH and SD-LWHA media (section 5.7.2). For a more stringent selection, 2.5 to 7.5 mM 3-amino-1,2,4-triazole (3-AT; Sigma-Aldrich, Munich, Germany) was added. Cell growth was monitored at 30 °C over seven days.

5.21.3 *In vitro* immuno pull-down assay

The interaction of recombinantly expressed proteins was analyzed biochemically by immuno pull-down assays. GST-tagged AP2-subunits were used as bait proteins and MBP-tagged PI4P 5-kinases as prey proteins. Pierce™ centrifuge columns (Thermo Fisher Scientific, Schwerte, Germany) were loaded with 100 µl Pierce™ glutathione agarose (Thermo Fisher Scientific, Schwerte, Germany) and the storage buffer was removed by centrifugation at 400 x *g* for 1 min. All subsequent centrifugation steps were performed in the same way. The prepared columns were washed three times each with 600 µl GST equilibration buffer (50 mM Tris/HCl pH 8.0, 150 mM NaCl) before adding the GST-tagged bait proteins and the GST control. Protein lysates were incubated for one hour at RT or overnight at 4 °C. The flow-through was discarded and washing was repeated three times as described above. 600 µl of protein lysates of MBP fusion proteins (MBP-PIP5K1/PIP5K2/PIP5K6) were then added to the column and incubated overnight at 4 °C. Unbound proteins were removed by washing three times before elution. Elution was performed four times with 50 µl elution buffer each (50 mM Tris/HCl pH 8.0, 150 mM NaCl, 50 mM glutathione) by incubating the elution buffer 10 min prior to centrifugation. The elution fractions were analyzed via SDS-PAGE (see section 5.17) followed by immunodetection (see section 5.19).

5.21.4 Bimolecular fluorescence complementation

Bimolecular fluorescence complementation (BiFC) was used to investigate possible interactions between proteins *in planta*. For this purpose, the N- and C-terminal half of the fluorescent protein EYFP are fused to each of the proteins under investigation. The two halves of EYFP may reconstitute when the tested proteins are in close spatial proximity through interaction and thus a fluorescence signal can be detected. BiFC constructs are described in 5.11.4 and were transformed transiently in *N. benthamiana* or *A. thaliana* (section 5.13). As a control of successful transformation, RFP expressed under the *pCaMV35S* promoter was used. Transformed plants were analyzed 24-72 h after infiltration by confocal laser-scanning microscopy as described in section 5.26.

5.21.5 Microscale thermophoresis for protein-protein interaction analysis

Microscale thermophoresis (MST) measures changes in the motion of fluorescently labelled molecules in a microscopic temperature gradient caused by the interaction with ligand molecules. By monitoring the changes in fluorescence intensities in a titration experimental setup, where the fluorescently labelled target has a set concentration and the concentration of the unlabeled ligand is varied, binding affinities can be determined (Wienken et al., 2010).

For testing protein-protein interactions between purified recombinant AP2-subunits and PI4P 5-kinases by MST, a Monolith NT.115 with the corresponding software MO.control (version 1.6.1., both NanoTemper Technologies GmbH, Munich, Germany) was used. The AP2-subunits as target proteins were labelled with a covalent sfGFP-tag and a His_6-tag for enrichment (see section 5.11.2) and their concentration was adjusted to a fixed fluorescence intensity. Enriched recombinant sfGFP-His_6 protein used as target served as a negative control. As ligand proteins, enriched MBP-PIP5K1, MBP-PIP5K2 or MBP-PIP5K6-His_6 were used and a 1:1 serial dilution over 16 different concentrations was prepared. After mixing 5 µl of target protein solution with 5 µl of ligand protein dilutions, the reactions were incubated for 10 min at RT before being loaded in Monolith NT.115 standard capillaries (NanoTemper Technologies GmbH, Munich, Germany). The total reaction volume was 10 µl and the measurement was performed with 20 % excitation power and medium MST-Power at an ambient temperature of 22 °C. All protein dilutions were prepared in MST buffer (50 mM Tris/HCl pH 7.5, 150 mM NaCl, 0.05 % (w/v) Tween-20) and centrifuged at 20,000 x *g* and 4 °C for 15 min before use. Data were analyzed using the signal from an MST-on time of 2.5 s with the MO.Affinity Analysis software (version v2.3., NanoTemper Technologies GmbH, Munich, Germany). K_D values were calculated by fitting the dose-response values using the equation:

$$f(c_{ligand}) = unbound + (bound - unbound) * \frac{\sqrt{(c_{ligand} + c_{target} + K_D)^2 - 4 * c_{ligand} * c_{target}}}{2 * c_{target}}$$

5.22 Analysis of protein-lipid interactions

Several different experimental approaches were used to determine lipid-binding features of AP2-subunits.

5.22.1 Lipid overlay assay

One approach to investigate possible protein-lipid interactions, was to analyze the binding of enriched recombinant proteins to commercial PIP strips (#P-6001, Echelon Biosciences Inc., MoBiTec GmbH, Göttingen, Germany) or to self-prepared membranes. For self-prepared membranes, 3 µl each of the lipid solutions (appendix Table 16) were spotted onto a nitrocellulose membrane at a concentration of 1 mg/ml in chloroform and dried for 20 min in a light-protected

environment. The following steps were carried out equally with both the commercial PIP strips and the self-prepared membranes. The membranes were blocked for 30 min in 3 % (w/v) milk powder in TBS buffer (section 5.19) before incubation with the purified proteins (0.5 to 1 µg/ml in 3 % (w/v) BSA or milk powder in TBS buffer) overnight at 4 °C. After the membrane was washed three times with TBS buffer, the bound proteins were detected by immunodetection as described in section 5.19. As a positive control the PtdIns(4,5)P_2-Grip (#G-4501; Echelon Biosciences Inc., MoBiTec, Göttingen, Germany) was used.

5.22.2 Liposome binding assay

Another approach was to analyze the binding of enriched recombinant proteins to artificial liposomes, for which different lipid compositions can be chosen. Liposome binding assays were performed both as a liposome sedimentation assay, and as a liposome flotation assay.

5.22.2.1 Liposome sedimentation assay

Liposome sedimentation assays were performed as described by Julkowska and colleagues (Julkowska et al., 2013). Liposomes for each reaction were prepared by mixing PtdCho as a carrier lipid with 10 mol % or 20 mol % of the respective PIs to be tested in a total lipid amount of 400 nmol. After drying, lipids were resuspended in 500 µl extrusion buffer (250 mM raffinose pentahydrate, 25 mM Tris-HCl pH 7.5, 1 mM DTT) and rehydrated for 90 min at RT with occasionally mixing. Afterwards, lipids were sonicated for 1 min and the multilamellar lipid vesicle mixtures were extruded 15 times through a polycarbonate membrane (pore size 0.2 µm, Whatman, Maidstone, United Kingdom) with filter supports using a mini-extruder (both Avanti Polar Lipids Inc., Merck, Darmstadt, Germany). Liposomes were washed by adding 1.5 ml binding buffer (125 mM KCl, 25 mM Tris-HCl pH 7.5, 1 mM DTT, 0.5 mM EDTA) and sedimented at 20,000 x *g* at 22 °C for 20 min. Liposome pellets were resuspended in 25 µl binding buffer and mixed with 0.5 µg, 1.0 µg or 1.5 µg purified recombinant MBP-fusion protein (section 5.16) in 25 µl volume per assay. After the protein-liposome mixture was incubated for 45 min at RT, liposomes were sedimented at 16,000 x *g* at 22 °C for 30 min. The supernatant was mixed with 16.7 µl 4x sample buffer (section 5.17). The sedimented liposomes were resuspended in 300 µl binding buffer and centrifuged again at 16,000 x *g* at 22 °C for 30 min. After discarding the supernatant, liposome pellets were then resuspended in 33 µl 1x sample buffer. 10 µl of supernatant and sediment sample each were analyzed by SDS-PAGE (section 5.17) and immuno detection of the fusion proteins (section 5.19).

5.22.2.2 Liposome flotation assay

Liposome flotation assays were performed according to Posor and colleagues (Posor et al., 2013). In brief, liposomes were prepared by mixing PtdCho as a carrier lipid with 10 mol % of the respective PIs in a total lipid amount of 572 nmol. Dried lipids were rehydrated in HEPES buffer

(50 mM HEPES pH 7.4, 100 mM KCl) for 1 h at RT with occasionally mixing. After extruding 17 times through a polycarbonate membrane (pore size 0.1 µm, Whatman, Maidstone, United Kingdom), 1.7 ml ddH_2O was added and liposomes were sedimented at 20,000 x *g* at 4 °C for 1 h. Sedimented liposomes were resuspended in 150 µl HEPES buffer, mixed with 2 µg recombinant MBP-fusion protein (section 5.16) and incubated for 45 min at RT. Protein-Liposome mixture was adjusted to 30 % (w/v) sucrose by adding 75 % (w/v) sucrose in HEPES buffer, transferred to TLS-55 centrifuge tube and overlaid with 200 µl 25 % (w/v) sucrose in HEPES buffer and subsequently 50 µl HEPES buffer. Liposomes were floated by centrifugation at 240,000 x *g* at 4 °C for 1 h using a Sorvall™ MTX 150 Micro-Ultracentrifuge with a S58A rotor (Thermo Fisher Scientific, Schwerte, Germany). The fractions were collected by first removing the bottom fraction, followed by the middle fraction and last the top fraction. 50 µl each of top and bottom fraction were analyzed via SDS-PAGE with subsequent immunodetection (sections 5.17 and 5.19).

5.22.3 Microscale thermophoresis for protein-lipid interaction analysis

For a quantitative evaluation of interactions between AP2-complex subunits and liposomes by MST, the experimental conditions used were largely the same as described in section 5.21.5 for protein-protein interactions, but that liposomes were used as ligands. For this purpose, liposomes composed of 90 mol % PtdCho and 10 mol % PIs were prepared as described by Julkowska and colleagues (section 5.22.2.1; Julkowska et al. (2013)), with the following adaptions: After extrusion of the lipid suspension, 1.5 ml MST buffer (see section 5.21.5) without Tween-20 was added and the sample was centrifuged at 20,000 x *g* at 22 °C for 20 min. The sedimented liposomes were resuspended in MST buffer resulting in a concentration of 3 mM total lipid. For the MST measurements, the serial dilution of liposomes in MST buffer started at 3 mM, leading to the lowest concentration of 45.78 nM. As target proteins, sfGFP-His_6-tagged AP2-subunits (see section 5.11.2) were used at a fixed concentration of approximately 40 nM, which were normalized by the total fluorescence count. Enriched recombinant sfGFP-His_6 protein served as a negative control.

5.23 Isolation and transformation of Arabidopsis mesophyll protoplasts

The isolation and preparation of Arabidopsis mesophyll protoplasts was carried out following the protocol of Yoo and colleagues (Yoo et al., 2007). Leaves from six- to eight-week-old Arabidopsis plants were cut into thin strips and transferred into enzyme solution (0.4 M Mannitol, 20 mM KCl, 20 mM MES pH 5.7, 1.5 % (w/v) Cellulase Onozuka R-10, 0.4 % (w/v) Maceroenzyme R-10 (both SERVA Electrophoresis GmbH, Heidelberg, Germany), 10 mM $CaCl_2$, 0.1 g/ml BSA). The leaf strips in the enzyme solution were incubated for a total of three and a half hours at RT protected from light, of which the first 30 min were under vacuum infiltration and the last 30 min with gentle shaking. The released protoplasts were then filtered through a 100 µM nylon sieve and sedimented at 200 x *g* and 11 °C for 2 min. The protoplasts were washed twice by resuspending

in 2 ml W5 buffer (154 mM NaCl, 125 mM $CaCl_2$, 5 mM KCl, 2 mM MES pH 5.7) and sedimentation by gravity over a time period of 40 min each on ice in the dark. After washing, the protoplasts were resuspended in MMG buffer (0.4 mM mannitol, 15 mM $MgCl_2$, 4 mM MES pH 5.7) with a density of approximately $2x10^5$ cells ml^{-1}.

For transformation 10 to 20 µg plasmid DNA (see section 5.11.5) per 100 µl protoplast suspension were combined and gently mixed. After adding 110 µl PEG solution (0.2 M mannitol, 100 mM $CaCl_2$, 40 % (w/v) PEG 4000) and gentle mixing, the reaction was incubated for 10 min at RT before adding 440 µl W5 buffer. The protoplasts were sedimented at 150 x *g* for 2 min, resuspended in 100 µl WI buffer (0.5 mM mannitol, 20 mM KCl, 4 mM MES pH 5.7) and incubated overnight at RT protected from light. Transformed protoplasts were used for the determination of endocytosis rates as described in section 5.25.1.

5.24 Transient transformation of *N. tabacum* pollen tubes by particle bombardment

For expression of fluorescently labelled fusion proteins in *N. tabacum* pollen tubes transient transformation via biolistic particle delivery was used. This method uses helium pressure to introduce DNA-coated microcarriers, here gold particles, into cells. The constructs used for this are described in section 5.11.5.

5.24.1 DNA-precipitation on gold particles

The gold particles were washed before used for precipitation of plasmid DNA. Therefore 50 mg of gold particles (1 µm, BioRad Laboratories GmbH, Munich, Germany) were mixed vigorously for 2 min with 1 ml 96 % (v/v) EtOH. The particles were sedimented at 15,000 x *g* for 10 s, supernatant was removed and washed two more times under the same conditions. After the last washing step with EtOH, the particles were washed twice with 1 ml ddH_2O before resuspending in ddH_2O with a concentration of 50 mg/ml and storing at -20 °C.

For the precipitation of plasmid DNA on the prepared gold particles, 12.5 µl of gold particle suspension were mixed thoroughly with 3 to 6 µg of plasmid DNA for 30 s. Subsequently 50 µl of 2.5 M $CaCl_2$ was added, the suspension was mixed again for 30 s and 20 µl of 0.1 M spermidine was added. After mixing for 1 min, the gold particles were sedimented at 15,000 x *g* for 10 s and washed three times with 200 µl 96 % (v/v) EtOH each. The DNA-coated particles were resuspended in 30 µl EtOH and stored at -20 °C. The amount of plasmid DNA used was dependent on the construct and listed in Table 12.

Table 12. Plasmid amounts used for particle bombardment.

Plasmid	Amount used
pEntryA-pLAT52::EYFP	4 µg
pEntryA-pLAT52::EYFP-AP2-α1/α1$_{DDDD}$	4 µg
pEntryA-pLAT52::EYFP-AP2-µ/µ$_{DAD}$/µ$_{DD-DDD}$	5 µg

pEntryA-pLAT52::EYFP-AP2-σ/$σ_{DDD}$	4 µg
pEntryA-Redstar-PLC-PH	5.5 µg

5.24.2 Preparation and particle bombardment of *N. tabacum* pollen

Mature pollen grains from four flowers of eight- to nine-week-old plants per transformation were collected and resuspended in 2 ml pollen media (5 % (w/v) sucrose, 12.5 % (w/v) PEG-6000, 0.03 % (w/v) casein hydrolysate, 15 mM MES/KOH pH 5.8, 1 mM $CaCl_2$, 1 mM KCl, 0.8 mM $MgSO_4$, 1.6 mM H_3BO_3, 30 µM $CuSO_4$,10 µg/ml rifampicin; Read et al. (1993)). Pollen grains were transferred by filtration to a cellulose acetate filter (0.2 µm, Sartorius, Göttingen, Germany) and stored in a moist environment until transformation.

The pollen grains were immediately transformed by biolistic bombardment using a helium-driven particle accelerator (PDS-1000/He, BioRad Laboratories GmbH, Munich, Germany). For this purpose, the DNA-coated gold particles were loaded onto macrocarriers (BioRad Laboratories GmbH, Munich, Germany) and bombarded using 1350 psi rupture discs (BioRad Laboratories GmbH, Munich, Germany) and a vacuum of 28 inches of mercury. After bombardment, the transformed pollen grains were transferred in 350 µl pollen media and distributed equally onto three microscope glass slides. The pollen were grown for 3-6 h in a moist environment before analyzing phenotypes or endocytosis rates via microscopy (see 5.25.2 and 5.26).

5.25 Determination of endocytic rates

5.25.1 BFA treatments of Arabidopsis seedlings and protoplasts

Arabidopsis seedlings and mesophyll protoplasts were both treated with the fungal metabolite Brefeldin A (BFA), resulting in the accumulation of endosomal bodies (BFA-bodies), that are decorated by proteins that can no longer be exocytosed. The BFA-body properties can be used as an indication of endocytic internalization rates.

For an approximate estimation of PM-endocytosis in five-day-old Arabidopsis seedlings, membranes of root epidermal cells were stained with the amphiphilic styryl tracer dye N-(3-triethylammoniumpropyl)-4-(6-(4-(diethylamino) phenyl) hexatrienyl) pyridinium dibromide (FM4-64) prior to treatment with BFA. Seedlings were incubated for 10 min in 2 µM FM4-64 (#S6689; Sigma-Aldrich, Munich, Germany) in ½ MS medium (section 5.7.4), washed for 1 min in fresh ½ MS media and consecutively incubated in 50 µM BFA (#ab120299; Abcam, Cambridge, United Kingdom) in ½ MS medium for 15-60 min before microscopic imaging (section 5.26). Transformed Arabidopsis protoplasts were pretreated with 10 µM cycloheximide (CHX; #C7698 Sigma-Aldrich, Munich, Germany) in WI buffer (section 5.23) for 30 min to inhibit *de novo* protein biosynthesis before incubating with 50 µM BFA in WI buffer. Imaging was performed 30-60 min after BFA treatment as described in section 5.26.

The number of BFA-bodies per cell in Arabidopsis seedlings was determined by manually counting the BFA-bodies per cell in Z-projections over few confocal planes. For the quantification of BFA-bodies in transformed protoplasts, the PM signal was deleted in Z-projections over the whole protoplast and BFA-bodies were counted using the ImageJ/Fiji 3D Objects Counter (Schindelin et al., 2012).

5.25.2 Monitoring of dye uptake in tobacco pollen tubes

To assess endocytic rates in tobacco pollen tubes, the internalization of FM4-64 over a time course of 85 min was monitored, as described previously (Hempel et al., 2017). Transformed pollen tubes were stained with FM4-64 by applying 60 µl of 25 µM FM4-64 in pollen medium (section 5.24.2) dropwise to pollen tubes that were grown on microscopy glass slides as described in section 5.24.2. Imaging by confocal laser-scanning microscopy was performed as described in section 5.26. The analysis of the endocytosis rate was performed by calculating the ratio of the mean cytosolic FM4-64 fluorescence intensity and the mean PM FM4-64 fluorescence intensity. Fluorescence intensities were measured at the lateral region of the pollen tube, starting 6-10 µm distal to the tip using ImageJ/Fiji (Figure 23; Schindelin et al. (2012)), as this is described as the region in the pollen tube tip were clathrin coated vesicles are internalized (Zonia & Munnik, 2008). Cyt:PM ratios were calculated for the time periods between 0-15 min and between 60-85 min after staining.

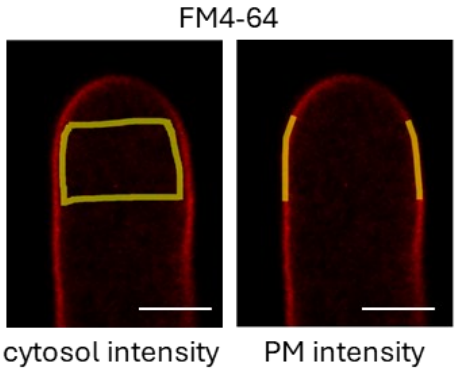

Figure 23. Analysis of the endocytic rate in tobacco pollen tubes stained with FM4-64. The endocytosis rate in transformed and stained tobacco pollen tubes was analyzed by calculating the ratio of the mean cytosolic FM4-64 fluorescence intensity (left) and the mean plasma membrane FM4-64 fluorescence intensity (right). Fluorescence intensities were measured at the lateral region of the pollen tube, starting 6-10 µm distal to the tip using ImageJ/Fiji (Schindelin et al., 2012). Scale bar = 5 µm.

5.26 Microscopy

Microscopic images were either taken with an inverted confocal laser-scanning microscope LSM 880 (Carl Zeiss, Jena, Germany) or a Cell observer microscope (Carl Zeiss, Jena, Germany) with a Yokogawa CSU-X1 spinning disk (SD) head. Confocal laser-scanning microscopy (CLSM) scans single points in a specimen at a time to acquire the entire image with a high resolution. Hence CLSM can

have a relatively slow acquisition time, which can be addressed by using a spinning disk (SD) confocal system. Instead of scanning a single confocal point, the SD system employs a rotating array of pinholes and micro-lenses in the optical path. This setup creates multiple confocal points across the imaging area, significantly speeding up the acquisition process while also being less phototoxic, making it ideal for live-cell imaging and capturing dynamic processes.

When pollen tube phenotypes were analyzed, SD microscopy was performed using a 63x oil immersion objective and a Photometrics Evolve 512 Delta EM-CCD camera for image acquisition. Z-stacks images were taken with 0.3 µm slices spanning the width of the pollen tube. Additionally, brightfield time series were taken, where images were captured every 10 s over a period of 180 s to assess whether pollen tubes have cytoplasmatic streaming and are still growing. Images were acquired using ZEN blue image analysis software (Carl Zeiss, Jena, Germany). Pearsons's correlation coefficients *R* were generated with the ImageJ/Fiji plugin JACoP (Bolte & Cordelières, 2006) using single focal plane images for analysis.

CLSM was performed for all other experiments that were analyzed via microscopy. Images were acquired with a 40x objective without immersion or with water immersion (Plan-Apochromat 40x/0.95 Korr M27; C-Apochromat 40x/1.2 W Korr FCS M27; both Carl Zeiss, Jena, Germany). Z-stacks were generated with 0.5-1 µm between slices, depending on the optimal increment of the used objective. The pinhole was kept at ~1 Airy unit. Multiple fluorophores were detected using separate tracks. During SD and CLSM microscopy fluorophores were excited and emission was detected at the wavelengths displayed in Table 13. Image processing was performed using ImageJ/Fiji (Schindelin et al., 2012).

Table 13. Excitation and emission wavelengths used for the analyzed fluorophores. CLSM: confocal laser-scanning microscope. SD: spinning disk microscope.

Microscope	Fluorophore	Excitation wavelength [nm]	Emission wavelength [nm]
CLSM	EYFP	514	496-554
SD		488	503-546
CLSM	mCherry	561	579-633
SD	Redstar	561	583-700
CLSM	chlorophyll A	633	652-721
CLSM	FM4-64	514	592-758
CLSM	Di-4-ANEPPDHQ	488	499-580 nm (ordered) 619-750 nm (disordered)

5.27 Statistics and data management

Data were analyzed for statistical relevance by two-sided Student's *t*-test with Microsoft Office 365 (Microsoft Deutschland GmbH, Munich, Germany). Error bars in generated line graphs represent the sample standard deviation. Whiskers in boxplots indicate the minimum and maximum values, boxes are drawn from the first quartile to third quartile. Values are defined as outliers, when they significantly differ from the range of the rest of the data, specifically when they are 1.5 times larger or smaller than the interquartile range.

6. References

Abramson, J., Adler, J., Dunger, J., Evans, R., Green, T., Pritzel, A., Ronneberger, O., Willmore, L., Ballard, A. J., Bambrick, J., Bodenstein, S. W., Evans, D. A., Hung, C. C., O'Neill, M., Reiman, D., Tunyasuvunakool, K., Wu, Z., Žemgulytė, A., Arvaniti, E., … Jumper, J. M. (2024). Accurate structure prediction of biomolecular interactions with AlphaFold 3. *Nature 2024 630:8016*, *630*(8016), 493–500. https://doi.org/10.1038/s41586-024-07487-w

Adamowski, M., Narasimhan, M., Kania, U., Glanc, M., De Jaeger, G., & Friml, J. (2018). A Functional Study of AUXILIN-LIKE1 and 2, Two Putative Clathrin Uncoating Factors in Arabidopsis. *The Plant Cell*, *30*(3), 700–716. https://doi.org/10.1105/tpc.17.00785

An, G. (1987). *[17] Binary ti vectors for plant transformation and promoter analysis* (pp. 292–305). https://doi.org/10.1016/0076-6879(87)53060-9

Aniento, F., Sánchez de Medina Hernández, V., Dagdas, Y., Rojas-Pierce, M., & Russinova, E. (2022). Molecular mechanisms of endomembrane trafficking in plants. *The Plant Cell*, *34*(1), 146–173. https://doi.org/10.1093/plcell/koab235

Arora, D., & Van Damme, D. (2021). Motif-based endomembrane trafficking. *Plant Physiology*, *186*(1), 221–238. https://doi.org/10.1093/plphys/kiab077

Bairstow, S. F., Ling, K., Su, X., Firestone, A. J., Carbonara, C., & Anderson, R. A. (2006). Type Iγ661 Phosphatidylinositol Phosphate Kinase Directly Interacts with AP2 and Regulates Endocytosis. *Journal of Biological Chemistry*, *281*(29), 20632–20642. https://doi.org/10.1074/jbc.M601465200

Baral, A., Irani, N. G., Fujimoto, M., Nakano, A., Mayor, S., & Mathew, M. K. (2015). Salt-Induced Remodeling of Spatially Restricted Clathrin-Independent Endocytic Pathways in Arabidopsis Root. *The Plant Cell*, *27*(4), 1297–1315. https://doi.org/10.1105/tpc.15.00154

Bashline, L., Li, S., Anderson, C. T., Lei, L., & Gu, Y. (2013). The endocytosis of cellulose synthase in Arabidopsis is dependent on μ2, a clathrin-mediated endocytosis adaptin. *Plant Physiology*, *163*(1), 150–160. https://doi.org/10.1104/PP.113.221234

Bashline, L., Li, S., Zhu, X., & Gu, Y. (2015). The TWD40-2 protein and the AP2 complex cooperate in the clathrin-mediated endocytosis of cellulose synthase to regulate cellulose biosynthesis. *Proceedings of the National Academy of Sciences*, *112*(41), 12870–12875. https://doi.org/10.1073/pnas.1509292112

Beacham, G. M., Partlow, E. A., & Hollopeter, G. (2019). Conformational regulation of AP1 and AP2 clathrin adaptor complexes. *Traffic*, *20*(10), 741–751. https://doi.org/10.1111/tra.12677

Beacham, G. M., Partlow, E. A., Lange, J. J., & Hollopeter, G. (2018). NECAPs are negative regulators of the AP2 clathrin adaptor complex. *ELife*, *7*. https://doi.org/10.7554/ELIFE.32242

Bednarek, S. Y., & Backues, S. K. (2010). Plant dynamin-related protein families DRP1 and DRP2 in plant development. *Biochemical Society Transactions*, *38*(3), 797–806. https://doi.org/10.1042/BST0380797

Bhat, R. A., & Panstruga, R. (2005). Lipid rafts in plants. *Planta*, *223*(1), 5–19. https://doi.org/10.1007/s00425-005-0096-9

Bloch, D., Pleskot, R., Pejchar, P., Potocký, M., Trpkošová, P., Cwiklik, L., Vukašinović, N., Sternberg, H., Yalovsky, S., & Žárský, V. (2016). Exocyst SEC3 and phosphoinositides define sites of exocytosis in pollen tube initiation and growth. *Plant Physiology*, pp.00690.2016. https://doi.org/10.1104/pp.16.00690

Bolte, S., & Cordelières, F. P. (2006). A guided tour into subcellular colocalization analysis in light microscopy. *Journal of Microscopy*, *224*(3), 213–232. https://doi.org/10.1111/J.1365-2818.2006.01706.X

Borner, G. H. H., Sherrier, D. J., Weimar, T., Michaelson, L. V., Hawkins, N. D., MacAskill, A., Napier, J. A., Beale, M. H., Lilley, K. S., & Dupree, P. (2005). Analysis of Detergent-Resistant Membranes in Arabidopsis. Evidence for Plasma Membrane Lipid Rafts. *Plant Physiology*, *137*(1), 104–116. https://doi.org/10.1104/pp.104.053041

Bradford, M. M. (1976). A rapid and sensitive method for the quantitation of microgram quantities of protein utilizing the principle of protein-dye binding. *Analytical Biochemistry*, *72*(1–2), 248–254. https://doi.org/10.1016/0003-2697(76)90527-3

Brzeska, H., Guag, J., Remmert, K., Chacko, S., & Korn, E. D. (2010). An Experimentally Based Computer Search Identifies Unstructured Membrane-binding Sites in Proteins. *Journal of Biological Chemistry*, *285*(8), 5738–5747. https://doi.org/10.1074/jbc.M109.066910

Cao, Y., He, Q., Qi, Z., Zhang, Y., Lu, L., Xue, J., Li, J., & Li, R. (2020). Dynamics and Endocytosis of Flot1 in Arabidopsis Require CPI1 Function. *International Journal of Molecular Sciences*, *21*(5), 1552. https://doi.org/10.3390/ijms21051552

Chen, X., Naramoto, S., Robert, S., Tejos, R., Löfke, C., Lin, D., Yang, Z., & Friml, J. (2012). ABP1 and ROP6 GTPase Signaling Regulate Clathrin-Mediated Endocytosis in Arabidopsis Roots. *Current Biology*, *22*(14), 1326–1332. https://doi.org/10.1016/j.cub.2012.05.020

Clough, S. J., & Bent, A. F. (1998). Floral dip: a simplified method for Agrobacterium-mediated transformation of Arabidopsis thaliana. *The Plant Journal*, *16*(6), 735–743. https://doi.org/10.1046/j.1365-313x.1998.00343.x

Colin, L. A., & Jaillais, Y. (2020). Phospholipids across scales: lipid patterns and plant development. *Current Opinion in Plant Biology*, *53*, 1–9. https://doi.org/10.1016/j.pbi.2019.08.007

Collins, B. M., McCoy, A. J., Kent, H. M., Evans, P. R., & Owen, D. J. (2002). Molecular Architecture and Functional Model of the Endocytic AP2 Complex. *Cell*, *109*(4), 523–535. https://doi.org/10.1016/S0092-8674(02)00735-3

Corpet, F. (1988). Multiple sequence alignment with hierarchical clustering. *Nucleic Acids Research*, *16*(22), 10881–10890. https://doi.org/10.1093/nar/16.22.10881

Dahhan, D. A., Reynolds, G. D., Cárdenas, J. J., Eeckhout, D., Johnson, A., Yperman, K., Kaufmann, W. A., Vang, N., Yan, X., Hwang, I., Heese, A., De Jaeger, G., Friml, J., Van Damme, D., Pan, J., & Bednarek, S. Y. (2022). Proteomic characterization of isolated Arabidopsis clathrin-coated vesicles reveals evolutionarily conserved and plant-specific components. *The Plant Cell*, *34*(6), 2150–2173. https://doi.org/10.1093/plcell/koac071

De Franceschi, N., Wild, K., Schlacht, A., Dacks, J. B., Sinning, I., & Filippini, F. (2014). Longin and GAF Domains: Structural Evolution and Adaptation to the Subcellular Trafficking Machinery. *Traffic*, *15*(1), 104–121. https://doi.org/10.1111/TRA.12124

De Meyer, A., Grones, P., & Van Damme, D. (2023). How will I recognize you? Insights into endocytic cargo recognition in plants. *Current Opinion in Plant Biology*, *75*, 102429. https://doi.org/10.1016/j.pbi.2023.102429

Di Rubbo, S., Irani, N. G., Kim, S. Y., Xu, Z. Y., Gadeyne, A., Dejonghe, W., Vanhoutte, I., Persiau, G., Eeckhout, D., Simon, S., Song, K., Kleine-Vehn, J., Friml, J., De Jaeger, G., Van Damme, D., Hwang, I., & Russinova, E. (2013). The clathrin adaptor complex AP-2 mediates endocytosis of brassinosteroid insensitive1 in Arabidopsis. *The Plant Cell*, *25*(8), 2986–2997. https://doi.org/10.1105/TPC.113.114058

Doumane, M., Lebecq, A., Colin, L., Fangain, A., Stevens, F. D., Bareille, J., Hamant, O., Belkhadir, Y., Munnik, T., Jaillais, Y., & Caillaud, M. C. (2021). Inducible depletion of PI(4,5)P2 by the synthetic iDePP system in Arabidopsis. *Nature Plants*, *7*(5), 587–597. https://doi.org/10.1038/s41477-021-00907-z

Dragwidge, J. M., & Van Damme, D. (2020). Visualising endocytosis in plants: past, present, and future. *Journal of Microscopy*, *280*(2), 104–110. https://doi.org/10.1111/jmi.12926

Dragwidge, J. M., Wang, Y., Brocard, L., De Meyer, A., Hudeček, R., Eeckhout, D., Grones, P., Buridan, M., Chambaud, C., Pejchar, P., Potocký, M., Winkler, J., Vandorpe, M., Serre, N., Fendrych, M., Bernard, A., De Jaeger, G., Pleskot, R., Fang, X., … Damme, V. (2024). Biomolecular condensation orchestrates clathrin-mediated endocytosis in plants. *Nature Cell Biology 2024*, 1–12. https://doi.org/10.1038/s41556-024-01354-6

Fan, L., Hao, H., Xue, Y., Zhang, L., Song, K., Ding, Z., Botella, M. A., Wang, H., & Lin, J. (2013). Dynamic analysis of Arabidopsis AP2 σ subunit reveals a key role in clathrin-mediated

endocytosis and plant development. *Development*, *140*(18), 3826–3837. https://doi.org/10.1242/dev.095711

Fratini, M., Krishnamoorthy, P., Stenzel, I., Riechmann, M., Matzner, M., Bacia, K., Heilmann, M., & Heilmann, I. (2021). Plasma membrane nano-organization specifies phosphoinositide effects on Rho-GTPases and actin dynamics in tobacco pollen tubes. *The Plant Cell*, *33*(3), 642–670. https://doi.org/10.1093/plcell/koaa035

Frescatada-Rosa, M., Stanislas, T., Backues, S. K., Reichardt, I., Men, S., Boutté, Y., Jürgens, G., Moritz, T., Bednarek, S. Y., & Grebe, M. (2014). High lipid order of Arabidopsis cell-plate membranes mediated by sterol and DYNAMIN-RELATED PROTEIN1A function. *The Plant Journal*, *80*(5), 745–757. https://doi.org/10.1111/tpj.12674

Frick, M., Bright, N. A., Riento, K., Bray, A., Merrified, C., & Nichols, B. J. (2007). Coassembly of Flotillins Induces Formation of Membrane Microdomains, Membrane Curvature, and Vesicle Budding. *Current Biology*, *17*(13), 1151–1156. https://doi.org/10.1016/j.cub.2007.05.078

Furt, F., König, S., Bessoule, J.-J., Sargueil, F., Zallot, R., Stanislas, T., Noirot, E., Lherminier, J., Simon-Plas, F., Heilmann, I., & Mongrand, S. (2010). Polyphosphoinositides Are Enriched in Plant Membrane Rafts and Form Microdomains in the Plasma Membrane. *Plant Physiology*, *152*(4), 2173–2187. https://doi.org/10.1104/pp.109.149823

Furt, F., Simon-Plas, F., & Mongrand, S. (2011). Lipids of the Plant Plasma Membrane. In *Plant Cell Monographs* (Vol. 19, pp. 3–30). Springer Verlag. https://doi.org/10.1007/978-3-642-13431-9_1

Gadeyne, A., Sánchez-Rodríguez, C., Vanneste, S., Di Rubbo, S., Zauber, H., Vanneste, K., Van Leene, J., De Winne, N., Eeckhout, D., Persiau, G., Van De Slijke, E., Cannoot, B., Vercruysse, L., Mayers, J. R., Adamowski, M., Kania, U., Ehrlich, M., Schweighofer, A., Ketelaar, T., … Van Damme, D. (2014). The TPLATE adaptor complex drives clathrin-mediated endocytosis in plants. *Cell*, *156*(4), 691–704. https://doi.org/10.1016/J.CELL.2014.01.039

Gaidarov, I., & Keen, J. H. (1999). Phosphoinositide–Ap-2 Interactions Required for Targeting to Plasma Membrane Clathrin-Coated Pits. *The Journal of Cell Biology*, *146*(4), 755–764. https://doi.org/10.1083/jcb.146.4.755

Gerth, K., Lin, F., Menzel, W., Krishnamoorthy, P., Stenzel, I., Heilmann, M., & Heilmann, I. (2017). Guilt by Association: A Phenotype-Based View of the Plant Phosphoinositide Network. *Annual Review of Plant Biology*, *68*(1), 349–374. https://doi.org/10.1146/annurev-arplant-042916-041022

Gnyliukh, N., Johnson, A., Nagel, M.-K., Monzer, A., Babić, D., Hlavata, A., Alotaibi, S. S., Isono, E., Loose, M., & Friml, J. (2024). Role of the dynamin-related protein 2 family and SH3P2 in

clathrin-mediated endocytosis in *Arabidopsis thaliana*. *Journal of Cell Science*, *137*(8). https://doi.org/10.1242/jcs.261720

Goddard, T. D., Huang, C. C., Meng, E. C., Pettersen, E. F., Couch, G. S., Morris, J. H., & Ferrin, T. E. (2018). UCSF ChimeraX: Meeting modern challenges in visualization and analysis. *Protein Science : A Publication of the Protein Society*, *27*(1), 14–25. https://doi.org/10.1002/PRO.3235

Grebnev, G., Ntefidou, M., & Kost, B. (2017). Secretion and Endocytosis in Pollen Tubes: Models of Tip Growth in the Spot Light. *Frontiers in Plant Science*, *8*. https://doi.org/10.3389/fpls.2017.00154

Grefen, C., & Blatt, M. R. (2012). A 2in1 Cloning System Enables Ratiometric Bimolecular Fluorescence Complementation (rBiFC). *BioTechniques*, *53*(5), 311–314. https://doi.org/10.2144/000113941

Gu, M., Liu, Q., Watanabe, S., Sun, L., Hollopeter, G., Grant, B. D., & Jorgensen, E. M. (2013). AP2 hemicomplexes contribute independently to synaptic vesicle endocytosis. *ELife*, *2013*(2). https://doi.org/10.7554/ELIFE.00190

Hao, H., Fan, L., Chen, T., Li, R., Li, X., He, Q., Botella, M. A., & Lin, J. (2014). Clathrin and Membrane Microdomains Cooperatively Regulate RbohD Dynamics and Activity in *Arabidopsis* . *The Plant Cell*, *26*(4), 1729–1745. https://doi.org/10.1105/tpc.113.122358

Heilmann, I. (2016). Phosphoinositide signaling in plant development. *Development*, *143*(12), 2044–2055. https://doi.org/10.1242/dev.136432

Heilmann, M., & Heilmann, I. (2015). Plant phosphoinositides—complex networks controlling growth and adaptation. *Biochimica et Biophysica Acta (BBA) - Molecular and Cell Biology of Lipids*, *1851*(6), 759–769. https://doi.org/10.1016/j.bbalip.2014.09.018

Heilmann, M., & Heilmann, I. (2024). Getting attached to membranes—How plant signaling networks employ PtdIns(4,5)P2. *Plant Physiology*. https://doi.org/10.1093/PLPHYS/KIAE393

Hempel, F., Stenzel, I., Heilmann, M., Krishnamoorthy, P., Menzel, W., Golbik, R., Helm, S., Dobritzsch, D., Baginsky, S., Lee, J., Hoehenwarter, W., & Heilmann, I. (2017). MAPKs Influence Pollen Tube Growth by Controlling the Formation of Phosphatidylinositol 4,5-Bisphosphate in an Apical Plasma Membrane Domain. *The Plant Cell*, *29*(12), 3030–3050. https://doi.org/10.1105/tpc.17.00543

Hirst, J., Schlacht, A., Norcott, J. P., Traynor, D., Bloomfield, G., Antrobus, R., Kay, R. R., Dacks, J. B., & Robinson, M. S. (2014). Characterization of TSET, an ancient and widespread membrane trafficking complex. *ELife*, *3*. https://doi.org/10.7554/eLife.02866

Holstein, S. E. H., & Oliviusson, P. (2005). Sequence analysis of Arabidopsis thaliana E/ANTH-domain-containing proteins: membrane tethers of the clathrin-dependent vesicle budding machinery. *Protoplasma*, *226*(1–2), 13–21. https://doi.org/10.1007/S00709-005-0105-7

Höning, S., Ricotta, D., Krauss, M., Späte, K., Spolaore, B., Motley, A., Robinson, M., Robinson, C., Haucke, V., & Owen, D. J. (2005). Phosphatidylinositol-(4,5)-Bisphosphate Regulates Sorting Signal Recognition by the Clathrin-Associated Adaptor Complex AP2. *Molecular Cell*, *18*(5), 519–531. https://doi.org/10.1016/j.molcel.2005.04.019

Inoue, H., Nojima, H., & Okayama, H. (1990). High efficiency transformation of Escherichia coli with plasmids. *Gene*, *96*(1), 23–28. https://doi.org/10.1016/0378-1119(90)90336-P

Ischebeck, T., Stenzel, I., & Heilmann, I. (2008). Type B Phosphatidylinositol-4-Phosphate 5-Kinases Mediate Arabidopsis and Nicotiana tabacum Pollen Tube Growth by Regulating Apical Pectin Secretion. *The Plant Cell*, *20*(12), 3312–3330. https://doi.org/10.1105/tpc.108.059568

Ischebeck, T., Stenzel, I., Hempel, F., Jin, X., Mosblech, A., & Heilmann, I. (2011). Phosphatidylinositol-4,5-bisphosphate influences Nt-Rac5-mediated cell expansion in pollen tubes of Nicotiana tabacum. *The Plant Journal*, *65*(3), 453–468. https://doi.org/10.1111/j.1365-313X.2010.04435.x

Ischebeck, T., Vu, L. H., Jin, X., Stenzel, I., Löfke, C., & Heilmann, I. (2010). Functional cooperativity of enzymes of phosphoinositide conversion according to synergistic effects on pectin secretion in tobacco pollen tubes. *Molecular Plant*, *3*(5), 870–881. https://doi.org/10.1093/MP/SSQ031

Ischebeck, T., Werner, S., Krishnamoorthy, P., Lerche, J., Meijón, M., Stenzel, I., Löfke, C., Wiessner, T., Im, Y. J., Perera, I. Y., Iven, T., Feussner, I., Busch, W., Boss, W. F., Teichmann, T., Hause, B., Persson, S., & Heilmann, I. (2013). Phosphatidylinositol 4,5-Bisphosphate Influences PIN Polarization by Controlling Clathrin-Mediated Membrane Trafficking in *Arabidopsis*. *The Plant Cell*, *25*(12), 4894–4911. https://doi.org/10.1105/tpc.113.116582

Isono, E., Li, J., Pulido, P., Siao, W., Spoel, S. H., Wang, Z., Zhuang, X., & Trujillo, M. (2024). Protein degrons and degradation: Exploring substrate recognition and pathway selection in plants. *The Plant Cell*, *36*(9), 3074–3098. https://doi.org/10.1093/plcell/koae141

Ito, H., Fukuda, Y., Murata, K., & Kimura, A. (1983). Transformation of intact yeast cells treated with alkali cations. *Journal of Bacteriology*, *153*(1), 163–168. https://doi.org/10.1128/jb.153.1.163-168.1983

Jackson, L. P., Kelly, B. T., McCoy, A. J., Gaffry, T., James, L. C., Collins, B. M., Höning, S., Evans, P. R., & Owen, D. J. (2010). A Large-Scale Conformational Change Couples Membrane Recruitment to Cargo Binding in the AP2 Clathrin Adaptor Complex. *Cell*, *141*(7), 1220–1229. https://doi.org/10.1016/j.cell.2010.05.006

Jaillais, Y., Bayer, E., Bergmann, D. C., Botella, M. A., Boutté, Y., Bozkurt, T. O., Caillaud, M.-C., Germain, V., Grossmann, G., Heilmann, I., Hemsley, P. A., Kirchhelle, C., Martinière, A., Miao, Y., Mongrand, S., Müller, S., Noack, L. C., Oda, Y., Ott, T., … Gronnier, J. (2024). Guidelines for naming and studying plasma membrane domains in plants. *Nature Plants*. https://doi.org/10.1038/s41477-024-01742-8

Jaillais, Y., & Ott, T. (2020). The Nanoscale Organization of the Plasma Membrane and Its Importance in Signaling: A Proteolipid Perspective. *Plant Physiology*, *182*(4), 1682–1696. https://doi.org/10.1104/PP.19.01349

Jelínková, A., Malínská, K., Simon, S., Kleine-Vehn, J., Pařezová, M., Pejchar, P., Kubeš, M., Martinec, J., Friml, J., Zažímalová, E., & Petrášek, J. (2010). Probing plant membranes with FM dyes: tracking, dragging or blocking? *The Plant Journal*, *61*(5), 883–892. https://doi.org/10.1111/j.1365-313X.2009.04102.x

Jerabek-Willemsen, M., Wienken, C. J., Braun, D., Baaske, P., & Duhr, S. (2011). Molecular Interaction Studies Using Microscale Thermophoresis. *ASSAY and Drug Development Technologies*, *9*(4), 342–353. https://doi.org/10.1089/adt.2011.0380

Johnson, A., Dahhan, D. A., Gnyliukh, N., Kaufmann, W. A., Zheden, V., Costanzo, T., Mahou, P., Hrtyan, M., Wang, J., Aguilera-Servin, J., Van Damme, D., Beaurepaire, E., Loose, M., Bednarek, S. Y., & Friml, J. (2021). The TPLATE complex mediates membrane bending during plant clathrin–mediated endocytosis. *Proceedings of the National Academy of Sciences*, *118*(51). https://doi.org/10.1073/pnas.2113046118

Johnson, A., & Vert, G. (2017). Single Event Resolution of Plant Plasma Membrane Protein Endocytosis by TIRF Microscopy. *Frontiers in Plant Science*, *8*. https://doi.org/10.3389/fpls.2017.00612

Johnsson, N., & Varshavsky, A. (1994). Split ubiquitin as a sensor of protein interactions in vivo. *Proceedings of the National Academy of Sciences*, *91*(22), 10340–10344. https://doi.org/10.1073/pnas.91.22.10340

Julkowska, M. M., Rankenberg, J. M., & Testerink, C. (2013). *Liposome-Binding Assays to Assess Specificity and Affinity of Phospholipid–Protein Interactions* (pp. 261–271). https://doi.org/10.1007/978-1-62703-401-2_24

Kadlecova, Z., Spielman, S. J., Loerke, D., Mohanakrishnan, A., Reed, D. K., & Schmid, S. L. (2017). Regulation of clathrin-mediated endocytosis by hierarchical allosteric activation of AP2. *Journal of Cell Biology*, *216*(1), 167–179. https://doi.org/10.1083/jcb.201608071

Kahlfeldt, N., Vahedi-Faridi, A., Koo, S. J., Schäfer, J. G., Krainer, G., Keller, S., Saenger, W., Krauss, M., & Haucke, V. (2009). Molecular Basis for Association of PIPKIγ-p90 with Clathrin Adaptor

AP-2. *Journal of Biological Chemistry*, *285*(4), 2734–2749. https://doi.org/10.1074/jbc.M109.074906

Kaksonen, M., & Roux, A. (2018). Mechanisms of clathrin-mediated endocytosis. *Nature Reviews Molecular Cell Biology*, *19*(5), 313–326. https://doi.org/10.1038/nrm.2017.132

Kaneda, M., van Oostende-Triplet, C., Chebli, Y., Testerink, C., Bednarek, S. Y., & Geitmann, A. (2019). Plant AP180 N-Terminal Homolog Proteins Are Involved in Clathrin-Dependent Endocytosis during Pollen Tube Growth in Arabidopsis thaliana. *Plant and Cell Physiology*, *60*(6), 1316–1330. https://doi.org/10.1093/pcp/pcz036

Kastner, C., Wagner, V. C., Fratini, M., Dobritzsch, D., Fuszard, M., Heilmann, M., & Heilmann, I. (2022). The pollen-specific class VIII-myosin ATM2 from Arabidopsis thaliana associates with the plasma membrane through a polybasic region binding anionic phospholipids. *Biochimie*, *203*, 65–76. https://doi.org/10.1016/j.biochi.2022.10.002

Kelly, S. M., Jess, T. J., & Price, N. C. (2005). How to study proteins by circular dichroism. *Biochimica et Biophysica Acta (BBA) - Proteins and Proteomics*, *1751*(2), 119–139. https://doi.org/10.1016/j.bbapap.2005.06.005

Kim, S. Y., Xu, Z.-Y., Song, K., Kim, D. H., Kang, H., Reichardt, I., Sohn, E. J., Friml, J., Juergens, G., & Hwang, I. (2013). Adaptor Protein Complex 2–Mediated Endocytosis Is Crucial for Male Reproductive Organ Development in Arabidopsis. *The Plant Cell*, *25*(8), 2970–2985. https://doi.org/10.1105/tpc.113.114264

König, S., Ischebeck, T., Lerche, J., Stenzel, I., & Heilmann, I. (2008). Salt-stress-induced association of phosphatidylinositol 4,5-bisphosphate with clathrin-coated vesicles in plants. *Biochemical Journal*, *415*(3), 387–399. https://doi.org/10.1042/BJ20081306

Kost, B. (2008). Spatial control of Rho (Rac-Rop) signaling in tip-growing plant cells. *Trends in Cell Biology*, *18*(3), 119–127. https://doi.org/10.1016/j.tcb.2008.01.003

Kovtun, O., Dickson, V. K., Kelly, B. T., Owen, D. J., & Briggs, J. A. G. (2020). Architecture of the AP2/clathrin coat on the membranes of clathrin-coated vesicles. *Science Advances*, *6*(30). https://doi.org/10.1126/sciadv.aba8381

Kraus, M., Pleskot, R., & Van Damme, D. (2024). Structural and Evolutionary Aspects of Plant Endocytosis. *Annual Review of Plant Biology*, *75*(1), 521–550. https://doi.org/10.1146/annurev-arplant-070122-023455

Krauss, M., Kukhtina, V., Pechstein, A., & Haucke, V. (2006). Stimulation of phosphatidylinositol kinase type I-mediated phosphatidylinositol (4,5)-bisphosphate synthesis by AP-2μ–cargo complexes. *Proceedings of the National Academy of Sciences*, *103*(32), 11934–11939. https://doi.org/10.1073/pnas.0510306103

Laemmli, U. K. (1970). Cleavage of Structural Proteins during the Assembly of the Head of Bacteriophage T4. *Nature*, *227*(5259), 680–685. https://doi.org/10.1038/227680a0

Lazo, G. R., Stein, P. A., & Ludwig, R. A. (1991). A DNA Transformation–Competent Arabidopsis Genomic Library in Agrobacterium. *Bio/Technology*, *9*(10), 963–967. https://doi.org/10.1038/nbt1091-963

Lebecq, A., Doumane, M., Fangain, A., Bayle, V., Leong, J. X., Rozier, F., Marques-Bueno, M. del, Armengot, L., Boisseau, R., Simon, M. L., Franz-Wachtel, M., Macek, B., Üstün, S., Jaillais, Y., & Caillaud, M.-C. (2022). The Arabidopsis SAC9 enzyme is enriched in a cortical population of early endosomes and restricts PI(4,5)P2 at the plasma membrane. *ELife*, *11*. https://doi.org/10.7554/eLife.73837

Li, R., Liu, P., Wan, Y., Chen, T., Wang, Q., Mettbach, U., Baluška, F., Šamaj, J., Fang, X., Lucas, W. J., & Lin, J. (2012). A Membrane Microdomain-Associated Protein, Arabidopsis Flot1, Is Involved in a Clathrin-Independent Endocytic Pathway and Is Required for Seedling Development. *The Plant Cell*, *24*(5), 2105–2122. https://doi.org/10.1105/tpc.112.095695

Li, X., & Pan, S. Q. (2017). Agrobacterium delivers VirE2 protein into host cells via clathrin-mediated endocytosis. *Science Advances*, *3*(3). https://doi.org/10.1126/SCIADV.1601528

Lin, F., Krishnamoorthy, P., Schubert, V., Hause, G., Heilmann, M., & Heilmann, I. (2019). A dual role for cell plate-associated PI4Kβ in endocytosis and phragmoplast dynamics during plant somatic cytokinesis. *The EMBO Journal*, *38*(4). https://doi.org/10.15252/embj.2018100303

Liu, C., Li, Z., Tian, D., Xu, M., Pan, J., Wu, H., Wang, C., & Otegui, M. S. (2022). AP1/2β-mediated exocytosis of tapetum-specific transporters is required for pollen development in Arabidopsis thaliana. *The Plant Cell*, *34*(10), 3961–3982. https://doi.org/10.1093/PLCELL/KOAC192

Liu, D., Kumar, R., Claus, L. A. N., Johnson, A. J., Siao, W., Vanhoutte, I., Wang, P., Bender, K. W., Yperman, K., Martins, S., Zhao, X., Vert, G., van Damme, D., Friml, J., & Russinova, E. (2020). Endocytosis of BRASSINOSTEROID INSENSITIVE1 Is Partly Driven by a Canonical Tyr-Based Motif. *The Plant Cell*, *32*(11), 3598–3612. https://doi.org/10.1105/TPC.20.00384

Luttgeharm, K. D., Chen, M., Mehra, A., Cahoon, R. E., Markham, J. E., & Cahoon, E. B. (2015). Overexpression of Arabidopsis Ceramide Synthases Differentially Affects Growth, Sphingolipid Metabolism, Programmed Cell Death, and Mycotoxin Resistance. *Plant Physiology*, *169*(2), 1108–1117. https://doi.org/10.1104/pp.15.00987

Mamode Cassim, A., Gouguet, P., Gronnier, J., Laurent, N., Germain, V., Grison, M., Boutté, Y., Gerbeau-Pissot, P., Simon-Plas, F., & Mongrand, S. (2019). Plant lipids: Key players of plasma membrane organization and function. *Progress in Lipid Research*, *73*, 1–27. https://doi.org/10.1016/j.plipres.2018.11.002

Mamode Cassim, A., Grison, M., Ito, Y., Simon-Plas, F., Mongrand, S., & Boutté, Y. (2020). Sphingolipids in plants: a guidebook on their function in membrane architecture, cellular processes, and environmental or developmental responses. *FEBS Letters*, *594*(22), 3719–3738. https://doi.org/10.1002/1873-3468.13987

Markham, J. E., Molino, D., Gissot, L., Bellec, Y., Hématy, K., Marion, J., Belcram, K., Palauqui, J. C., Satiat-Jeunemaître, B., & Faure, J. D. (2011). Sphingolipids containing very-long-chain fatty acids define a secretory pathway for specific polar plasma membrane protein targeting in Arabidopsis. *The Plant Cell*, *23*(6), 2362–2378. https://doi.org/10.1105/TPC.110.080473

Mei, K., & Guo, W. (2018). The exocyst complex. *Current Biology*, *28*(17), R922–R925. https://doi.org/10.1016/j.cub.2018.06.042

Meijer, H. J. G., Berrie, C. P., Iurisci, C., Divecha, N., Musgrave, A., & Munnik, T. (2001). Identification of a new polyphosphoinositide in plants, phosphatidylinositol 5-monophosphate (PtdIns5P), and its accumulation upon osmotic stress. *Biochemical Journal*, *360*(Pt 2), 491. https://doi.org/10.1042/0264-6021:3600491

Men, S., Boutté, Y., Ikeda, Y., Li, X., Palme, K., Stierhof, Y.-D., Hartmann, M.-A., Moritz, T., & Grebe, M. (2008). Sterol-dependent endocytosis mediates post-cytokinetic acquisition of PIN2 auxin efflux carrier polarity. *Nature Cell Biology*, *10*(2), 237–244. https://doi.org/10.1038/ncb1686

Menzel, W., Stenzel, I., Helbig, L., Krishnamoorthy, P., Neumann, S., Eschen-Lippold, L., Heilmann, M., Lee, J., & Heilmann, I. (2019). A PAMP-triggered MAPK cascade inhibits phosphatidylinositol 4,5-bisphosphate production by PIP5K6 in Arabidopsis thaliana. *New Phytologist*, *224*(2), 833–847. https://doi.org/10.1111/nph.16069

Möckli, N., Deplazes, A., Hassa, P. O., Zhang, Z., Peter, M., Hottiger, M. O., Stagljar, I., & Auerbach, D. (2007). Yeast Split-Ubiquitin-Based Cytosolic Screening System to Detect Interactions Between Transcriptionally Active Proteins. *BioTechniques*, *42*(6), 725–730. https://doi.org/10.2144/000112455

Mueller-Roeber, B., & Pical, C. (2002). Inositol Phospholipid Metabolism in Arabidopsis. Characterized and Putative Isoforms of Inositol Phospholipid Kinase and Phosphoinositide-Specific Phospholipase C. *Plant Physiology*, *130*(1), 22–46. https://doi.org/10.1104/pp.004770

Murray, M. G., & Thompson, W. F. (1980). Rapid isolation of high molecular weight plant DNA. *Nucleic Acids Research*, *8*(19), 4321–4326. https://doi.org/10.1093/nar/8.19.4321

Nagano, M., Ishikawa, T., Fujiwara, M., Fukao, Y., Kawano, Y., Kawai-Yamada, M., & Shimamoto, K. (2016). Plasma Membrane Microdomains Are Essential for Rac1-RbohB/H-Mediated Immunity in Rice. *The Plant Cell*, *28*(8), 1966–1983. https://doi.org/10.1105/tpc.16.00201

Nakano-Kobayashi, A., Yamazaki, M., Unoki, T., Hongu, T., Murata, C., Taguchi, R., Katada, T., Frohman, M. A., Yokozeki, T., & Kanaho, Y. (2007). Role of activation of PIP5Kγ661 by AP-2 complex in synaptic vesicle endocytosis. *The EMBO Journal*, *26*(4), 1105–1116. https://doi.org/10.1038/sj.emboj.7601573

Narasimhan, M., Johnson, A., Prizak, R., Kaufmann, W. A., Tan, S., Casillas-Pérez, B., & Friml, J. (2020). Evolutionarily unique mechanistic framework of clathrin-mediated endocytosis in plants. *ELife*, *9*. https://doi.org/10.7554/eLife.52067

Owen, D. J., Collins, B. M., & Evans, P. R. (2004). Adaptors for clathrin coats: structure and function. *Annual Review of Cell and Developmental Biology*, *20*, 153–191. https://doi.org/10.1146/ANNUREV.CELLBIO.20.010403.104543

Owen, D. M., Rentero, C., Magenau, A., Abu-Siniyeh, A., & Gaus, K. (2012). Quantitative imaging of membrane lipid order in cells and organisms. *Nature Protocols*, *7*(1), 24–35. https://doi.org/10.1038/nprot.2011.419

Paez Valencia, J., Goodman, K., & Otegui, M. S. (2016). Endocytosis and Endosomal Trafficking in Plants. *Annual Review of Plant Biology*, *67*(1), 309–335. https://doi.org/10.1146/annurev-arplant-043015-112242

Partlow, E. A., Cannon, K. S., Hollopeter, G., & Baker, R. W. (2022). Structural basis of an endocytic checkpoint that primes the AP2 clathrin adaptor for cargo internalization. *Nature Structural & Molecular Biology 2022 29:4*, *29*(4), 339–347. https://doi.org/10.1038/s41594-022-00749-z

Platre, M. P., Bayle, V., Armengot, L., Bareille, J., Marquès-Bueno, M. del M., Creff, A., Maneta-Peyret, L., Fiche, J.-B., Nollmann, M., Miège, C., Moreau, P., Martinière, A., & Jaillais, Y. (2019). Developmental control of plant Rho GTPase nano-organization by the lipid phosphatidylserine. *Science*, *364*(6435), 57–62. https://doi.org/10.1126/science.aav9959

Posor, Y., Eichhorn-Gruenig, M., Puchkov, D., Schöneberg, J., Ullrich, A., Lampe, A., Müller, R., Zarbakhsh, S., Gulluni, F., Hirsch, E., Krauss, M., Schultz, C., Schmoranzer, J., Noé, F., & Haucke, V. (2013). Spatiotemporal control of endocytosis by phosphatidylinositol-3,4-bisphosphate. *Nature*, *499*(7457), 233–237. https://doi.org/10.1038/nature12360

Putta, P., Creque, E., Piontkivska, H., & Kooijman, E. E. (2020). Lipid−protein interactions for ECA1 an N-ANTH domain protein involved in stress signaling in plants. *Chemistry and Physics of Lipids*, *231*, 104919. https://doi.org/10.1016/j.chemphyslip.2020.104919

Rausche, J., Stenzel, I., Stauder, R., Fratini, M., Trujillo, M., Heilmann, I., & Rosahl, S. (2021). A phosphoinositide 5-phosphatase from *Solanum tuberosum* is activated by PAMP-treatment and may antagonize phosphatidylinositol 4,5-bisphosphate at *Phytophthora infestans* infection sites. *New Phytologist*, *229*(1), 469–487. https://doi.org/10.1111/nph.16853

Read, S. M., Clarke, A. E., & Bacic, A. (1993). Stimulation of growth of cultured Nicotiana tabacum W 38 pollen tubes by poly(ethylene glycol) and Cu(II) salts. In *Protoplasma* (Vol. 177).

Reynolds, G. D., Wang, C., Pan, J., & Bednarek, S. Y. (2018). Inroads into Internalization: Five Years of Endocytic Exploration. *Plant Physiology*, *176*(1), 208–218. https://doi.org/10.1104/PP.17.01117

Roche, Y., Gerbeau-Pissot, P., Buhot, B., Thomas, D., Bonneau, L., Gresti, J., Mongrand, S., Perrier-Cornet, J., & Simon-Plas, F. (2008). Depletion of phytosterols from the plant plasma membrane provides evidence for disruption of lipid rafts. *The FASEB Journal*, *22*(11), 3980–3991. https://doi.org/10.1096/fj.08-111070

Rohde, G., Wenzel, D., & Haucke, V. (2002). A phosphatidylinositol (4,5)-bisphosphate binding site within μ2-adaptin regulates clathrin-mediated endocytosis. *The Journal of Cell Biology*, *158*(2), 209–214. https://doi.org/10.1083/jcb.200203103

Schindelin, J., Arganda-Carreras, I., Frise, E., Kaynig, V., Longair, M., Pietzsch, T., Preibisch, S., Rueden, C., Saalfeld, S., Schmid, B., Tinevez, J.-Y., White, D. J., Hartenstein, V., Eliceiri, K., Tomancak, P., & Cardona, A. (2012). Fiji: an open-source platform for biological-image analysis. *Nature Methods*, *9*(7), 676–682. https://doi.org/10.1038/nmeth.2019

Siao, W., Wang, P., Zhao, X., Vu, L. D., De Smet, I., & Russinova, E. (2023). Phosphorylation of ADAPTOR PROTEIN-2 μ-adaptin by ADAPTOR-ASSOCIATED KINASE1 regulates the tropic growth of Arabidopsis roots. *The Plant Cell*, *35*(9), 3504–3521. https://doi.org/10.1093/plcell/koad141

Simons, K., & Ikonen, E. (1997). Functional rafts in cell membranes. *Nature*, *387*(6633), 569–572. https://doi.org/10.1038/42408

Singer, S. J., & Nicolson, G. L. (1972). The Fluid Mosaic Model of the Structure of Cell Membranes. *Science*, *175*(4023), 720–731. https://doi.org/10.1126/SCIENCE.175.4023.720

Singh, M. K., & Jürgens, G. (2018). Specificity of plant membrane trafficking – ARFs, regulators and coat proteins. *Seminars in Cell & Developmental Biology*, *80*, 85–93. https://doi.org/10.1016/j.semcdb.2017.10.005

Sousa, E., Kost, B., & Malhó, R. (2008). Arabidopsis Phosphatidylinositol-4-Monophosphate 5-Kinase 4 Regulates Pollen Tube Growth and Polarity by Modulating Membrane Recycling. *The Plant Cell*, *20*(11), 3050–3064. https://doi.org/10.1105/tpc.108.058826

Tejos, R., Sauer, M., Vanneste, S., Palacios-Gomez, M., Li, H., Heilmann, M., van Wijk, R., Vermeer, J. E. M., Heilmann, I., Munnik, T., & Friml, J. (2014). Bipolar Plasma Membrane Distribution of Phosphoinositides and Their Requirement for Auxin-Mediated Cell Polarity and Patterning in Arabidopsis. *The Plant Cell*, *26*(5), 2114–2128. https://doi.org/10.1105/tpc.114.126185

Ternes, P., Feussner, K., Werner, S., Lerche, J., Iven, T., Heilmann, I., Riezman, H., & Feussner, I. (2011). Disruption of the ceramide synthase LOH1 causes spontaneous cell death in Arabidopsis thaliana. *The New Phytologist*, *192*(4), 841–854. https://doi.org/10.1111/J.1469-8137.2011.03852.X

Towbin, H., Staehelin, T., & Gordon, J. (1979). Electrophoretic transfer of proteins from polyacrylamide gels to nitrocellulose sheets: procedure and some applications. *Proceedings of the National Academy of Sciences*, *76*(9), 4350–4354. https://doi.org/10.1073/pnas.76.9.4350

Ungewickell, E., Ungewickell, H., Holstein, S. E. H., Lindner, R., Prasad, K., Barouch, W., Martini, B., Greene, L. E., & Eisenberg, E. (1995). Role of auxilin in uncoating clathrin-coated vesicles. *Nature*, *378*(6557), 632–635. https://doi.org/10.1038/378632a0

van den Bogaart, G., Meyenberg, K., Diederichsen, U., & Jahn, R. (2012). Phosphatidylinositol 4,5-Bisphosphate Increases Ca2+ Affinity of Synaptotagmin-1 by 40-fold. *Journal of Biological Chemistry*, *287*(20), 16447–16453. https://doi.org/10.1074/jbc.M112.343418

Wang, C., Hu, T., Yan, X., Meng, T., Wang, Y., Wang, Q., Zhang, X., Gu, Y., Sánchez-Rodríguez, C., Gadeyne, A., Lin, J., Persson, S., Van Damme, D., Li, C., Bednarek, S. Y., & Pan, J. (2016). Differential Regulation of Clathrin and Its Adaptor Proteins during Membrane Recruitment for Endocytosis. *Plant Physiology*, *171*(1), 215–229. https://doi.org/10.1104/pp.15.01716

Wang, P., Pleskot, R., Zang, J., Winkler, J., Wang, J., Yperman, K., Zhang, T., Wang, K., Gong, J., Guan, Y., Richardson, C., Duckney, P., Vandorpe, M., Mylle, E., Fiserova, J., Van Damme, D., & Hussey, P. J. (2019). Plant AtEH/Pan1 proteins drive autophagosome formation at ER-PM contact sites with actin and endocytic machinery. *Nature Communications*, *10*(1), 5132. https://doi.org/10.1038/s41467-019-12782-6

Wang, P., Siao, W., Zhao, X., Arora, D., Wang, R., Eeckhout, D., Van Leene, J., Kumar, R., Houbaert, A., De Winne, N., Mylle, E., Vandorpe, M., Korver, R. A., Testerink, C., Gevaert, K., Vanneste, S., De Jaeger, G., Van Damme, D., & Russinova, E. (2023). Adaptor protein complex interaction map in Arabidopsis identifies P34 as a common stability regulator. *Nature Plants 2023 9:2*, *9*(2), 355–371. https://doi.org/10.1038/s41477-022-01328-2

Wienken, C. J., Baaske, P., Rothbauer, U., Braun, D., & Duhr, S. (2010). Protein-binding assays in biological liquids using microscale thermophoresis. *Nature Communications*, *1*(1), 100. https://doi.org/10.1038/ncomms1093

Willemsen, V., Friml, J., Grebe, M., Van Den Toorn, A., Palme, K., & Scheres, B. (2003). Cell polarity and PIN protein positioning in Arabidopsis require STEROL METHYLTRANSFERASE1 function. *The Plant Cell*, *15*(3), 612–625. https://doi.org/10.1105/TPC.008433

Wrobel, A. G., Kadlecova, Z., Kamenicky, J., Yang, J.-C., Herrmann, T., Kelly, B. T., McCoy, A. J., Evans, P. R., Martin, S., Müller, S., Salomon, S., Sroubek, F., Neuhaus, D., Höning, S., & Owen, D. J. (2019). Temporal Ordering in Endocytic Clathrin-Coated Vesicle Formation via AP2 Phosphorylation. *Developmental Cell*, *50*(4), 494-508.e11. https://doi.org/10.1016/j.devcel.2019.07.017

Wu, Z., Fan, C., Man, Y., Zhang, Y., Li, R., Li, X., Jing, Y., & Voll, L. M. (2021). Both Clathrin-Mediated and Membrane Microdomain-Associated Endocytosis Contribute to the Cellular Adaptation to Hyperosmotic Stress in Arabidopsis. *International Journal of Molecular Sciences Article J. Mol. Sci*, *2021*, 12534. https://doi.org/10.3390/ijms222212534

Yalovsky, S., Bloch, D., Sorek, N., & Kost, B. (2008). Regulation of Membrane Trafficking, Cytoskeleton Dynamics, and Cell Polarity by ROP/RAC GTPases. *Plant Physiology*, *147*(4), 1527. https://doi.org/10.1104/PP.108.122150

Yamaoka, S., Shimono, Y., Shirakawa, M., Fukao, Y., Kawase, T., Hatsugai, N., Tamura, K., Shimada, T., & Hara-Nishimura, I. (2013). Identification and dynamics of arabidopsis adaptor protein-2 complex and its involvement in floral organ development. *Plant Cell*, *25*(8), 2958–2969. https://doi.org/10.1105/tpc.113.114082

Yan, X., Wang, Y., Xu, M., Dahhan, D. A., Liu, C., Zhang, Y., Lin, J., Bednarek, S. Y., & Pan, J. (2021). Cross-talk between clathrin-dependent post-Golgi trafficking and clathrin-mediated endocytosis in Arabidopsis root cells. *The Plant Cell*, *33*(9), 3057–3075. https://doi.org/10.1093/PLCELL/KOAB180

Yoo, S.-D., Cho, Y.-H., & Sheen, J. (2007). Arabidopsis mesophyll protoplasts: a versatile cell system for transient gene expression analysis. *Nature Protocols*, *2*(7), 1565–1572. https://doi.org/10.1038/nprot.2007.199

Yoshinari, A., Hosokawa, T., Amano, T., Beier, M. P., Kunied, T., Shimada, T., Hara-Nishimur, I., Naito, S., & Takano, J. (2019). Polar Localization of the Borate Exporter BOR1 Requires AP2-Dependent Endocytosis. *Plant Physiology*, *179*(4), 1569. https://doi.org/10.1104/PP.18.01017

Yperman, K., Papageorgiou, A. C., Merceron, R., De Munck, S., Bloch, Y., Eeckhout, D., Jiang, Q., Tack, P., Grigoryan, R., Evangelidis, T., Van Leene, J., Vincze, L., Vandenabeele, P., Vanhaecke, F., Potocký, M., De Jaeger, G., Savvides, S. N., Tripsianes, K., Pleskot, R., & Van Damme, D. (2021). Distinct EH domains of the endocytic TPLATE complex confer lipid and protein binding. *Nature Communications*, *12*(1), 3050. https://doi.org/10.1038/s41467-021-23314-6

Yperman, K., Wang, J., Eeckhout, D., Winkler, J., Dai Vu, L., Vandorpe, M., Grones, P., Mylle, E., Kraus, M., Merceron, R., Nolf, J., Mor, E., De Bruyn, P., Loris, R., Potocký, M., Savvides, S. N.,

De Rybel, B., De Jaeger, G., Van Damme, D., & Pleskot, R. (2021). Molecular architecture of the endocytic TPLATE complex. In *Sci. Adv* (Vol. 7). http://advances.sciencemag.org/

Yu, M., Liu, H., Dong, Z., Xiao, J., Su, B., Fan, L., Komis, G., Šamaj, J., Lin, J., & Li, R. (2017). The dynamics and endocytosis of Flot1 protein in response to flg22 in Arabidopsis. *Journal of Plant Physiology*, *215*, 73–84. https://doi.org/10.1016/j.jplph.2017.05.010

Zaccai, N. R., Kadlecova, Z., Dickson, V. K., Korobchevskaya, K., Kamenicky, J., Kovtun, O., Umasankar, P. K., Wrobel, A. G., Kaufman, J. G. G., Gray, S. R., Qu, K., Evans, P. R., Fritzsche, M., Sroubek, F., Höning, S., Briggs, J. A. G., Kelly, B. T., Owen, D. J., & Traub, L. M. (2022). FCHO controls AP2's initiating role in endocytosis through a PtdIns(4,5)P2-dependent switch. *Science Advances*, *8*(17). https://doi.org/10.1126/sciadv.abn2018

Žárský, V., Kulich, I., Fendrych, M., & Pečenková, T. (2013). Exocyst complexes multiple functions in plant cells secretory pathways. *Current Opinion in Plant Biology*, *16*(6), 726–733. https://doi.org/10.1016/J.PBI.2013.10.013

Zhang, Y., Chen, M., Siemiatkowska, B., Toleco, M. R., Jing, Y., Strotmann, V., Zhang, J., Stahl, Y., & Fernie, A. R. (2020). A Highly Efficient Agrobacterium-Mediated Method for Transient Gene Expression and Functional Studies in Multiple Plant Species. *Plant Communications*, *1*(5), 100028. https://doi.org/10.1016/j.xplc.2020.100028

Zhang, Y., Immink, R., Liu, C.-M., Emons, A. M., & Ketelaar, T. (2013). The Arabidopsis exocyst subunit SEC3A is essential for embryo development and accumulates in transient puncta at the plasma membrane. *The New Phytologist*, *199*(1), 74–88. https://doi.org/10.1111/nph.12236

Zhang, Y., Persson, S., Hirst, J., Robinson, M. S., van Damme, D., & Sánchez-Rodríguez, C. (2015). Change your Tplate, change your fate: plant CME and beyond. *Trends in Plant Science*, *20*(1), 41–48. https://doi.org/10.1016/j.tplants.2014.09.002

Zhao, X., Zhang, X., Qu, Y., Li, R., Baluška, F., & Wan, Y. (2015). Mapping of Membrane Lipid Order in Root Apex Zones of Arabidopsis thaliana. *Frontiers in Plant Science*, *6*. https://doi.org/10.3389/fpls.2015.01151

Zhao, Y., Yan, A., Feijó, J. A., Furutani, M., Takenawa, T., Hwang, I., Fu, Y., & Yang, Z. (2010). Phosphoinositides regulate clathrin-dependent endocytosis at the tip of pollen tubes in Arabidopsis and tobacco. *The Plant Cell*, *22*(12), 4031–4044. https://doi.org/10.1105/tpc.110.076760

Zhong, R., & Ye, Z. H. (2003). The SAC Domain-Containing Protein Gene Family in Arabidopsis. *Plant Physiology*, *132*(2), 544. https://doi.org/10.1104/PP.103.021444

Zonia, L., & Munnik, T. (2008). Vesicle trafficking dynamics and visualization of zones of exocytosis and endocytosis in tobacco pollen tubes. *Journal of Experimental Botany*, *59*(4), 861–873. https://doi.org/10.1093/jxb/ern007

7. Appendix

7.1 Additional experimental data

```
HsAP2α1 44 FKGDKALDGYSKKKYVCKLLFIFLLGH 71
AtAP2α1 38 FKNEKVLTPYKKKKYVWKMLYIHMLGY 65

HsAP2μ 331 SGVQVICMKGKAKYKASENAIVWKIKR 358
AtAP2μ 336 AKTNFQVTTGRAKYNPSIDCLVWKIRK 363
```

Figure 24. Alignment of human and Arabidopsis AP2-subunits α1 and μ. Residues that are responsible for lipid-binding in human AP2-subunits and the respective aligned residues in the Arabidopsis AP2-subunits are highlighted in grey. Residues in the Arabidopsis AP2-subunits, were a computer-based sequence analysis suggested regions enriched in basic and hydrophobic amino acids (BH-search; Brzeska et al. (2010)) that may confer a lipid-binding capability, are marked red.

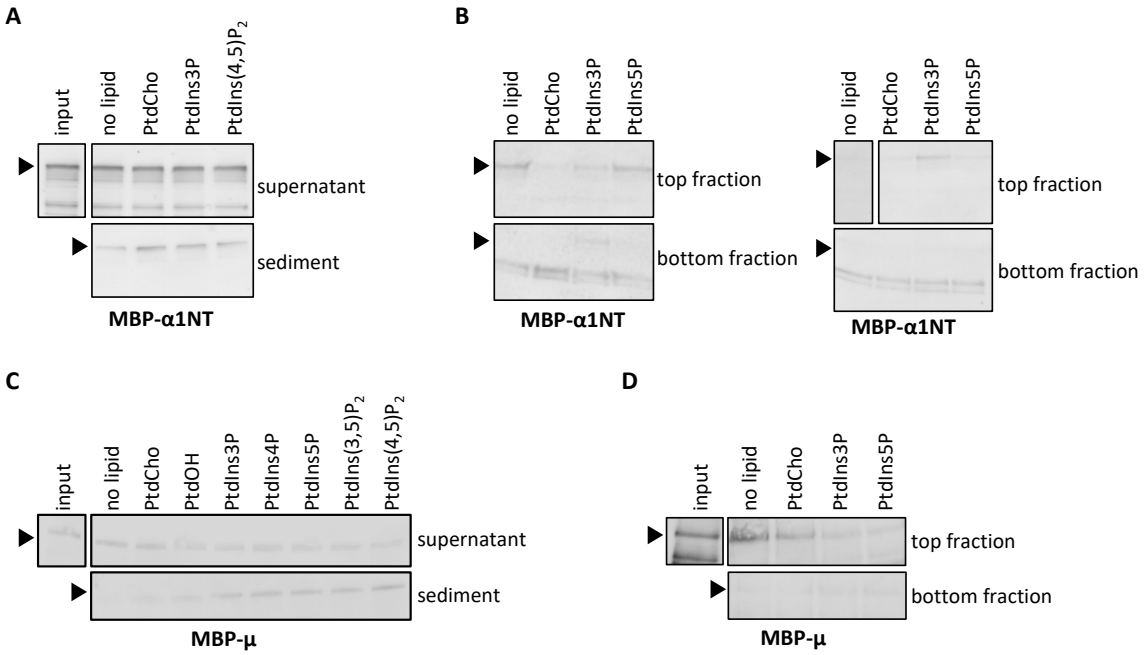

Figure 25. Liposome binding assays of MBP-α1NT and MBP-μ. Representative liposome binding assays with MBP-α1NT and MBP-μ were performed as sedimentation assays (Julkowska et al., 2013) or as flotation assays (Posor et al., 2013). Black arrowheads mark the expected molecular size of the fusion proteins: MBP-α1NT, 65.2 kDa; MBP-μ, 92 kDa. **A** Liposome sedimentation assay, three independent experiments with 90 mol % PtdCho + 10 mol % PIs with 0.5 μg, 1.0 μg or 1.5 μg protein and one independent experiments with 90 mol % PtdCho:PtdEtn (1:1) + 10 mol % PIs and 0.5 μg protein showed similar results. **B** Liposome flotation assays, 90 mol % PtdCho + 10 mol % PIs, two independent experiments with 2 μg protein showed differing results as indicated on left and right panel. **C** Liposome sedimentation assay, one independent experiments with 90 mol % PtdCho + 10 mol % PIs and two independent experiments with 80 mol % PtdCho + 20 mol % PIs with 0.5 μg protein showed similar results. **D** Liposome flotation assay, two independent experiments with 90 mol % PtdCho + 10 mol % PIs, with either 1μg or 2 μg protein showed similar results.

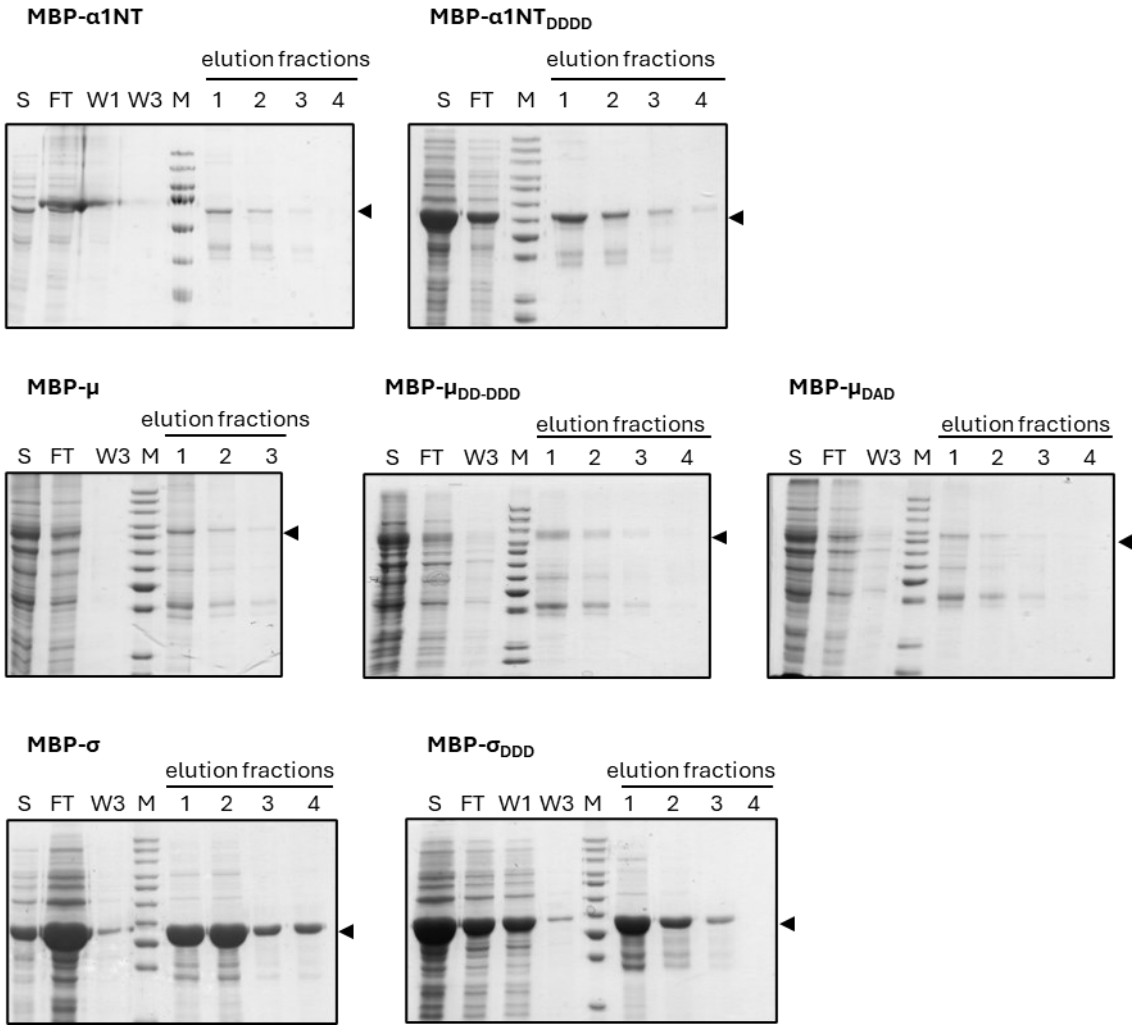

Figure 26. Enrichment of MBP-tagged AP2-subunits by affinity chromatography. MBP-tagged wild type and substituted AP2-subunits were expressed in *E. coli* BL21 (DE3) and enriched with an amylose matrix. 10 µl of protein-sample were applied to an SDS-PAGE, PageRuler^{TM} Prestained Protein Ladder was used as molecular size marker and proteins were stained with Coomassie. S: soluble fraction after cell disruption; FT: flow through; W3: washing step three; 1-4: number of elution fractions. Black arrowheads mark the expected molecular size of the fusion proteins: MBP-α1NT/α1NT$_{DDDD}$, 65.2 kDa; MBP-μ/μ$_{DD-DDD}$/μ$_{DAD}$, 92 kDa; MBP-σ/σ$_{DDD}$, 60 kDa.

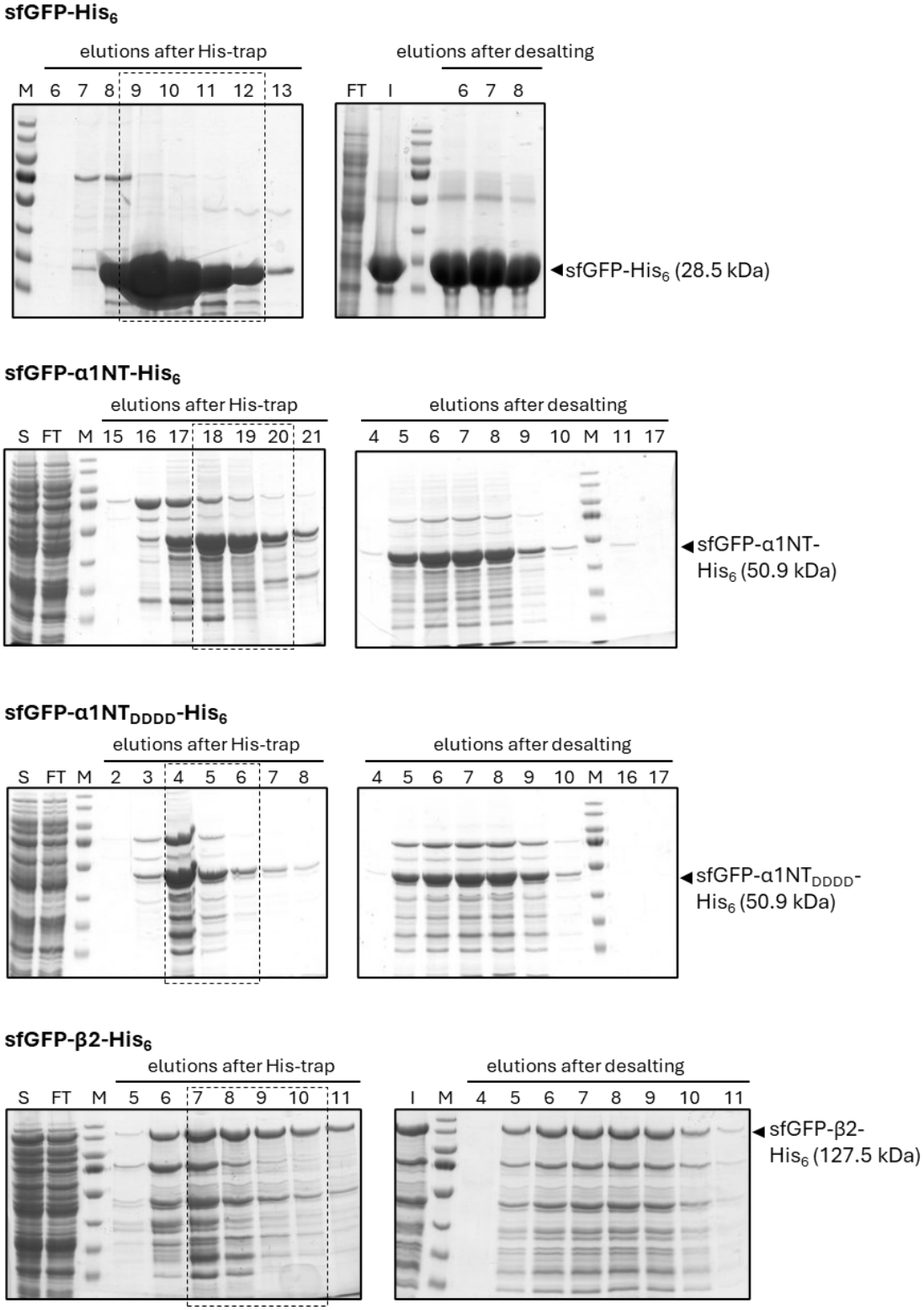

Figure 27. Enrichment of sfGFP-His$_6$, sfGFP-α1NT-His$_6$, sfGFP-α1NT$_{DDDD}$-His$_6$ and sfGFP-β2-His$_6$. Displayed are Coomassie-stained SDS-PAGE gels of the enriched fusion proteins. Fusion proteins were expressed in *E. coli* Rosetta2 and enriched with a HisTrap HP His-tag protein purification column using the ÄKTA pure™ system. After the HisTrap column, a buffer exchange was performed with selected elution fractions (indicated by dashed lines) using HiTrap desalting columns. 10 µl of protein-sample were applied to an SDS-PAGE, PageRuler™ Prestained Protein Ladder was used as molecular size marker and proteins were stained with Coomassie. S: soluble fraction after cell disruption; FT: flow through. Black arrowheads mark the expected molecular size of the fusion proteins.

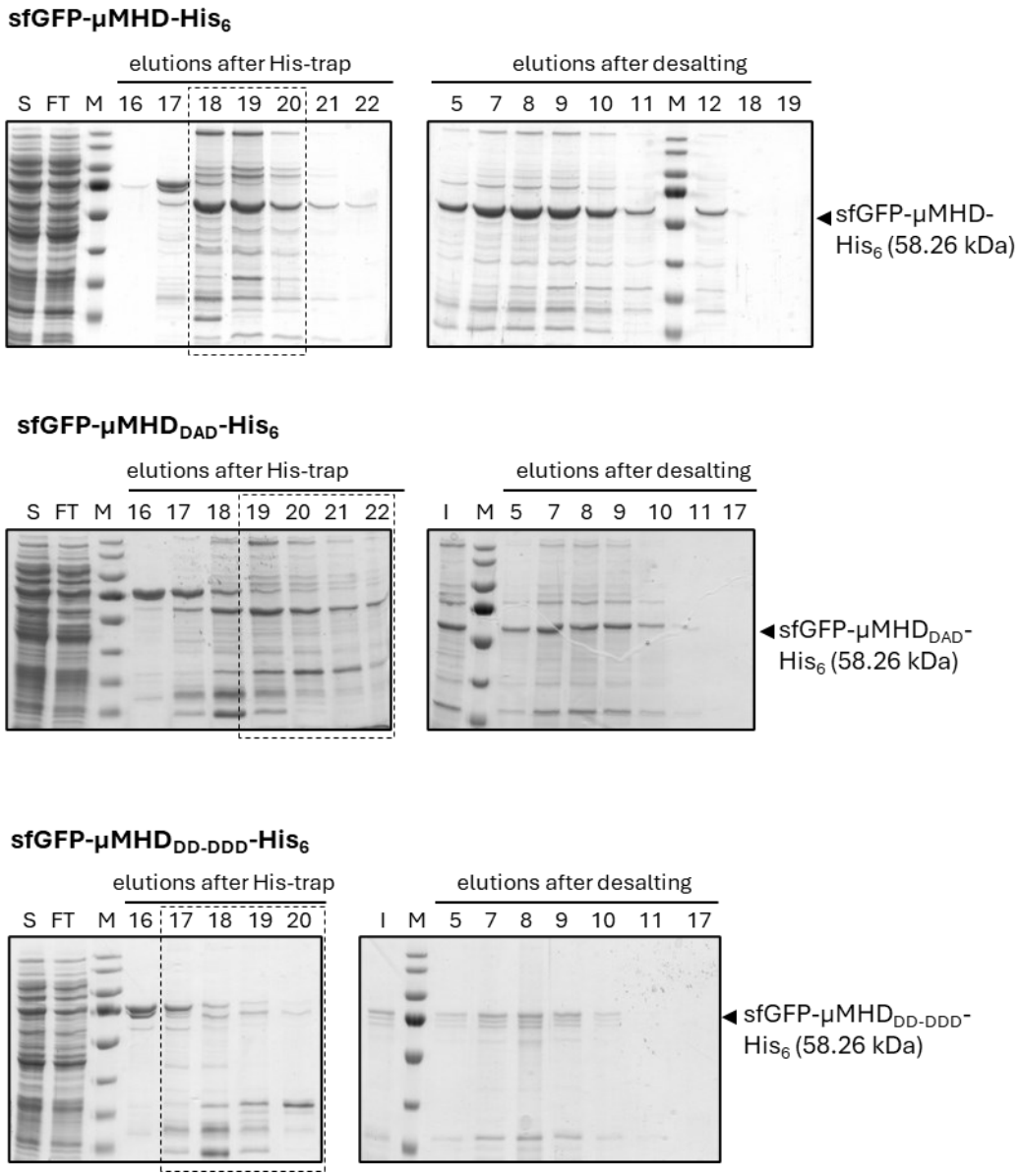

Figure 28. Enrichment of sfGFP-µMHD-His$_6$, sfGFP-µMHD$_{DAD}$-His$_6$ and sfGFP-µMHD$_{DD-DDD}$-His$_6$. Displayed are Coomassie-stained SDS-PAGE gels of the enriched fusion proteins. Fusion proteins were expressed in *E. coli* Rosetta2 and enriched with a HisTrap HP His-tag protein purification column using the ÄKTA pure™ system. After the HisTrap column, a buffer exchange was performed with selected elution fractions (indicated by dashed lines) using HiTrap desalting columns. 10 µl of protein-sample were applied to an SDS-PAGE, PageRuler™ Prestained Protein Ladder was used as molecular size marker and proteins were stained with Coomassie. S: soluble fraction after cell disruption; FT: flow through. Black arrowheads mark the expected molecular size of the fusion proteins.

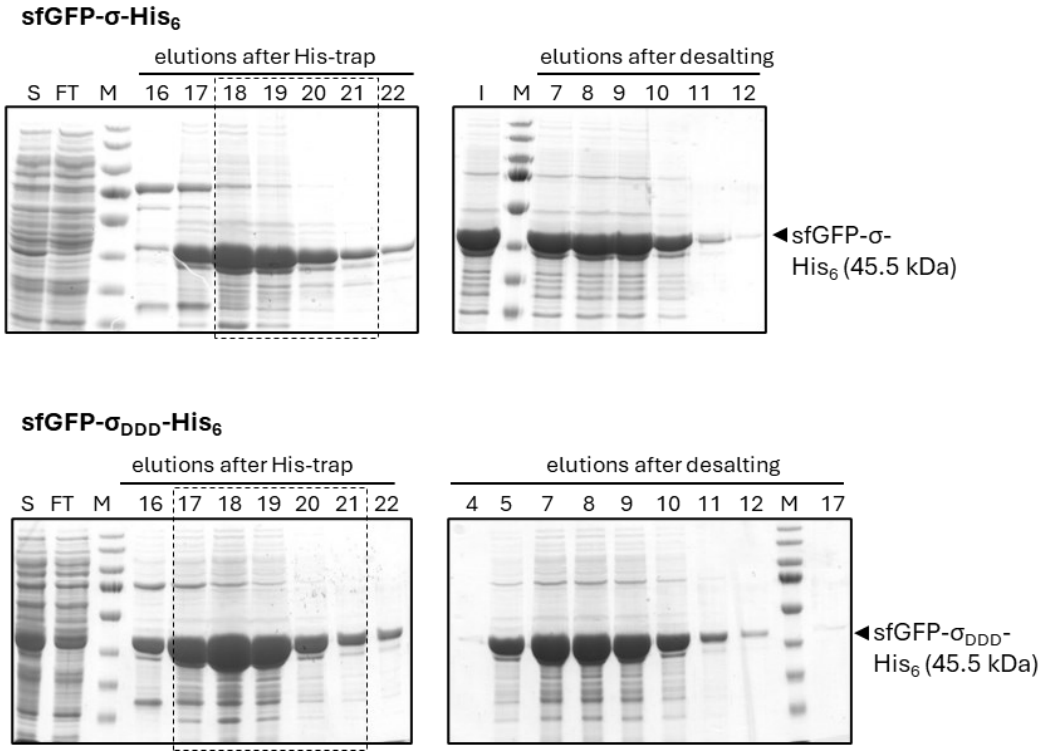

Figure 29. Enrichment sfGFP-σ-His$_6$ and sfGFP-σ$_{DDD}$-His$_6$. Displayed are Coomassie-stained SDS-PAGE gels of the enriched fusion proteins. Fusion proteins were expressed in *E. coli* Rosetta2 and enriched with a HisTrap HP His-tag protein purification column using the ÄKTA pure™ system. After the HisTrap column, a buffer exchange was performed with selected elution fractions (indicated by dashed lines) using HiTrap desalting columns. 10 µl of protein-sample were applied to an SDS-PAGE, PageRuler™ Prestained Protein Ladder was used as molecular size marker and proteins were stained with Coomassie. S: soluble fraction after cell disruption; FT: flow through. Black arrowheads mark the expected molecular size of the fusion proteins.

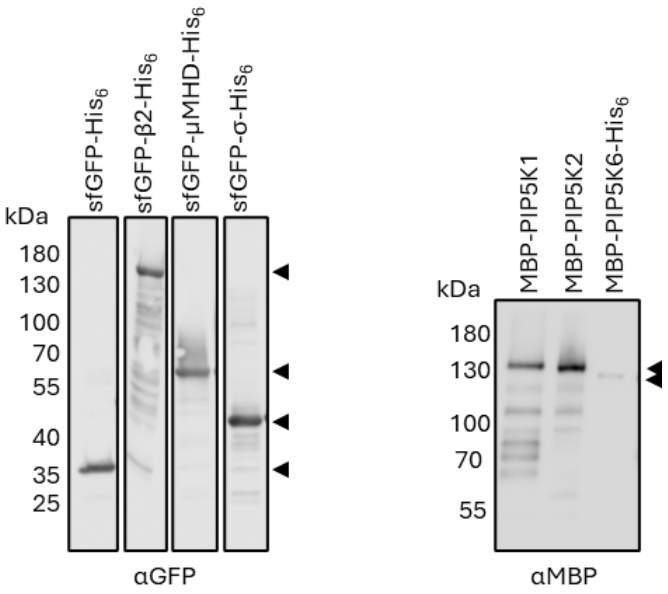

Figure 30. Immuno detection of proteins used in MST protein-protein interaction assays. Proteins were applied to an SDS-PAGE with concentration ratios used in MST measurements. After transferring to a nitrocellulose membrane, target proteins were detected by αGFP antibodies (left panel) and ligand proteins by αMBP antibodies (right panel). Black arrowheads mark the expected molecular size of the fusion proteins: sfGFP-β2-His_6 , 127.5 kDa; sfGFP-μMHD-His_6, 58.26 kDa; sfGFP-σ-His_6, 45.5 kDa; sfGFP-His_6, 28.5 kDa; MBP-PIP5K1/2, 128 kDa; MBP-PIP5K6-His_6, 123 kDa. MBP-PIP5K1/2 was enriched by Dr. Lennart Schwalgun (Dept. of Plant Biochemistry) and MBP-PIP5K6-His_6 by Dr. Alexandra Schutkowski (Dept. of Plant Biochemistry).

Table 14. Signal to noise ratio and response amplitude of the protein-protein interaction MST-assays. Signal to noise ratios below 5 are considered too low. The response amplitude is defined as the difference between the MST signal of the target and of the target-ligand-complex. Response amplitudes below 1.5 are considered too low. Data represent the mean values of four independent MST-measurements each.

	signal to noise ratio			**response amplitude**		
	MBP-PIP5K1	MBP-PIP5K2	MBP-PIP5K6-His_6	MBP-PIP5K1	MBP-PIP5K2	MBP-PIP5K6-His_6
sfGFP-His_6	2.7	n.a.	n.a.	1.0	n.a.	n.a.
sfGFP-β2-His_6	7.3	28.9	8.9	5.1	31.5	5.2
sfGFP-μMHD-His_6	19	57.7	13.1	18.4	55.2	10.3
sfGFP-σ-His_6	9.4	31.8	5.8	3.6	21.2	2.5

Table 15. Signal to noise ratio and response amplitude of the protein-lipid interaction MST-assays. Signal to noise ratios below 5 are considered too low. The response amplitude is defined as the difference between the MST signal of the target and of the target-ligand-complex. Response amplitudes below 1.5 are considered too low. Data represent the mean values of four independent MST-measurements each.

	signal to noise ratio			**response amplitude**		
	PtdIns(4,5)P_2	PtdIns4P	PtdOH	PtdIns(4,5)P_2	PtdIns4P	PtdOH
sfGFP-α1NT-His_6	10.1	6.7	20.2	3.1	5.9	15.0
sfGFP-α1NT_{DDDD}-His_6	5.4	12.8	19.0	3.2	11.7	18.3
sfGFP-His_6	n.a.	169.0	n.a.	n.a.	48.2	n.a.
sfGFP-σ-His_6	6.9	6.1	18.7	4.1	5.9	14.3
sfGFP-$σ_{DDD}$-His_6	7.0	11.0	15.8	5.3	7.4	9.8
sfGFP-His_6	161.4	153.6	n.a.	31.4	38.3	n.a.
sfGFP-μMHD-His_6	25.4	17.1	21.3	23.8	18.5	18.8
sfGFP-μMHD_{DAD}-His_6	30.0	21.0	13.1	25.3	23.2	15.3
sfGFP-μMHD_{DD-DDD}-His_6	41.2	19.3	34.5	26.6	13.8	19.5
sfGFP-His_6	n.a.	n.a.	n.a.	n.a.	n.a.	n.a.

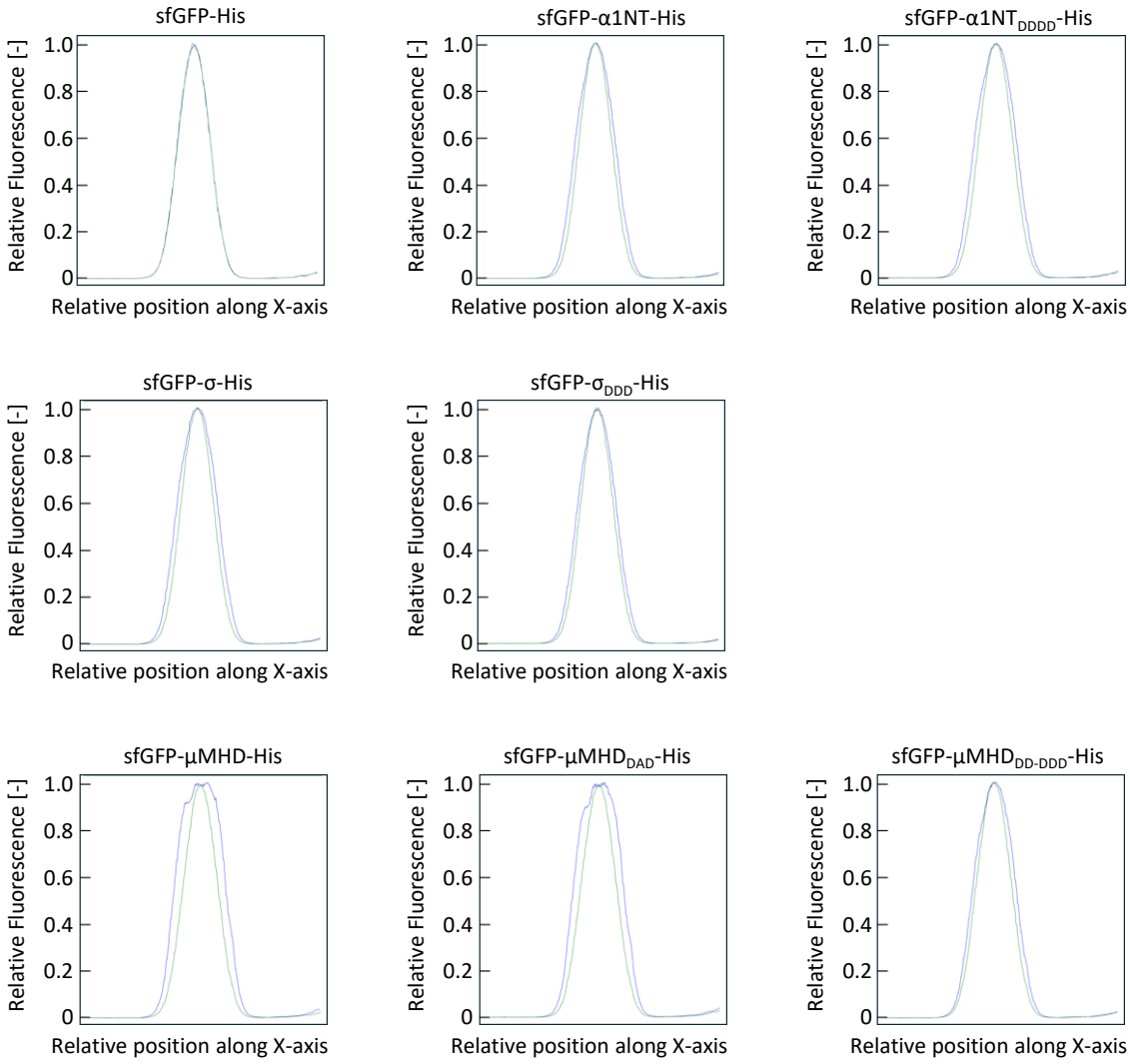

Figure 31. Capillary cross-scans of sfGFP-His$_6$ fusion proteins used for MST measurements. Capillary shapes reflect the fluorescence profile along the diameter of the capillary measured before the IR-laser impulse (green curve) and after the IR-laser impulse (blue curve). Shown are representative capillary shapes for sfGFP-His$_6$, sfGFP-α1NT/α1NT$_{DDDD}$-His$_6$, sfGFP-σ/σ$_{DDD}$-His$_6$ and sfGFP-μMHD/μMHD$_{DAD}$/μMHD$_{DD-DDD}$-His$_6$ from one capillary each.

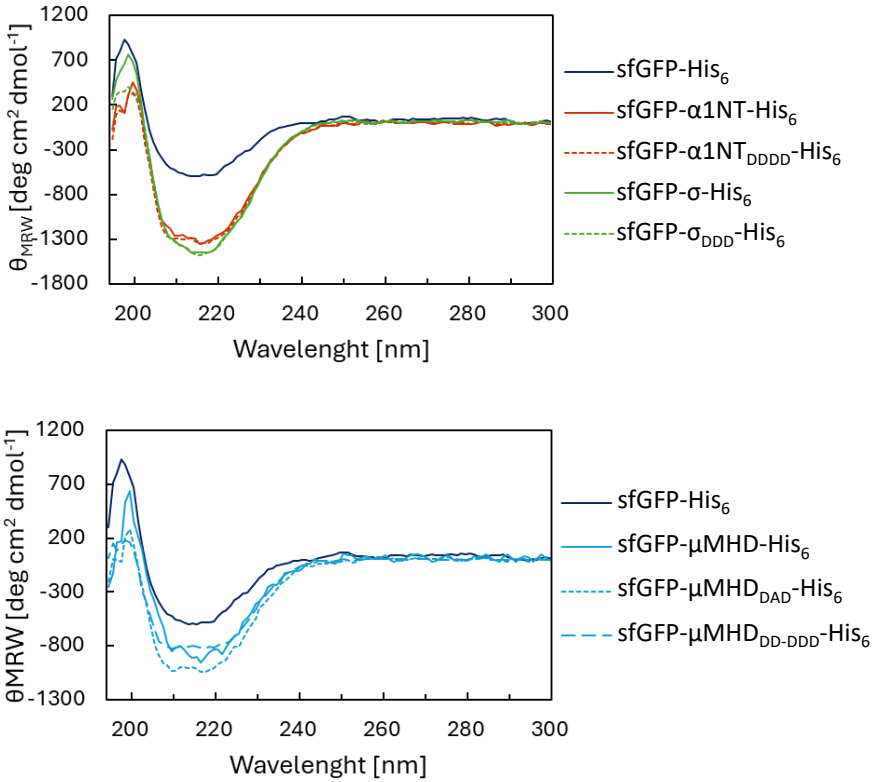

Figure 32. CD-spectra of enriched sfGFP-His$_6$ fusion proteins. Data were obtained for the far- and near-UV range using an optical path length of 1 mm. Measurements were performed at 20 °C, with 50 nm/min scan speed, 1 nm pitch, 1 nm slit widths and 1 s response time and 16 accumulations. CD-spectra were corrected by the buffer-signal and converted to the mean residue ellipticity. Each spectrum was recorded once.

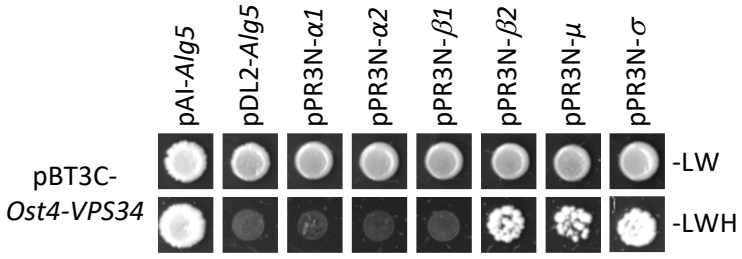

Figure 33. AP2-subunits interact with VPS34 in yeast two-hybrid analysis. Split-ubiquitin based yeast two-hybrid with VPS34 fused to the C-terminal ubiquitin half, an Ost4 ER membrane-anchor and transcription factors as bait protein. AP2-subunits were used as prey proteins fused to the N-terminal ubiquitin half, pAI-Alg5 and pDL2-Alg5 were used as positive and negative control. Transformed yeast was grown on selective media lacking leucine and tryptophan (-LW) as control for transformation with bait and prey vectors. Growth on media lacking additional histidine (-LWH) indicated protein-protein interaction. Data is representative for three independent experiments testing five colonies each per transformation.

7.2 Additional information on material and methods

7.2.1 Phospholipids

Table 16. Phospholipids used in this study. All Phospholipids were purchased from Avanti Polar Lipids Inc. (Merck, Darmstadt, Germany).

Phospholipid	Product number
18:1 PtdIns3P	850150P
18:1 PtdIns4P	850151P
18:1 PtdIns5P	850152P
18:1 PtdIns(3,5)P_2	850154P
18:1 PtdIns(4,5)P_2	850155P
18:1 PtdCho	850375P
18:1 PtdOH	840875P
18:1 PtdEtn	850725P
18:1 PtdSer	840035P
18:1 PtdIns	850142P

7.2.2 Oligonucleotides

Table 17. Oligonucleotides used for genotyping.

Plant line	Name	Sequence (5'-3')
SALK	Salk_LB3.1	ATTTTGCCGATTTCGGAAC
SAIL	Sail_LB1	GCCTTTTCAGAAATGGATAAATAGCCTTGCTTCC
ap2α1	A1LP	ATTTCTTCGATTGAAGGTGCC
(SALK_045252C)	A1RP	CATATGGCCAAAATCCACATC
ap2μ	μLP	TCACTTGGAAATTGGTCTTGG
(SAIL_165_A05)	μRP	CAAACCTGTTCCAAATGCAAC
ap2σ	σLP	TGGAACTTCAGGGAAACTGTG
(SALK_141555)	σRP	TTGTTTGCGAAAATCAAAAGC
pip5k1 pip5k2	PIP5K1LP	ACTAAAGGGCAATAATCCTTCCACC
(SALK_146728-pip5k1)	PIP5K1RP	GCAAATTCTCATGGCCAAGTGGA
(SALK_012487-pip5k2)	PIP5K2LP	CAGGTTTGATACAATGCACACCAT
	PIP5K2RP	TGGGAGTCTGATGGAGAAGCTG
loh1 loh3	Loh1LP	TTCCTTCTTATGTGATTGTAAAGAGAA
(SALK_080371-loh1)	Loh1RP	TGGTTGATCAGGCCAAATCT
(SALK_150849-loh3)	Loh3LP	TTCTCGATTTTGTGCTTGCTC
	Loh3RP	CACCCATTAGCGATCAGAATC

Table 18. Oligonucleotides used for cloning.

cDNA	Oligoname Sequence (5'-3')	Vector
pAP2-α1	pAP2A1_for ATGCGGCCATTACGGCCATATACAACCAGATTTTTACTAT	*pEntryA*
	pAP2A1_rev ATGCGGCCGAGGCGGCCGGTTGAACCAAATCCTCAAATCC	*pEntryA*
pAP2-μ	pAP2mu_for ATGCGGCCATTACGGCCTAACCCCAGATATCAAATTC	*pEntryA*
	pAP2mu_rev ATGCGGCCGAGGCGGCCCTTCGATCTGAGATTCGAAA	*pEntryA*
pAP2-σ	pAP2S_for ATGCGGCCATTACGGCCTACTTGGACCTCTACTTCAT	*pEntryA*
	pAP2S_rev ATGCGGCCGAGGCGGCCTTTCTCTGCAAAATCTAATG	*pEntryA*
AP2-α1/α1$_{DDDD}$	AP2A1/2-pBT3C_for ATGCGGCCATTACGGCCAATGACCGGAATGAGAGGTCT	*pBT3-C-OST4*
	AP2A1-pBT3C_rev ATGCGGCCGAGGCGGCCAAAAGTAAGCCAGCGAGCAT	*pBT3-C-OST4*
	AP2-A1-AscIfor ATGCGGCGCGCCATGACCGGAATGAGAGGTCT	*pEntryD* *pEntryA*
	AP2-A1-NheIrev-stop ATGCGCTAGCAAGTAAGCCAGCGAGCATAGC	*pEntryD*
	AP2A1-NheIrev+stop ATGCGCTAGCTTAAAGTAAGCCAGCGAGCAT	*pEntryA*
	B1-Alpha1-sense GGGGACAAGTTTGTACAAAAAAGCAGGCTTAATGACCGGAATGAG AGGTCT	*pDONR^{TM}-221-P1P4*
	B4-Alpha1-anti GGGGACAACTTTGTATAGAAAAGTTGGGTGAAGTAAGCCAGCGAG CATAG	*pDONR^{TM}-221-P1P4*
AP2-α1NT/α1NT$_{DD}$ $_{DD}$	A1NT-NotIfor ATGCGCGGCCGCATGACCGGAATGAGAGGTCT	*pMAL-c5G*
	A1NT-BamHIrev ATGCGGATCCTTAAGACGTCAAGACACCAAGAT	*pMAL-c5G*
	A1NT-SalIfor ATGCGTCGACATGACCGGAATGAGAGGTCT	*pET-28b(+)*

	A1NT-NotI-rev-stop ATGCGCGGCCGCAGACGTCAAGACACCAAGA	*pET-28b(+)*
AP2-α2	AP2A1/2-pBT3C_for ATGCGGCCATTACGGCCAATGACCGGAATGAGAGGTCT	*pBT3-C-OST4*
	AP2A2-pBT3C_rev ATGCGGCCGAGGCGGCCAAGTAAGCCAGCAAGCAT	*pBT3-C-OST4*
AP2-β2	AP2B2-pBT3C-for ATGCGGCCATTACGGCCAATGAGCGGTCATGATTCTAA	*pBT3-C-OST4*
	AP2B2-pBT3C-rev ATGCGGCCGAGGCGGCCAAAGCCTTGAAGAGAATTTCGA	*pBT3-C-OST4*
	AP2B2-SalI-for ATGCGTCGACATGAGCGGTCATGATTCTAA	*pET-28b(+)*
	AP2B2-NotI-rev-stop ATGCGCGGCCGCAGCCTTGAAGAGAATTT	*pET-28b(+)*
	B1-Beta2-sense GGGGACAAGTTTGTACAAAAAAGCAGGCTTAATGAGCGGTCATGA TTCTAA	*pDONR™-221-P1P4*
	B4-Beta2-anti GGGGACAACTTTGTATAGAAAAGTTGGGTGAGCCTTGAAGAGAAT TTCGA	*pDONR™-221-P1P4*
AP2-μ/μ_{DAD}/μ_{DD-DDD}	AP2mu-pBT3C-for ATGCGGCCATTACGGCCAATGCCGGTGGCTGCTTCCG	*pBT3-C-OST4*
	AP2mu-pBT3C-rev ATGCGGCCGAGGCGGCCAAGCATCTGATCTCGTAAGAT	*pBT3-C-OST4*
	MU-NotIfor ATGCGCGGCCGCATGCCGGTGGCTGCTTCCGCCAT	*pMAL-c5G*
	MU-SalIrev ATGCGTCGACTCAGCATCTGATCTCGTAAGAT	*pMAL-c5G*
	AP2-mu-AscIfor ATGCGGCGCGCCATGCCGGTGGCTGCTTCCG	*pEntryA*
	AP2-M-NotIrev ATGCGCGGCCGCTCAGCATCTGATCTCGTAAGA	*pEntryA*
	B3-mu-sense GGGGACAACTTTGTATAATAAAGTTGGAATGCCGGTGGCTGCTTCC G	*pDONR™-221-P3P2*
	B2-mu-anti	*pDONR™-221-P3P2*

	GGGGACCACTTTGTACAAGAAAGCTGGGTGGCATCTGATCTCGTA AGATC	
	B2-mu-anti+stop GGGGACCACTTTGTACAAGAAAGCTGGGTTCAGCATCTGATCTCGT AAGATC	*pDONR™-221-P3P2*
	B1-mu-sense GGGGACAAGTTTGTACAAAAAAGCAGGCTTAATGCCGGTGGCTGC TTCCG	*pDONR™-221-P1P4*
	B4-mu-anti GGGGACAACTTTGTATAGAAAAGTTGGGTGGCATCTGATCTCGTA AGATC	*pDONR™-221-P1P4*
AP2-µMHD/ µMHD$_{DAD}$/ µMHD$_{DD-DDD}$	muMHD-NotIfor ATGCGCGGCCGCATGAAGAATGAGGTGTTTC	*pMAL-c5G*
	MU-SalIrev ATGCGTCGACTCAGCATCTGATCTCGTAAGAT	*pMAL-c5G*
	µMHD-SalI-for ATGCGTCGACATGAAGAATGAGGTGTTTC	*pET-28b(+)*
	µMHD-NotI-rev-stop ATGCGCGGCCGCGCATCTGATCTCGTAAGAT	*pET-28b(+)*
AP2-σ/σ$_{DDD}$	AP2sigmaNdeI-for ATGCCATATGATCCGATTCATATTATT	*pMAL-c5G*
	AP2sigmaEcoRI-rev ATGCGAATTCTCACTGTAGCTTCTCGAGTT	*pMAL-c5G*
	AP2-S-SalI-for ATGCGTCGACATGATCCGATTCATATTATT	*pET-28b(+)*
	AP2S-NotI-rev-stop ATGCGCGGCCGCCTGTAGCTTCTCGAGTTCT	*pET-28b(+)*
	AP2-S-AscIfor ATGCGGCGCGCCATGATCCGATTCATATTATT	*pEntryD pEntryA*
	AP2-S-NheIrev-stop ATGCGCTAGCCTGTAGCTTCTCGAGTTCT	*pEntryD*
	AP2S-NheIrev+stop ATGCGCTAGCTCACTGTAGCTTCTCGAGTTCT	*pEntryA*
	B3-AP2S-sense GGGGACAACTTTGTATAATAAAGTTGGAATGATCCGATTCATATTA TT	*pDONR™-221-P3P2*

	B2-AP2S-anti GGGGACCACTTTGTACAAGAAAGCTGGGTCTGTAGCTTCTCGAGTTCT	*pDONR^{TM}-221-P3P2*
	B2-AP2S-anti+stop GGGGACCACTTTGTACAAGAAAGCTGGGTTCACTGTAGCTTCTCGAGTTCT	*pDONR^{TM}-221-P3P2*
	B1-Sigma-sense GGGGACAAGTTTGTACAAAAAAGCAGGCTTAATGATCCGATTCATATTATT	*pDONR^{TM}-221-P1P4*
	B4-Sigma-anti GGGGACAACTTTGTATAGAAAAGTTGGGTGCTGTAGCTTCTCGAGTTCTG	*pDONR^{TM}-221-P1P4*
PIP5K1	B3-PIP5K1sense GGGGACAACTTTGTATAATAAAGTTGGAATGAGTGATTCAGAAGAAGAC	*pDONR^{TM}-221-P3P2*
	B2-PIP5K1anti GGGGACCACTTTGTACAAGAAAGCTGGGTGGCCCTCTTCAATGAAGATCC	*pDONR^{TM}-221-P3P2*
	B1-PIP5K1sense GGGGACAAGTTTGTACAAAAAAGCAGGCTTAATGAGTGATTCAGAAGAAGAC	*pDONR^{TM}-221-P1P4*
	B4-PIP5K1anti GGGGACAACTTTGTATAGAAAAGTTGGGTGTTAGCCCTCTTCAATGAAGAT	*pDONR^{TM}-221-P1P4*
sfGFP	sfGFP-NcoI-for+2 ATGCCCATGGGCATGAGTAAAGGCGAAGAGCTGTT	*pET-28b(+)*
	sfGFP-SalI-rev-stop ATGCGTCGACTTTATACAGCTCGTCCATCC	*pET-28b(+)*
RbohD	RBOHD_ascIfor ATGCGGCGCGCCAAAATGAGACGAGGCAATTC	*pEntryA*
	RBOHD_BamHIrev ATGCGGATCCCTAGAAGTTCTCTTTGTGGA	*pEntryA*

Table 19. Oligonucleotides used for mutagenesis PCR.

cDNA	**Oligoname** **Sequence (5'-3)**
AP2-α1$_{DDDD}$	AP2A1mut_DDDDfor

	TTTTGACACCATATGATGATGATGATTATGTCTGGAAAAT
	AP2A1mut_DDDDrev
	ATTTTCCAGACATAATCATCATCATCATATGGTGTCAAAA
AP2-μ_{DAD}	AP2mu_DADfor
	AATACAATCCATCAGATGCAGATTTGGTTTGGAAGAT
	AP2mu_DADrev
	ATCTTCCAAACCAAATCTGCATCTGATGGATTGTATT
AP2-μ_{DD-DDD}	AP2mu_mutDfor
	TACAATCCATCAATCGATTGCTTGGTTTGGGATATAGATGATTTCCCAGGGCAAA
	AP2mu_mutDrev
	CCAAACCAAGCAATCGATTGATGGATTGTAATCAGCATCACCAGTTGT
AP2-σ_{DDD}	AP2S_mutDDD_for1
	ATGCCATATGATGATCCGATTCATATTATTGCAGAACGATCAAGGTAAGACTCGT
	AP2_mutDDD_rev1
	CCTGTATATCACCTTGTGTGTATCAAACTCAAC
	AP2_mutDDD_for2
	ACACACAAGGTGATATACAGGGATTATGCTGGATTGTTTTTC

Table 20. Oligonucleotides used for sequencing.

cDNA	**Oligoname**	**Sequence (5'-3)**
pMAL-c5G	pMAL-for	ATGCCGAACATCCCGCAGAT
	pMAL-rev	TTGTCCTACTCAGGAGAGCGTT
pCaMV35S	35S-for	TATATAAGGAAGTTCATTT
pT7	T7-for	TAATACGACTCACTATAGGG
	M13-for	CCCAGTCACGACGTTGTAAAACG
EYFP	VYFP-for	CTGAAGTTCATCTGCACCACCGGCAAG
	VYFP-rev	CTTGCCGGTGGTGCAGATGAACTTCAG
	HYFP-for	TACCAGTCCGCCCTGAGCAAAGA
mCherry	HmCherry-rev	GTCTTGACCTCAGCGTCGTAG
AP2-α1/α1$_{DDDD}$	AP2-A1for	ATGACCGGAATGAGAGGTCT
AP2-α1NT/α1NT$_{DDDD}$	AP2-A1m1for	TCCAGGTTAAGGCAATGA
	AP2-A1m2for	TTCTAGCTAGACAACCTGG
	AP2-A1m3for	TTGGCATCAAAGCTGAAT
	AP2-A1rev	TTAAAGTAAGCCAGCGAG

	AP2-A1m1rev	TATCGTTCCGCACTGTATT
	AP2-A1m2rev	GACAACTTGAGTACGCCTC
	A1/2_NT_rev	TTAAGACGTCAAGACACCAA
AP2- α2	AP2-A2for	ATGACCGGAATGAGAGGTCT
	AP2-A2m1for	CAGGTTAAGGCAATGAGGGC
	AP2-A2m2for	TGAACTCTTTAGCATCTTAC
	AP2-A2m3for	CATCAAAGCTGAATGGAGAG
	AP2-A2rev	TTAAAGTAAGCCAGCAAG
	AP2-A2m1rev	CAGTGCGGAACGATATTAT
AP2-β2	AP2-B2-for	ATGAGCGGTCATGATTCTAA
	AP2-B2-rev	TCAAGCCTTGAAGAGAATTT
	AP2-B2-m1for	ACTAGCACAGATGTGATTCG
	AP2-B2-m2for	TCTATCGACTGATCCTGAGG
	AP2-B2m1rev	GTGTGATCCTCTTCAGAAA
AP2-μ/μ_{DAD}/μ_{DD-DDD}	AP2-mufor	ATGCCGGTGGCTGCTTCCG
AP2-μMHD/	AP2-mu-m1for	AAAGGCAATGTTCTTCGGT
μMHD_{DAD}/	AP2-murev	TCAGCATCTGATCTCGTAA
μMHD_{DD-DDD}	AP2-mum1rev	AGACGCTATTAGAAATAACT
AP2-σ/σ_{DDD}	AP2-Sigmafor	ATGATCCGATTCATATTATT
	AP2-Sigmarev	TCACTGTAGCTTCTCGAGTT
RbohD	RBOHD_for	ATGAAAATGAGACGAGGCAA
	RBOHD_m1for	TCTCCGGCGATGCAATCACA
	RBOHD_m2for	AGCGGGATAGTCGTCGGTGT
	RBOHD_m3for	TTCTCCGAGCAGACGGAGGA

Figures

Tables

Danksagung

An dieser Stelle möchte ich mich bei vielen Leuten herzlich bedanken, ohne die diese Arbeit so nicht entstanden wäre.

Mein größter Dank gilt dabei Prof. Dr. Ingo Heilmann. Du hast mir die Möglichkeit gegeben an diesem spannenden Thema zu arbeiten. Vielen Dank für deine Betreuung, unzählige Meetings mit vielen Diskussionen und Denkanstößen, viele aufmunternde Worte und deine Unterstützung beim Anfertigen dieser Arbeit. Danke für dein Vertrauen, deine ansteckende Begeisterung über neue Ergebnisse und viele lustige Momente.

Vielen Dank auch an Dr. Mareike Heilmann. Danke für deine Hilfe im Labor, für all deine Ideen und Anregungen zum Projekt. Danke nicht nur für die fachliche Hilfe, sondern auch für dein immer offenes Ohr egal zu welchem Thema und viele lange Gespräche.

Ingo und Mareike, über die letzten Jahre habe ich die tolle Arbeitsatmosphäre in eurer Gruppe zu schätzen gelernt. Danke für die vielen schönen und lehrreichen Jahre die ich mittlerweile seit meiner Bachelorarbeit bei euch verbringen durfte. Mir haben unsere Ausflüge nach Amsterdam und Prag sehr viel Spaß gemacht!

Ich möchte auch den Gutachtern für die Zeit danken, die sie meiner Arbeit widmen.

Mein Dank gilt auch der Finanzierung durch die Deutsche Forschungsgesellschaft im Rahmen des Projektes He3424/6-2.

Ich habe auch außerhalb der AG Heilmann viel Hilfe und Unterstützung erhalten. Ein großes Dankeschön geht dabei an Dr. Diana Kalbas für die Einführung und Hilfe bei den MST-Experimenten, ohne die ich diese Methode wahrscheinlich nicht hätte nutzen können. Vielen Dank auch an Prof. Dr. Kirsten Bacia für die Bereitstellung des Spinning-Disk Mikroskops und PD Dr. Hauke Lilie für den sfGFP Klon. Danke an PD Dr. Schiene-Fischer für die Hilfe mit der CD-Spektroskopie und dass ich das Gerät nutzen konnte. Vielen Dank auch an alle die mir geholfen haben das Di-4-ANEPPDHQ ImageJ Makro wieder zum Laufen zu bringen: Dr. Praveen Krishnamoorthy, Dr. Jan Ebenhan und PD Dr. Birgit Möller.

Ich möchte an dieser Stelle auch allen aktuellen und ehemaligen Mitgliedern der AG Heilmann danken. Danke für die Bereitstellung von Plasmiden, Proteinen und eure Hilfsbereitschaft im Labor. Danke an Marion und Kristin für die Unterstützung durch viele technische Arbeiten und die Hilfe bei etlichen Genotypisierungen. Ihr habt mir viel Arbeit abgenommen. Danke Vera für die Hilfe mit den Pollenschlauch-Experimenten und dem Spinning-Disk Mikroskop.

Ein großes Dankeschön geht an alle meine Doktoranden-Kollegen und Kolleginnen über die Jahre, für viele schöne, lustige und auch konstruktive Kaffeepausen, Mittagessen oder gemeinsame Kochabende. Danke Angela, Johanna und Ema für lustige Stunden in unserem Büro.

Zu guter Letzt ein riesiges Dankeschön an meine Familie und Freunde. Danke für eure Unterstützung!

Curriculum Vitae

Johanna Uhlenberg

Education

since 03.2021	**Research assistant - PhD student**
	Martin Luther University Halle-Wittenberg
	Department of Plant Biochemistry
10.2018 - 12.2020	**Master of Science (Biochemistry)**
	Martin Luther University Halle-Wittenberg
10.2015 - 09.2018	**Bachelor of Science (Biochemistry)**
	Martin Luther University Halle-Wittenberg
08.2007 - 07.2015	**A-levels (Allgemeine Hochschulreife)**
	Immanuel-Kant-Gymnasium Lachendorf

Publications and Conferences

Launhardt L, Uhlenberg J, Stellmach H, Schomburg M, Hause B, Heilmann I, Heilmann M (2023) Association of the Arabidopsis oleoyl Δ12-desaturase FAD2 with pre-cis-Golgi stacks at endoplasmic reticulum-Golgi-exit sites. Plant J 117: 242-263.

Johanna Uhlenberg, Mareike Heilmann, Ingo Heilmann (09.2024) The role of regulatory lipids during the regulation of endocytosis at the plant plasma membrane. Botanik-Tagung 2024, Halle (Saale) (Poster).

Johanna Uhlenberg, Ingo Heilmann (06.2024) Characterization of lipid-binding features of Arabidopsis endocytic adaptor complex 2 (AP2)-subunits, and a possible link to actin. European Plant Cytoskeletal Club 2024, Prague (Poster).

Johanna Uhlenberg, Ingo Heilmann (07.2023) The role of regulatory lipids during the initiation of endocytosis at the plant plasma membrane. 10th European Symposium on Plant Lipids, Amsterdam (Poster).

Erklärung

Hiermit erkläre ich, dass ich die vorliegende Dissertation selbständig und ohne fremde Hilfe verfasst habe, keine anderen als die angegebenen Quellen und Hilfsmittel benutzt habe und die den benutzten Werken wörtlich oder inhaltlich entnommenen Stellen als solche kenntlich gemacht habe.

Des Weiteren erkläre ich, bisher keine vergeblichen Promotionsversuche unternommen zu haben und die Dissertation in der gegenwärtigen bzw. in einer anderen Fassung nicht bereits an einer anderen Fakultät vorgelegt zu haben.

Halle (Saale), _____ _____

Johanna Uhlenberg